NUMERICAL MODELLING OF TWO HMX-BASED PLASTIC-BONDED EXPLOSIVES AT THE MESOSCALE

Caroline A. Handley

A Thesis Submitted for the Degree of PhD
at the
University of St. Andrews

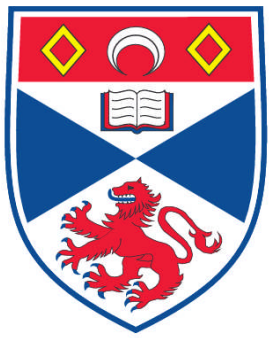

2011

Numerical modelling of two HMX-based plastic-bonded explosives at the mesoscale

Caroline A. Handley

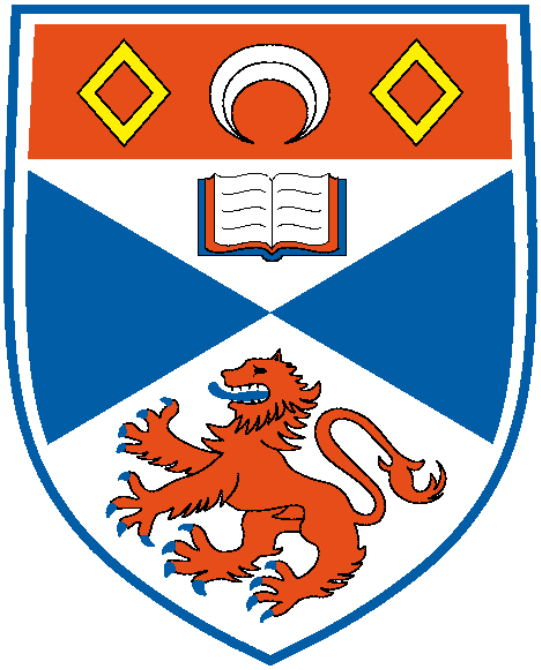

Thesis submitted for the degree of Doctor of Philosophy
of the University of St Andrews

January 31, 2011

Abstract

Mesoscale models are needed to predict the effect of changes to the microstructure of plastic-bonded explosives on their shock initiation and detonation behaviour. This thesis describes the considerable progress that has been made towards a mesoscale model for two HMX-based explosives PBX9501 and EDC37. In common with previous work in the literature, the model is implemented in hydrocodes that have been designed for shock physics and detonation modelling. Two relevant physics effects, heat conduction and Arrhenius chemistry, are added to a one-dimensional Lagrangian hydrocode and correction factors are identified to improve total energy conservation. Material models are constructed for the HMX crystals and polymer binders in the explosives, and are validated by comparison to Hugoniot data, Pop-plot data and detonation wave profiles. One and two-dimensional simulations of PBX9501 and EDC37 microstructures are used to investigate the response of the bulk explosive to shock loading. The sensitivity of calculated temperature distributions to uncertainties in the material properties data is determined, and a thermodynamic explanation is given for time-independent features in temperature profiles. Hotspots are widely accepted as being responsible for shock initiation in plastic-bonded explosives. It is demonstrated that, although shock heating of crystals and binder is responsible for temperature localisation, it is not a feasible hotspot mechanism in PBX9501 and EDC37 because the temperatures generated are too low to cause significant chemical reaction in the required timescales. Critical hotspot criteria derived for HMX and the binders compare favourably to earlier studies. The speed of reaction propagation from hotspots into the surrounding explosive is validated by comparison to flame propagation data, and the temperature of the gaseous reaction products is identified as being responsible for negative pressure dependence. Hotspot size, separation and temperature requirements are identified which can be used to eliminate candidate mechanisms in future.

Declaration

1. Candidate's declarations:

   I, Caroline Angela Handley, hereby certify that this thesis, which is approximately 54,000 words in length, has been written by me, that it is the record of work carried out by me and that it has not been submitted in any previous application for a higher degree.

   I was admitted as a research student in September 2004 and as a candidate for the degree of PhD in October 2005; the higher study for which this is a record was carried out in the University of St Andrews between 2004 and 2010.

   date ..... signature of candidate .....

2. Supervisor's declaration:

   I hereby certify that the candidate has fulfilled the conditions of the Resolution and Regulations appropriate for the degree of PhD in the University of St Andrews and that the candidate is qualified to submit this thesis in application for that degree.

   date ..... signature of supervisor .....

3. Permission for electronic publication:

   In submitting this thesis to the University of St Andrews I understand that I am giving permission for it to be made available for use in accordance with the regulations of the University Library for the time being in force, subject to any copyright vested in the work not being affected thereby. I also understand that the title and the abstract will be published, and that a copy of the work may be made and supplied to any bona fide library or research worker, that the thesis will be electronically accessible for personal or research use unless exempt by award of an embargo as requested below, and that the library has the right to migrate the thesis into new electronic forms as required to ensure continued access to the thesis. I have obtained any third-party copyright permissions that may be required in order to allow such access and migration, or have requested the appropriate embargo below.

   The following is an agreed request by candidate and supervisor regarding the electronic publication of this thesis. Access to printed copy and electronic publication of thesis through the University of St Andrews.

   date ..... signature of candidate .....

   date ..... signature of supervisor .....

Acknowledgments

I would like to thank my supervisors Dr Alec Milne (Fluid Gravity Engineering Ltd, St Andrews) and Prof. Alan Hood (School of Mathematics and Statistics, University of St Andrews) for their help and guidance throughout the course of this work. I am grateful to Dr Aaron Longbottom (Fluid Gravity), Dr Nicholas Whitworth and Dr Peter Langridge (both at AWE, Aldermaston), who provided me with source code and documentation for ReactDiff, Peruse and Petra respectively. I also thank members of the Material Modelling Group at AWE for many useful discussions, especially Hugh James, Brian Lambourn and Dr Graham Ball. Jack Reaugh (Lawrence Livermore National Laboratory) and Dr Greg Pearce have been a great help in proof-reading this thesis. Thanks are also due to my husband Nicholas Handley, my parents Nigel and Angela Charlwood and my parents-in-law Stephen and Vivienne Handley for their patience during my PhD studies. I also gratefully acknowledge the financial support of AWE. This thesis has been approved for release by the Ministry of Defence and is copyright:

Contents

Notation and units

Symbol	Meaning	Unit
3α	volume coefficient of thermal expansion	K^{-1}
β_{L}	linear artificial viscosity coefficient	-
β_{Q}	quadratic artificial viscosity coefficient	-
γ	ratio of specific heat capacities for an ideal gas	-
Γ	Grüneisen gamma	-
λ	burn fraction	-
ρ	density	g/cm^3
ρ_0	initial density	g/cm^3
$\phi(S)$	function of entropy	kJ/g
χ	correction factor	$\mathrm{J}/\mathrm{g}\,\mathrm{K}$
a	Hugoniot parameter	km/s
b	Hugoniot parameter	-
A	JWL parameter	GPa
B	JWL parameter	GPa
C	JWL parameter	GPa
c	sound speed	km/s
c_{s}	sound speed of the solid	km/s
c_{g}	sound speed of the gas	km/s
c_{p}	specific heat capacity at constant pressure	$\mathrm{J}/\mathrm{g}\,\mathrm{K}$
c_{v}	specific heat capacity at constant volume	$\mathrm{J}/\mathrm{g}\,\mathrm{K}$
$c_{\mathrm{v,s}}$	specific heat capacity of the solid	$\mathrm{J}/\mathrm{g}\,\mathrm{K}$
$c_{\mathrm{v,CJ}}$	specific heat capacity at the CJ state	$\mathrm{J}/\mathrm{g}\,\mathrm{K}$
$\mathcal{D}$	diffusion coefficient	m^2/s

Symbol	Meaning	Unit
D_{CJ}	Chapman-Jouguet detonation velocity	km / s
e	specific internal energy	kJ / g
e_{s}	specific internal energy of the solid	kJ / g
e_{g}	specific internal energy of the gas	kJ / g
E_i	activation energy for reaction i	kJ / mol
f_i	mass fraction of species i (dynamic)	-
$\dot{f}_i$	chemical reaction rate for species i	μs^{-1}
k	thermal conductivity	W / m K
K	detonation wave curvature	cm^{-1}
K_{S}	bulk modulus	GPa
M_i	molar mass of species i	g / mol
n_i	molar density of species i	mol / cm^3
n_{t}	total number of chemical species	-
N_i	mass fraction of species i (static)	-
p	pressure	GPa
p_{s}	pressure of the solid	GPa
p_{g}	pressure of the gas	GPa
q_i	specific energy released by reaction i	kJ / g
$\dot{q}$	rate of chemical energy release	kJ / g µs
Q	artificial viscous pressure	GPa
r_i	thickness of region i	cm
R	molar gas constant	J / mol K
R_1	JWL parameter	-
R_2	JWL parameter	-
S	specific entropy	J / g K
t	time	µs
T	temperature	K
T_0	initial temperature	K
T_{CJ}	temperature at the CJ state	K
u, u_{p}	particle velocity	km / s
U_{s}	shock velocity	km / s

Symbol	Meaning	Unit
v	specific volume $v = 1/\rho$	$\mathrm{cm}^3\,/\,\mathrm{g}$
v_0	initial specific volume	$\mathrm{cm}^3\,/\,\mathrm{g}$
v_s	specific volume of the solid	$\mathrm{cm}^3\,/\,\mathrm{g}$
v_g	specific volume of the gas	$\mathrm{cm}^3\,/\,\mathrm{g}$
v_CJ	specific volume at the CJ state	$\mathrm{cm}^3\,/\,\mathrm{g}$
V	volume	cm^3
w	JWL parameter	-
x	distance	cm
z_i	frequency factor for reaction i	$\mu\mathrm{s}^{-1}$
Z_i	frequency factor for reaction i (static)	$\mu\mathrm{s}^{-1}$
$\mathcal{Z}_i$	frequency factor for reaction i (dynamic)	$\mu\mathrm{s}^{-1}$

A combination of CGS and SI units have been used in this thesis. These are chosen for their convenience in modelling explosives and their prevalence in the literature. However, material model parameters will occasionally be quoted in a different set of units based on g, cm, µs and Mbar for ease of use in future hydrocode simulations. The conversion factor is $1\,\mathrm{Mbar} = 100\,\mathrm{GPa} = 100\,\mathrm{kJ}\,/\,\mathrm{cm}^3$. In some figures, cubic centimetres (cm^3) will be abbreviated as “cc”.

Chapter 1

Introduction

1.1 Motivation

Explosives are substances that can decompose exceedingly rapidly to produce hot, high pressure gases. They need not have a particularly high energy density; for instance, there is more energy per unit mass in chocolate than in many explosives, but in explosives this energy can be released very quickly, in nanoseconds. Two common explosives are cyclotetramethylene-tetranitramine (HMX) and triamino-trinitrobenzene (TATB), with molecular formulae $C_4H_8N_8O_8$ and $C_6H_6N_6O_6$ respectively [1]. The fuel and oxidiser are both located within a single explosive molecule, enabling extremely fast chemical reactions under certain circumstances. Explosives are used for mining and engineering purposes, but most research is directed towards military applications. Usually, it is the expansion of the hot, high pressure gases produced by the explosive that is used to generate useful work, for example breaking rock or accelerating metal. However, explosives can only be used if they are safe to handle. They need to react predictably when required (this is known as performance), but remain intact and inert at all other times (known as safety) [2].

Explosives can react when they are heated or mechanically insulted. Understanding at precisely what temperature an explosive will begin to decompose, or at what strength of mechanical insult, is vital to ensure their safety. The propensity of an explosive to initiate (start reacting) is known as its sensitivity. A sensitive explosive will initiate following a weaker mechanical insult than an insensitive explosive, and so is less safe to handle.

The sensitivity of explosives is controlled by a number of factors including composition (whether it is made mainly from HMX or TATB, for example), initial temperature, porosity and microstructure [3]. Current models for predicting the sensitivity of explosives use continuum representations that ignore many details of the microstructure. This means that they are unable to predict the effect of changes to the microstructure caused by a new manufacturing technique or as the explosive ages in storage. Such changes may affect the sensitivity and therefore the safety of the explosive. The aim of this work is to begin constructing a mesoscale model for explosives that accurately represents their microstructure and will eventually be able to predict its effect on sensitivity.

Like many materials, the behaviour of explosives is strongly rate-dependent. Responses vary from creep and chemical degradation which take place over timescales of months or years, to detonation chemistry that completes in nanoseconds. No single model can be expected to account for this diversity. This work focuses on understanding the response of condensed phase (solid or liquid) explosives to shock and detonation waves, which cause chemical reactions over microsecond to nanosecond timescales. Although this has been an active area of research for more than a century, the complexity of the interaction between shock waves, chemical reactions and the microstructure of explosives means that much is still not understood.

1.2 Shocks and detonations in condensed explosives

There are two classes of explosives: low and high explosives [4]. Low explosives are often used as propellants in rocket motors and fireworks, for example. In low explosives, the chemical reactions can build up to a fast but sub-sonic deflagration wave. This is in contrast to high explosives, the subject of this thesis, in which the chemical reactions can generate a super-sonic wave known as a detonation wave that travels at speeds between 1 and 10 km / s. A detonation wave is a self-supporting shock wave.

A shock wave [5] forms when a strong pressure pulse is introduced into either an inert material or an explosive, as illustrated in figure 1.1. Since the wave speed increases with pressure at high pressures (above the material's elastic limit), the top of the pressure pulse travels faster than the bottom. This means that the front of the pressure pulse gets steeper as the wave propagates, becoming a near-discontinuity (whose thickness is limited by viscosity) that is known as a shock front, and the back of the pressure pulse spreads out

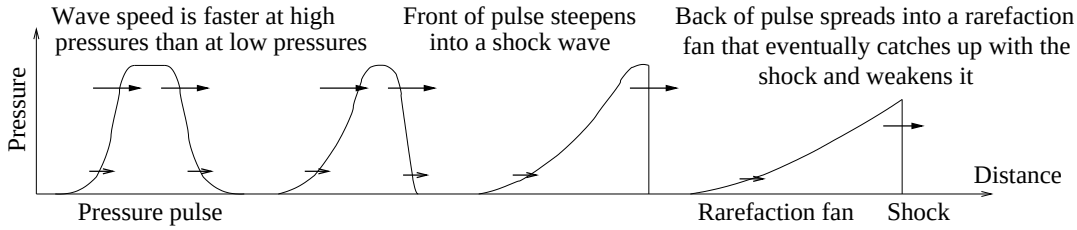

Figure 1.1: Sketch illustrating how a strong pressure pulse forms into a shock wave and rarefaction fan as it propagates through a material.

into a rarefaction fan. Eventually, if the pressure pulse is unsupported, the rarefaction will catch up with the shock front and weaken it. In a detonation [6], the shock wave is supported by chemical reactions triggered by the jump in temperature associated with the shock front. Since these reactions take a finite time to complete, the chemical energy of the explosive is released over a short distance known as the reaction zone. For a steady planar detonation wave, the end of the reaction zone coincides with the sonic point. This is the point at which the flow switches from super-sonic to sub-sonic. Rarefactions and other waves can affect the flow behind the sonic point, but they cannot affect what is happening ahead of the sonic point. Therefore, a steady planar detonation wave propagates at a constant detonation velocity determined by the response of the explosive ahead of the sonic point, irrespective of how it was created. In divergent curved geometries, the reaction zone extends past the sonic point, reducing the energy available to support the detonation wave and lowering its velocity.

In designed applications of explosives, detonations are initiated using purpose-built detonators [1]. However, detonations may also occur as a result of high speed impacts in accident scenarios or experimental configurations. The simplest case is a one-dimensional projectile impact which drives a sustained shock wave into the explosive, raising its temperature, pressure and density. The response depends on whether the explosive is homogeneous or heterogeneous, as shown in figure 1.2.

Homogeneous explosives [7] have a uniform composition, e.g., liquid nitromethane. The shock propagates at a constant velocity in these explosives, heating the explosive to a single bulk temperature. Provided the bulk temperature is sufficiently high, chemical reactions begin everywhere in the explosive but thermal explosion occurs first at the interface between the projectile and the explosive, where the reaction time has been longest. This creates a super-detonation wave that propagates through the already-shocked explosive, until it catches up with the shock front. After a short time, when the detonation

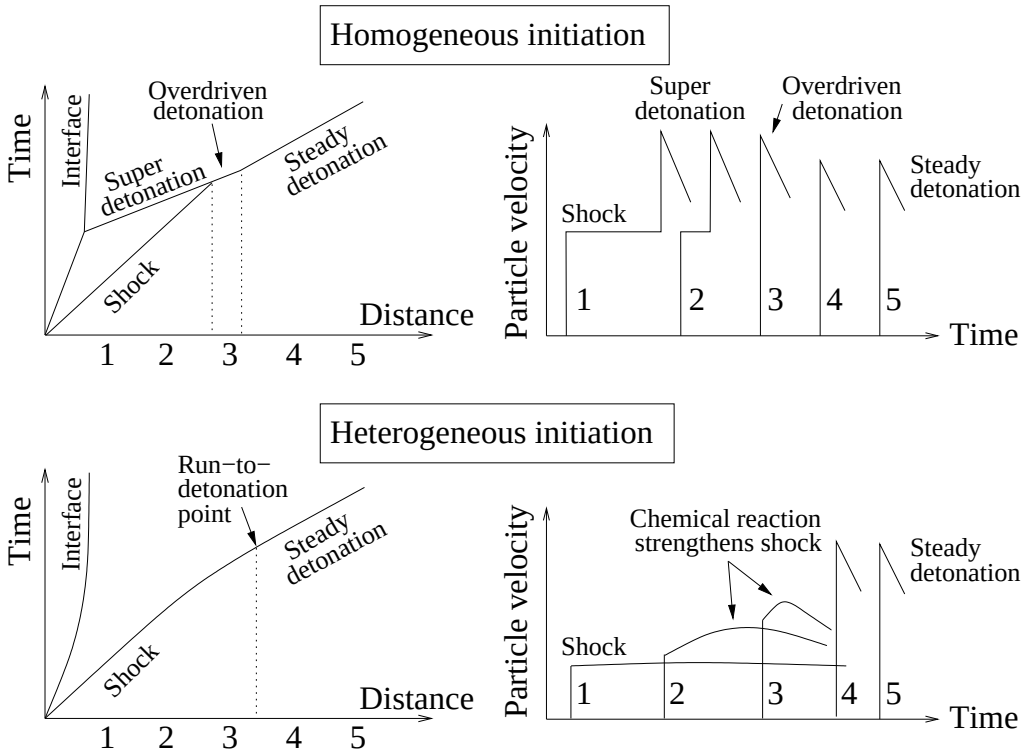

Figure 1.2: Illustration of the differences between homogeneous and heterogeneous shock initiation. The time versus distance plots (left) show how waves propagate through the explosive [7, 8]. The particle velocity histories (right) demonstrate the features that are observed in the results of embedded-gauge experiments [9].

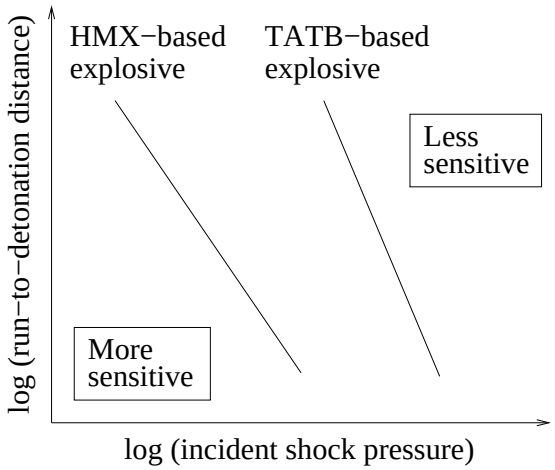

Figure 1.3: A Pop-plot is a logarithmic plot of the run-to-detonation distance (or time) versus incident shock pressure. HMX-based explosives detonate at weaker shock pressures than TATB-based explosives, i.e. they are more sensitive. Equivalently, HMX-based explosives have shorter run-to-detonation distances than TATB-based explosives subjected to the same incident shock.

is over-driven, the wave settles down to a steady detonation. Homogeneous explosives are relatively insensitive because the incident shock must be strong enough to heat the bulk explosive to above its chemical activation energy. Owing to their initially-uniform composition, homogeneous explosives are not often modelled at the mesoscale.

Heterogeneous explosives [8] have a non-uniform microstructure and are often porous, e.g., plastic-bonded explosives. These explosives are more sensitive than would be expected from their bulk temperature. It is widely accepted that reaction begins (i.e. ignition occurs) at localised hot regions, known as hotspots, that are created by shock interactions with the heterogeneous microstructure. Reaction then spreads from the hotspots into the surrounding cooler explosive (the growth phase). Growing chemical reactions behind the shock front raise the pressure and temperature, strengthening and accelerating the shock front. In turn, this produces higher temperatures and faster reactions until eventually the shock transits to a detonation wave. The point at which this occurs is known as the run-to-detonation distance (or time).

A logarithmic plot of the run-to-detonation distance or time versus incident shock pressure is known as a Pop-plot after Ramsay and Popolato, who noticed that shock initiation data are approximately linear when presented in this way [10]. Pop-plots for different explosives (e.g., HMX and TATB) can be quite different from each other, as sketched in figure 1.3. HMX-based explosives are more sensitive than TATB compositions: they require a significantly lower incident shock pressure to generate the same run-to-detonation distance. This is due to their different chemical reactivities which result in longer reaction zones in TATB-based explosives than in HMX. While the eventual aim is that mesoscale models will be formulated for a variety of different types of explosives, it is sensible to focus on a single type initially.

Plastic-bonded explosives are solids with complicated heterogeneous microstructures in their initial unreacted state. The majority of plastic-bonded explosive compositions are made by pressing together a mixture of coarse and fine explosive crystals that have each been coated with a thin layer of polymeric binder [1]. The pressing process may introduce cracks and pores or other heterogeneities into the microstructure of the explosive. To facilitate the construction of a mesoscale model, it is desirable to choose an explosive with as simple a microstructure as possible. Since TATB crystals are elongated and highly anisotropic, TATB-based explosives have 3D microstructures and often exhibit anisotropic responses in experimental configurations. In contrast, HMX crystals are round (i.e. aspect ratio $\simeq$ 1) and approximately isotropic, making them more appropri-

ate for mesoscale modelling in 1D and 2D. It is for this reason that this work will focus on two well-characterised HMX-based explosives. PBX9501 comprises 95% by weight HMX and 5% binder, with 1.6% porosity [11]. EDC37 comprises 91% HMX and 9% binder, with <0.2% porosity [12]. These two explosives make an interesting comparison because they exhibit similar shock sensitivity despite significant differences in porosity.

Pores are often thought to be responsible for shock initiation in plastic-bonded explosives, since porosity is known to have a significant effect on the Pop-plot. For example, the run-to-detonation distance of an HMX-based explosive PBX9404 at 3 GPa input pressure falls from 9 mm at 1.4% porosity to 5 mm at 7.8% porosity [11], representing a significant increase in sensitivity. Pores can trigger reaction in shocked heterogeneous explosives by creating hotspots on their collapse. Pore collapse has been the subject of much research owing to its amenability to analytic and computational modelling, and reviews are given by several authors, e.g., Bourne [13] and Fried [14]. Some continuum models treat pore collapse as the only active hotspot mechanism in plastic-bonded explosives, but a variety of other hotspot mechanisms can also be responsible for ignition. For example, shear bands may occur in a shocked explosive when thermal softening exceeds work hardening, leading to localised deformation and heating due to viscoplastic work [15]. The similar response of PBX9501 and EDC37 under shock initiation suggests that a hotspot mechanism other than pore collapse may be dominant in these explosives.

In two landmark papers [16, 17], Field presented evidence for the ten hotspot mechanisms that may cause ignition in explosives and propellants, using the concept of critical hotspots. A super-critical hotspot is sufficiently large and hot that it can itself react, and go on to spread reaction into the cooler surrounding explosive, before it is cooled by heat conduction. A sub-critical hotspot is too small or too cool, so that it dies away before it can react significantly. A critical hotspot lies on the boundary between these two regimes; it is just large and hot enough to react and initiate the surrounding explosive. Field used experimentally-determined criteria [18] that critical hotspots in explosives have dimensions of typically 0.1 to 10 μm, durations of 10^{-5} to 10^{-3} s and temperatures greater than ~700 K to evaluate candidate hotspot mechanisms. However, he did not consider the simplest mechanism responsible for temperature localisation in plastic-bonded explosives: the shock heating of crystals and binder. One of the aims of this work is to determine whether this is a feasible hotspot mechanism in PBX9501 and EDC37.

Critical hotspots have been the subject of much research because they are important in a variety of physical systems, for example, engines [19], propellants [20] and explo-

sives [21, 22]. Previous studies have investigated the size, duration and temperature of critical hotspots in explosives. The governing heat conduction and chemistry equations need to be solved numerically even if simple material models are used [23]. Critical hotspot criteria for realistic models of HMX were first determined using heat transfer codes [e.g., 24]. These studies have since been extended to include the effects of hydrodynamics, after thermal solvers were embedded in hydrocodes [25, 26]. In this work, critical hotspot criteria will be determined for the HMX and binder components of PBX9501 and EDC37 for comparison to results in the literature.

1.3 Hydrocode modelling of explosives

Models describing the response of explosives to shock and detonation waves are usually implemented in multi-material hydrodynamics computer codes or "hydrocodes" [27, 28]. Like computational fluid dynamics codes, hydrocodes solve the Euler equations for the conservation of mass, momentum and energy. An additional relation known as the equation of state for each material is required to close the system of equations. Hydrocodes differ from computational fluid dynamics codes in their use of advanced equations of state to model solids in addition to liquids and gases. Coupled with a method for dealing with shock discontinuities, hydrocodes allow the shock compression of realistic materials to be simulated in complex engineering geometries and are a valuable tool for understanding the results from experiments. Hydrocode models for detonating explosives date back over sixty years and have steadily gained in complexity as computing power has increased. There are three types of model in common use: programmed burn, detonation shock dynamics and reactive burn. These are related to two fundamental models of detonation: the CJ and ZND theories.

The CJ theory was developed by Chapman [29] and Jouguet [30]. It assumes that the detonation wave causes each element of explosive to transform instantaneously from its initial unreacted state into gaseous detonation products. The behaviour of the detonation products is represented by their equation of state, as sketched in pressure versus specific volume space in figure 1.4. A straight line drawn through the initial state of the unreacted explosive is tangent to the equation of state of the detonation products at a unique point known as the "CJ state". This straight line represents the only stable state for a detonation wave and its gradient determines the detonation velocity D_{CJ}, which is a constant.

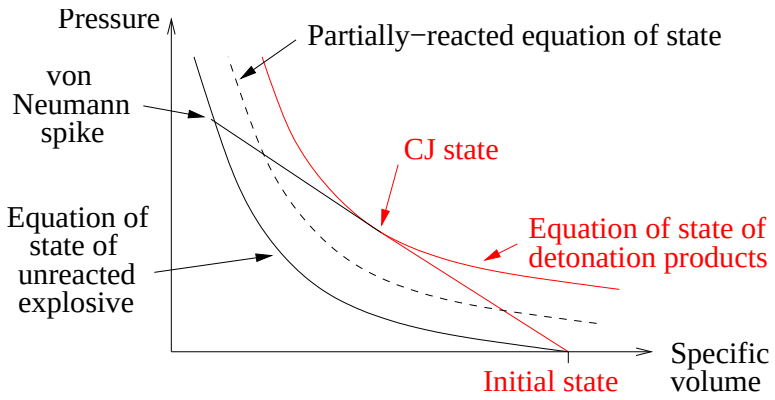

Figure 1.4: Sketch illustrating Chapman-Jouguet theory (in red) and the additions made by Zeldovich, von Neumann and Doering (in black). CJ theory assumes that the explosive transforms instantaneously into gaseous detonation products. ZND theory accounts for a finite reaction zone between the von Neumann spike and the CJ state.

Zeldovich [31], von Neumann [32] and Doering [33] independently made additions to CJ theory to account for finite chemical reaction rates. ZND theory assumes that the detonation wave shocks the unreacted explosive to a high-temperature state, initiating chemical reactions which transform the explosive into gaseous detonation products over a finite reaction zone. As sketched in figure 1.4, the equations of state for the unreacted explosive and the detonation products are both required. In ZND theory, a straight line through the initial and CJ states is extended until it intercepts the equation of state of the unreacted explosive, at a point known as the "von Neumann spike". In a 1D steady detonation, the explosive is shocked to this high-pressure spike state. As chemical reactions proceed, the pressure falls as the explosive passes (along the straight black line in figure 1.4) through partially-reacted equations of state on its way down to the CJ state (the sonic point), which is reached at the end of the reaction zone.

Programmed burn is the simplest hydrocode model for explosives and is based on CJ theory. One or more detonation points are defined for each region of explosive. For each computational cell in that region, the straight-line distance from the detonation point is calculated and the constant detonation velocity D_{CJ} is used to determine the time at which the cell will react (its "burn time"), before the hydrocode simulation commences. At the burn time, and over a finite burn interval determined by the size of the cell, the cell pressure is increased from zero towards the CJ pressure p_{CJ}. Thereafter, the cell is treated as containing only gaseous detonation products. Only the initial state of the explosive and the equation of state of the detonation products are required as input to the model. Programmed burn is suitable for modelling detonation propagation in explosives where

CJ theory is a good approximation – these are known as "ideal" explosives. However, all real explosives show some degree of non-ideal behaviour.

Detonation shock dynamics [34, 35] includes a key property of non-ideal explosives: the observed variation in detonation velocity with charge size or, equivalently, with wave curvature. As with programmed burn, the cell pressure is increased from zero towards p_{CJ} at a pre-determined burn time. However, the burn time calculation does not assume a constant detonation velocity but requires a relationship to be supplied for the variation in detonation velocity D with wave curvature K. The $D(K)$ curve is determined empirically for each explosive from a series of detonation propagation experiments at different charge sizes. The model requires as input the initial state of the explosive, the equation of state of the detonation products and the $D(K)$ relation. In some implementations, the equation of state of the detonation products is modified with K, to ensure that it is consistent with the local value of D. Detonation shock dynamics can be used for modelling detonation propagation in non-ideal explosives, but it does not account for shock initiation behaviour.

Reactive burn models represent shock initiation and detonation propagation behaviour in explosives, and are run as an integral part of the hydrocode simulation. Examples include the Ignition and Growth model [36], the Wescott, Stewart and Davis model [37] and the CREST model [38]. A finite reaction rate converts the unreacted explosive to detonation products and is often assumed to be pressure-dependent, but temperature or entropy-dependent rates are also used. Reactive burn models require as input the initial state of the explosive, the equations of state of the unreacted explosive and the gaseous detonation products, and the reaction rate. The number and variety of models in current use reflects the fact that the behaviour of heterogeneous explosives in the shock regime is not fully understood, so empirical reaction rates are used. The ability of a model to predict shock initiation and detonation propagation phenomena is highly dependent on the quality of its reaction rate, which is tuned to a suite of experimental data on each explosive composition. Continuum reactive burn models do not account for the microstructure of the explosive, and so are unable to predict the effect of microstructural changes on shock initiation and detonation behaviour.

In recent years, model developers have turned to smaller length-scales in an attempt to learn more about the underlying mechanisms of shock initiation. The microstructures of two plastic-bonded explosives, PBX9501 and EDC37, are illustrated in figures 1.5 and 1.6. The complicated geometry arises when the mixture of coarse and fine explosive crystals, each coated with a thin layer of polymeric binder and having random crystallo-

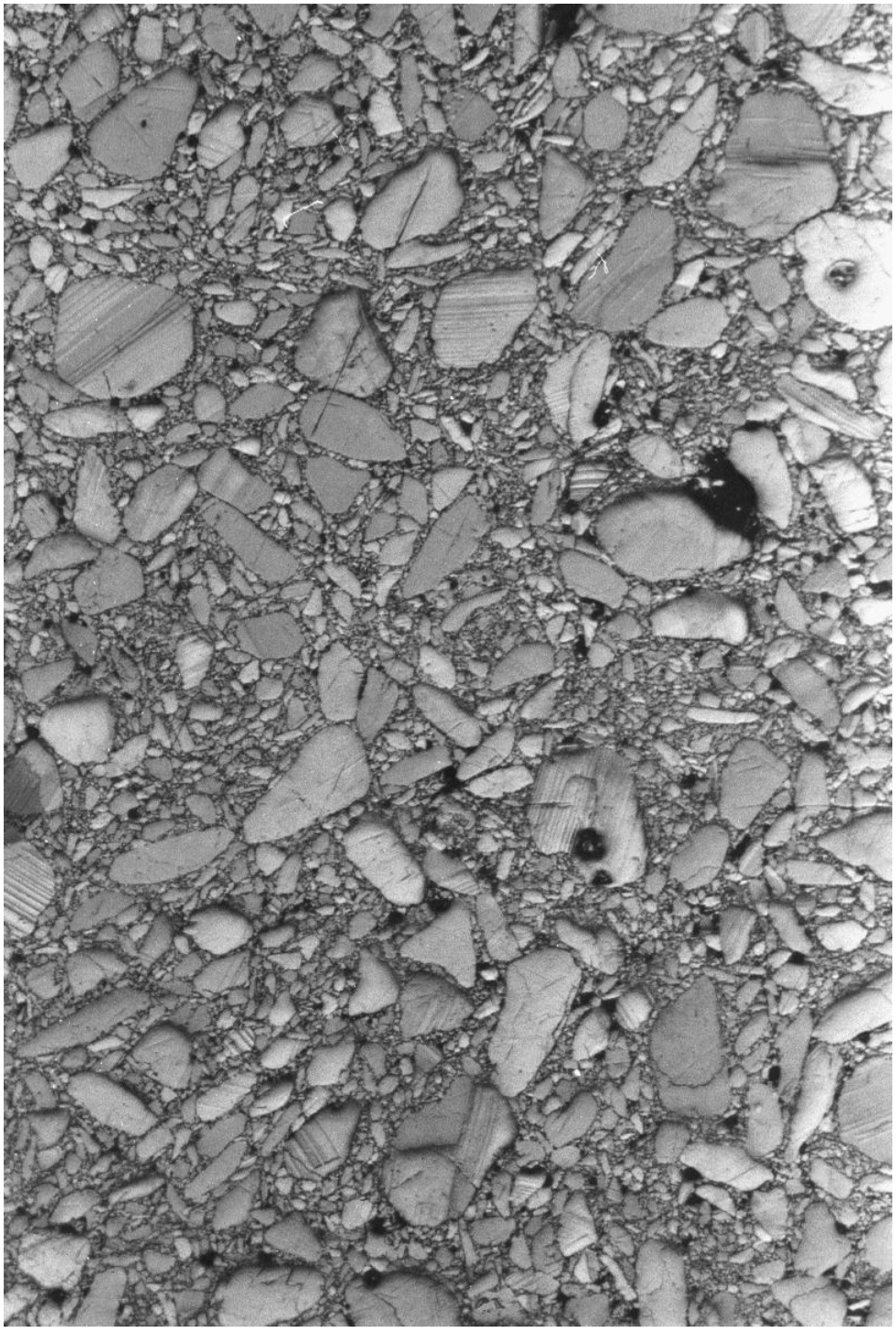

Figure 1.5: Micrograph of EDC37 [39] showing a mixture of coarse and fine HMX crystals with diameters between 0.1 and 200 μm, each surrounded by a thin layer of binder. The scratches and dark holes (known as "pull-outs") are thought to be artefacts of the sample preparation, but it is clear that many of the larger striped crystals are twinned. The scale is such that the height of the picture is ~1 mm.

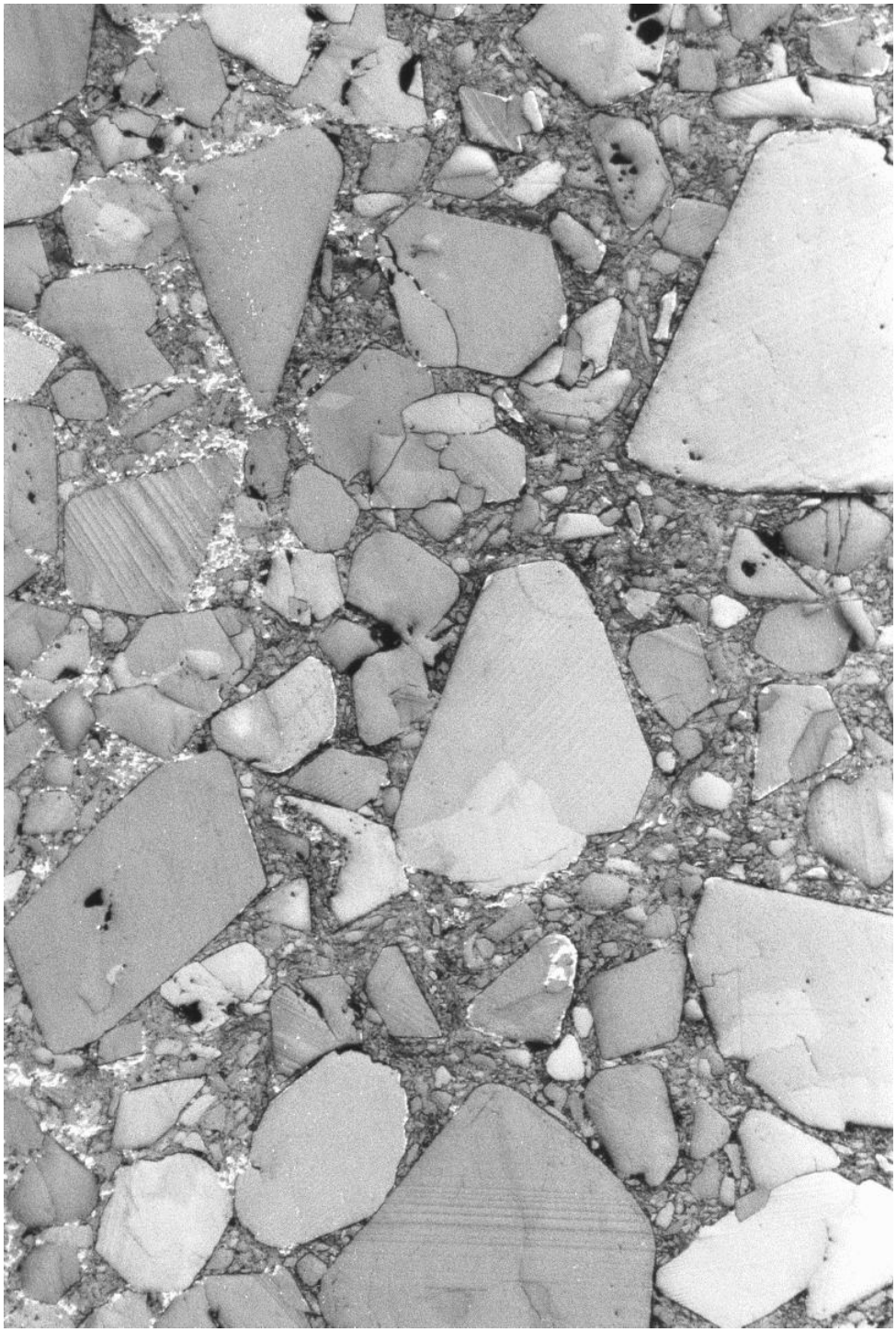

Figure 1.6: Micrograph of PBX9501 [39] showing a mixture of coarse and fine HMX crystals with diameters between 1 and 1000 μm, for comparison with figure 1.5. Some of the large crystals have cracked under the high pressures applied during the manufacturing process. The colour differences between the crystals are caused by their random crystallographic orientations. The scale is such that the height of the picture is ~1 mm.

graphic orientations, is pressed during the manufacturing process. The different shapes and sizes of the crystals in PBX9501 and EDC37 produce different microstructure characteristics; for example, some of the large grains in pressed PBX9501 are cracked [40] while EDC37 crystals are believed to be relatively undamaged [41]. The crystal size distribution changes during the manufacturing process [42, 43], but accurate distributions can be obtained by analysing micrographs [44]. Crystal size effects are known to have an influence on the sensitivity of explosives. For example, experimental data for a cast explosive indicate that large grains are more sensitive than small grains at low pressures, while small grains are more sensitive at high pressures [45]. Although explanations for such effects have been suggested, microscale and mesoscale models are needed to verify the mechanisms responsible and to make predictions for other compositions.

Microscale studies use atomistic and molecular dynamics modelling to investigate both the inert and reactive response of explosive crystals under shock compression. For example, molecular dynamics simulations have been used to investigate the thermal conductivity of liquid HMX [46] and the decomposition of HMX at 3500 K [47], both quantities that would be very difficult to measure experimentally. However, the quality of molecular dynamics simulations depends on the representation of the force field, the computational method, the importance of quantum effects that are not accounted for in a classical simulation, and the convergence that is achieved [48]. In addition, the length and time-scales that can be accessed by molecular dynamics simulations are highly constrained (to micrometres and nanoseconds) by the available computing power and data analysis techniques. While investigations of hotspot mechanisms might be possible with molecular dynamics in the near future, modelling the entire run-to-detonation process in a plastic-bonded explosive is not feasible. Since the aim of this work is to produce a model that can predict the effect of microstructure on shock initiation and detonation propagation over centimetres and microseconds, microscale modelling is not a suitable approach.

Mesoscale models account for the microstructure of plastic-bonded explosives at the scale of the crystals and binder. Since the crystals in PBX9501 and EDC37 have diameters between 0.1 and 1000 μm, a mesoscale model of these explosives would be expected to have a mesh size of approximately 0.1 μm which is significantly smaller than the 100 μm meshing typically used for continuum reactive-burn models. Mesoscale models often use the same hydrocode techniques as continuum models but with material models that have been constructed for the crystal and binder components individually, rather than

for the plastic-bonded explosive as a whole. The material properties data required to parametrise these models is drawn from experiments and from the results of microscale simulations. In this way, mesoscale models can build on microscale studies and it is envisaged that improvements to continuum reactive-burn models will, in turn, be based on the results of mesoscale simulations. This approach is known as multiscale modelling and is often employed for complex materials like explosives. The mesoscale modelling work presented in this thesis will contribute to the construction of multiscale models for PBX9501 and EDC37.

1.4 Mesoscale modelling of plastic-bonded explosives

There are two main approaches to mesoscale modelling. The first is to construct a reactive-burn model that is aware of the microstructure of the explosive. It includes parameters for the grain size, porosity, etc., and is able to account for their effect on shock initiation and detonation propagation. Examples include the statistical hotspot models by Nichols [49] and Hamate [50], the grain burning model by Milne [51], the mixture model by Swift [52] and the hotspot population dynamics model proposed by Lambourn [53]. Such models are based on mesoscale concepts but they contain empirical parameters that must be tuned to macroscopic experiments or to more fundamental models, potentially limiting their predictive capability. Therefore, this approach is not developed further here.

The second approach is to explicitly model the microstructure of the explosive in a computer simulation. Ideally, a 3D representative volume would be constructed corresponding to the exact microstructure of the explosive and containing pores, crystal defects and other heterogeneities. When the microstructure is shocked, the material models in the code would produce physically-realistic temperatures for the hotspots and the bulk explosive. Chemical reaction would begin in the hotspots and spread through the surrounding cooler explosive, until it is consumed. A macroscopic average of thermodynamic quantities across the microstructure would reproduce experimental shock and detonation phenomena. Unfortunately, the meshing requirements of such an “ideal” model are currently prohibitive and, more importantly, much of the detailed physics and chemistry is not known. To make progress, researchers have focused on particular aspects of the problem by, for example, neglecting hotspots.

Microstructure simulations of HMX-based explosives have been conducted in four different regimes and with a variety of computational methods. The low-rate stress-strain response of PBX9501 has been studied by Mas [54, 55]. The compaction of granular HMX was investigated by Menikoff [56, 57] in an Eulerian hydrocode, and by Panchadhar [58] using a Lagrangian code with an inter-granular friction model. The weak-shock response of PBX9501 microstructures has been simulated using a particle-in-cell approach [59, 60, 61] and with the discrete element method [62], although this technique is not widely used owing to the problems identified by Tang [63]. These problems include the lack of a mathematical proof for the method and numerical anisotropy caused by the orderly arrangement of elements. The shock initiation and detonation regime that is the focus of this work has previously been studied in Eulerian hydrocodes by Baer [64, 65, 66], Brundage [67], Conley [68, 69, 70, 71] and Reaugh [26]. Since they are well established for shock and detonation modelling, Lagrangian and Eulerian hydrocodes will be used in this work.

Explosive microstructures have been represented both in 2D and 3D; for example, two dimensions were favoured by Conley and Panchadhar, while Baer and Brundage used three dimensions. Mesoscale simulations on inert materials have demonstrated the importance of 3D modelling; for example, Benson [72] concluded that a better representation of the shock compaction of copper powder would be achieved in 3D. In addition, Flinn [73] stated that 3D simulations would be needed to account for the effect of inter-granular gases in the dynamic consolidation of stainless-steel powders, because the open path between particles cannot be represented in 2D. However, 3D simulations are significantly more computationally expensive than 2D simulations, which in turn are more expensive than 1D simulations. This limits the mesh resolution that can be achieved and therefore the accuracy of the simulation. In this work, both 1D and 2D simulations will be used to investigate the response of PBX9501 and EDC37 at the mesoscale. Direct comparison will be made between 2D and 1D calculations in plane, cylindrical and spherical geometries to assess the effect of reducing the 3D microstructure to fewer dimensions.

Mesoscale modelling has been applied to a variety of HMX compositions. Baer [66] and Conley [69] found that the presence of inter-granular voids in porous HMX leads to greater deformation of the grains and higher temperatures than in simulations with binder between the grains. In addition to temperature distributions, Conley has investigated the effects of particle size and the timescales for thermal equilibrium to be achieved in PBX9501. He found that temperature reaches quasi-equilibrium more quickly than pres-

sure, and pressure fluctuations persist long after the shock front has passed. In this work, pressure and temperature fluctuations in PBX9501 microstructures will be compared to results in the literature. None of these papers simulates EDC37 despite its being a well characterised explosive [74, 75, 76]. An aim of this work is to address this gap in the literature by performing direct comparisons between mesoscale simulations of PBX9501 and EDC37.

Methods of creating geometries for microstructure simulations fall into two categories: constructing an artificial geometry and using tomography data. In the first category, the simplest method is to use ordered particle arrays to create an artificial geometry [e.g., 66] using a simple particle size distribution [e.g., 26]. The drop-and-fill approach was found to be inadequate for creating low-porosity geometries representative of plastic-bonded explosives [64]. Monte Carlo methods have been used successfully by Bardenhagen [60] and by Baer with realistic particle size distributions. Artificial geometry methods often treat HMX crystals as spherical (or circular in 2D), which is not realistic for modelling inter-granular interactions like friction. Although Monte Carlo methods are available here [77], a simple technique that could analyse tomography data is preferred to ensure that computational microstructures are as realistic as possible. Either 2D micrographs [e.g., 69 and 78] or 3D tomography data [e.g., 67 and 79] can be used to construct microstructure geometries. These methods are capable of producing representative particle size distributions, depending on the resolution of the data, and there is no restriction on the shape of the explosive crystals. Simple artificial geometries and realistic geometries constructed from micrographs of PBX9501 and EDC37 will both be used in this work.

A variety of material models have been used in mesoscale simulations of HMX-based explosives. These are often divided into two parts: an equation of state describing the response of the material to isotropic compression and a strength model for the deviatoric response to shear. In common with most mesoscale models in the literature, a Mie-Grüneisen form of equation of state will be used in this work. Several strength models have been used for the components of plastic-bonded explosives including visco-elastic [55, 62, 63], visco-plastic [58, 68] and elastic-plastic [e.g., 56, 66 and 67] models. Owing to this lack of consensus and the paucity of strength data on the components of PBX9501 and EDC37, the incorporation of strength effects is left for future work. Some mesoscale models have included additional physical effects, for example Conley developed a model for the shear viscosity of HMX [68] and viscosity has been used to represent frictional work at grain interfaces [56]. Panchadhar included friction in his Lagrangian

model of the compaction of granular HMX, but did not seem to account for the reduction in frictional heating due to melting, despite the HMX exceeding its melting temperature in his simulations [58]. Friction is difficult to represent in Eulerian hydrocodes so, in common with many of the mesoscale studies in the literature, it is not modelled in this work. Artificial viscous pressure will be used to treat shocks but a physical viscosity model is not included. Although a few studies have investigated heat conduction [26, 65], it is not often included in microstructure simulations because of the additional computational effort required and the small distances over which it operates. However, thermal conductivity will be included in this work owing to its importance in controlling the behaviour of hotspots. The material models used in mesoscale modelling are often empirical and require calibration to experimental data. Menikoff published an excellent compilation of experimental data for HMX in reference 80, which provides many of the material model parameters used in this work.

Although explosives are by their very nature highly reactive materials, they are often treated as inert in mesoscale modelling studies [e.g., 57, 64 and 69] because of uncertainties in the underlying chemical reaction mechanisms and the computational expense of reactive simulations. Neglecting chemical reaction may be an appropriate assumption in situations where little reaction is expected over timescales of interest, e.g., for low strain-rate simulations. In the shock initiation regime, inert simulations have been used to investigate the shock response of plastic-bonded explosive microstructures without the complicating influence of chemical reaction. Reactive simulations of shock initiation require very fine meshing to resolve hotspots accurately, and centimetre-long computational domains to capture the entire shock-to-detonation transition. To the best of our knowledge, such simulations have not yet been undertaken, and addressing this gap in the literature is a long-term aim of this work. To reduce the computational expense, some mesoscale studies have used Arrhenius reaction rates to represent the reaction in hotspots, followed by an empirical pressure-dependent burning law describing the propagation of the reactive wave into the surrounding explosive [70, 71]. Other models use entirely pressure-based rates [64, 66] for reaction in hotspots and the bulk explosive.

The majority of reactive mesoscale models use Arrhenius temperature-dependent rates [e.g., 52, 67 and 81] to be consistent with the established chemical literature. Arrhenius reaction-rate schemes for explosives are both single step [82, 83] and multi step [e.g., 14, 84 and 85]. Conley [68] dismissed single-step schemes as being unable to predict reliable thermal-explosion ignition times over a wide temperature range, and used

McGuire-Tarver multi-step kinetics [86] to represent HMX in the shock initiation regime. Despite this, Reaugh found it necessary to modify one of the McGuire-Tarver parameters to significantly increase the reaction rate at high temperatures [26, 87] and Menikoff uses a single-step rate for modelling HMX detonation [83]. In this work, single-step and multi-step Arrhenius schemes have both been tested but a single-step reaction is used for the majority of the simulations.

1.5 Research plan

The long-term aim of this study is to construct a mesoscale model for shock initiation and detonation propagation in two plastic-bonded explosives, PBX9501 and EDC37, that is able to predict the effect of changes to their microstructure. It was decided at the outset that the model will directly represent the heterogeneous microstructure of the explosives in a hydrocode, following the approach of Baer [64, 65, 66], Conley [68, 69] and others. Since PBX9501 and EDC37 are heterogeneous explosives, the model must represent not only the bulk response of the microstructure but also the hotspots where chemical reaction begins and the propagation of reaction from hotspots into the bulk. Developing such a model is a long-term research project owing to its complexity and because the underlying physics and chemistry is not thoroughly understood. It is envisaged that model development will take place in three phases:

Phase 1. Model the bulk response:

Incorporate appropriate physics for modelling bulk response in a hydrocode.

Construct material models for the crystal and binder components and validate by comparison to suitable experimental data.

Investigate the bulk response of shocked explosive.

Phase 2a. Model hotspot mechanisms:

Incorporate appropriate physics for modelling hotspots in a hydrocode.

Model hotspot mechanisms and rank them in order of importance.

Develop approximate models for key hotspot mechanisms if mesh resolution is insufficient to represent them explicitly.

Phase 2b. Model the reaction propagation from hotspots into the bulk:

Understand how reaction spreads from hotspots into the surrounding explosive.

Develop an approximate model for reaction propagation if mesh resolution is insufficient to represent it explicitly, and implement in a hydrocode.
Investigate the interaction of reactive waves from multiple hotspots.

Phase 3. Full microstructure simulations:
Establish location of potential hotspot sites from experimental data.
Incorporate hotspots in a hydrocode with appropriate statistics.
Investigate the combined bulk and hotspot response of shocked explosive.
Validate the model by comparison to reactive-burn models and shock initiation data.

This work addresses phase 1 and some aspects of phase 2. The main focus is on modelling the bulk response of PBX9501 and EDC37. This allows the "background" effect of the shock heating of HMX crystals and binder to be established without the complicating influence of hotspots. The available hydrocodes did not include heat conduction or Arrhenius chemistry, two physical effects that are important for mesoscale modelling, so these are implemented in a one-dimensional Lagrangian hydrocode. Appropriate material models are constructed for the HMX and binder components from available data. These are used to investigate the bulk response of PBX9501 and EDC37 microstructures and the predicted shock temperature distributions are compared to results from the literature. The capability to model the experimental data relevant to the bulk response of these explosives will also be assessed. Critical hotspot criteria will be determined for comparison to results in the literature, and the propagation of reaction from hotspots into the bulk explosive will be investigated using flame propagation simulations. The feasibility of shock heating of crystals and binder as a hotspot mechanism in PBX9501 and EDC37 will be determined. Assessing the remaining hotspot and reaction propagation mechanisms (e.g., pore collapse and shear banding) will require additional physics to be incorporated into the available hydrocodes, and so the remainder of phases 2 and 3 is left for the future.

1.5.1 Thesis outline

This thesis is divided into eight chapters. Chapter 2 discusses the physics relevant to mesoscale modelling in the shock to detonation regime. The hydrodynamics computer codes used in later chapters are described and the technique developed to generate computational microstructures is presented. In chapter 3, material modelling assumptions are discussed and new models are constructed for the HMX and binder components

of PBX9501 and EDC37. The models are validated by comparison to Hugoniot data, Pop-plot data and detonation wave profiles in chapter 4. In chapter 5, shock heating of crystals and binder is investigated and it is confirmed that the results are not sensitive to geometry, meshing or reasonable changes to the material properties data. Critical hotspots are determined for HMX and the binders in chapter 6, and the effects of initial temperature, geometry and mesh density are established. The observed reaction propagation speed is validated using diamond anvil cell data, and implications are drawn that can be used to rank hotspot mechanisms in the future. In chapter 7, one and two-dimensional hydrocode calculations are used to determine bulk temperature distributions in inert PBX9501 and EDC37. The sensitivity to computational settings, geometry and uncertainties in the material properties is investigated. Pressure versus specific volume data and pressure/temperature profiles are also obtained. The thesis is concluded in chapter 8, where key points of interest from the earlier chapters and areas that represent novel work are highlighted. Suggestions will be made for future research on the development of a mesoscale model for PBX9501 and EDC37.

1.6 Summary

This thesis describes the first phase in a research project to develop a mesoscale model for two HMX-based plastic-bonded explosives, PBX9501 and EDC37, that is able to predict the effect on sensitivity of changes to their microstructure. Shocks and detonation waves, and their effects on homogeneous and heterogeneous explosives, have been introduced. Current programmed burn, detonation shock dynamics and reactive burn models do not describe the response of explosive microstructures, and microscale studies are limited by computing power, motivating the development of mesoscale models. The existing literature has been reviewed and several gaps have been identified. These will be addressed in this work by modelling EDC37 in addition to PBX9501 and by investigating the shock heating of crystals and binder as a potential hotspot mechanism.

Chapter 2

Computational techniques

This chapter presents the computational techniques that will be used for mesoscale modelling of explosives in the shock to detonation regime. Section 2.1 will discuss which physical processes are relevant and which can be neglected, resulting in a complete set of reactive-flow equations that include the effects of hydrodynamics, chemistry and heat conduction. An introduction to the well-established hydrocodes used to solve these equations, and details of a one-dimensional Eulerian hydrocode that was written during the early stages of this work, will be given in section 2.2. Since heat conduction and Arrhenius chemistry were not previously available in the codes, section 2.3 will describe how they were implemented in a one-dimensional Lagrangian hydrocode. The method developed to analyse micrographs of PBX9501 and EDC37 and to generate computational microstructure geometries will be discussed in section 2.4. Finally, a summary of the chapter will be given in section 2.5.

2.1 Relevant physics

Plastic-bonded explosives are initially-solid materials with a complex microstructure. In the shock to detonation regime, they may be subjected to a variety of hydrodynamic phenomena including shocks, compressions and release waves, all of which will modify the explosive's thermodynamic state depending on its material properties. Any significant increase in temperature will cause chemical reactions to proceed, converting the solid unreacted explosive into gaseous reaction products. The resulting energy release and

equation of state change will cause additional pressure waves to propagate through the microstructure. Although the laws of hydrodynamics require that pressure be continuous across material interfaces, temperature and density discontinuities can occur. Any temperature and composition variations may be reduced by the effects of heat conduction and species diffusion.

In general, modelling problems similar to this are known as "reactive flow". The equations used to model reactive flow can be found in many textbooks, e.g., reference 88. They include five types of physical processes: motion and compression, chemical reactions, diffusion effects, radiation transport, and waves. Not all of these effects are relevant to shock initiation of plastic-bonded explosives owing to the scales over which they operate. The length-scales of interest for mesoscale modelling are between 0.1 μm and 1 m, representing the smallest crystal size and the maximum extent of typical explosive charges respectively. Relevant timescales are between nanoseconds and microseconds, which are typical of wave reverberation times in hotspots and run-to-detonation times respectively. The physical processes that will be neglected in this work are discussed below.

- Viscosity affects the behaviour of a fluid under shear motion. For many fluids (known as Newtonian fluids), the shear stress is proportional to the spatial derivative of velocity [89]. The proportionality factor is known as the viscosity coefficient μ and is typically in the range 0.001 to 0.1 Pa s for liquids [80]. Viscosity is significant over length-scales $\Delta x \lesssim \mu/\rho u$. For typical densities ρ of 2 g / cm^3 in plastic-bonded explosives and particle velocities u of 0.3 km / s in the shock initiation regime, Δx lies between 2 nm and 0.2 μm. This is only just within the length-scales of interest for mesoscale modelling, so it is reasonable to neglect fluid viscosity. In contrast to liquids where viscosity results from molecular diffusion, viscosity in solids is an approximation to rate-dependent plasticity and $\mu \sim 100$ Pa s [80]. Therefore, viscosity may be significant over length-scales $\Delta x \sim 0.2$ mm which are directly relevant to mesoscale modelling, if strength effects are significant. Since strength is in this work (see section 3.1), solid viscosity will also be neglected for consistency.

- Multi-phase flow applies when there are two or more distinct phases present, e.g., dust suspended in air. Such flows are different to the multi-species flow described in this thesis because the phases have different velocities, so additional equations are required to describe how the two phases interact. Multi-phase flow has been used in modelling granular energetic materials [90] and can be important for aluminised explosives. However, multi-phase flow is commonly neglected in conventional ex-

plosives like PBX9501 and EDC37 because experimental evidence shows that convection is not significant near theoretical maximum density [91, 92]. In addition, the fast chemical reactions and the isolation of individual reaction centres (hotspots) mean that there is limited potential for motion within the partially-reacted explosive during shock initiation. For these reasons, multi-phase flow will be neglected.

- Radiation transport is widely neglected in explosives modelling, although some experimentalists have suggested that radiative heating may play a role in shock initiation [93]. An order of magnitude estimate of its significance can be made using the Stefan-Boltzmann law [94] that the power per unit area radiated by a black body is σT^4 where $\sigma = 5.67 \times 10^{-8}\,\mathrm{W/m^2\,K^4}$ and T is the temperature. For detonation products at 3000 K and unreacted explosive at 300 K, the power radiated is $4.6 \times 10^6\,\mathrm{J/m^2\,s}$. In comparison, the energy released by detonating HMX is approximately $10^{10}\,\mathrm{J/m^3}$. For a detonation velocity of $\sim$10 km/s, the power per unit area released by chemical reactions within the explosive is $\sim 10^{14}\,\mathrm{J/m^2\,s}$. This is eight orders of magnitude greater than the radiated power and demonstrates that radiation transport can be neglected.

- Electromagnetic forces are usually ignored in explosives modelling, although the possibility of applied electromagnetic fields being able to enhance detonation behaviour has been studied [95]. In the absence of an applied field, any electromagnetic forces must be internally generated due to charge separation and motion. Temperatures in detonating explosives (3000 K) are much lower than the temperatures required to ionise the C, H, N and O atoms they contain (approximately 10^5 K). Therefore, the electromagnetic forces will act over distances comparable to the molecular separation. For explosives with a density of $\sim 2\,\mathrm{g/cm^3}$ and molecular mass $\sim$300 g/mol, the number of molecules in a volume of $1\,\mu\mathrm{m}^3$ can be calculated from the Avogadro constant $6{\times}10^{23}\,\mathrm{mol^{-1}}$. The number of molecules across the length of a 1 µm cubic computational cell is $\sim$1600. Since the molecular separation is three orders of magnitude less than the computational mesh size, electromagnetic forces are expected to be insignificant at the mesoscale and can be neglected.

- External forces like gravity have a small effect on the µs timescales of relevance in the shock regime and are rarely included in explosives modelling. For example, the velocity imparted to a material over 10 µs by the gravitational acceleration at the Earth's surface is $9.81{\times}10^{-8}$ km/s, significantly less than typical particle velocities of 0.3 km/s in the shock initiation regime. Therefore, external forces like gravity

can safely be neglected.

The four physical processes that remain after neglecting the above effects are hydrodynamics, chemical reaction, heat conduction and species diffusion, as described by equations 2.1 to 2.5 for fluids. Strength in solid materials introduces extra terms into these equations. The behaviour of a solid can be split into isotropic and deviatoric components [96], represented by independent equation of state and strength models respectively. Since strength will be neglected in this work (see section 3.1), the additional terms are omitted from the following equations. Equations 2.1 to 2.5 are the reactive-flow equations as they apply to mesoscale modelling of explosives.

$$\frac{\partial \rho}{\partial t} + \nabla \cdot (\rho \boldsymbol{u}) = 0 \tag{2.1}$$

$$\frac{\partial (\rho u_i)}{\partial t} + \nabla \cdot (\rho u_i \boldsymbol{u}) + \nabla_i (p + Q) = 0 \qquad \text{for } i = 1, 2, 3 \tag{2.2}$$

$$\frac{\partial (\rho e)}{\partial t} + \nabla \cdot (\rho e \boldsymbol{u}) + (p + Q) \nabla \cdot \boldsymbol{u} = \rho \dot{q} + \nabla \cdot (k \nabla T) \tag{2.3}$$

$$\frac{\partial n_j}{\partial t} + \nabla \cdot (n_j \boldsymbol{u}) = \dot{n}_j + \nabla \cdot (\mathcal{D} \nabla n_j) \qquad \text{for } j = 1 \ldots n_\mathrm{t} \tag{2.4}$$

$$p = p(\rho, e) \qquad \text{and} \qquad T = T(\rho, e) \tag{2.5}$$

The mass conservation equation 2.1 relates the rate of change of density ρ with time t to spatial derivatives of the particle velocity vector $\boldsymbol{u}$, with components u_i. The momentum conservation equations 2.2 in the three dimensions i relate the rate of change of momentum to the spatial derivatives of pressure p and artificial viscous pressure Q. The energy conservation equation 2.3 describes the effect on the specific internal energy e of the hydrodynamic work, the chemical energy release rate $\dot{q}$ and thermal conduction, through the thermal conductivity k and the spatial gradient of temperature T. The species conservation equations 2.4 for the rate of change of the molar density (number of moles per unit volume) of each chemical species n_j depend on the chemical reaction rates $\dot{n}_j$ and the diffusion coefficient $\mathcal{D}$. There are n_t species conservation equations in total, where n_t is the total number of species involved in the chemical reaction scheme. The equation of state (equations 2.5) describes the isotropic response of the material to changes in density ρ and specific internal energy e. For future reference, a list of the notation used in this thesis is given on page v.

Equations 2.1 to 2.5 above are written in the laboratory reference frame, known as the Eulerian frame. It is useful to convert the equations to a reference frame that moves with the material, known as the Lagrangian frame. The Lagrangian time derivative $\mathrm{D}/\mathrm{D}t$ can

be related to the Eulerian time derivative $\partial/\partial t$ via

$$\frac{\mathrm{D}\phi}{\mathrm{D}t} \equiv \frac{\partial\phi}{\partial t} + \boldsymbol{u}\cdot\nabla\phi, \tag{2.6}$$

where ϕ is any physical quantity [89]. Manipulating equations 2.1 to 2.4 using equation 2.6, the reactive-flow modelling equations become in the Lagrangian frame

$$\begin{aligned}
&\frac{\mathrm{D}(\rho\delta V)}{\mathrm{D}t} = 0\\
&\rho\frac{\mathrm{D}u_i}{\mathrm{D}t} + \nabla_i(p+Q) = 0 \qquad \text{for } i = 1,2,3\\
&\rho\frac{\mathrm{D}e}{\mathrm{D}t} + (p+Q)\nabla\cdot\boldsymbol{u} = \rho\dot{q} + \nabla\cdot(k\nabla T)\\
&\frac{1}{\delta V}\frac{\mathrm{D}(n_j\delta V)}{\mathrm{D}t} = \dot{n}_j + \nabla\cdot(\mathcal{D}\nabla n_j) \qquad \text{for } j = 1\ldots n_\mathrm{t}\\
&p = p(\rho,e) \qquad \text{and} \qquad T = T(\rho,e),
\end{aligned} \tag{2.7}$$

where δV is the volume of a small element of the material. Use of the Lagrangian frame allows the advection terms, which have the form $\nabla\cdot(\phi\boldsymbol{u})$ in the Eulerian equations 2.1 to 2.4, to be removed. These terms describe how material flows from one computational cell to another and can lead to numerical diffusion in Eulerian hydrocodes [28]. (Advection will be discussed in section 2.2.) Equations 2.7 are the complete set of equations that will be considered in this work. The four physical processes they describe will be discussed separately in sections 2.1.1 to 2.1.4, and computational techniques used to solve them will be presented in section 2.2. The equations of state $p(\rho,e)$ and $T(\rho,e)$ represent the behaviour of the material and will be the subject of chapter 3.

2.1.1 Hydrodynamics

In this thesis, the term "hydrodynamics" is used to describe unsteady, compressible, inviscid flow of any material. The hydrodynamic equations are known as the Euler equations and can be found in many textbooks, e.g., reference 89. In the Lagrangian frame they are

$$\begin{aligned}
&\frac{\mathrm{D}(\rho\delta V)}{\mathrm{D}t} = 0\\
&\rho\frac{\mathrm{D}u_i}{\mathrm{D}t} = -\nabla_i(p+Q) \qquad \text{for } i = 1,2,3\\
&\rho\frac{\mathrm{D}e}{\mathrm{D}t} = -(p+Q)\nabla\cdot\boldsymbol{u}.
\end{aligned} \tag{2.8}$$

They can be derived by considering the conservation of mass, momentum and energy for a small element of material. The hydrodynamics equations 2.8 are written in terms of specific internal energy e rather than total energy for two reasons [28]. Firstly, if they were written in terms of total energy, then e would need to be calculated as the difference between the total energy and the kinetic energy for use in the equation of state. Since the total and kinetic energies are large and similar in magnitude in the shock regime, the calculation of e would be prone to numerical errors. Secondly, in Eulerian hydrocodes, unrealistic heating errors can be reduced if specific internal energy is advected rather than total energy.

The artificial viscous pressure Q is included in the hydrodynamics equations 2.8 in order to model shock discontinuities by spreading the shock front over several computational cells [97]. Care must be taken to choose an appropriate form of artificial viscosity that has good directional properties and introduces sufficient shock smearing to prevent oscillations, while minimising its diffusive effect [98]. Riemann solvers and flux limiters [28] are alternative techniques for dealing with shocks which have their own advantages and disadvantages, but they will not be used in this work.

Analytic solutions to the hydrodynamics equations can provide a useful test of the accuracy of numerical schemes. For example, solutions to the Riemann problem [99] include equations for shocks and rarefactions generated at the interface between two uniform regions. These provide an analytic solution to the Sod shock tube [100] which is regularly used as a hydrocode test problem. Another example is the Rankine-Hugoniot equations which relate the thermodynamic states before and after a shock, and can be found in any textbook on shock physics, e.g., reference 1. These equations are used to generate the analytic solution to the plate-impact test problem in section 2.2. Although analytic solutions to various idealised hydrodynamics problems are available, the multiple wave interactions that occur at the mesoscale make an analytic approach not feasible for modelling the shock-to-detonation transition in plastic-bonded explosives. This is why a numerical approach is followed in this work.

2.1.2 Chemistry

Chemical reactions are of fundamental importance in explosives. The build-up of chemical reaction behind the shock front is responsible for the growth to detonation, and its subsequent self-sustaining propagation. As mentioned in sections 1.4 and 3.4, there is

still considerable uncertainty regarding the detailed reaction kinetics in explosives, despite many decades of research. Many continuum reactive-burn models use pressure-based reaction rates based on empirical observations [e.g., 36]. However, chemists favour the Arrhenius temperature-dependent reaction rates that will be used in this work [6]. In the Lagrangian frame and for a single-step reaction A $\overset{1}{\rightarrow}$ B, the governing energy conservation equation is

$$\frac{\mathrm{D}e}{\mathrm{D}t} = \dot{q} = q_1 n_\mathrm{A} z_1 e^{-E_1/RT} \tag{2.9}$$

and the species conservation equations are

$$\begin{aligned} \frac{1}{\delta V}\frac{\mathrm{D}(n_\mathrm{A}\delta V)}{\mathrm{D}t} &= \dot{n_\mathrm{A}} = -n_\mathrm{A} z_1 e^{-E_1/RT} \\ \frac{1}{\delta V}\frac{\mathrm{D}(n_\mathrm{B}\delta V)}{\mathrm{D}t} &= \dot{n_\mathrm{B}} = n_\mathrm{A} z_1 e^{-E_1/RT}, \end{aligned} \tag{2.10}$$

where q_1 is the heat released by reaction 1, z_1 is the frequency factor for the reaction, E_1 is the activation energy and R is the molar gas constant. For a single-step reaction, the unreacted explosive is species A and the reaction products are species B, with molar densities n_A and n_B respectively. The Arrhenius reaction rate can be derived from kinetic theory [101] by assuming that molecules must acquire activation energy E_1 before they can react. Arrhenius reactions present a challenge to computational schemes because the rate of reaction can be slow for a long time, before the temperature rises sufficiently for rapid reaction to proceed [88]. A stiff ordinary differential equation solver may need to be used, as will be discussed in section 2.3.2.

2.1.3 Heat conduction

Heat conduction is neglected in many hydrocodes because it is a relatively slow effect on the centimetre length-scales of interest in engineering applications. However, it is recognised that heat conduction plays an important role in determining whether hotspots are sub-critical or super-critical (see chapter 6) and so heat conduction needs to be included in mesoscale models. In the Lagrangian frame, the governing equation is

$$\rho\frac{\mathrm{D}e}{\mathrm{D}t} = \nabla\cdot(k\nabla T), \tag{2.11}$$

where k is the thermal conductivity and T is the temperature. This is Fourier's law of thermal conduction [102] that the heat flux is proportional to the local temperature gradient ∇T. Section 2.3 will describe how heat conduction was implemented in a one-dimensional hydrocode. The dependence on the spatial gradient of the temperature means that heat conduction cannot be implemented on a cell-by-cell basis like equation of state or strength models, but must be integrated into the energy conservation equation.

2.1.4 Species diffusion

In many computational fluid dynamics codes for reactive flow, species diffusion is included in addition to thermal conduction [88]. However, hydrocode models of plastic-bonded explosives usually do not include species diffusion, and Reaugh [103] has demonstrated that species diffusion can be neglected at the high pressures of relevance to shock initiation. In the Lagrangian frame, the species diffusion equations are

$$\frac{1}{\delta V}\frac{\mathrm{D}(n_j \delta V)}{\mathrm{D}t} = \nabla \cdot (\mathcal{D} \nabla n_j) \qquad \text{for } j = 1 \ldots n_\mathrm{t},$$

where n_j is the molar density of species j, $\mathcal{D}$ is the diffusion coefficient and n_t is the total number of species. This is Fick's law of diffusion [102] that the flux is proportional to the local concentration gradient, and is analogous to the heat conduction equation. To determine whether it is appropriate to neglect species diffusion in this work, compare the magnitudes of the two effects. Using the material properties data for HMX and the binders in PBX9501 and EDC37 from section 3.2, an estimate for the timescale of thermal conduction is

$$\Delta t \sim \frac{\rho c_\mathrm{v} (\Delta x)^2}{k} \sim (5 \times 10^6 \,\mathrm{s}\,/\,\mathrm{m}^2)(\Delta x)^2,$$

where c_v is the specific heat capacity and Δx is a relevant length-scale. Bedrov [104] derived the self-diffusion coefficient for liquid HMX from molecular dynamics simulations. His values ranged from $0.06{\times}10^{-9}\,\mathrm{m}^2\,/\,\mathrm{s}$ at 550 K to $0.325{\times}10^{-9}\,\mathrm{m}^2\,/\,\mathrm{s}$ at 800 K, leading to the following estimates for the timescale of species diffusion in liquid HMX:

$$\Delta t \sim \frac{(\Delta x)^2}{\mathcal{D}} \sim \begin{cases} (1.7 \times 10^{11}\,\mathrm{s}\,/\,\mathrm{m}^2)(\Delta x)^2 & \text{for liquid HMX at 550 K} \\ (3.1 \times 10^{9}\,\mathrm{s}\,/\,\mathrm{m}^2)(\Delta x)^2 & \text{for liquid HMX at 800 K} \end{cases}$$

In solid HMX, the diffusion times will be higher because the crystal lattice inhibits molecular motion. These estimates show that species diffusion in HMX is much slower than thermal conduction. In addition, these timescales can be compared to the reaction duration in detonating PBX9501 and EDC37. From the particle-velocity gauge traces for an EDC37 experiment which detonates, the reaction time is approximately 0.028 μs [75]. For a steady-state detonation speed of 8.8 mm/μs, the reaction zone length is therefore 0.25 mm. For diffusion or heat conduction to have an effect over even a tenth of this length would take 1 ms, four orders of magnitude slower than the reaction time. This suggests that both heat conduction and diffusion are of little interest in the detonation regime. In the shock initiation regime, the longer reaction time ~1 μs means that heat conduction could have an effect over short distances (e.g., for hotspots), but species diffusion is several orders of magnitude slower. Therefore, it is reasonable to neglect species diffusion in both the shock initiation and detonation regimes, so species diffusion is omitted from this work.

2.2 Hydrocodes

The two major classes of hydrocodes, Lagrangian and Eulerian, are illustrated in figure 2.1. A Lagrangian hydrocode solves the conservation equations on a grid that moves with the material. This has the advantages of automatically providing increased resolution where the material is compressed and allowing accurate modelling of material interfaces, but the disadvantages that the mesh may be difficult to construct in complex geometries (such as a granular explosive microstructure) and may tangle as the calculation proceeds [105]. An Eulerian code uses a fixed grid, through which material can flow.

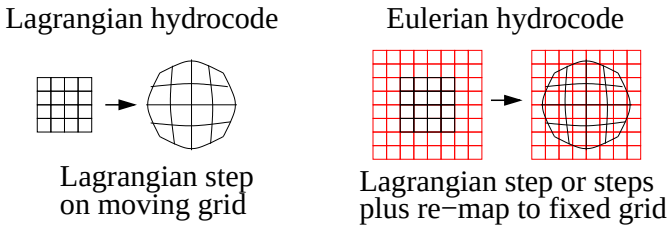

Figure 2.1: Illustration of the differences between Lagrangian and Eulerian hydrocodes. Both types of hydrocode advance the solution to the next timestep using a Lagrangian step. After a few timesteps, Eulerian codes perform an advection step to re-map the solution back to the original fixed grid.

This is often achieved by initially advancing the conservation equations with a few (typically 1, 2 or 4) Lagrangian steps, before an advection step is used to re-map the solution back to the original fixed grid [106]. Eulerian codes have the advantage of being robust because mesh-tangling is avoided, and unimportant material can be allowed to move off the computational domain through the use of transmissive boundaries. Disadvantages are that the advection step reduces accuracy and mixed cells at interfaces do not easily allow physical effects like slide and friction to be modelled. Some codes make a compromise between these two extremes: Arbitrary Lagrangian Eulerian codes use a Lagrangian grid that can move in a semi-Eulerian way to avoid mesh tangling [105]. Adaptive Mesh Refinement codes use an Eulerian grid with sub-divided cells to increase mesh resolution in areas of interest. All of these types of hydrocode are available but four codes will be used in this work. They are all multi-material hydrocodes that use predictor-corrector schemes to advance the hydrodynamic equations 2.8 in time on a staggered grid.

- Peruse [107] is a one-dimensional Lagrangian hydrocode, whose source code and documentation were provided by Whitworth [108]. Section 2.3.2 will describe the modifications that have been made to Peruse in order to incorporate the effects of heat conduction and Arrhenius chemistry. The updated Peruse code will be used for one-dimensional simulations throughout this work.

- As will be discussed below, Chec is a one-dimensional Eulerian hydrocode. It was written during the initial stages of this work to demonstrate that an understanding of hydrocode numerics had been achieved. However, an Eulerian code provides no advantage over a Lagrangian code in one dimension where mesh tangling cannot occur, so Chec will not be used in subsequent chapters.

- Corvus [105] is a two-dimensional Arbitrary Lagrangian Eulerian hydrocode. It has been used for only a few simulations in this work, although its potential for use in future work to investigate hotspot mechanisms (where interface effects might be important) is recognised.

- Petra [109] is a two-dimensional Eulerian hydrocode. Langridge kindly modified the code to accept microstructure geometries as input (see section 2.4), and provided the resulting executable and documentation [110]. Petra does not currently have heat conduction and Arrhenius chemistry capabilities, so it can only be used for modelling inert explosive. Chapter 7 will make extensive use of Petra to investigate bulk temperature distributions in PBX9501 and EDC37.

Peruse, Corvus and Petra are well-established codes that have all passed a suite of test problems and so they will be used without detailed examination in this work. In contrast, Chec is a new code and its performance against two test problems will be presented below.

2.2.1 Chec: a 1D Eulerian hydrocode

Chec is a one-dimensional Eulerian hydrocode that was written (in Fortran 90) during the initial stages of this work. Chec solves the Eulerian reactive-flow modelling equations 2.1 to 2.5 in one-dimensional plane geometry neglecting chemistry, heat conduction and diffusion. A polytropic gas is used for the equation of state:

$$p = (\gamma - 1)\rho e, \tag{2.12}$$

where γ is the ratio of specific heat at constant pressure to that at constant volume. This can be derived from the more familiar ideal gas equations $p = \rho RT$ and $e = c_v T$, for constant c_v, which were originally determined experimentally but can also be derived from kinetic theory [101]. The temperature T is eliminated in equation 2.12 to create an equation of state (EOS) of the form $p(\rho, e)$ which is sufficient to solve the hydrodynamic equations. A temperature relation $T(\rho, e)$ is only required when additional physics like heat conduction is modelled. The polytropic gas equation of state is used here because it is convenient for hydrocode testing purposes owing to its simple analytic form, but it begins to break down even for gases under atmospheric conditions [88], and is inadequate for modelling both solid unreacted explosives and hot, high-pressure gaseous reaction products. For these reasons, more advanced equations of state will be used elsewhere in this work (see chapter 3).

A simple quadratic artificial viscous pressure [97] is used:

$$Q = \begin{cases} 0 & \text{for } \frac{\partial u}{\partial x} \geq 0 \\ \beta_Q \rho \Delta x^2 \left(\frac{\partial u}{\partial x}\right)^2 & \text{for } \frac{\partial u}{\partial x} \leq 0, \end{cases} \tag{2.13}$$

where Δx is the computational cell size and β_Q is a constant known as the quadratic artificial viscosity coefficient. This is known as the standard form by Noh [111] and, although it smooths shock discontinuities sufficiently to enable hydrocode calculations to run, it fails to entirely eliminate oscillations behind shocks. These can be mitigated by adding a linear artificial viscosity term $\beta_L \rho c \Delta x (\partial u / \partial x)$ [112], where β_L is the linear

artificial viscosity coefficient and c is the sound speed. More advanced artificial viscosity forms, for example monotonic viscosity [27] and Wilkins viscosity [98], are implemented in Peruse and Petra and will be used in subsequent chapters to produce better results.

Chec is an explicit finite-difference code. This means that the flow variables are advanced to time t^{n+1} using the known values at the previous time t^n, in contrast to an implicit or semi-implicit scheme where a combination of values at t^{n+1} and t^n is used. Explicit schemes are favoured for unsteady flow since they are more accurate and computationally efficient [89]. However, the timestep $\Delta t = t^{n+1} - t^n$ used in an explicit scheme needs to be controlled to ensure stability. The Courant-Friedrichs-Lewy (CFL) condition for hyperbolic equations is used:

$$\Delta t = \frac{C\Delta x}{c}, \tag{2.14}$$

where C is the Courant factor. It is necessary that $C \leq 1$ for stability but it is desirable that C should be as close to 1 as possible to enable an accurate solution to be obtained [89]. A predictor-corrector scheme is used in Chec to provide second-order accuracy in time. In the predictor step, the numerical solution is advanced to time $t^{n+1/2}$ with first-order accuracy to calculate a half-timestep pressure and artificial viscosity. These are then used in the corrector step to advance the solution from t^n to t^{n+1} with second-order accuracy.

A staggered grid is used: the velocity u is stored at cell edges while ρ, e, p and Q are stored at cell centres. Staggered grids allow strength models to be implemented relatively easily and are generally favoured by the hydrocode community [105]. Two different boundary conditions, reflective and transmissive, are implemented in Chec using a ghost cell at each end of the computational domain. The final boundary condition needed to run a hydrocode simulation is the initial condition at t^0. The initial geometry is defined in the hydrocode input and the thermodynamic state within each computation cell is calculated during initialisation.

In common with most hydrocodes, Chec uses operator splitting to solve the hydrodynamics equations in a series of steps [27]. These steps, which are based on the scheme in Petra [109], are summarised in figure 2.2. The left side of the flow-chart describes how the solution is advanced to the next timestep on a Lagrangian mesh. The right side shows the advection step that is used to re-map the solution back to the fixed grid. During the Lagrangian predictor step, the particle velocity and specific internal energy are advanced to $t^{n+1/2}$ using the momentum and energy conservation equations, in order to calculate

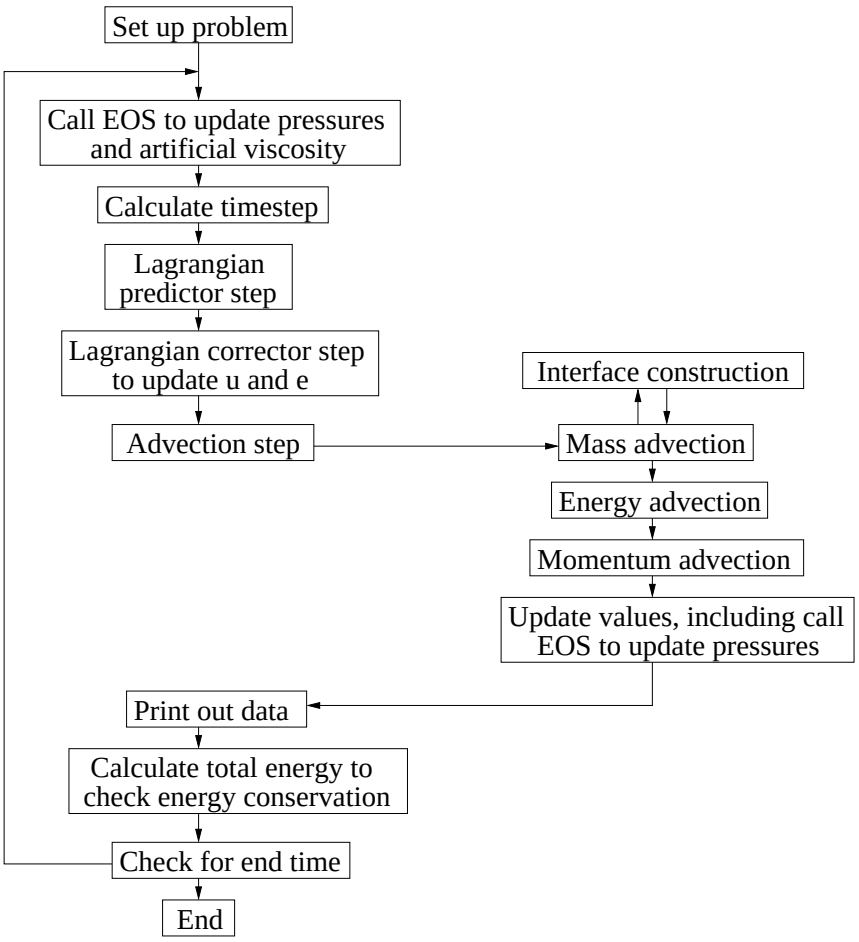

Figure 2.2: A flow-chart for the computational scheme in Chec. To achieve second-order accuracy, a predictor step calculates the pressure and artificial viscosity at the half-timestep, before the full-timestep Lagrangian corrector step. The advection step is used to remap the full-timestep solution back to the fixed computational grid.

half-timestep values for pressure and artificial viscosity. The velocity and specific internal energy updates are repeated using the half-timestep values for p and Q during the corrector step. During the advection step, the mass, energy and momentum conservation equations are used to calculate the density, specific internal energy and particle velocities at t^{n+1}, before the equation of state is called to determine the pressure and artificial viscosity.

The total energy is calculated at the end of each timestep to check that total energy conservation across the computational grid is satisfactory. A consequence of expressing the hydrodynamics equations in terms of specific internal energy rather than total energy is that the momentum advection step does not conserve kinetic energy exactly [28]. In common with many Eulerian codes, Chec includes an energy dissipation function to add

the kinetic energy lost from each cell to its internal energy, subject to an artificial viscosity cutoff of $Q \geq 10^{-3}p$. The cutoff ensures that dissipated kinetic energy is converted to internal energy only in the presence of shocks, where this process is physically reasonable.

First, second and third-order van Leer advection schemes [106] have been implemented to allow the differences between the three schemes to be observed. The first-order scheme is significantly more diffusive than the higher-order schemes but flux limiters are needed to reduce non-physical oscillations with the second and third-order methods [109]. An interface construction method is needed to reduce numerical diffusion at material interfaces [28]. The Simple Line Interface Calculation (SLIC) scheme [113] is used in Chec. This recognises six fluid configuration types and allocates volume fluxes for each material according to its position relative to the surrounding computational cells. SLIC is a relatively simple first-order algorithm and more advanced techniques, e.g. Youngs' method [109], are often used in 2D and 3D hydrocodes. Another error arises when mixed cells (containing more than one material) are used in Eulerian hydrocodes. During the Lagrangian step, the compression of a mixed cell is distributed evenly between the materials present in the cell. This assumption is not appropriate when one material is significantly softer than the others, so inaccurate pressures and temperatures will be produced. A pressure relaxation option is included in many Eulerian hydrocodes to allow the materials within a cell to approach pressure equilibrium at the end of the Lagrangian step. However, this option is not available in Chec.

Chec uses well-established methods to solve the hydrodynamics equations and so it is not useful to describe its workings in detail here. Instead, the results of two one-dimensional test problems (sketched in figure 2.3) will be shown to demonstrate that the code works correctly. The analytic solution [99] to the Sod shock-tube problem is compared to the results of a Chec simulation at 15 µs in figure 2.4, showing that the code performs reasonably well. The internal energy overshoot at $x = 64$ cm is due to the wall heating effect that will be discussed below. The oscillations near $x = 50$ cm are a start-up error caused by the initial shock discontinuity, and could be reduced by suppressing the timestep at the start of the calculation. Importantly, Chec gives results of similar quality to other hydrocodes [105, 107] with 100 zones across the computational domain, the mesh resolution originally defined for the Sod shock-tube problem [100].

The results of a plate impact simulation are compared with the analytic solution at 5 µs in figure 2.5. The wall heating effect reduces the density and increases the internal energy at the boundary between the two regions ($x = 4.5$ cm). Apart from this, figure 2.5 shows

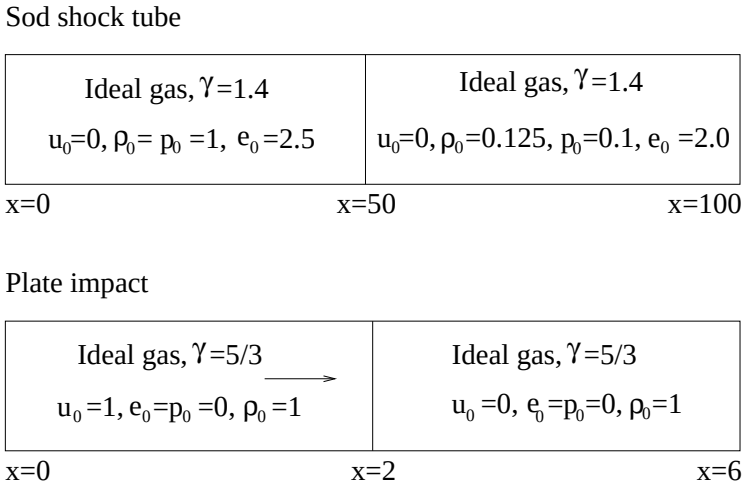

Figure 2.3: Two standard one-dimensional hydrocode test problems: the Sod shock-tube problem (above) and a plate-impact problem (below). Any set of self-consistent units can be used: in figures 2.4 and 2.5 we use g, cm, μs and Mbar to be consistent with other hydrocodes.

that the code gives good results for the plate impact test problem. The satisfactory results for both test problems demonstrate that, by writing Chec, an understanding of hydrocode numerics has been achieved.

The wall heating errors observed in figures 2.4 and 2.5 are a well-documented effect, described by Noh [111]. They are caused by near-discontinuous shocks being driven into the computational domain at $t = 0\,\mu s$. The shocks must travel through several computational cells before the artificial viscosity is able to smear them sufficiently. This means that internal energy is over-predicted, and density under-predicted, at the interface. The effect can be reduced by introducing heat conduction to dissipate the excess energy and/or by the use of adaptive mesh refinement, but it cannot be eliminated. Wall heating errors occur in most of the simulations described in this thesis, and their effects will be described as they arise in each of the chapters.

Noh [111] also defined a spherical rigid-wall impact geometry that is routinely used as a hydrocode test problem. It highlights two types of errors associated with the use of artificial viscosity: the wall heating error described above and the overheating that occurs in convergent geometry. Since the second error does not occur in plane geometry and Chec does not have the capability to run in cylindrical or spherical geometry, the Noh test problem is not used here.

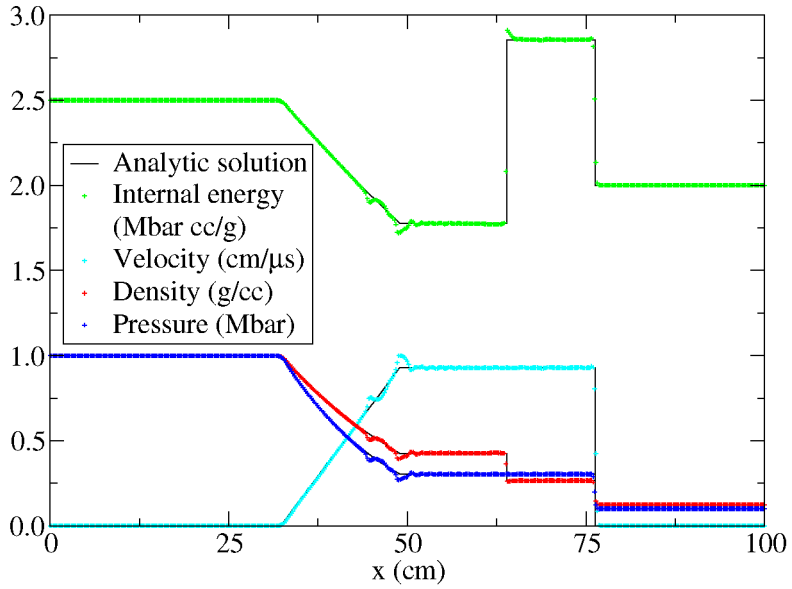

Figure 2.4: The analytic solution to the Sod shock-tube problem (black lines) is compared to the results of a Chec simulation (points) with 500 zones across the 100 cm computational domain, at time $t = 15\,\mu s$, showing reasonably good agreement.

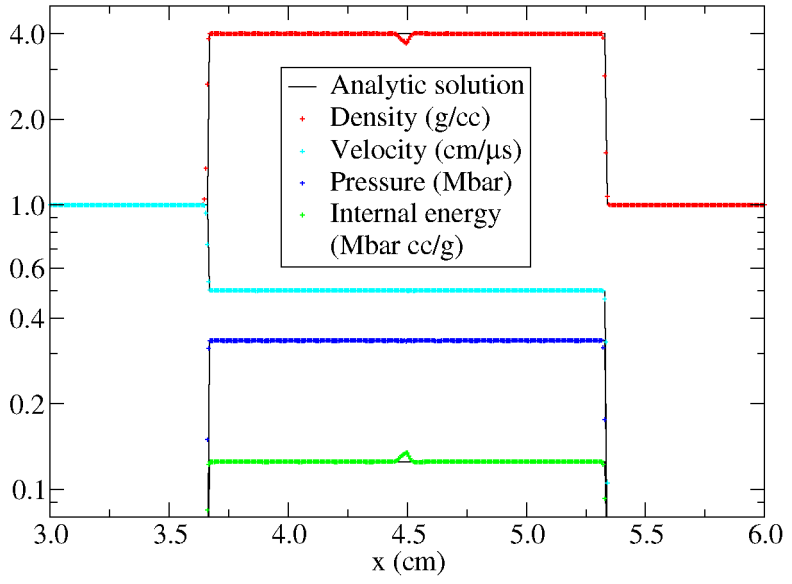

Figure 2.5: The analytic solution to a plate-impact test problem (black lines) is compared to the results of a Chec simulation (points) with 1000 zones across the 6 cm computational domain, at time $t = 5\,\mu s$, showing good agreement.

2.3 Heat conduction and Arrhenius chemistry

As discussed in section 2.1, heat conduction and Arrhenius chemistry are important physical effects in shocked explosives. Neither of these effects were previously available in Peruse [107], although Whitworth has included a rudimentary implementation in recent versions [114]. This makes two significant approximations: that the internal energy e can be related to the temperature T and the specific heat capacity c_v via the ideal gas equation $e = c_v T$, and that the reaction rate is decoupled from the hydrodynamics. Neither of these approximations are deemed to be acceptable in this work, and so a new implementation of heat conduction and Arrhenius chemistry in Peruse was required. The new coding was based on the numerical scheme in ReactDiff, a static chemical reaction and thermal diffusion code [115].

2.3.1 ReactDiff

Fluid Gravity's ReactDiff code solves the equations for chemical reaction and heat conduction, treating the problem as static and one-dimensional. Compared to the full reactive-flow equations 2.7, hydrodynamics and species diffusion are neglected and so an equation of state is not required. A variety of chemical reaction schemes are available in ReactDiff but, as an example, McGuire & Tarver's [86] three-step reaction scheme $\mathrm{A} \xrightarrow{1} \mathrm{B} \xrightarrow{2} 2\mathrm{C} \xrightarrow{3} \mathrm{D}$ for HMX will be described. For this scheme, ReactDiff solves the following equations:

$$\begin{aligned}
c_v \frac{\partial T}{\partial t} &= \frac{\nabla \cdot (k \nabla T)}{\rho} + N_A q_1 Z_1 e^{-E_1/RT} + N_B q_2 Z_2 e^{-E_2/RT} + {N_C}^2 q_3 Z_3 e^{-E_3/RT} \\
\frac{\partial N_A}{\partial t} &= -N_A Z_1 e^{-E_1/RT} \\
\frac{\partial N_B}{\partial t} &= N_A Z_1 e^{-E_1/RT} - N_B Z_2 e^{-E_2/RT} \\
\frac{\partial N_C}{\partial t} &= N_B Z_2 e^{-E_2/RT} - {N_C}^2 Z_3 e^{-E_3/RT} \\
\frac{\partial N_D}{\partial t} &= {N_C}^2 Z_3 e^{-E_3/RT},
\end{aligned} \tag{2.15}$$

where q_i is the heat released by reaction i, Z_i is the static frequency factor, E_i is the activation energy and R is the molar gas constant. N_j are the mass fractions of the unreacted explosive A, partially reacted species B and C, and the reaction products D. These static

equations contain two simplifications compared to the dynamic chemical reaction equations 2.9 and 2.10. The first is that the specific internal energy has been replaced with temperature using the thermodynamic relation

$$\left(\frac{\partial e}{\partial t}\right)_v = c_v \frac{\partial T}{\partial t},$$

where $v = 1/\rho$ is specific volume. This neglects the contribution of compression to the change in specific internal energy because v is constant in a static code. The second simplification is the use of the static mass fractions N_j which can be related to molar densities n_j as follows:

$$N_j = n_j M_j / \rho_0, \tag{2.16}$$

where M_j is the molar mass of species j and ρ_0 is the density (a constant). The derivation of the static mass-fraction equations 2.15 from the conventional molar density equations is given in appendix A.

ReactDiff uses an operator splitting method to solve equations 2.15 in two steps. Firstly, the effect of the chemical reaction is evaluated using the Livermore ordinary differential equation solver, VODE [116, 117]. This solves the initial value problem for stiff or non-stiff systems of first order ordinary differential equations. Integration method 22 is used, which is the recommended option for stiff equations with a full Jacobian, where the code is required to calculate the Jacobian automatically. Secondly, the effect of heat conduction is calculated using a Crank-Nicholson scheme [89]. This is a semi-implicit method that combines the stability of an implicit method with second-order accuracy in both space and time. The change in temperature in each computational cell due to heat conduction depends on the temperatures in its nearest neighbours, creating a tridiagonal set of simultaneous equations. These are solved using a tridiagonal matrix solver from chapter 2.4 of reference 118. The numerical scheme is unconditionally stable, but the user is required to specify a sufficiently small timestep to produce accurate results. Both isothermal and adiabatic boundary conditions are available in ReactDiff.

2.3.2 Peruse implementation

To incorporate chemical reactions and heat conduction in Peruse, the existing hydrodynamics coding was extended to include heat conduction and chemistry terms, so that

the modified code solves the Lagrangian reactive-flow modelling equations 2.7 neglecting species diffusion. The implementation of heat conduction and chemistry in Peruse uses an operator-splitting method: the contribution due to hydrodynamics is calculated first, followed by chemical reaction and then heat conduction. The chemistry and conduction steps are based on those in ReactDiff but it is necessary to modify the chemical reaction equations to account for the effects of dynamics, and additional correction factors are required to improve total energy conservation. These are discussed below.

In ReactDiff, the governing equations 2.15 are written in terms of N_j, the static mass fraction of species j. To account for the compression of computational cells in Peruse, the dynamic mass fraction f_j is used instead:

$$f_j = n_j M_j / \rho, \tag{2.17}$$

where M_j is the molar mass of species j and ρ is the density (a variable). Following the analysis in appendix A, the species conservation equations require additional density factors to be included for second- or higher-order reaction rates. For example, McGuire & Tarver's [86] three-step reaction scheme for HMX becomes

$$\begin{aligned}
\dot{f}_\mathrm{A} &= -f_\mathrm{A} Z_1 e^{-E_1/RT} \\
\dot{f}_\mathrm{B} &= f_\mathrm{A} Z_1 e^{-E_1/RT} - f_\mathrm{B} Z_2 e^{-E_2/RT} \\
\dot{f}_\mathrm{C} &= f_\mathrm{B} Z_2 e^{-E_2/RT} - \frac{\rho}{\rho_0} {f_\mathrm{C}}^2 Z_3 e^{-E_3/RT} \\
\dot{f}_\mathrm{D} &= \frac{\rho}{\rho_0} {f_\mathrm{C}}^2 Z_3 e^{-E_3/RT}.
\end{aligned} \tag{2.18}$$

Correction factors

The Lagrangian reactive flow equations 2.7 contain hydrodynamics terms expressed as functions of specific internal energy e, and chemical reaction and heat conduction terms dependent on temperature T. For the ideal gas equation of state, it is easy to convert between the two using $e = c_\mathrm{v} T$. For more advanced equations of state, like those described in chapter 3, e is a function of both T and specific volume v. In addition, for chemically reactive materials, there may be two or more species with different equations of state, making the conversion between e and T more difficult. The following method that has been developed for use in Peruse is similar to the source term method described in reference 119 and used in ALE3D, a coupled thermal/chemical/mechanical code [120, 121].

The equations of state (see chapter 3) treat reacting explosive as a mixture of solid unreacted explosive and gaseous reaction products, with specific internal energies e_s and e_g and specific volumes v_s and v_g. It is assumed that the solid and gaseous components are in pressure and temperature equilibrium. The burn fraction λ is defined as the mass fraction of detonation products in the mixture, and the mixing rules are

$$v = (1-\lambda)v_s + \lambda v_g \tag{2.19}$$

$$e = (1-\lambda)e_s + \lambda e_g. \tag{2.20}$$

The equations of state for the unreacted explosive and reaction products provide relationships $e_s(T, v_s)$ and $e_g(T, v_g)$ respectively. Substituting these into equation 2.20 and eliminating v_g using equation 2.19 allows the specific internal energy to be written as $e(T, v, v_s, \lambda)$. Taking the derivative with respect to time gives

$$\frac{\mathrm{D}e}{\mathrm{D}t} = \underbrace{\left(\frac{\partial e}{\partial T}\right)_{v,v_s,\lambda}\frac{\mathrm{D}T}{\mathrm{D}t}}_{1} + \underbrace{\left(\frac{\partial e}{\partial v}\right)_{T,v_s,\lambda}\frac{\mathrm{D}v}{\mathrm{D}t}}_{2} + \underbrace{\left(\frac{\partial e}{\partial v_s}\right)_{T,v,\lambda}\frac{\mathrm{D}v_s}{\mathrm{D}t}}_{3} + \underbrace{\left(\frac{\partial e}{\partial \lambda}\right)_{T,v,v_s}\frac{\mathrm{D}\lambda}{\mathrm{D}t}}_{4}. \tag{2.21}$$

Equation 2.21 expresses the fact that the rate of change of specific internal energy e depends not only on the temperature T but also on the specific volume v, the specific volume of the solid component v_s (representing how that specific volume is divided between the solid and gaseous components) and the burn fraction λ. Each of the terms 1 to 4 needs to be accounted for to accurately convert the specific internal energy to temperature for the chemistry and heat conduction steps. Detailed working for each of the terms is given in appendix B. The result is that the dependence on $\mathrm{D}v/\mathrm{D}t$ and $\mathrm{D}v_s/\mathrm{D}t$ can be eliminated, leaving

$$\frac{\mathrm{D}e}{\mathrm{D}t} = \left(c_v + \underbrace{\left(\frac{\partial e}{\partial v_s}\right)_{T,v,\lambda}\frac{\Theta}{\Psi}}_{\chi}\right)\frac{\mathrm{D}T}{\mathrm{D}t} + \left(\underbrace{e_g - e_s + (v_s - v_g)\left(\frac{\partial e_g}{\partial v_g}\right)_T + \left(\frac{\partial e}{\partial v_s}\right)_{T,v,\lambda}\frac{\Xi}{\Psi}}_{\frac{\mathrm{d}e}{\mathrm{d}\lambda}}\right)\frac{\mathrm{D}\lambda}{\mathrm{D}t}, \tag{2.22}$$

where

$$c_v = (1-\lambda)c_{v,s} + \lambda c_{v,CJ}$$

$$\Theta = \frac{\left(\frac{\partial p_g}{\partial e_g}\right)_{v_g}}{\left(\frac{\partial T_g}{\partial e_g}\right)_{v_g}} - \frac{\left(\frac{\partial p_s}{\partial e_s}\right)_{v_s}}{\left(\frac{\partial T_s}{\partial e_s}\right)_{v_s}}$$

$$\Xi = \left(\frac{\partial p_g}{\partial v_g}\right)_{e_g} \frac{(v_s - v_g)}{\lambda} - \left(\frac{\partial p_g}{\partial e_g}\right)_{v_g} \frac{\left(\frac{\partial T_g}{\partial v_g}\right)_{e_g}}{\left(\frac{\partial T_g}{\partial e_g}\right)_{v_g}} \frac{(v_s - v_g)}{\lambda}$$

$$\Psi = \left(\frac{\partial p_s}{\partial v_s}\right)_{e_s} - \left(\frac{\partial p_s}{\partial e_s}\right)_{v_s} \frac{\left(\frac{\partial T_s}{\partial v_s}\right)_{e_s}}{\left(\frac{\partial T_s}{\partial e_s}\right)_{v_s}} - \left(\frac{\partial p_g}{\partial v_g}\right)_{e_g} \frac{(\lambda - 1)}{\lambda} + \left(\frac{\partial p_g}{\partial e_g}\right)_{v_g} \frac{\left(\frac{\partial T_g}{\partial v_g}\right)_{e_g}}{\left(\frac{\partial T_g}{\partial e_g}\right)_{v_g}} \frac{(\lambda - 1)}{\lambda}.$$

Equation 2.22 is more conveniently written as

$$\frac{De}{Dt} = (c_v + \chi)\frac{DT}{Dt} + \frac{de}{d\lambda}\frac{D\lambda}{Dt}. \tag{2.23}$$

This can be compared to the familiar relation for a single material at constant volume:

$$\frac{De}{Dt} = c_v \frac{DT}{Dt}.$$

The terms χ and $de/d\lambda$ are "correction factors" needed to account for the change in specific internal energy as the reaction progresses and the specific volume of the computational cell is redistributed between the solid and gas components. The correction factors allow the energy conservation equation 2.9 for McGuire & Tarver's [86] three-step reaction scheme to be written as

$$\frac{DT}{Dt} = \frac{\left[q_1 f_A Z_1 e^{-E_1/RT} + q_2 f_B Z_2 e^{-E_2/RT} + q_3 \frac{\rho}{\rho_0} {f_C}^2 Z_3 e^{-E_3/RT} - \frac{de}{d\lambda}\frac{D\lambda}{Dt}\right]}{c_v + \chi} \tag{2.24}$$

during the operator-split chemistry step. It is assumed that species A and B are solid, and C and D are gaseous. Therefore, the mass fraction of gaseous reaction products is given by $\lambda = f_C + f_D$, so $D\lambda/Dt = f_B Z_2 e^{-E_2/RT}$.

The correction factors significantly improve energy conservation, but the way in which they are implemented is important. For example, a static simulation with $q_1 = q_2 = q_3 = 0$ should have $\Delta e = 0$ as the material converts from solid unreacted explosive to gaseous reaction products. For one of the test problems described below, it is found that $\Delta e \sim 600\,\mathrm{J/g}$ when the correction factors are omitted, $\Delta e \sim 1\,\mathrm{J/g}$ when the correction factors are calculated at the start of the chemistry step, and $\Delta e \sim 0.006\,\mathrm{J/g}$ when the correction factors are updated for each iteration within the chemistry step (i.e. they are sub-cycled). This indicates that the correction factors should be sub-cycled to achieve the best conservation of specific internal energy, which in turn influences the total energy

conservation that can be achieved by the code, although the convergence criteria used to achieve pressure and temperature equilibrium within the equation of state also play a role (see section 3.5). With sub-cycled correction factors, Peruse achieves total energy conservation to 10^{-3} % or better over a suite of test problems.

Numerical scheme

The modified numerical scheme in Peruse is illustrated in figure 2.6. Operator splitting is used to solve the hydrodynamics, chemical kinetics and heat conduction terms in turn. As in ReactDiff, the Livermore ordinary differential equation solver VODE is used for the chemical kinetics and a tridiagonal matrix solver is used for the heat conduction terms, which are formulated using a semi-implicit Crank-Nicholson scheme. A new equation of state routine is used to achieve pressure and temperature equilibrium between unreacted explosive and reaction products. This iterates on v_s and e_s to achieve $p_s = p_g$ and $T_s = T_g$

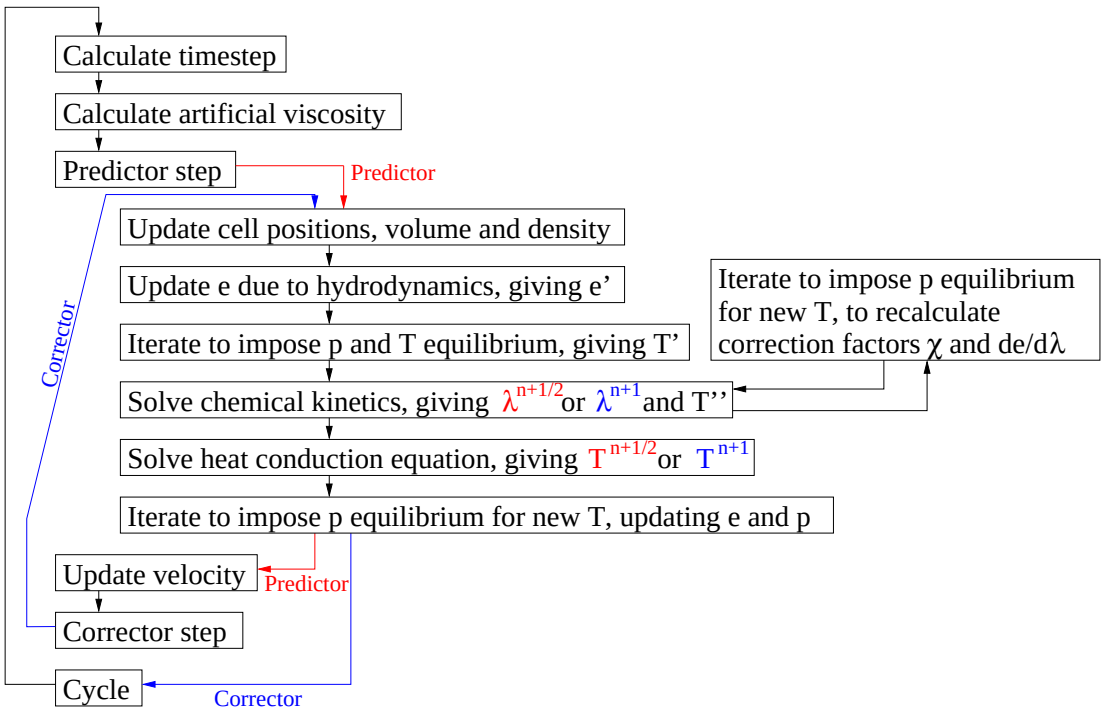

Figure 2.6: A flow-chart of the computational scheme in Peruse. The chemical kinetics and heat conduction terms are implemented within the existing predictor-corrector algorithm [107], to give second-order accuracy. The predictor step (coloured red) gives the pressure at the half timestep $t^{n+1/2}$, for use in the velocity update. The corrector step (blue) then re-calculates all the hydrodynamic quantities at the full timestep t^{n+1}.

as discussed in section 3.5. To sub-cycle the correction factors χ and $\mathrm{d}e/\mathrm{d}\lambda$ as discussed above, it is necessary for the chemical kinetics solver VODE to access the equation of state routine which, in this case, iterates on v_s only in order to achieve $p_s = p_g$. If the iterations fail to converge, start of timestep correction factors are used instead to increase code robustness at the expense of total energy conservation.

The timestep in Peruse is based on the Courant-Friedrichs-Lewy (CFL) condition as described section 2.2.1. The additional numerics that have been incorporated in Peruse to model heat conduction and chemistry are unconditionally stable, and so no modifications to the timestep calculation were needed. The effect of changing the Courant factor on the accuracy of the numerical solution will be investigated in section 7.1.3.

Either adiabatic or isothermal boundary conditions can be used in ReactDiff [115]. To implement isothermal boundary conditions in Peruse would require that the internal energy in the boundary cells be adjusted to maintain a constant temperature. This would be complicated and, although isothermal boundary conditions can be used to investigate hotspots [e.g., 24], it was judged that they are not of great relevance to shock initiation simulations of explosive microstructures, the eventual aim of this study. Therefore, only adiabatic boundary conditions were implemented in Peruse; these can be used with either the free or reflective hydrodynamic boundary conditions that were previously available.

Test problems

No significant modifications to a hydrocode can be trusted until they have been thoroughly tested. The modified Peruse code was subjected to extensive testing, resulting in the identification of a variety of code bugs that were subsequently resolved. A full list of the test problems that were eventually passed by Peruse is given below:

Sod shock tube [100]
Noh problem [111]
Beryllium stopping shell [105]
Reactive burn model tests (not relevant to this work)
Carslaw & Jaeger problem [122] - ReactDiff only
ODTX test problems [24, 86, 123] - ReactDiff only
Heat conduction test problem - comparison to ReactDiff
Heat conduction & chemistry test - comparison to ReactDiff
Plate impact test for solid equation of state - comparison to Corvus

Plate impact test for gas equation of state - comparison within Peruse
Plate impact test for solid and gas mixture
Static explosion in HMX - qualitative comparison to ReactDiff
Static explosion in binder - qualitative comparison to HMX
Dynamic explosion in HMX - qualitative comparison to static and inert calculations
Detonation in HMX - comparison to Menikoff [83] and PBX9501 gauge data [124]
Dynamic reaction of HMX and binder in plane geometry
Dynamic reaction of HMX and binder in spherical geometry

The heat conduction & chemistry test problem will be described in more detail as an example. This static test problem comprises an HMX region which extends from radius 0 to 0.5 μm and is initially at 724 K, surrounded by an inert binder region between radius 0.5 and 5.0 μm. The initial temperature of the binder is set to 882 K and it is given thermal properties representative of the binder in PBX9501. Adiabatic boundary conditions are used in plane, cylindrical and spherical geometry. To run this test problem in Peruse, the equation of state mixture treatment was modified so that the unreacted equation of state is used for all values of the burn fraction λ, and the unreacted equation of state parameters a, b and Γ were all set to zero, to ensure that the problem remains static by preventing the pressure rising above zero as chemical reaction proceeds. Results for spherical geometry are shown in figure 2.7. Overall, the ReactDiff and Peruse calculations agree remarkably well and total energy is conserved to within 2×10^{-6} %, so it was judged that Peruse had passed the heat conduction & chemistry test problem.

Space does not permit the results of all the test problems to be given here. However, it was concluded that Peruse had passed a comprehensive suite of test problems by performing as expected and with good total energy conservation. This enables the modified Peruse hydrocode, which incorporates heat conduction and Arrhenius chemistry, to be used with confidence in this work.

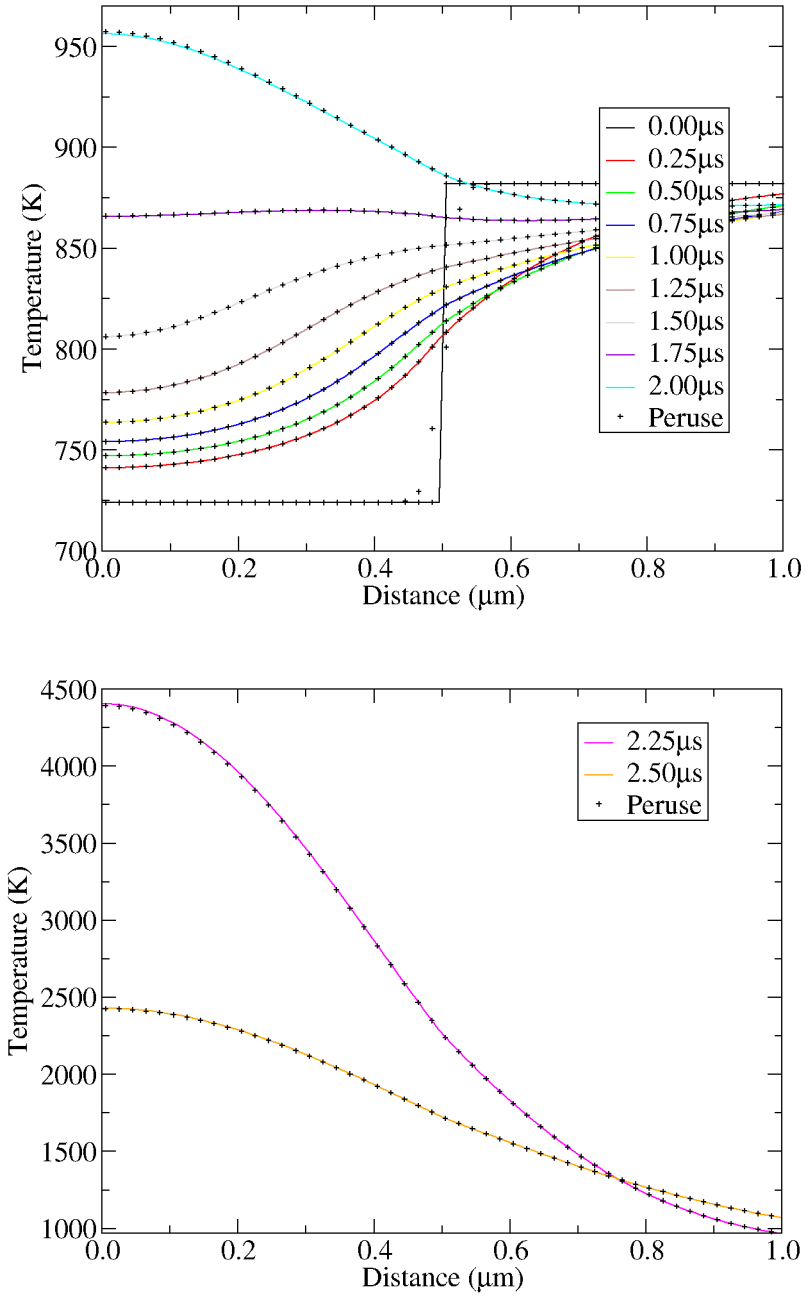

Figure 2.7: Comparison between ReactDiff (coloured lines) and Peruse (black points) for the heat conduction & chemistry test problem for PBX9501, in spherical geometry. The top graph shows the early time behaviour at relatively low temperatures, while the bottom graph shows the high-temperature explosion behaviour.

2.4 Generating computational microstructures

Previous studies have used two different techniques to construct computational geometries for simulations of plastic-bonded explosives. The first is to generate artificial geometries using knowledge of the size and shape of the explosive crystals [e.g., 64, 66 and 125]. Such methods have the advantage of being independent of experimental data (which may not be available), but the disadvantage that key features of real explosive microstructures may be missed. The second technique is to analyse experimental micrography or tomography data. Although 3D tomography data have been used for mesoscale modelling [67, 79], such data are not yet available for PBX9501 or EDC37 (partly owing to poor X-ray contrast between HMX and the binder materials). In this work, 2D optical micrography data will be used to generate computational microstructures because high-resolution images are available for these explosives [39]. Since the methods used previously [e.g., 69 and 78] were not available for this study, a simple technique was developed to analyse micrographs. Apart from the artefacts mentioned below, it is necessary to assume that the 2D micrographs are representative of the interior of an explosive charge. In future, it should be possible to test this assumption using 3D tomography data.

The micrographs of PBX9501 and EDC37 are illustrated in figures 1.5 and 1.6 on pages 10 and 11. A mixture of coarse and fine crystals can be seen, each of which is coated in a thin layer of binder. The dark holes (known as "pull-outs") are thought to have been crystals that were accidentally removed from the surface of the sample during polishing. The pull-outs and scratches are therefore artefacts of the sample preparation and should be ignored for the purposes of constructing a computational geometry. Some of the larger crystals are twinned: alternating layers of molecules have moved to a different crystallographic orientation in response to an applied stress, making them appear striped. Such features, along with pores and other defects that may not be visible, will not be represented in the simulations in this work since they will later be accounted for by hotspot models.

A thresholding tool was written to convert micrographs into a format suitable for hydrocode input. Peruse and Petra were modified (by Langridge [110] in Petra's case) to use the resulting input file to over-write the initial material properties on a cell-by-cell basis. In Peruse, a row number must be specified to select the appropriate one-dimensional strip of microstructural information. Although Petra has mixed-cell capabilities, Peruse is a Lagrangian code whose cells contain only one material. Since it is desirable to be able

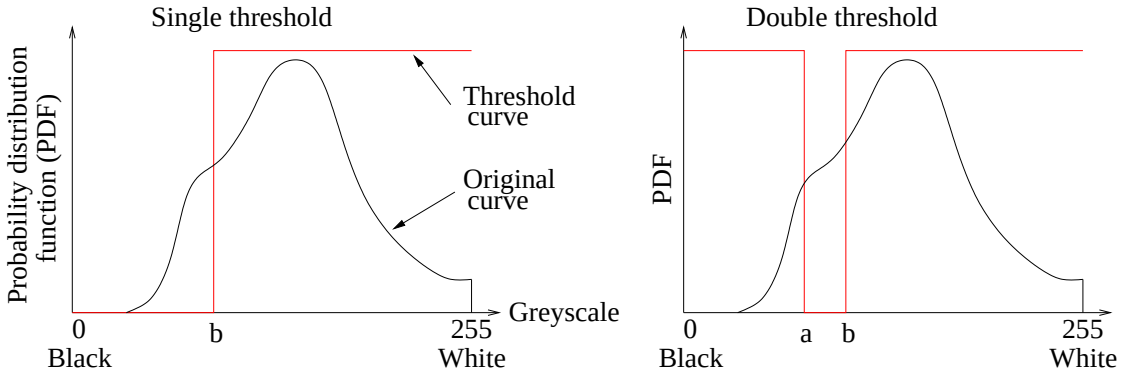

Figure 2.8: Sketch illustrating the function of the thresholding tool that was developed to convert micrographs into a format suitable for hydrocode input. A single threshold converts pixels darker than greyscale b to black and lighter pixels to white. A double threshold converts pixels darker than a or lighter than b to white, and pixels with greyscale values between a and b to black.

to use the same input file for calculations in both hydrocodes, an input file containing no mixed cells was preferred. This was achieved by analysing the micrographs (figures 1.5 and 1.6). By eye, it is easy to make the distinction between the light-grey crystals and the dark-grey binder between. However, the crystals appear in a variety of shades of grey and the images contain pull-outs, twinned crystals and scratches. These features mean that, if hydrocode cell volume fractions were assigned purely based on greyscale values, the initial computational geometry would comprise mainly grey, mixed cells with isolated spots of binder in the pull-out locations. To avoid this, a simple thresholding technique was used as illustrated in figure 2.8.

A single threshold can be applied at a greyscale value b to set pixels darker than the threshold to black and pixels lighter than the threshold to white. The value of b can be chosen so that the proportion of crystals and binder in the geometry corresponds to that in the real explosive composition. An example of this approach is shown in figure 2.9, where the EDC37 micrograph in figure 1.5 has been subjected to a single threshold at $b = 75$. This approach has the advantage of removing texture from the image but the dark pull-outs are over-emphasized. This results in a high concentration of binder in the pullout regions, which is not representative of a real microstructure. To avoid this problem, a double threshold can be applied at greyscale values of a and b. Pixels darker than the lower threshold a and lighter than the upper threshold b are set to white, while pixels whose greyscale values lie between a and b are set to black. The lower threshold a can be chosen by trial and error to produce an image visually representative of the original micrograph (i.e. not over-emphasizing noise or producing excessive concentrations of

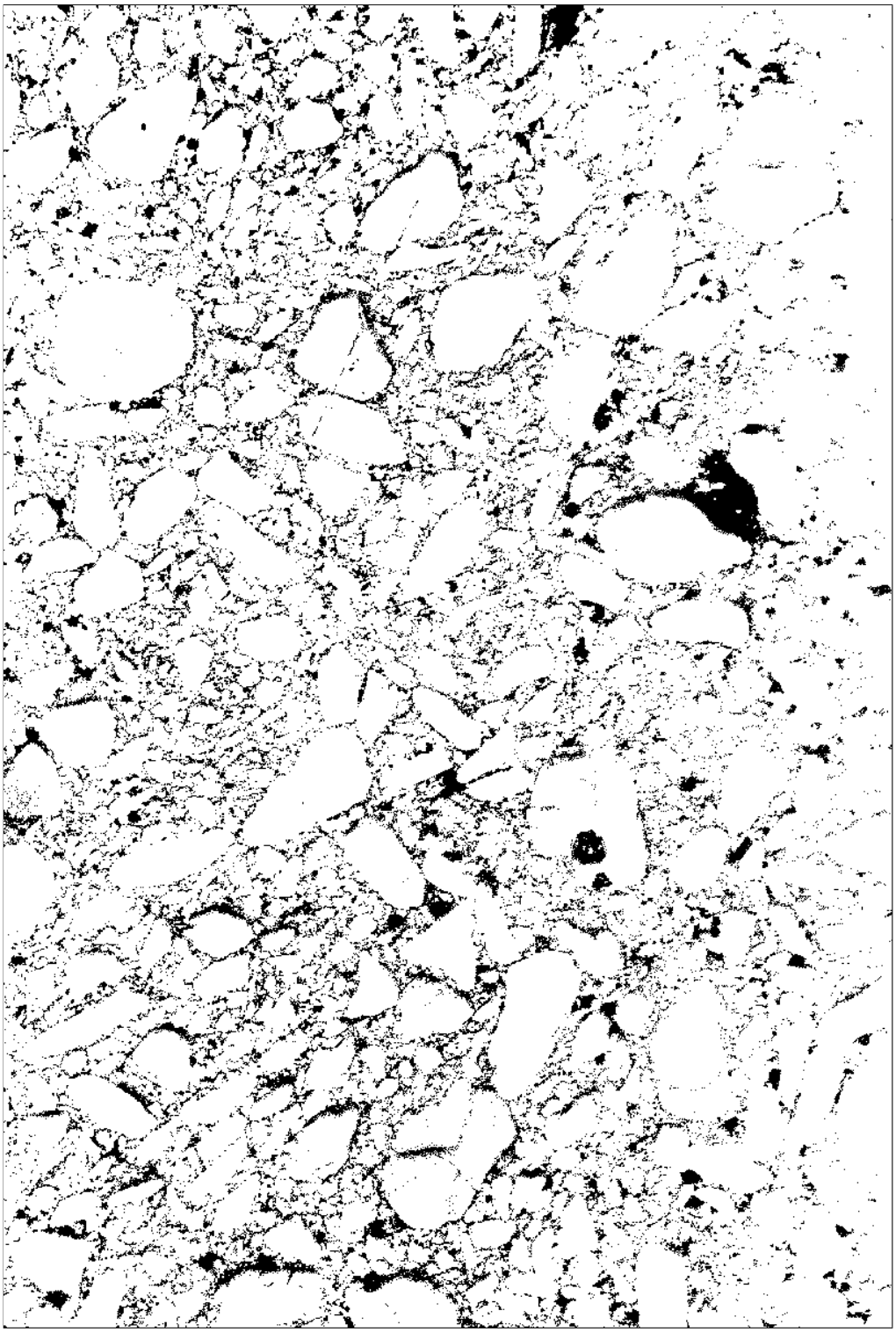

Figure 2.9: EDC37 micrograph (figure 1.5) after a single threshold has been applied at a value of $b = 75$. High binder concentrations, that are not representative of the original micrograph, are observed in pull-out regions.

binder), with the upper threshold b being chosen to produce the correct proportion of crystals and binder in the geometry. Figure 2.10 shows the effect of applying a double threshold at $a = 60$ and $b = 85$ to the original EDC37 micrograph in figure 1.5. The pull-outs have been removed from the image, allowing a sensible distribution of binder in the regions between the big crystals.

Owing to its advantages over the single threshold approach, the double threshold technique has been used to provide microstructure geometries in this work. Although it does not exploit the advanced graphics techniques sometimes used for mesoscale modelling in the literature [e.g., 126 and 127], it is sufficient for the purposes of this work. A disadvantage of this simple technique is that changes in image intensity due to illumination like those in figure 1.5, which fades towards the right-hand side, are not corrected. This results in lower binder concentrations on the right-hand side of the computational geometry in figure 2.10 which can affect the shock velocity in microstructure simulations (see section 7.3).

The computational geometry used in chapter 7 for EDC37 is shown in figure 2.10 and contains 90.8 wt% HMX and 9.2 wt% binder. The geometry for PBX9501 is in figure 2.11 and contains 95.0 wt% HMX and 5.0 wt% binder. In reality, EDC37 comprises 91 % HMX and 9 % binder by weight and PBX9501 contains 95 % HMX and 5 % binder. While it is desirable that the computational geometries have representative proportions of crystals and binder, it is not essential that they match exactly, as will be explained with reference to figure 2.12. An EDC37 or PBX9501 explosive charge is formulated to meet a bulk composition specification, but it will be cut into small samples for use in micrography. These small samples may each contain a slightly different proportion of crystals and binder but their average composition must be the same as the specification so that, if the entire explosive charge were to be re-assembled, it would have the correct composition. Similarly, if each 3D sample were divided into 2D slices and then into 1D lines, the average composition of the 2D slices or the 1D lines must be the same as the specification, even though the composition of individual slices or lines may vary. Following this logic, the 2D microstructures used in this work (illustrated in figures 2.10 and 2.11) can be deemed to be representative of EDC37 and PBX9501 because they have compositions close to the ratio of HMX crystals and binder in real explosive charges. The effect of changes to the microstructure geometry on temperature distributions will be assessed in section 7.1.4.

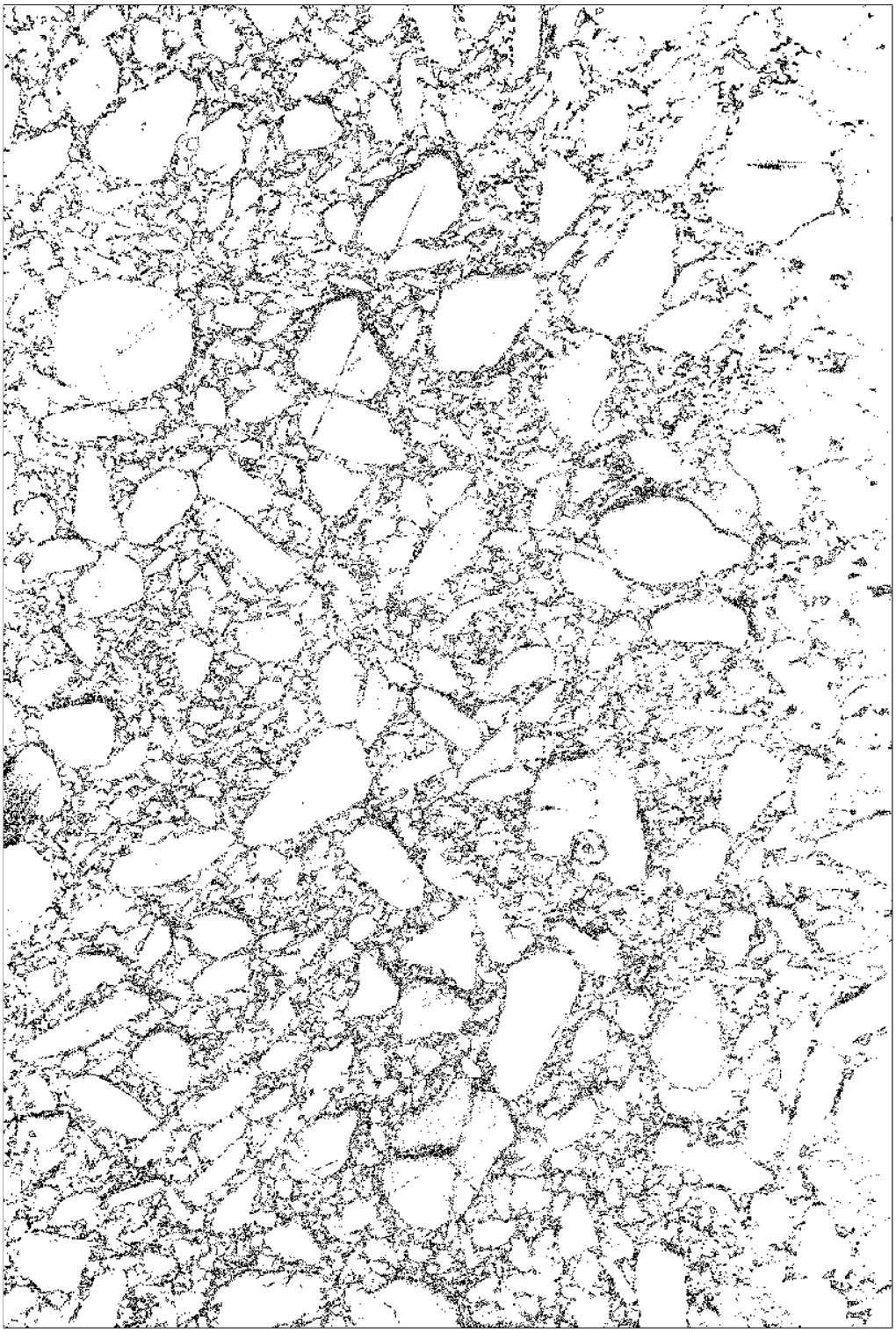

Figure 2.10: EDC37 micrograph (figure 1.5) after a double threshold has been applied at $a = 60$ and $b = 85$. The image is visually representative of the original micrograph and pull-outs have been removed. This geometry will be used for EDC37 in chapter 7.

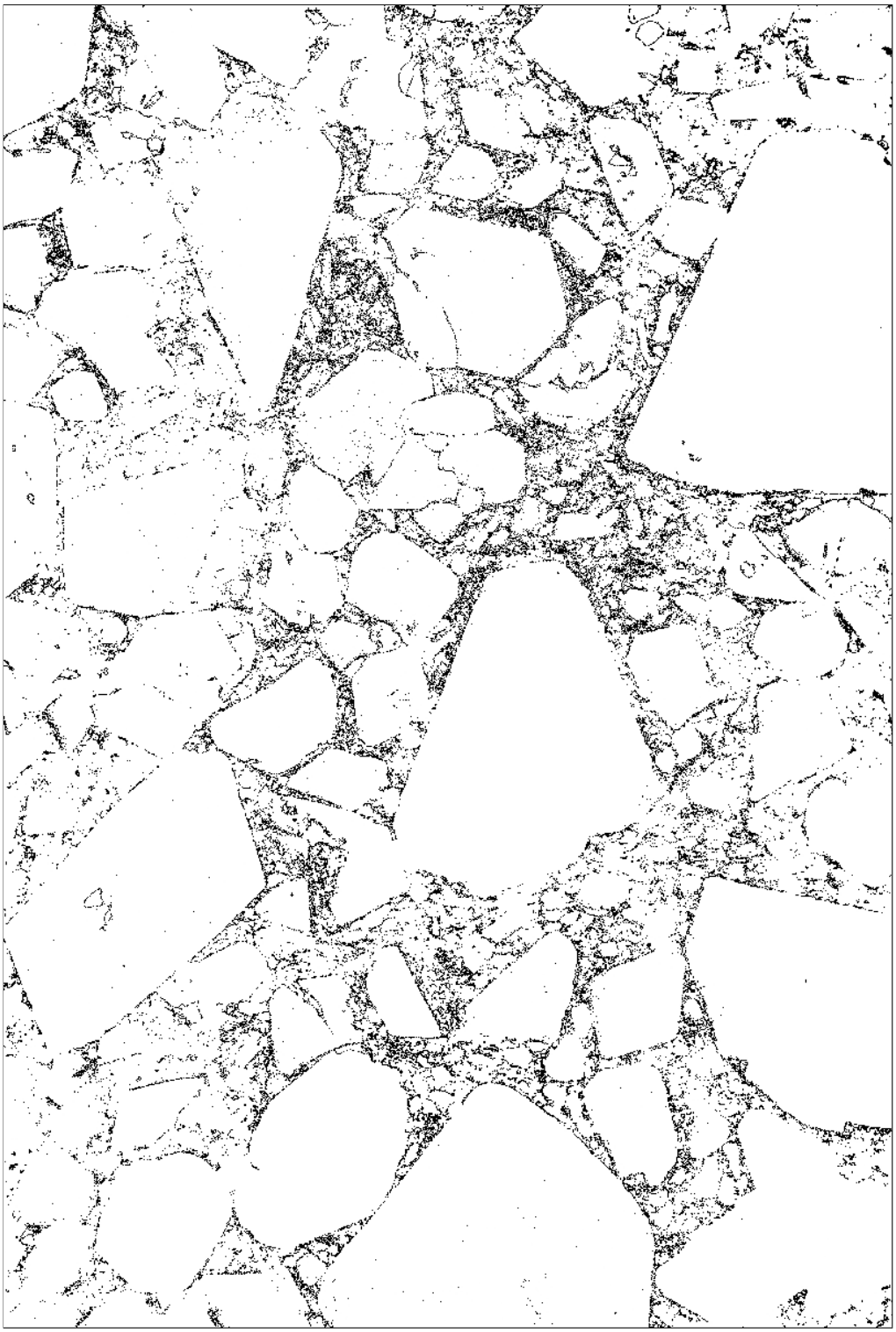

Figure 2.11: PBX9501 micrograph (figure 1.6) after a double threshold has been applied at $a = 60$ and $b = 98$. The image is visually representative of the original micrograph and will be used for PBX9501 in chapter 7.

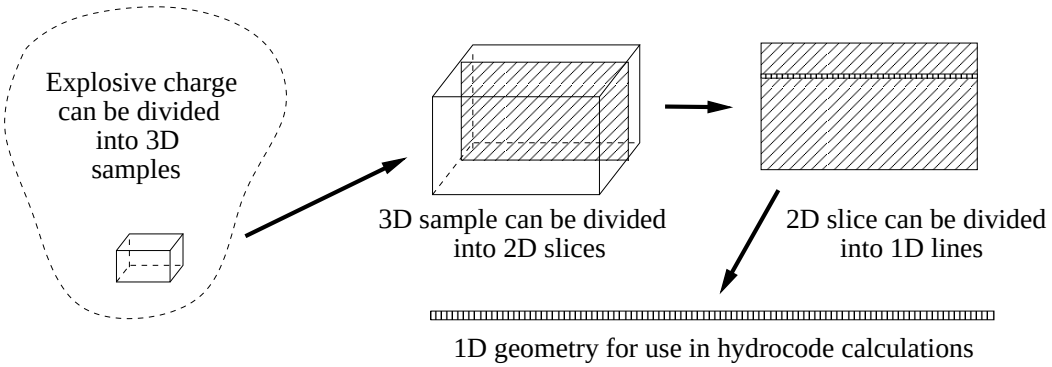

Figure 2.12: Explosive microstructures in one, two and three dimensions to illustrate the argument that, while the *average* composition of two-dimensional slices or one-dimensional lines through the microstructure must be the same as the bulk composition specification, each individual sample may contain a slightly different proportion of crystals and binder.

2.5 Summary

The physics relevant to mesoscale modelling of plastic-bonded explosives in the shock to detonation regime includes hydrodynamics, chemistry and heat conduction. The hydrocodes used in this work have been introduced, and an understanding of hydrocode numerics and the wall heating effect has been demonstrated. The implementation of heat conduction and chemistry in a one-dimensional Lagrangian hydrocode required the reaction-rate equations to be expressed in terms of dynamic mass fractions, and correction factors were needed to accurately convert between specific internal energy and temperature. The technique developed to analyse and correct micrographs for artefacts, in order to generate realistic 2D computational microstructures, has also been described.

Chapter 3

Material models & uncertainties

The two plastic-bonded explosives considered in this work both comprise over 90% by weight HMX crystals. The crystal size distribution varies between 1 and 1000 μm diameter in PBX9501 [128] and between 0.1 and 200 μm in EDC37 [41]. The HMX crystals are bound together by a polymeric binder; in PBX9501 this is a 50:50 mixture of a polyurethane called estane and a nitroplasticiser called BDNPA-F, with a small quantity of anti-oxidant [11]. The binder in EDC37 is composed of 1 part nitrocellulose (NC) to 8 parts K10 liquid plasticiser (a mixture of 65 % by weight dinitroethylbenzene and 35 % trinitroethylbenzene), with a small percentage of ethyl centralite stabiliser [12]. PBX9501 is pressed to a lower density relative to its theoretical maximum density than EDC37, so it is more porous. These details are summarised below:

PBX9501: 95 % by weight HMX, 5 % estane / BDNPA-F binder, with 1.6 % porosity
EDC37: 91 % by weight HMX, 9 % NC / K10 binder, with <0.2 % porosity

In order to represent the microstructure of these explosives in hydrocode calculations, separate HMX and binder regions are used, and each requires a material model. Although the explosive properties of PBX9501 and EDC37 are primarily due to the HMX crystals, the binders are also reactive and so it is necessary to represent both the unreacted material and the reaction products of all three species. This is accomplished using an equation of state for the solid unreacted material (section 3.2) and an equation of state for the gaseous reaction products (section 3.3), along with a chemical reaction scheme (section 3.4) and a mixing rule to define the properties of partially reacted states (section 3.5). In this chapter, the different equation of state and reaction rate forms available in the literature will be reviewed and suitable material properties data will be identified. The error bars

associated with the data will be used in later chapters to assess the effect of uncertainties in each of the material model parameters on hydrocode simulations.

3.1 Modelling assumptions

Although it is desirable to represent the complex response of plastic-bonded explosives as accurately as possible, it is not feasible to include every conceivable material property. A variety of modelling assumptions can be justified by a lack of relevant experimental data or an immaturity of knowledge in the literature. The material modelling assumptions made in this work are discussed below.

3.1.1 Strength

Unreacted explosives are solids but they are often modelled as strengthless, in contrast to metals whose behaviour in shock experiments can be dominated by their strength. For example, the dynamic yield strength of metals controls their deformation in Taylor rod impact tests [129]. The strength of plastic-bonded explosives is controlled by the individual strengths of the crystal and binder components and also by their bond strength. For example, quasi-static tests [130] show that the tensile failure of EDC37 is due to strain localisation in the binder and binder-HMX debonding at room temperature, but due to HMX cracking at low temperatures (and probably, owing to time-temperature superposition, at high rates). While it is undoubtedly important to understand all of these effects in structural analysis models, they need only be included in this work if they have a significant effect on shock initiation and detonation behaviour. The strongest component of PBX9501 and EDC37 is the HMX, whose yield strength of approximately 0.2 GPa [80] is similar in magnitude to that of many metals [131]. However, this is an order of magnitude less than typical shock strengths in experiments of between 2 and 10 GPa. Elastic precursors have been observed in low-pressure ($\leq$2.4 GPa) shock experiments on single crystal HMX [132, 133] but particle-velocity gauge experiments on PBX9501 [134] and EDC37 [75] at higher pressures show little evidence of precursors. This is because the precursor wave structure disappears when the shock velocity is greater than the longitudinal sound speed of 3.82 and 3.17 km/s for single-crystal HMX in the (011) and (010) orientations [133]. The weakest shock initiation experiments have shock velocities

~3.5 km/s; at this shock velocity, only some of the HMX crystals will be orientated correctly to produce a shock precursor. Overall, any precursor signal is washed out by the noise on the experimental particle-velocity traces. Since strength effects are not apparent in shock initiation and detonation experiments, strength will be neglected in this work. This simplifies the reactive-flow equations 2.7 that must be solved but it is recognised that this could be a significant omission. Therefore, the consequences of neglecting strength will be investigated in sections 7.2.7 and 7.3.6.

3.1.2 Equations of state for intermediate species

Neglecting strength means that the material response in hydrocode calculations is isotropic and can be described entirely by the equation of state (equations 2.5). An equation of state is needed for each inert material. Reactive materials, like explosives, can transform from their unreacted form to reaction products via a series of intermediate states, and an equation of state is needed to represent the properties of each state. For plastic-bonded explosives, the unreacted components are solid while the reaction products are gases, so at least two different equations of state are necessary. If intermediate states are included, then additional equations of state are needed.

As will be discussed in section 3.4, multi-step Arrhenius reaction rates are often used in mesoscale modelling of explosives [e.g., 135] and different thermal properties may be used to represent each of the intermediate states. Some researchers have estimated equations of state for the intermediate species [e.g., 68] but these are based on very few data points and are often only slightly modified versions of the equations of state for the unreacted explosive or the reaction products. The equations of state of intermediate species are almost impossible to measure experimentally because chemical reactions in shocked explosives complete in microseconds, so intermediate species only exist for nanoseconds and are highly reactive. In addition to the fast timescales and non-equilibrium conditions, temperatures and pressures can be higher than 1000 K and 10 GPa which are challenging for current diagnostic techniques. Thermochemical codes like Cheetah [136] are frequently used to estimate the properties of reaction products under these conditions but they are based on the assumption of chemical equilibrium, and so have limited potential to be used for intermediate species. For the above reasons, equations of state for intermediate reaction species are difficult to define.

It will be assumed in this work that all reaction species can be treated using either

the solid unreacted equation of state or the reaction products equation of state. This could lead to computational difficulties for multi-step reaction schemes with an initial endothermic step, since the fall in energy associated with the chemical reaction would force the equation of state into regions for which it was not designed, and where negative energies could occur. Although multi-step schemes are investigated in this work, the chemical reactions in HMX and the binder materials will be represented by single-step Arrhenius chemistry (see section 3.4) and so this error cannot occur.

3.1.3 Equation of state mixing rules

In order to represent it in a hydrocode calculation, the explosive is divided into small computational cells. At any one time, some of the molecules contained within the cell will be unreacted and others will have converted into reaction products. The reaction progress variable λ represents the mass fraction of reaction products in the mixture, i.e. $\lambda = 0$ for unreacted explosive and $\lambda = 1$ for fully reacted explosive. The unreacted equation of state defines the behaviour of the cell when $\lambda = 0$ and the reaction products equation of state is used when $\lambda = 1$. For partially-reacted states where $0 < \lambda < 1$, the two equations of state are combined using a mixing rule. Two mixing rules are generally used in reactive burn models. The ISE model [137] assumes that the unreacted explosive and reaction products are thermally isolated but in pressure equilibrium. The unreacted explosive is forced to lie on the isentrope through the shock state, with the reaction products taking up the remaining cell volume. Although this model has been used in continuum reactive-burn models [e.g., 38], it is incompatible with Arrhenius reaction rates since there is no feedback mechanism by which the temperature of the unreacted explosive can increase. A more common assumption is that the unreacted explosive and reaction products are in both pressure and temperature equilibrium [e.g., 36]. However, for a 0.2 µm mesh and following the reasoning in section 2.1.4, the timescales for thermal conduction and wave propagation are 0.2 µs and 0.0001 µs respectively suggesting that pressure equilibrium is reached long before temperature equilibrium. Therefore, the mixture probably lies somewhere between these two approximations, but defining an appropriate mixture rule is difficult.

Therefore, it will be assumed that the unreacted explosive and reaction products are in pressure and temperature equilibrium in this work, allowing direct comparison with other studies, e.g., reference 69. However, it should be noted that this assumption will influence

all the pressures and temperatures calculated in hydrocode calculations for the partially-reacted HMX and binder, and so it also affects the reaction rate. It would be possible to investigate the effect of this assumption by constructing an alternative equation of state using another mixing rule but this is left for future work.

3.1.4 Temperature calculation

Equations of state are often written as $p(v, e)$, i.e. the pressure p is a function of specific volume v and specific internal energy e. An additional relation $T(v, e)$ is required when temperature-dependent physics is included in hydrocode calculations. Provided appropriate equations of state are used, the temperature T can be calculated analytically. For example, the ideal-gas equation of state has $T = e/c_v$, where c_v is the specific heat at constant volume. Grüneisen equations of state constructed using isentropes as their reference curves [e.g., 138] also have analytic expressions for temperature [139]. When other reference curves such as the Hugoniot are used, an analytic method may be available under specific conditions (see appendix C). For example, the temperature equations for the linear shock velocity versus particle velocity equation of state are analytic if Grüneisen $\Gamma = 1$, $3/2$ or 2. Temperature calculations are further simplified if heat capacity is constant. The assumptions of $\Gamma = 1$ and $c_v = \text{const.}$ will be made in the one-dimensional Peruse calculations described in this thesis.

An alternative method for calculating temperature in hydrocodes is to use a tabular form. The equation of state package used by Corvus and Petra contains a numerical integration package which calculates temperatures for solid materials described using any equation of state, as follows. The user defines the heat capacity $c_v(T)$ at v_0 within the temperature range of interest, allowing the code to calculate $e(v_0, T)$ by integration of

$$\left(\frac{\partial e}{\partial T}\right)_v = c_v.$$

Isentropes through those $e(v_0, T)$ points are determined using

$$\left(\frac{\partial e}{\partial v}\right)_S = -p.$$

Then Grüneisen $\Gamma(v, e)$ from the equation of state enables T to be calculated as a function

of v along the isentropes, using

$$\left(\frac{\partial \ln T}{\partial \ln v}\right)_S = -\Gamma.$$

This enables a table of v, e and T to be constructed before the hydrocode simulation commences. Linear interpolation is used to determine temperatures between points in the table as the calculation proceeds. This method does not require Γ and c_v to be constant and can be used to check the validity of these assumptions if sufficient data are available to define $c_v(T)$ and $\Gamma(v, e)$, as will be discussed in section 7.2.

3.1.5 Thermal conductivity

The incorporation of thermal conduction in Peruse was discussed in section 2.3.2. To simplify the coding, a single constant value of thermal conductivity k is used for each material (i.e. the unreacted HMX and its reaction products both have the same value of k, but the binder can have a different value). However, experimental measurements of k for a variety of materials show both temperature and pressure dependence [140] and HMX is no exception [80, 141]. In addition, the gaseous reaction products have lower thermal conductivity than the solid unreacted explosive, although quoted values for the reduction in k on reaction from solid HMX to gas vary between 20 % [68] and 90 % [135]. However, the considerable uncertainty in the values of k for HMX and the binders in the shock and detonation regimes suggests that the assumption of constant k is reasonable. The validity of this assumption will be tested using a range of values for k in hydrocode simulations in sections 5.3, 6.4 and 7.2.5.

In addition, it will be assumed that there is perfect contact between HMX and binder regions, so heat can flow unimpeded across the interface. Although this is not a good approximation for many systems [142], there are no experimental data for the thermal contact conductance between HMX and binder materials. Plastic-bonded explosives are manufactured by coating the crystals with liquid binder, before they are pressed into the explosive charge and machined into test specimens. Although there is generally close contact between the HMX and binder, the machining process can weaken the plastic-bonded explosive and potentially render the contact imperfect [77]. However, the extent of debonding is difficult to quantify and any gaps will close under shock loading. Therefore, the assumption of perfect contact is reasonable for these materials.

3.1.6 Latent heat

In this work, no account has been made for the latent heats associated with melting or other phase transitions. The $\beta - \delta$ phase transition in HMX has been investigated experimentally in several studies [143, 144, 145]. Menikoff [80] suggests that, although the $\beta - \delta$ phase transition is important for cook-off experiments involving relatively slow heating, the fast heating during shock loading may lead to a direct $\beta-$liquid transition. In common with most mesoscale modelling studies, the enthalpy change associated with the $\beta-\delta$ phase transition ($\sim$0.03 kJ / g) will be neglected in this work. Menikoff [80] estimates the latent heat of melting as 0.2 kJ / g for HMX. This is considerably less than the energy released by chemical reactions in HMX ($\sim$5 kJ / g) and will also be neglected.

3.1.7 Porosity

PBX9501 and EDC37 are both porous; that is, their densities are lower than their theoretical maximum densities (TMD). The pores, which may be filled with air or solvent vapours from the manufacturing process, will collapse when the explosive is shocked, creating hotspots [17]. The average response of the bulk explosive and the hotspots can be represented using continuum porosity models like the snow-plough model [146]. Figure 3.1 shows that the temperature T_2 calculated using a continuum porosity model is higher than the temperature T_1 in shocked fully-dense explosive. A simple picture of the mesoscale response is that the bulk explosive (away from the hotspots) is at T_1 with the hotspots at T_3, such that the average temperature is T_2 for consistency with the continuum model. In reality, the situation is more complicated because interactions between the HMX and binder components cause a distribution of bulk temperatures and different hotspot mechanisms produce a variety of hotspot temperatures. These concepts have been explored in more detail by Lambourn [53]. An aim of this work is to establish the effect of the bulk heating of PBX9501 and EDC37 without the complicating influence of hotspots. Ideally, microstructure simulations that do not include hotspots should have bulk densities equal to the theoretical maximum density of the composition, so that they are shocked to temperature T_1. This allows the additional effect of hotspots at temperature T_3 to be included in future work, and is why the HMX and binder will be modelled as fully dense in this work.

In addition to its effect on temperature, porosity changes the shock response of the

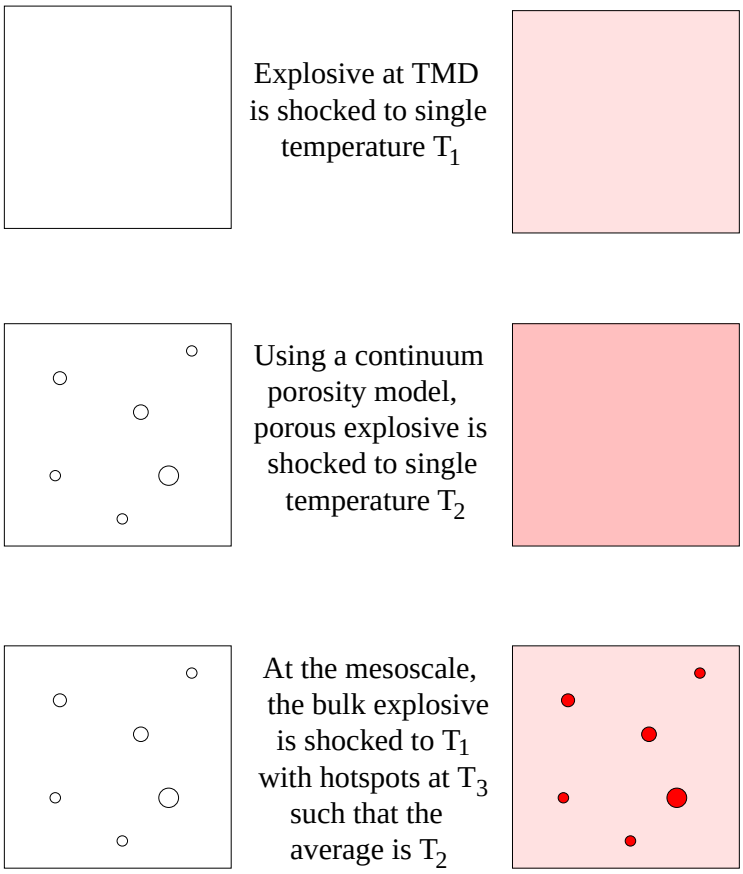

Figure 3.1: Illustration of the different approaches to modelling porous explosives at the continuum and meso-scales. At the mesoscale, the shock temperature T_1 achieved in the bulk of a porous explosive (i.e. away from the hotspots) is equal to the temperature in a non-porous explosive at theoretical maximum density (TMD).

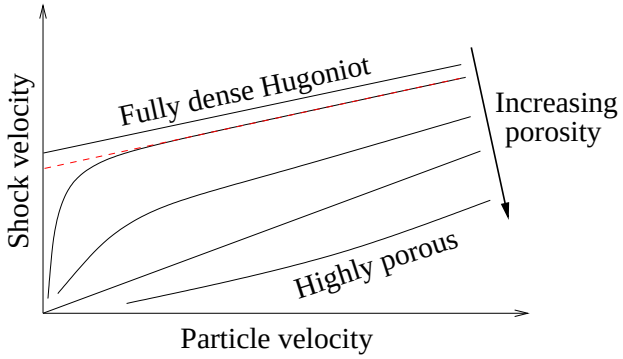

Figure 3.2: Sketch of the effect of porosity on the shock velocity versus particle velocity Hugoniot using the snow-plough model [146]. The red dashed line illustrates the effect of using slightly-porous Hugoniot data without correcting the data back to TMD.

explosive. The locus of all possible states behind a shock front is known as the Hugoniot, which can be expressed as a relation between any two of five variables: the pressure, density, specific internal energy, shock velocity and particle velocity [1]. The effect of porosity on the shock velocity versus particle velocity Hugoniot at the continuum scale is shown in figure 3.2. Using the snow-plough model, even a very small amount of porosity has a significant effect on the shock velocity at low particle velocities. At high particle velocities, increasing porosity causes the Hugoniot curve to shift downwards to lower shock velocities. Often, experimental data are only available for porous explosives and they should be corrected back to TMD using a continuum porosity model like the snow-plough model in order to construct an equation of state for use in mesoscale modelling [138]. However, the red dashed line in figure 3.2 illustrates that it is not a bad approximation to use Hugoniot data from a slightly-porous explosive as if it were fully dense. This is why Hugoniot data for HMX at 1.891 $\mathrm{g/cm^3}$ will be used in constructing the unreacted equation of state in section 3.2, without correcting the data back to TMD at 1.905 $\mathrm{g/cm^3}$. Although this leads to a bulk density that is less than the TMD of PBX9501 and EDC37, microstructure simulations in section 7.3 give good agreement with experimental Hugoniot data, showing that this is a reasonable approximation.

3.1.8 Sound speed

A sound speed estimate is required in order to determine a stable time-step using the CFL condition (section 2.2.1). Calculating an accurate sound speed c for the reacting mixture is complicated. A simple approximation is to use the maximum of the solid and gaseous sound speeds c_s and c_g in the timestep calculation. This relies on the assumption that the sound speed of the mixture c satisfies the relation:

$$c^2 < \max\left({c_\mathrm{s}}^2, {c_\mathrm{g}}^2\right)$$

This is a safe assumption in a composite material such as PBX9501 or EDC37 since the wandering path a sound wave would have to make through the composite microstructure is longer than a straight path through a homogeneous sample of the component with the highest sound speed. Gudmundsson and Celius [147] found that "the speed of sound in gas-liquid mixtures is much lower than the speed of sound in the individual phases", suggesting that the above assumption is reasonable. An advantage is that it provides an over-estimate of the sound speed, ensuring that the computational scheme will re-

main stable, but a significant over-estimate would have an adverse effect on accuracy. Computational results from a static explosion test problem in Peruse show that the estimated sound speed in HMX that has almost converted to gaseous reaction products is $c = c_s = 6.6\,\mathrm{km/s}$, compared to $c_g = 5.2\,\mathrm{km/s}$ in the pure reaction products. The similar magnitude of these two values indicates that this assumption does not greatly reduce the accuracy of the numerical scheme.

3.1.9 Turbulence

Turbulence can be a dominant mechanism in gaseous energetic materials [102] and there have been many experimental and theoretical studies of its effect [e.g., 148]. A turbulent mechanism of energy transfer has been suggested as being responsible for the discrepancy between laminar burning rates $<1\,\mathrm{m/s}$ and the $\sim 100\,\mathrm{m/s}$ burning rates necessary to explain shock initiation in plastic-bonded explosives [149, 150]. Despite this, turbulence is usually neglected in both continuum and mesoscale models of plastic-bonded explosives, in part owing to the inherent uncertainties in modelling it [151]. Turbulence will be neglected in this work for consistency with the majority of studies in the literature, but it is recommended that an analysis of the effects of turbulence is attempted in future work.

3.1.10 Anisotropy

The anisotropic response of HMX crystals under shock loading has been demonstrated experimentally [e.g., 152]. Anisotropy can be a significant effect in TATB-based plastic-bonded explosives because the elongated crystals can become preferentially aligned during the manufacturing process. However, HMX-based explosives generally respond isotropically because the round crystals are unlikely to be crystallographically aligned. At the mesoscale, the anisotropic behaviour of each crystal will perturb the passage of a shock wave through the plastic-bonded explosive. Detailed models for HMX anisotropy have been constructed in hydrocodes [e.g., 153] and it is possible to gauge the effect of anisotropy on mesoscale simulations by assigning different equation of state and strength properties to each HMX crystal [e.g., 64]. Unfortunately, this technique is not easy to implement here because the computational microstructure geometry does not distinguish between individual crystal and binder regions. In common with many mesoscale models, anisotropy will be neglected from this work and evaluating its effect is left for the future.

3.2 Equation of state for unreacted explosive

A variety of equations of state (EOS) are used to represent unreacted explosives. Sewell and Menikoff developed a complete equation of state for β-HMX to fit isothermal compression data, with a specific heat computed from molecular dynamics calculations [154]. The widely-used Ignition and Growth model [36] employs a Jones-Wilkins-Lee (JWL) equation of state for both the unreacted explosive and the reaction products. The CREST reactive-burn model uses a finite strain form for the unreacted equation of state [155]. A simplified ignition and growth model known as JWL++, which is applied to a wide range of explosives, has a Murnaghan form for its unreacted equation of state [156]. The Murnaghan EOS is also used in the Arrhenius reactive-burn model CHARM [157]. Several studies have used a Mie-Grüneisen equation of state with a linear shock velocity versus particle velocity Hugoniot (known as a linear Grüneisen EOS). Baer used this form of equation of state for mesoscale modelling of HMX crystal assemblies [64], as did Conley [68, 69] and Menikoff [56, 158].

A range of unreacted equations of state were already available for use in Peruse, Corvus and Petra. These include the polytropic gas EOS, several varieties of polynomial EOS, Grüneisen EOS based on linear or cubic shock velocity versus particle velocity Hugoniot fits, the JWL EOS from Ignition and Growth, and the finite-strain form used in CREST. To allow testing against existing coding and to avoid this work being dominated by EOS development, it was decided that one of these readily-available EOS would be used. Criteria for choosing an unreacted EOS were that it should be sufficiently advanced to represent the observed shock response of HMX and the binder materials (this eliminated the polytropic gas EOS), while having a simple parameter-fitting method and easy availability of appropriate materials data. This last point is especially important for mesoscale modelling of explosives because relevant data on the HMX and binder components are scarce. The linear Grüneisen equation of state satisfies all these criteria. It has the advantage of being widely used, as it is appropriate for the many materials [159] that have an approximately linear shock velocity U_s versus particle velocity u_p Hugoniot

$$U_s = a + bu_p,$$

where a and b are fitting parameters. Its main disadvantage is a singularity in the $p(v)$ Hugoniot at density $\rho^* = \rho_0 b/(b-1)$, where ρ_0 is the initial density. This can cause numerical difficulties when a finite timestep causes the material density to jump from

one side of the singularity to the other non-physical side. However, this did not occur very often in the hydrocode simulations described in this thesis. Therefore, the linear Grüneisen EOS will be used for the unreacted HMX and binder materials.

In general, Grüneisen EOS can be written as $p(v,e) = p_r(v) + \frac{\Gamma(v)}{v}(e - e_r(v))$, where r is a suitable reference curve. For the linear Grüneisen EOS, the Hugoniot $U_s = a + bu_p$ is used as the reference curve. After some manipulation [146], the linear Grüneisen EOS can be written as

$$p_s(v_s, e_s) = \frac{a^2(v_0 - v_s)}{[v_0 - b(v_0 - v_s)]^2} + \frac{\Gamma(v_s)}{v_s}\left(e_s - \frac{a^2(v_0 - v_s)^2}{2[v_0 - b(v_0 - v_s)]^2}\right), \tag{3.1}$$

where the subscript s is included because this EOS will be used for the solid, unreacted materials. Following the analysis in appendix C and assuming Grüneisen $\Gamma(v_s) = \Gamma_0 = 1$ and constant $c_{v,s}$, the temperature can be calculated using

$$T_s(v_s, e_s) = \left(\frac{v_0}{v_s}\right)^{\Gamma_0}\left[T_0 + \frac{1}{c_{v,s}}\left(\frac{v_s}{v_0}\right)^{\Gamma_0}(e_s - e_i(v_s))\right], \tag{3.2}$$

where

$$\begin{aligned} e_i(v_s) \;=\; & \frac{-a^2}{b^3}\left(\frac{v_0}{v_s}\right)\left[\frac{3b(v_0 - v_s)}{2v_0} + (3-b)\ln\left\{\frac{v_0 - b(v_0 - v_s)}{v_0}\right\}\right. \\ & \left. -\left(b - \frac{3}{2}\right)\frac{b(v_0 - v_s)}{v_0 - b(v_0 - v_s)}\right]. \end{aligned}$$

These equations, or their equivalents, were already available for use in the hydrocodes Peruse, Corvus and Petra. They have been incorporated into the new heat conduction and chemistry coding in Peruse and will be used to represent the unreacted HMX and binder components in this work.

3.2.1 Unreacted equation of state parameters

The parameters needed to represent the unreacted materials are initial density $\rho_0 = 1/v_0$ (assumed to be equal to theoretical maximum density), initial temperature T_0, solid heat capacity $c_{v,s}$, Hugoniot parameters a and b and constant Grüneisen Γ_0. The thermal conductivity k will also be included in this section although it applies to both the unreacted explosive and the reaction products. Best estimates of appropriate values to use for each of these parameters are given below. The quoted error bars will be used in sections 5.3

and 7.2 to investigate the effect of their uncertainties on hydrocode simulations.

The initial temperature of $T_0 = 295\,\mathrm{K} = 22\,^\circ\mathrm{C}$ will be used in 1D Peruse calculations as a mid-value for room temperature; reasonable maximum and minimum limits for T_0 are $298\,\mathrm{K} = 25\,^\circ\mathrm{C}$ and $291\,\mathrm{K} = 18\,^\circ\mathrm{C}$. The Petra coding is restricted to a constant value of $T_0 = 300\,\mathrm{K} = 27\,^\circ\mathrm{C}$, so this will be used for the 2D simulations. Grüneisen Γ_0 is limited to a value of 1.0 in Peruse to simplify the temperature calculation method. This is a sensible choice since $\Gamma_0 = 1.25 \pm 0.75$ for most materials [146], and there are few references in the literature suggesting that Γ_0 should be different to 1.0 for HMX or the binder materials.

HMX

The theoretical maximum density of HMX is $1.905\,\mathrm{g/cm^3}$ [160] but Hugoniot data are only available at lower densities. In Gibbs & Popolato [11], $U_s(\mathrm{km/s}) = (2.901 \pm 0.407) + (2.058 \pm 0.490)u_p$ for solvent-pressed HMX at $\rho_0 = 1.891\,\mathrm{g/cm^3}$. A different fit to the same data but missing out one of the points is quoted in reference 159 as $U_s = (3.07 + 1.79u_p)\,\mathrm{km/s}$. Three Hugoniot points for single-crystal HMX with $\rho_0 = 1.9\,\mathrm{g/cm^3}$ are listed in Gibbs & Popolato, fitted to $U_s = (5.80 + 0.59u_p)\,\mathrm{km/s}$ in reference 159. The Hugoniot $U_s = (2.74 + 2.6u_p)\,\mathrm{km/s}$, $\Gamma_0 = 1$ for $\rho_0 = 1.9\,\mathrm{g/cm^3}$ from Olinger, Roof & Cady is frequently quoted [160]. The Gibbs & Popolato Hugoniot is chosen here because it is widely used by other researchers and the data points on which it is based are quoted. The error bars suggest that a could be as high as $3.308\,\mathrm{km/s}$ or as low as $2.494\,\mathrm{km/s}$, and b could be as high as 2.548 or as low as 1.568. The corresponding density of $1.891\,\mathrm{g/cm^3}$ will be used in the calculations, but this could be as high as $1.905\,\mathrm{g/cm^3}$.

The temperature-dependent specific heat quoted in Dobratz [160] is broadly consistent with values measured experimentally by Hanson-Parr [161] and Shoemaker [162]. Values of specific heat used by modellers vary around $1.0\,\mathrm{J/g\,K}$ [e.g., 56]. Menikoff [80] compares the experimental values of Hanson-Parr and Shoemaker and concludes that $c_{p,s}$ for β-HMX is linear between $1.0\,\mathrm{J/g\,K}$ at 294 K and $1.4\,\mathrm{J/g\,K}$ at the δ phase transition 438 K. Above this temperature the measurements differ wildly, likely due to some decomposition occurring. For higher temperatures, table 3.1 gives specific heats from quantum chemistry and molecular dynamics calculations [80], which are accurate to within 10 to 20 %. Therefore, the heat capacity of HMX could be as low as $0.8\,\mathrm{J/g\,K}$ or as high as $2.1\,\mathrm{J/g\,K}$. An "average" value of $1.1\,\mathrm{J/g\,K}$ was chosen as being appropriate at intermedi-

T (K)	300	500	1000	1500	> 3000
$c_{v,s}$ (J / g K)	0.8	1.2	1.7	1.9	2.1

Table 3.1: Temperature-dependent specific heat for HMX, from reference 80.

ate temperatures for mesoscale simulations. Note that the difference between the specific heat at constant pressure $c_{p,s}$ and at constant volume $c_{v,s}$ is small, e.g., for $c_{v,s} = 0.8\,\mathrm{J/g\,K}$ at 300 K, $c_{p,s} = 0.84\,\mathrm{J/g\,K}$ for HMX. This is much less than the uncertainty in the data, so the difference between $c_{p,s}$ and $c_{v,s}$ is neglected in this work.

Several measurements of the thermal conductivity k of HMX are available in the literature. In his three-step reaction scheme for HMX, A → B → 2C → 12D, Conley [68] uses values of $k_A = 0.51\,\mathrm{W/m\,K}$, $k_B = 0.45\,\mathrm{W/m\,K}$ and $k_C = k_D = 0.41\,\mathrm{W/m\,K}$. Shoemaker [162] measured $k_{\beta\text{-HMX}} = (0.47 - 5.4 \times 10^{-4} T(\mathrm{K}))\,\mathrm{W/m\,K}$ in the range 50 – 180 °C. This differs by 50 % from the results of Hanson-Parr [161], who found $k = (0.498 - 4.82 \times 10^{-4} T(°\mathrm{C}))\,\mathrm{W/m\,K}$ in the range 20 – 170 °C. Menikoff [80] demonstrates that the Hanson-Parr result is consistent with other measurements in references 11 and 160, adding that the thermal conductivity is 0.36 W / m K at melting (558 K) and continues to decrease in the liquid phase with roughly the same slope until about 700 K, where it levels off with a value of $k \sim 0.26\,\mathrm{W/m\,K}$. This is consistent with conclusions from molecular dynamics simulations [46]. An "average" value of $k = 0.4\,\mathrm{W/m\,K}$ seems appropriate for use here, bearing in mind that it could be as high as 0.5 or as low as 0.2 W / m K.

The hydrocodes used in this work use a system of units based on g, cm, μs and Mbar (see page vii). For ease of use in future work, the unreacted equation of state parameters for HMX are converted into hydrocode units in the table below:

ρ_0	T_0	$c_{v,s}$	k	a	b	Γ_0
1.891	295	1.1×10^{-5}	0.4×10^{-13}	0.2901	2.058	1.0
g / cm^3	K	Mbar cm^3 / g K	Mbar cm^2 / μs K	cm / μs		

Table 3.2: Linear Grüneisen equation of state parameters for unreacted HMX.

Binder in PBX9501

In the literature, a variety of densities are quoted for the binder in PBX9501 but some of these are for neat estane at 1.186 g / cm^3 [159] rather than the estane / BDNPA-F binder

actually used in PBX9501, at 1.27 g/cm^3 [163, 164]. For the Hugoniot, Marsh [159] has $a = 2.32$ km/s and $b = 1.70$ for estane at $\rho_0 = 1.186$ g/cm^3. Conley [68] uses $a = 2.35$ km/s and $b = 1.70$ with $\rho_0 = 1.1$ g/cm^3. Values of $a = 2.4$ km/s and $b = 1.70$ will be used in this work because they are consistent with Baer's quadratic $U_s(u_p)$ relation [163]. Fitting reasonable straight lines to Baer's Hugoniot curve gives maximum and minimum values of 3.0 and 1.7 km/s for a and 2.4 and 1.2 for b. The minimum value of 1.7 km/s for a is consistent with Dick's experimental value of 1.69 km/s for the sound speed in the estane / BDNPA-F binder.

The heat capacity of estane is quoted as $c_{p,s} = 1.56$ J/g K in the range 37 – 60 °C and 1.68 J/g K in the range 75 – 200 °C [160], although Conley uses $c_{p,s} = 1.0$ J/g K [68]. A value of $c_{v,s} = 1.6$ J/g K has been chosen for use in simulations. Following Menikoff [80], analysis using Dulong & Petit's law suggests that $c_{v,s}$ could be as high as 3.2 J/g K at elevated temperatures. Data on the thermal conductivity of PBX9501's binder are scarce. Conley uses 0.51 W/m K [68] but a measurement for estane [160] at 314 K gave 0.148 W/m K. Recent measurements of the thermal conductivity of EDC37's binder at Cambridge University [165] suggested $k = 0.2$ W/m K. The value of 0.2 W/m K has been chosen as a reasonable value for both binder materials, although k could reasonably be as high as 0.5 or as low as 0.1 W/m K.

These parameters are converted into hydrocode units in the table below:

ρ_0	T_0	$c_{v,s}$	k	a	b	Γ_0
1.27	295	1.6×10^{-5}	0.2×10^{-13}	0.24	1.70	1.0
g / cm^3	K	Mbar cm^3 / g K	Mbar cm^2 / μs K	cm / μs		

Table 3.3: Linear Grüneisen EOS parameters for the unreacted binder in PBX9501.

Binder in EDC37

The density of the binder in EDC37 is 1.391 g/cm^3 [41]. Owing to a lack of experimental data and because the binder is gelatinous and rubbery, Hugoniot parameters were estimated from data for other polymers [159]. E.g.,

rubber at $\rho_0 = 1.372$ g/cm^3 has a Hugoniot of $U_s = (1.84 + 1.44u_p)$ km/s,
phenolic at $\rho_0 = 1.380$ g/cm^3 has a Hugoniot of $U_s = (2.85 + 1.40u_p)$ km/s,
sylgard at $\rho_0 = 1.037$ g/cm^3 has a Hugoniot of $U_s \sim (1.6 + 1.6u_p)$ km/s, and
cyclohexadiene at $\rho_0 = 0.840$ g/cm^3 has a Hugoniot of $U_s = (1.87 + 1.33u_p)$ km/s.

Therefore, it was decided to use a Hugoniot of $U_s = (2.0 + 1.4u_p)\,\mathrm{km/s}$ for the binder in EDC37. Reasonable maximum and minimum values are 3.0 and 1.0 km/s for a, and 2.5 and 1.0 for b. The new Hugoniot data that became available during this work will be used to validate the equation of state in section 4.1.

The heat capacity of EDC37's binder has been measured as $1.6\,\mathrm{J/g\,K}$ over the temperature range 20-70 °C [165], so this is taken as the value for use in this work. Following Menikoff [80], analysis using Dulong & Petit's law suggests that $c_{v,s}$ could be as high as $2.7\,\mathrm{J/g\,K}$ at elevated temperatures. Measurements of the thermal conductivity of EDC37's binder gave $k = 0.2\,\mathrm{W/m\,K}$ [165]. Following the reasoning for the binder in PBX9501, k could be as high as 0.5 or as low as $0.1\,\mathrm{W/m\,K}$.

These parameters are converted into hydrocode units in the table below:

ρ_0	T_0	$c_{v,s}$	k	a	b	Γ_0
1.391	295	1.6×10^{-5}	0.2×10^{-13}	0.2	1.4	1.0
$\mathrm{g/cm^3}$	K	$\mathrm{Mbar\,cm^3/g\,K}$	$\mathrm{Mbar\,cm^2/\mu s\,K}$	$\mathrm{cm/\mu s}$		

Table 3.4: Linear Grüneisen EOS parameters for the unreacted binder in EDC37.

3.3 Equation of state for reaction products

Several different equations of state can be found in the literature for the gaseous reaction products of explosives. By far the most widely-used analytic EOS is the Jones-Wilkins-Lee (JWL) form [166]. This is an empirical EOS that was developed by matching the expansion velocity of metal cases surrounding a detonating explosive, for example in the cylinder test [76]. The JWL EOS is used in many reactive burn models including Ignition and Growth [36], JWL++ [156] and CREST [38]. Kerley lists a number of deficiencies with the JWL EOS [167]. Of particular note is his suggestion that, because of its specific heat deficiencies, the JWL EOS is "inappropriate in problems where the reaction kinetics depend explicitly on temperature". However, the JWL EOS continues to be used in Arrhenius-based models, e.g., CHARM [157]. The Williamsburg EOS provides an alternative to the JWL [168, 169]. Since its general form can be justified from molecular interactions, it has the potential to be more accurate when extrapolated outside its fitting regime. However, the Williamsburg EOS is not available in the hydrocodes used here.

An alternative to analytic equations of state is to use a tabular form. Although tabular EOS can be constructed using a variety of means (e.g., quantum mechanical calculations), reaction products EOS are usually generated using thermochemical codes like Cheetah [136]. These codes assume thermodynamic equilibrium between reaction product species to allow an estimate of the equation of state to be made. Cheetah is available and has been used in this work to estimate thermal properties and JWL parameters for the reaction products, where experimental data are lacking. However, tabular equations of state are not currently implemented in Peruse and, while tabular forms are available in Corvus and Petra, they are not used for explosives. For this reason and to allow comparison with other models, it was decided to use the JWL equation of state for reaction products in this work.

The JWL equation of state is a Grüneisen EOS with an isentrope as the reference curve and $\Gamma(v_g) = w$. It can be written as

$$p_g(v_g, e_g) = \left(1 - \frac{wv_0}{R_1 v_g}\right) A \exp\left[-R_1 \frac{v_g}{v_0}\right] + \left(1 - \frac{wv_0}{R_2 v_g}\right) B \exp\left[-R_2 \frac{v_g}{v_0}\right] + \frac{we_g}{v_g}, \tag{3.3}$$

where the subscript g is included to refer to the gaseous reaction products and v_0 is the initial specific volume of the solid unreacted explosive. The JWL coefficients are A, B, C, R_1 and R_2. Following the analysis in appendix C and assuming constant $c_{v,CJ}$, the temperature can be calculated using

$$T_g = \left(\frac{v_{CJ}}{v_g}\right)^w \left[T_{CJ} + \frac{1}{c_{v,CJ}} \left(\frac{v_g}{v_{CJ}}\right)^w (e_g - e_i(v_g))\right], \tag{3.4}$$

where

$$e_i(v_g) = \frac{v_0}{R_1} A \exp\left[-R_1 \frac{v_g}{v_0}\right] + \frac{v_0}{R_2} B \exp\left[-R_2 \frac{v_g}{v_0}\right] + \frac{C v_0}{w} \left(\frac{v_0}{v_g}\right)^w.$$

These equations have been incorporated into the new heat conduction and chemistry coding in Peruse and will be used to represent the reaction products of HMX and the binder throughout this work.

3.3.1 Reaction products equation of state parameters

The parameters needed for the reaction products equation of state are the JWL coefficients A, B, C, R_1, R_2 and w, and the temperature T_{CJ}, heat capacity $c_{v,CJ}$ and specific volume v_{CJ} at the CJ point. The heat of reaction q is described in section 3.4.

HMX

JWL parameters for a variety of explosives are quoted in Dobratz [160]. The parameters listed for HMX are based on cylinder test data and so should be accurate. However, the quoted value of $q = 5.553\,\mathrm{kJ/g}$ is not consistent with the total heat of reaction from McGuire & Tarver's three-step reaction scheme [86], $q = 5.8618\,\mathrm{kJ/g}$. To obtain a consistent set of parameters with this value of q, the values of p_{CJ}, D_{CJ}, R_1, R_2 and w were left unchanged and well-known relations [146] were used to calculate new values of A, B, C and v_{CJ}. These are listed in table 3.5. The thermochemical code Cheetah [136] (with the exp6.2 library) was used to check the modified JWL parameters. When examined over a range of densities $\rho_0/\rho = 0.5$ to 200, the modified JWL agrees well with both a Cheetah isentrope for HMX and the Cheetah JWL, giving confidence that the JWL parameters are reasonable. No minimum or maximum values are quoted owing to the difficulty in estimating them.

Mader quotes two values of the CJ temperature from the BKW thermochemical code [170]: $T_{CJ} = 2364\,\mathrm{K}$ from RDX parameters and $T_{CJ} = 2693\,\mathrm{K}$ from TNT parameters. Menikoff assumes $T_{CJ} = 3000\,\mathrm{K}$ for the detonation products of PBX9501 [171]. Cheetah gives 3349 K for HMX at $1.891\,\mathrm{g/cm^3}$. A reasonable value of T_{CJ} for use in calculations would seem to be 3000 K, with a minimum of 2400 and a maximum of 4000 K to span the range of possible values. Values of $c_{v,CJ}$ in the literature vary between 1 and $3\,\mathrm{J/g\,K}$ [24]. An average value of $2\,\mathrm{J/g\,K}$ is a sensible choice, which agrees with Menikoff [171] and Cheetah.

A	B	C	R_1	R_2	w	T_{CJ}	$c_{v,CJ}$	v_{CJ}
7.717	0.1064	0.0085	4.2	1.0	0.3	3000	2.0×10^{-5}	0.3873
Mbar	Mbar	Mbar				K	$\mathrm{Mbar\,cm^3/g\,K}$	$\mathrm{cm^3/g}$

Table 3.5: JWL equation of state parameters for the reaction products of HMX.

Binders

No JWL parameters from experimental data are available for the binders in PBX9501 and EDC37, so Cheetah was used to estimate the reaction products EOS. The resulting JWLs in tables 3.6 and 3.7 are reasonable when compared to JWLs for HMX, PBX9501 and EDC37 over a range of densities $\rho_0/\rho = 0.5$ to 200, i.e. the JWLs for PBX9501 and EDC37 from references 76, 136 and 160 lie between those for HMX and the binder, although they are much closer to HMX because PBX9501 and EDC37 comprise >90 wt% HMX. As was the case for HMX, no maximum or minimum values are quoted and the value of v_{CJ} comes from the JWL parameters.

Cheetah was used to provide estimates of the thermal properties: $c_{v,CJ} = 2.877\,\mathrm{J/g\,K}$ and $T_{CJ} = 2000\,\mathrm{K}$ for the binder in PBX9501 and $c_{v,CJ} = 2.860\,\mathrm{J/g\,K}$ and $T_{CJ} = 2700\,\mathrm{K}$ for the binder in EDC37. Assuming the same percentage uncertainties as for HMX, reasonable maximum and minimum values for $c_{v,CJ}$ are 4.3 and 1.4 J/g K. For T_{CJ}, they are 2600 and 1400 K for the binder in PBX9501, and 3500 and 1900 K for the binder in EDC37.

A	B	C	R_1	R_2	w	T_{CJ}	$c_{v,CJ}$	v_{CJ}
2.0879	0.0071	0.0038	4.33	0.645	0.09	2000	2.877×10^{-5}	0.5901
Mbar	Mbar	Mbar				K	Mbar $\mathrm{cm^3/g\,K}$	$\mathrm{cm^3/g}$

Table 3.6: JWL EOS parameters for the reaction products of the binder in PBX9501.

A	B	C	R_1	R_2	w	T_{CJ}	$c_{v,CJ}$	v_{CJ}
2.8465	0.0440	0.0072	4.61	1.178	0.225	2700	2.86×10^{-5}	0.532
Mbar	Mbar	Mbar				K	Mbar $\mathrm{cm^3/g\,K}$	$\mathrm{cm^3/g}$

Table 3.7: JWL EOS parameters for the reaction products of the binder in EDC37.

3.4 Reaction rate

It is extremely difficult to measure the chemical reaction rates of explosives directly. Although there have been many studies of low-temperature decomposition [e.g., 172], these slow reactions are not relevant to the shock initiation and detonation regimes. Embedded gauge data give an insight into the reactive behaviour of explosives as they undergo the shock-to-detonation transition [e.g., 134], but not a direct measurement of the reaction

rate. Lagrangian analysis can be used to infer the reaction rate from embedded particle velocity gauge data but the technique is prone to errors and an assumption about the equation of state must be made [173]. Furthermore, such experiments give the integrated reaction of a plastic-bonded explosive (including hotspots) rather than the "pure" reaction of the HMX and binder materials that is needed for mesoscale modelling. To overcome these problems, researchers are turning to computational techniques. Molecular dynamics calculations are being used to study the detailed chemistry of HMX [e.g., 47 and 174] but these techniques are not yet able to define global reaction schemes. Owing to the lack of fundamental chemical data, an empirical approach is often taken to modelling reaction in plastic-bonded explosives.

A variety of different reaction-rate equations are used in reactive-burn models in the literature; just a few examples are given here. The Ignition and Growth model uses pressure and density-dependent reaction rates [36]. Although these were formulated to represent the ignition of hotspots and the growth of reaction from hotspots into the surrounding explosive, over time this has become an empirical model whose parameters often need to be modified for new experimental configurations. The Wescott, Stewart and Davis model [37] also uses pressure and density-dependent reaction rates, tuned to an impressive array of experimental data. Following a detailed analysis [175] of particle velocity gauge shock-initiation data which suggested that reaction rates should depend on shock strength rather than pressure, the CREST model uses entropy-dependent reaction rates [38]. The CHARM model uses an Arrhenius-based pore-collapse and burning model to simulate shock initiation experiments [157]. Other Arrhenuis reactive-burn models have been used to model shock initiation in conventional and non-ideal explosives [176, 177]. Some of these models are purely empirical while others attempt to account for the physics of shock initiation, but all have parameters that must be tuned to macroscopic experimental data. Such an approach is not appropriate for mesoscale modelling.

Various studies have focused on the detailed reaction kinetics of HMX. Arrhenius kinetics schemes have been proposed with single-step [83], three-step [86], four-step [135] or multi-step reactions [85]. These have been used both to model reaction in hotspots [24] and reaction propagation [26]. For the binders, several two-step Arrhenius schemes have been used [86, 135]. Although complex, these reaction schemes have the considerable advantage of being based on appropriate chemistry and tuned, where possible, to chemical data such as heats of formation. It is for these reasons that Arrhenius kinetics will be used in this work. Equations for the four Arrhenius reaction-rate schemes available in

Peruse are given below in terms of f_j, the mass fraction of species j in a dynamic code. The density factors ρ/ρ_0 are needed to convert the frequency factors Z_i from the static mass-fraction-based schemes often used in the literature [e.g., 86] to the dynamic mass-fraction-based scheme in Peruse (see appendix A). The terms $\dot{q}$ and $\frac{\mathrm{D}\lambda}{\mathrm{D}t}$ are for use in the conservation of energy equation 2.24.

1. $\underbrace{\mathrm{A}}_{\text{solid}} \overset{1}{\rightarrow} \underbrace{\mathrm{B}}_{\text{gas}}$ single-step reaction scheme for HMX [83].

$$
\begin{aligned}
\dot{f}_\mathrm{A} &= -f_\mathrm{A} Z_1 e^{-E_1/RT} \\
\dot{f}_\mathrm{B} &= f_\mathrm{A} Z_1 e^{-E_1/RT} \\
\dot{q} &= q_1 f_\mathrm{A} Z_1 e^{-E_1/RT} \\
\frac{\mathrm{D}\lambda}{\mathrm{D}t} &= f_\mathrm{A} Z_1 e^{-E_1/RT}
\end{aligned}
$$

2. $\underbrace{\mathrm{A}}_{\text{solid}} \overset{1}{\rightarrow} \mathrm{B}, \quad \mathrm{A} + \underbrace{\mathrm{B} \overset{2}{\rightarrow} 2\mathrm{C}}_{\text{gas}}$ two-step scheme for the binder in EDC37 [86].

$$
\begin{aligned}
\dot{f}_\mathrm{A} &= -f_\mathrm{A} Z_1 e^{-E_1/RT} - \frac{\rho}{2\rho_0} f_\mathrm{A} f_\mathrm{B} Z_2 e^{-E_2/RT} \\
\dot{f}_\mathrm{B} &= f_\mathrm{A} Z_1 e^{-E_1/RT} - \frac{\rho}{2\rho_0} f_\mathrm{A} f_\mathrm{B} Z_2 e^{-E_2/RT} \\
\dot{f}_\mathrm{C} &= \frac{\rho}{\rho_0} f_\mathrm{A} f_\mathrm{B} Z_2 e^{-E_2/RT} \\
\dot{q} &= q_1 f_\mathrm{A} Z_1 e^{-E_1/RT} + q_2 \frac{\rho}{\rho_0} f_\mathrm{A} f_\mathrm{B} Z_2 e^{-E_2/RT} \\
\frac{\mathrm{D}\lambda}{\mathrm{D}t} &= f_\mathrm{A} Z_1 e^{-E_1/RT} + \frac{\rho}{2\rho_0} f_\mathrm{A} f_\mathrm{B} Z_2 e^{-E_2/RT}
\end{aligned}
$$

3. $\underbrace{\mathrm{A} \overset{1}{\rightarrow} \mathrm{B}}_{\text{solid}} \overset{2}{\rightarrow} \underbrace{\mathrm{C}}_{\text{gas}}$ two-step scheme for the binders in EDC37 and PBX9501 [135].

$$
\begin{aligned}
\dot{f}_\mathrm{A} &= -f_\mathrm{A} Z_1 e^{-E_1/RT} \\
\dot{f}_\mathrm{B} &= f_\mathrm{A} Z_1 e^{-E_1/RT} - f_\mathrm{B} Z_2 e^{-E_2/RT} \\
\dot{f}_\mathrm{C} &= -f_\mathrm{B} Z_2 e^{-E_2/RT} \\
\dot{q} &= q_1 f_\mathrm{A} Z_1 e^{-E_1/RT} + q_2 f_\mathrm{B} Z_2 e^{-E_2/RT} \\
\frac{\mathrm{D}\lambda}{\mathrm{D}t} &= f_\mathrm{B} Z_2 e^{-E_2/RT}
\end{aligned}
$$

4. $\underbrace{\mathrm{A} \xrightarrow{1} \mathrm{B}}_{\text{solid}} \xrightarrow{2} \underbrace{2\mathrm{C} \xrightarrow{3} \mathrm{D}}_{\text{gas}}$ three-step scheme for HMX [86].

$$
\begin{aligned}
\dot{f}_\mathrm{A} &= -f_\mathrm{A} Z_1 e^{-E_1/RT} \\
\dot{f}_\mathrm{B} &= f_\mathrm{A} Z_1 e^{-E_1/RT} - f_\mathrm{B} Z_2 e^{-E_2/RT} \\
\dot{f}_\mathrm{C} &= f_\mathrm{B} Z_2 e^{-E_2/RT} - \frac{\rho}{\rho_0} {f_\mathrm{C}}^2 Z_3 e^{-E_3/RT} \\
\dot{f}_\mathrm{D} &= \frac{\rho}{\rho_0} {f_\mathrm{C}}^2 Z_3 e^{-E_3/RT} \\
\dot{q} &= q_1 f_\mathrm{A} Z_1 e^{-E_1/RT} + q_2 f_\mathrm{B} Z_2 e^{-E_2/RT} + q_3 \frac{\rho}{\rho_0} {f_\mathrm{C}}^2 Z_3 e^{-E_3/RT} \\
\frac{\mathrm{D}\lambda}{\mathrm{D}t} &= f_\mathrm{B} Z_2 e^{-E_2/RT}
\end{aligned}
$$

3.4.1 Arrhenius reaction-rate parameters

The reaction-rate equations above have been incorporated into the new heat conduction and chemistry coding in Peruse and will be used to represent the chemical reactions of HMX and the binder throughout this work. Note that Arrhenius kinetics are not yet available in Corvus or Petra. For each reaction rate i, three parameters are needed: the frequency factor Z_i, the activation energy E_i and the heat of reaction q_i.

HMX

Several different Arrhenius reaction rates for HMX are available in the literature. Henson [82, 178] collected together a wide variety of data for the time to explosion in HMX, including one-dimensional time-to-explosion (ODTX) and detonation data, and fitted them with a simple formula corresponding to a single step Arrhenius rate:

$$\ln t = \frac{E_1}{RT} - \ln Z_1 .$$

Unfortunately, this approach produces explosion times that disagree with the results of thermochemical calculations in ReactDiff [115] and with Hubbard & Johnson's approximate formula for the time to explosion from a single step Arrhenius rate [179]:

$$t = \frac{c_{\mathrm{v,s}} T^2 R}{Z_1 q_1 E_1} \exp\left(\frac{E_1}{RT}\right). \tag{3.5}$$

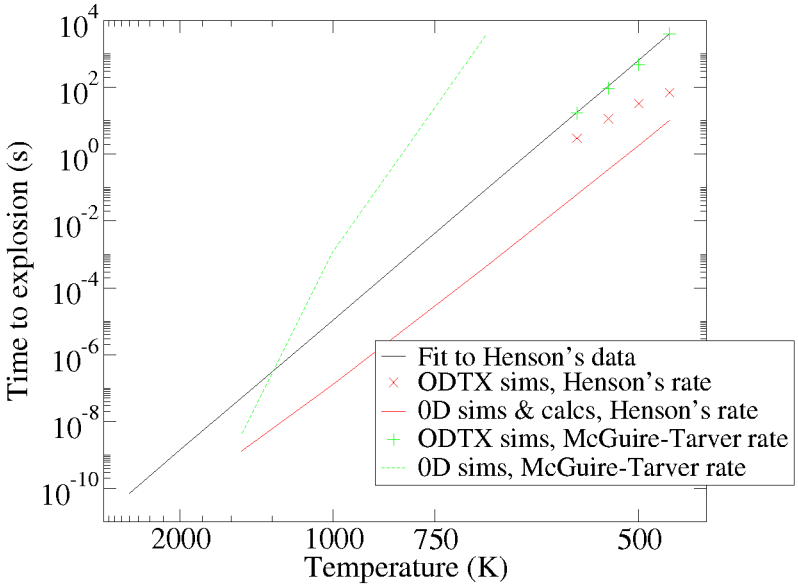

Figure 3.3: Arrhenius plot giving the time to explosion versus initial temperature for HMX. Explosion times calculated using Henson's rate parameters in ReactDiff simulations with uniform heating (0D sims) and using equation 3.5 (0D calcs) do not agree with his compilation of experimental data [82, 178]. McGuire & Tarver's rate parameters [86] give good agreement to the experimental data in ODTX simulations, but do not extrapolate well to high temperatures in 0D simulations. Therefore, both sets of parameters are unsuitable for use in this work.

The red line in figure 3.3 represents explosion times from both ReactDiff and equation 3.5 since they give similar results in 0D geometry, i.e. a single HMX region with uniform initial temperature. Figure 3.3 shows that Henson's reaction rate parameters (the red line) produce explosion times several orders of magnitude faster than Henson's experimental data (the black line). Although Henson's data are an excellent source of information on the chemistry of HMX, his reaction rate coefficients are not useful.

McGuire & Tarver [86] advocate a three-step scheme that has been fitted, using a heat transfer code, to data from ODTX experiments. The ODTX geometry is a 1.27 cm-diameter sphere of explosive, initially at room temperature, surrounded by anvils that are heated to a constant temperature [123]. Thermal conduction from the anvils into the sample raises its temperature, causing chemical reactions to begin. The time at which the anvils are forced apart by the accumulating high-pressure reaction products is recorded as the time to explosion. Although there are several options for deriving the corresponding time to explosion from ReactDiff simulations [115], the time at which there is a sudden increase in the concentration of the final reaction products is used in this work (see sec-

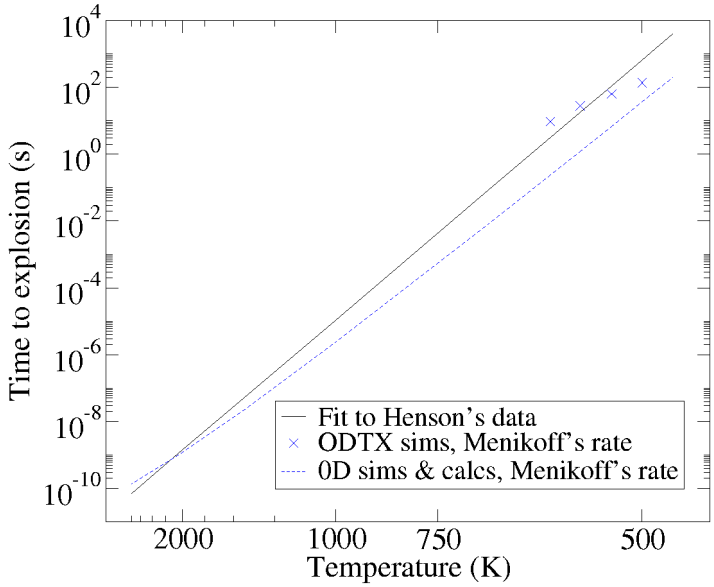

Figure 3.4: Arrhenius plot giving the time to explosion versus initial temperature for HMX. Uniform heating (0D sims & calcs) and ODTX simulations using Menikoff's reaction rate [83] give a good match to Henson's compilation of experimental data [82, 178] and were chosen for use in this work.

tion 5.1). Their dependence on heat conduction as well as Arrhenius chemistry makes ODTX simulations rather different in character to 0D simulations, but both sets of data are often represented on a single Arrhenius plot [e.g., 82]. Figure 3.3 shows that McGuire & Tarver's three-step reaction rate matches the experimental data in ODTX simulations (green pluses) but does not extrapolate well to high temperatures (green dashed line). It also fails to produce a self-sustaining detonation in one-dimensional hydrodynamics calculations. Henson et al. recently published a complex multi-step Arrhenius scheme for HMX [85] and Tarver has proposed a reaction scheme that accounts for cross-reactions between HMX and binder [180]. Although these have not been investigated in this work, they could be tried in future.

Menikoff [83] uses a single step Arrhenius reaction-rate based on Henson's data to model detonation in PBX9501. This has parameters $E_1 = 149\,\mathrm{kJ/mol}$ and $\ln Z_1 = 12.5$, for Z in $\mu\mathrm{s}^{-1}$. Using equation 3.5, Menikoff's rate produces explosion times (the blue dashed line in figure 3.4) which agree well with Henson's data at high temperatures where bulk heating is the most significant effect. ODTX simulations in ReactDiff show that Menikoff's parameters produce explosion times of the same order of magnitude as the experimental data, although with the wrong gradient. Using a single-step Arrhenius rate,

it is difficult to match both the gradient of the low-temperature ODTX data and the high-temperature explosion times. Menikoff's parameters are a good compromise and will be used in this work (table 3.8). They allow detonation to propagate in one-dimensional hydrodynamics calculations, an essential requirement for a mesoscale model that, it is hoped, will simulate the shock-to-detonation transition.

Maximum and minimum values for $\ln Z_1$ and E_1 were estimated by making reasonable changes to the Arrhenius plot in figure 3.4 using equation 3.5. The explosion time curve with the minimum gradient has $\ln Z_1 = 11.6$ and $E_1 = 140\,\mathrm{kJ/mol}$, while the curve with the maximum gradient has $\ln Z_1 = 13.8$ and $E_1 = 160\,\mathrm{kJ/mol}$, for Z in $\mu\mathrm{s}^{-1}$. Menikoff quotes $q_1 \sim 5\,\mathrm{kJ/g}$ [83]. In their three-step scheme, McGuire and Tarver [86] use $q = -100 + 300 + 1200\,\mathrm{cal/g} = 5.8618\,\mathrm{kJ/g}$, which is not dissimilar to Menikoff's value. The value of $q_1 = 5.8618\,\mathrm{kJ/g}$ was chosen for use in this work, since it has been used in deriving the JWL reaction products EOS for HMX and it is close to the value of $5.96\,\mathrm{kJ/g}$ from Cheetah [136].

$\ln Z_1$	E_1	q_1
12.5	1.49	0.058618
(Z in $\mu\mathrm{s}^{-1}$)	$\mathrm{Mbar\,cm^3/mol}$	$\mathrm{Mbar\,cm^3/g}$

Table 3.8: Single-step Arrhenius reaction-rate parameters for HMX in hydrocode units.

Binders

Only a limited data set is available for the reaction rates of either of the binders. For PBX9501's binder, some ODTX experimental data are available and are plotted in figure 3.5. Even accounting for the slower heat conduction expected in the ODTX geometry due to its lower thermal conductivity, this seems to indicate that the binder is more reactive than HMX at certain temperatures, which is surprising because PBX9501's binder is often described as inert. Extrapolating these data into the high temperature regime would be fraught with danger, but a simple approach is to assume that the binders behave in the same way as HMX. Appropriate values of $\ln Z$ and E_1 were determined by fitting equation 3.5 to the HMX data (the black line) in figure 3.5. Therefore, $E_1 = 149\,\mathrm{kJ/mol}$ is used for both binders, with $\ln Z_1 = 13.2$ for the binder in PBX9501 and 13.3 for the binder in EDC37 (table 3.9). The slight differences in $\ln Z_1$ arise because of the different thermal properties of the two binders.

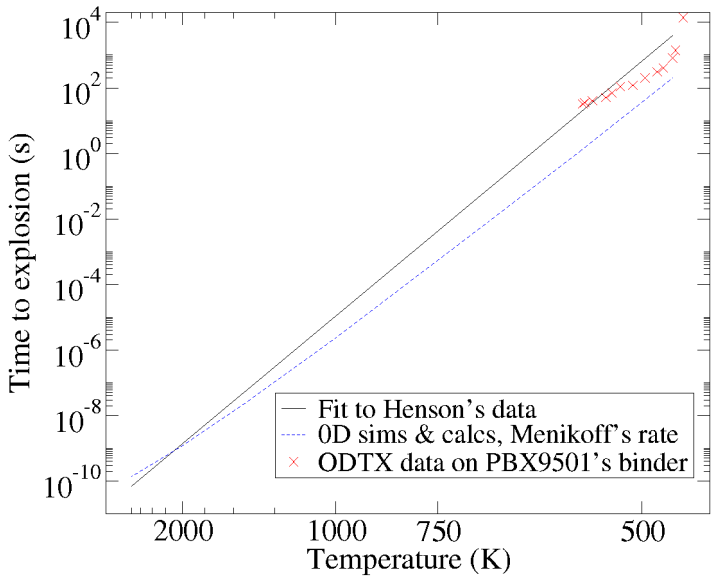

Figure 3.5: Arrhenius plot showing that ODTX experimental data for the binder in PBX9501 [135] are similar to Henson's compilation of HMX data [82, 178]. Reaction parameters derived from Menikoff's rate for HMX are used for the binders in PBX9501 and EDC37 in this work.

	$\ln Z_1$	E_1	q_1
PBX9501's binder	13.2	1.49	0.044959
EDC37's binder	13.3	1.49	0.039083
	(Z in μs^{-1})	Mbar cm^3 / mol	Mbar cm^3 / g

Table 3.9: Single-step Arrhenius reaction-rate parameters for the binders in PBX9501 and EDC37.

Although there is considerably more uncertainty in the Arrhenius reaction rate parameters for the binders than for HMX, a first guess for the maximum and minimum reaction rates is to use a similar range as for HMX. The time to explosion curve with minimum gradient would therefore correspond to $\ln Z_1 = 12.4$ and $E_1 = 140\,\mathrm{kJ/mol}$, while the curve with the maximum gradient has $\ln Z_1 = 14.6$ and $E_1 = 160\,\mathrm{kJ/mol}$. Values for the heat of reaction q_1 are calculated from the JWL EOS as 3.9083 kJ / g for the binder in EDC37 and 4.4959 kJ / g for the binder in PBX9501. Maximum and minimum values are not quoted owing to the difficulty in estimating them, and the requirement that the JWL reaction products equation of state is consistent with the value of q_1.

3.5 Mixing rule

As discussed in section 3.1, it is assumed that the unreacted explosive and reaction products in partially-reacted cells are in both pressure and temperature equilibrium. The particulate mixture rules for specific volume v and specific internal energy e are:

$$v = (1-\lambda)v_s + \lambda v_g \tag{3.6}$$

$$e = (1-\lambda)e_s + \lambda e_g \tag{3.7}$$

where subscript s is for the solid, unreacted explosive and g is for the gaseous reaction products. Solving for pressure equilibrium $p = p_s(v_s, e_s) = p_g(v_g, e_g)$ and temperature equilibrium $T = T_s(v_s, e_s) = T_g(v_g, e_g)$ requires iterating on v_s and e_s, since v_g and e_g can be calculated using equations 3.6 and 3.7. Following the recipe for conducting Newton-Raphson iterations in multiple dimensions in reference 118, the following system

$$\begin{pmatrix} \overbrace{\frac{\partial p_s}{\partial v_s} - \frac{\partial p_g}{\partial v_s}}^{\alpha_{1,1}} & \overbrace{\frac{\partial p_s}{\partial e_s} - \frac{\partial p_g}{\partial e_s}}^{\alpha_{1,2}} \\ \underbrace{\frac{\partial T_s}{\partial v_s} - \frac{\partial T_g}{\partial v_s}}_{\alpha_{2,1}} & \underbrace{\frac{\partial T_s}{\partial e_s} - \frac{\partial T_g}{\partial e_s}}_{\alpha_{2,2}} \end{pmatrix} \begin{pmatrix} \delta v_s \\ \delta e_s \end{pmatrix} = \begin{pmatrix} p_g - p_s \\ T_g - T_s \end{pmatrix}$$

can be solved iteratively using

$$\delta v_s = \frac{\alpha_{2,2}(p_g - p_s) - \alpha_{1,2}(T_g - T_s)}{\alpha_{1,1}\alpha_{2,2} - \alpha_{1,2}\alpha_{2,1}} \quad \text{and} \quad \delta e_s = \frac{\alpha_{1,1}(T_g - T_s) - \alpha_{2,1}(p_g - p_s)}{\alpha_{1,1}\alpha_{2,2} - \alpha_{1,2}\alpha_{2,1}}.$$

Convergence limits are chosen to achieve suitable energy conservation. For example, the total energy conservation in a Peruse test problem (the dynamic reaction of HMX and binder in plane geometry) improved from 10^{-2} % to $<10^{-4}$ % when the convergence criteria were tightened from $\Delta p < 10^{-4}$ GPa and $\Delta T < 10^{-2}$ K to $\Delta p < 10^{-5}$ GPa and $\Delta T < 10^{-4}$ K. Although it would be desirable to incorporate another iteration scheme for use in the case that the Newton-Raphson scheme fails to converge, this is difficult to do in more than one dimension [118] and so Peruse is programmed to stop running if convergence is not achieved. This did not prove to be a problem for any of the calculations described in this thesis.

3.6 Summary

The material models that will be used to represent the HMX and binder components of PBX9501 and EDC37 have been described. Linear shock velocity versus particle velocity Grüneisen equations of state have been chosen for the unreacted material, with JWL equations of state for the reaction products, and single step Arrhenius reaction rates. The assumptions and limitations of these models have been discussed. Although alternative material models for HMX and the binder in PBX9501 have been constructed by other authors, the models presented here are original and can be used for future research on these explosives. In addition, this is the first time that a material model, suitable for use in mesoscale shock to detonation simulations, has been developed for the binder in EDC37.

Chapter 4

Model validation

Although the material models used in this work are based on experimental data, it is important to validate them by comparison with the results of integrated experiments. Unfortunately, there have been few experiments on the individual components of plastic-bonded explosives because interest has historically been in the behaviour of the composite. Although the eventual aim of mesoscale modelling is to be able to reproduce shock and detonation phenomena in the composite, the very different responses of homogeneous and heterogeneous explosives means that this will not be possible until hotspots have been incorporated. Therefore, the models cannot yet be compared to the abundance of experimental data on PBX9501 and EDC37. In this chapter, the models for HMX and the binders will be tested against the three data sets that are currently applicable: Hugoniot data in section 4.1, Pop-plot data in section 4.2 and detonation wave profiles in section 4.3.

4.1 Hugoniot data

The Hugoniot is a curve representing the end states that can be achieved following the passage of a single shock wave through a material [1]. The unreacted equations of state used in this work use as their reference curve a linear Hugoniot relation $U_s = a + bu_p$ for each material (see section 3.2). The coefficients a and b for HMX and the binders in PBX9501 and EDC37 were fitted to a subset of the Hugoniot data that are now available. In this section, the unreacted equations of state will be validated by comparison to a wider data set. Matching Hugoniot data is a basic requirement of models that are designed for

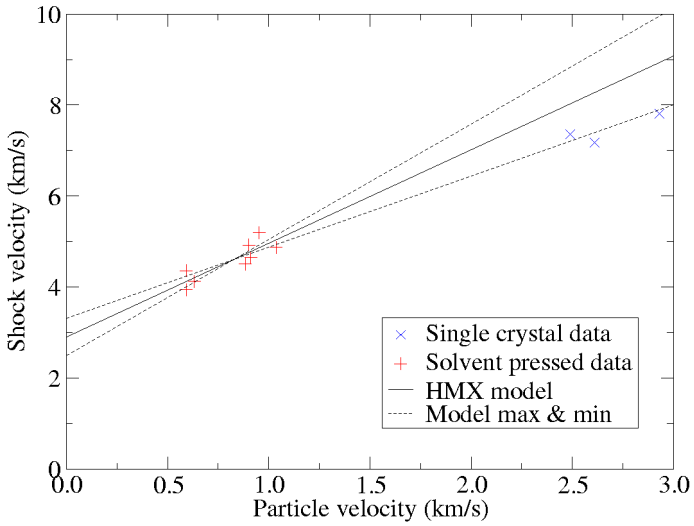

Figure 4.1: Hugoniot data for single crystal and solvent pressed HMX [11], compared to the HMX model from section 3.2. The model agrees reasonably well with the data.

use in the shock regime, so good agreement is expected.

The shock velocity versus particle velocity Hugoniot for HMX is shown in figure 4.1. The HMX model agrees well with the solvent-pressed data, which is not surprising because the coefficients were tuned to these data. Although the model does not pass through the single crystal data, these data do lie close to the maximum and minimum Hugoniot lines which will be used in subsequent chapters to evaluate the effect of the uncertainty in HMX Hugoniot parameters. Since the density of HMX is known accurately, this means that the post-shock state (at least in p, v, e space) is well represented in hydrocode calculations and has appropriate error bars. Suggestions for how the model could be improved are given in section 8.2.

Hugoniot data for the binder in PBX9501 are given in figure 4.2. It is not surprising that the model is a good fit to the data, because the linear Hugoniot parameters were chosen to be consistent with Baer's quadratic fit [163], which itself was optimised to these experimental data. The maximum and minimum Hugoniot lines bracket the majority of the data, showing that they are suitable for use in subsequent chapters to evaluate the uncertainties in binder Hugoniot data. Overall, figure 4.2 shows that the linear $U_s(u_p)$ relation for the binder in PBX9501 provides a reasonable fit to the Hugoniot data.

Hugoniot measurements became available for the binder in EDC37 during the course

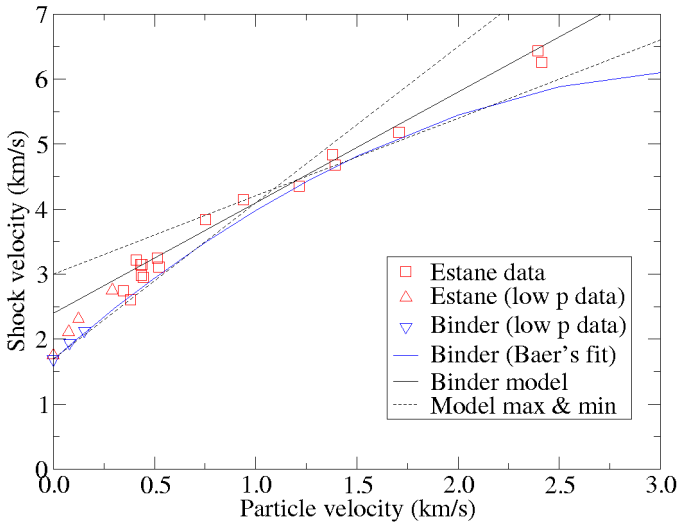

Figure 4.2: Hugoniot data for the binder in PBX9501, a 50:50 mixture of estane and BDNPA-F. The estane data are from reference 159, the low-pressure data on estane and the mixed binder are from 164 and Baer's quadratic Hugoniot, derived from an equation of state fitted to data from isentropic compression experiments, is from 163. The binder model and its maximum and minimum limits from section 3.2 agree well with the data.

of this work. A detailed analysis of stress gauge traces and VISAR data from ten gas-gun experiments in reference 181 yielded five accurate Hugoniot points in the range $u_p = 0.1$ to $0.8\,\mathrm{km/s}$. Ultrasonic measurements of the sound speed provide an additional data point at $u_p = 0.0\,\mathrm{km/s}$. Figure 4.3 shows that the binder model is a reasonable match to the data. A best fit to the experimental Hugoniot data gives $U_s = ([1.46 \pm 0.07] + [2.52 \pm 0.20]u_p)\,\mathrm{km/s}$, which lies between the nominal model and the Hugoniots with maximum and minimum reasonable gradient. This validates the model for EDC37's binder, demonstrating that it appropriately represents the shock state in hydrocode simulations and that the maximum and minimum parameters are reasonable.

Overall, figures 4.1, 4.2 and 4.3 show that the unreacted equations of state for HMX and the binders in PBX9501 and EDC37 give a good match to the experimental Hugoniot data. The Rankine-Hugoniot relations allow pressure, density and specific internal energy to be calculated from the $U_s(u_p)$ Hugoniot, but not the shock temperature which depends on $c_{v,s}$. Measurements of shock temperature are exceedingly difficult for explosives because only a fraction of a microsecond is available for measurement before chemical reactions heat the explosive to above its shock temperature. The lack of experimental

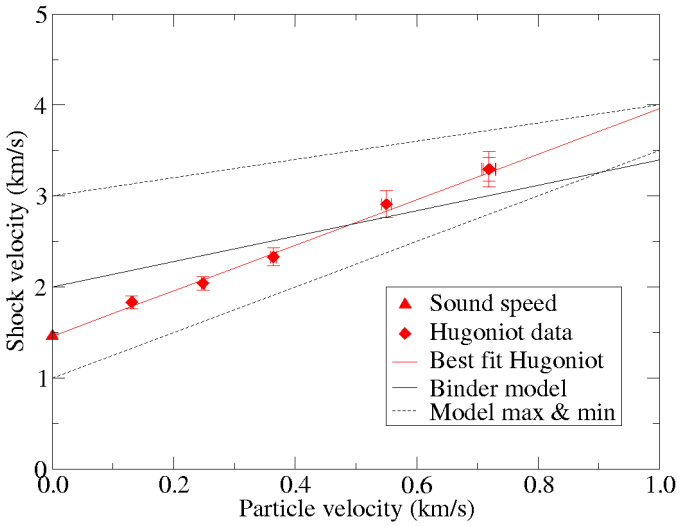

Figure 4.3: Hugoniot data for the binder in EDC37, which comprises 1 part nitrocellulose to 8 parts K10 liquid plasticizer, from a series of gas-gun experiments at Cambridge University [181]. The data cover a more limited range of particle velocities than in figures 4.1 and 4.2 owing to the capabilities of the single-stage gas gun.

data on shock temperatures is one of the reasons why reactive-burn models for explosives are often restricted to p, v, e space, since this avoids the need to use a complete equation of state $p(v, T)$. Although temperature-dependent reaction schemes are used in this work, validating the thermal behaviour of the unreacted equations of state has not been possible. The sensitivity of temperature distributions to uncertainties in thermal properties that will be demonstrated in section 7.2 highlights the importance of attempting to validate the thermal models in future work.

Another component of the unreacted equation of state is Grüneisen Γ, which controls the behaviour of the equation of state surface away from the Hugoniot reference curve. A value of Γ under ambient conditions can be calculated from the volume coefficient of thermal expansion 3α, the sound speed a and the heat capacity c_p via $\Gamma_0 = 3\alpha a^2/c_\mathrm{p}$ [146]. Using thermal expansion data from reference 145 and values for a and c_p from section 3.2, this gives $\Gamma_0 = 1.002$ for HMX which is remarkably close to the constant value of $\Gamma = 1$ used in this work. The variation of $\Gamma(v)$ with specific volume v could be obtained from Hugoniot data at various porosities, but these are not available for HMX or the binder materials. Until further experimental data become available, it will not be possible to thoroughly validate the treatment of Grüneisen Γ.

4.2 Pop-plot data

A Pop-plot gives the run-to-detonation distance as a function of input pressure for an explosive, neatly summarising its shock initiation behaviour [10]. The Pop-plot data for HMX [11] in figure 4.4 illustrate the importance of microstructure on the shock-to-detonation transition. Wedge-shaped single crystals of HMX that are "free of significant voids" [182] give 3 mm run-to-detonation distances at ~40 GPa pressures. In contrast, solvent-pressed HMX samples with complex microstructures give 3 mm run distances at 8 GPa. The solvent-pressed HMX is more sensitive (i.e. it requires a lower input pressure for the same run distance) because of the influence of hotspots on the reaction. The single crystals contain few hotspots, so they behave as a homogeneous explosive and need to be strongly shocked before reaction will build up into detonation. The solvent pressed material contains voids, crystal boundaries and other defects and so many hotspots are produced when it is shocked. It behaves as a heterogeneous explosive and can grow to detonation at modest input pressures.

Pop-plot data are often used to calibrate or validate reactive burn models, in particular their reaction rates. This is because hydrocode simulations of shock initiation are sensitive to the reaction rate and therefore to the unreacted equation of state on which the reaction rate depends, but are relatively insensitive to the equation of state of the reaction products. With validated unreacted equations of state, Pop-plot data can be used to test the reaction rates from section 3.4 in the shock initiation regime. The reaction rates in a mesoscale model are intended to represent the defect-free behaviour of each of the components, since the effect of hotspots will be accounted for separately. Since they contain few hotspots, the Pop-plot data from HMX single crystals will be used to validate the HMX material model in this section. It is not possible to validate the binder reaction rates because Pop-plot data are not available.

The single crystal Pop-plot data in reference 11 were determined from magnesium flyer plate impact experiments [182]. No attempt has been made to reproduce the experimental configuration, but Pop-plot points were extracted from simulations of a single HMX crystal hitting a rigid wall, to give a flat-topped shock initiation. The results from Peruse (which solves the reactive-flow equations 2.7 neglecting species diffusion) are shown in black in figure 4.4. The HMX model does not appear to agree very well with the experimental data; the simulations require ~10 GPa lower input shock strength to give similar run to detonation distances, i.e. the model is more sensitive than the data.

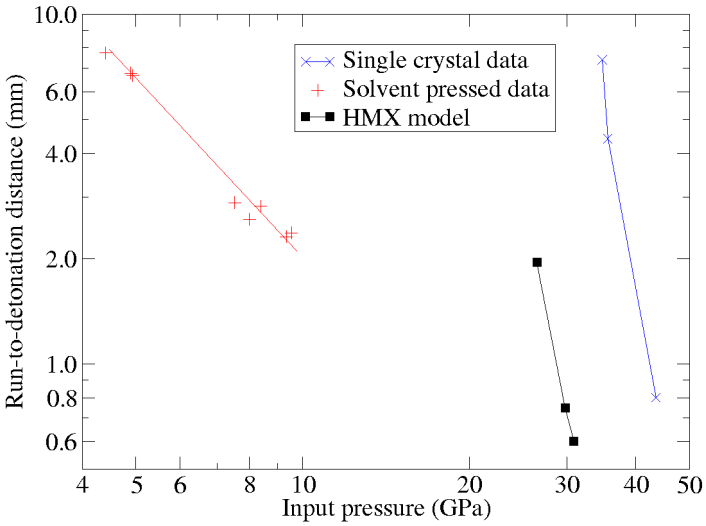

Figure 4.4: Pop-plot data for single HMX crystals (blue) and solvent pressed HMX for comparison (red) from reference 11. Peruse simulations for sustained shock initiation of a single HMX crystal (black) show that the HMX model is more sensitive than the data.

A first step towards improving the match of the HMX model to the Pop-plot data is to evaluate which of the material properties data in chapter 3 could influence the sensitivity. One candidate is the solid heat capacity $c_{v,s}$, which determines the shock temperature at a given input pressure and therefore the reaction rate. To check whether $c_{v,s}$ can make a big enough difference to the sensitivity of HMX to account for the 10 GPa difference in the Pop-plot, additional Peruse simulations were run at the upper limit of $c_{v,s} = 2.1\,\mathrm{J/g\,K}$. While a 38.0 GPa shock causes prompt detonation with the nominal value of $c_{v,s} = 1.1\,\mathrm{J/g\,K}$, little reaction occurs during the simulation for $c_{v,s} = 2.1\,\mathrm{J/g\,K}$. Even for sustained shock pressures as high as 43.2 GPa, reaction is still only building up by the time the shock wave reaches the end of the 3 mm crystal. For comparison, the experimental Pop-plot has a run distance of 0.80 mm at 43.5 GPa. With $c_{v,s} = 2.1\,\mathrm{J/g\,K}$, the HMX model is less sensitive than the experimental data.

Therefore, the HMX model brackets the single crystal Pop-plot data with reasonable variations to the solid heat capacity $c_{v,s}$. Although this does not prove that $c_{v,s}$ is responsible for the discrepancy between the simulations and the experiments, it shows that it is a likely candidate. Other possibilities include a multi-step chemical reaction scheme with an endothermic first rate. The constant value of $c_{v,s}$ used in this work could be adjusted to improve the fit to Pop plot data, but it is better to continue using the value derived from

experimental data to avoid masking other modelling deficiencies. Ways to improve the models will be suggested in section 8.2. For this work, it is considered sufficient that the HMX model brackets the Pop-plot data when $c_{v,s}$ is varied within its error bounds. These bounds will be used in later chapters to establish the sensitivity to uncertainties in the material properties data, so the "true" response of HMX should lie within the range of the calculated results.

A better way to validate the reaction rates for HMX and the binder materials would be to use embedded gauge data. In recent years, embedded particle velocity gauge experiments [e.g., 183] have provided a wealth of data on shock initiation in plastic-bonded explosives. Owing to the spatial and temporal-resolution these data provide, chemical reaction rates can be more tightly constrained using embedded gauge data than Pop-plot data. Unfortunately, the reaction rates for HMX and the binder materials can not yet be validated in this way owing to a lack of available data.

4.3 Detonation wave profiles

A detonation wave profile is a particle velocity history that has been recorded once steady detonation has been achieved in an explosive sample. High speed diagnostics are required to resolve the detonation wave profile in experiments, and so VISAR (Velocity Interferometer System for Any Reflector) or PDV (Photon Doppler Velocimetry) diagnostics are used at the interface between the sample and a window material [124]. Figure 4.5 shows the experimental configuration and a sketch of the resulting particle velocity histories. The arrival of the detonation shock wave at the interface causes the particle velocity to jump up to a velocity related to the von Neumann spike state. Chemical reaction in the explosive causes the particle velocity to fall between the spike and the sonic point which, in a one-dimensional experiment, corresponds to the end of the reaction zone. In the laboratory frame, the flow is super-sonic until the sonic point and is not influenced by the depth of the explosive sample. Therefore, detonation wave profiles from different experiments or measured at different depths within a single experiment are expected to agree between the von Neumann spike and the sonic point, provided the same explosive and window materials have been used and steady detonation has been achieved. After the sonic point, the flow is sub-sonic and so the particle velocity traces from different experiments will differ, as illustrated by the multiple Taylor wave curves in figure 4.5.

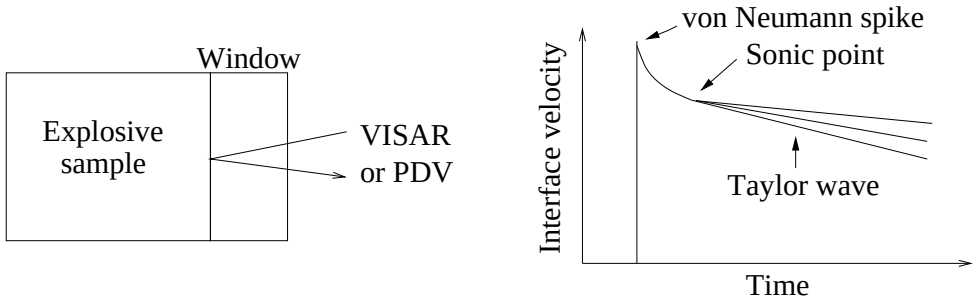

Figure 4.5: Sketch of the experimental configuration for detonation wave profile measurements (left) and the resulting particle velocity histories (right). The wave profiles from different experiments are expected to differ only after the sonic point when, in a one-dimensional experiment, the chemical reactions are complete.

Detonation wave profiles have been measured experimentally for HMX-based explosives [e.g., 124 and 184], but not for single crystals as far as I am aware. These data provide a useful test of the HMX model because detonation wave profiles are believed to depend on reactions that are due to bulk heating, rather than on the hotspot-driven reaction that is important in shock initiation [83]. Three features can be related to properties of the material model at the high shock strengths associated with detonation: the magnitudes of the von Neumann spike and sonic point are dependent on the unreacted and reaction products equations of state, and the time delay between the spike and the sonic point is caused by the duration of chemical reaction. However, exact agreement between Peruse simulations of single-crystal HMX and the experimental data on HMX-based plastic-bonded explosives is not expected for two reasons. Firstly, after the sonic point, detonation wave profiles depend strongly on the experimental configuration. A model would need to be able to reproduce exactly the shock initiation behaviour in the experiment, and in particular the run-to-detonation distance, in order to be able to match the detonation wave profile after the sonic point. This is not possible with a defect-free model whose run distance is considerably longer than for a heterogeneous plastic-bonded explosive, owing to the absence of hotspots. Agreement can only be hoped for in the region between the von Neumann spike and the sonic point. Secondly, techniques are still under development to improve the quality of the detonation wave profile measurements, and current data are under-resolved for HMX-based explosives [184]. Until the experimental development work is complete, it would be premature to attempt a thorough assessment of the ability of the HMX model to represent it. Therefore, only a brief comparison will be made in this section to detonation wave profile data for PBX9501.

Gustavsen has measured detonation wave profiles in PBX9501 using polymethyl-

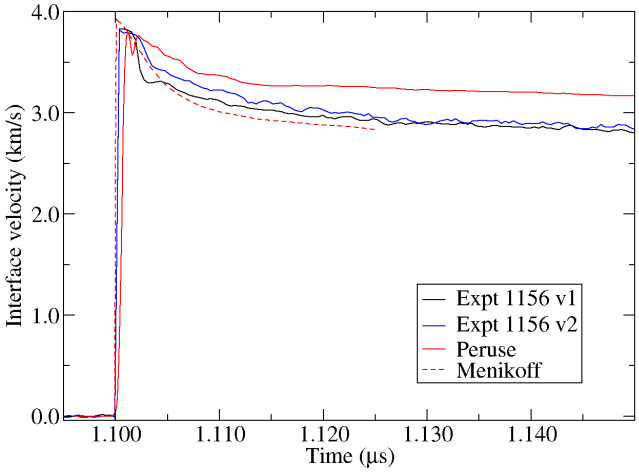

Figure 4.6: Simulated particle velocity histories for detonating HMX from Peruse and Menikoff [83], for comparison to experimental data for PBX9501 shot 1156 [124]. The particle velocity is recorded at the interface between the explosive sample and a PMMA window. Agreement between the simulations and the experiment is not expected beyond 25 or 30 ns after shock arrival.

methacrylate (PMMA) VISAR windows [124]. Interface velocity traces from one of his experiments, shot 1156, are given in figure 4.6. The black and blue traces correspond to the two VISARs used in the experiments, with different velocity-per-fringe constants. The sonic point is estimated to correspond to an interface velocity of 2.89 km / s, which occurs between 25 and 30 ns after the shock arrival for this experiment. Shot 1156 used a Vistal gas-gun flyer to drive a flat-topped shock at 5.2 GPa into a 23 mm PBX9501 sample, backed with a PMMA window. Since detonation wave profiles are insensitive to the experimental configuration until the sonic point, no attempt to reproduce the geometry of the experiments is made. The computational set-up comprises a 10 mm HMX sample backed by 1 mm PMMA, in plane geometry and with 200 zones / mm meshing. The HMX is initiated by adjusting the initial specific internal energy and density of the first 0.1 mm of HMX such that it is hot enough to react promptly at the start of the calculation. This is sufficient to initiate a detonation wave in the HMX, which propagates through the sample to the PMMA window. The interface velocity is obtained by recording the particle velocity history of computational gauges in the first PMMA zone.

The detonation wave profile produced by the HMX material model in Peruse is compared to the experimental data from shot 1156 in figure 4.6. The experimental data have been shifted in time so as to match the shock arrival time from the simulations. Pleasingly,

the simulated spike velocity is in good agreement with the experimental data. Although the situation is complicated by the presence of the PMMA window, this gives some reassurance that the unreacted equation of state is accurate in this regime. Unfortunately, the following drop in particle velocity is not as fast in the simulations as in the experiments. This could in part be due to inaccuracies in the equation of state used for PMMA, but it is the contribution of the HMX material model that concerns us here. A series of Peruse simulations were used to show that the velocity drop is not greatly influenced by the unreacted Hugoniot parameters, the specific heat of the unreacted HMX or the mesh density, but does depend on the reaction rate. In particular, increasing the Arrhenius parameter $\ln Z$ from 12.5 to 13, 14 or 15 (for Z in μs^{-1}) causes the fall-off time to shorten significantly. Comparing particle velocity histories from the Peruse simulation in figure 4.6 with burn fraction traces, reaction is 90 % completed within 4 ns of the shock arrival, and 99.9 % complete with 10 ns. Therefore, the sonic point occurs sooner in the simulations than it was estimated to do in the experiments. Agreement between the simulations and the experiments is not expected beyond the sonic point, or 1.115 µs in figure 4.6.

Menikoff has also modelled detonation wave profiles in PBX9501 using an Arrhenius reaction scheme [83]. Figure 4.6 shows that Menikoff slightly over-predicts the spike but achieves a better match to the following drop in interface velocity, despite having a similar reaction duration to Peruse (reaction is quoted as being 90 % complete in 4.3 ns). This may be due to the different equations of state he used for both the unreacted explosive and the reaction products, which lead to a shock temperature of 2500K compared to ~3000K in Peruse. It should also be noted that Menikoff adjusted the reaction rate parameter $\ln Z$ in order to match these experimental data. In section 3.4, the reaction rate parameters for HMX were derived by using Hubbard and Johnson's approximation to calculate explosion times consistent with Henson's compilation of HMX data, neglecting the behaviour of the equations of state. It has already been demonstrated in section 4.2 that reaction rates are sensitive to the unreacted equation of state. Calculated detonation wave profiles are also sensitive to the reaction products equation of state, which defines the sonic point. In the future, the match to detonation wave profiles could be improved by combining equation of state improvements with adjustments to the reaction-rate coefficients.

In conclusion, figure 4.6 shows that the HMX material model gives a reasonable match to detonation wave profile data on PBX9501, validating the model in the detonation regime. Unfortunately, it has not been possible to validate the models for the binders in this way because wave profile data are not available.

4.4 Summary

The material models constructed in chapter 3 have been tested against available experimental data. The unreacted equations of state give a good match to Hugoniot data for HMX and the binder materials. Single-crystal Pop-plot data show that the HMX model brackets the data within the uncertainties on solid heat capacity, validating the reaction rate in the shock initiation regime. Detonation wave profiles for HMX compare reasonably well with data for PBX9501, validating the model in the detonation regime.

Chapter 5

Shock heating of crystals and binder

The simplest possible hotspot mechanism in plastic-bonded explosives is shock heating of HMX crystals and binder. Owing to their differing material properties, higher temperatures are produced in the binder than in the crystals when the explosive is shocked. Subsequent chemical reactions may heat the binder further, amplifying the temperature difference between crystal and binder regions. Although this is not generally regarded as a hotspot mechanism [17], it does cause significant temperature localisation owing to the position of the binder in pockets surrounding the crystals. Therefore, it is possible that heat conduction from the binder to the crystals could cause sufficient chemical reaction in the crystals for them to explode. The accumulating pressure and temperature caused by the reaction of multiple crystals could eventually lead to detonation in the explosive.

Since the dominant physics controlling this process is heat conduction and Arrhenius chemistry, early work investigating this possible hotspot mechanism used ReactDiff. Although the results in section 5.1 indicate that the shock heating of crystals and binder is not a feasible hotspot mechanism, the effect of hydrodynamics could not be discounted. Section 5.2 will explain how Peruse was used to account for the combined effects of hydrodynamics, heat conduction and chemistry, and to determine conclusively whether this is a feasible mechanism in PBX9501 and EDC37. Since the material properties data for the HMX and binder components of these explosives are not well known, it is important to check that the uncertainties in the material properties do not affect the results. Exploratory Peruse simulations to determine the influence of these modelling uncertainties on the results are presented in section 5.3.

5.1 Initial investigation using ReactDiff

The following is a brief summary of an initial investigation into this hotspot mechanism. ReactDiff [115] was used to simulate spherical crystals of HMX with radius 0.45 μm coated in a thick layer of binder. ReactDiff solves the reactive-flow equations 2.7 neglecting hydrodynamics and species diffusion. McGuire & Tarver's [86] three-step reaction scheme A $\overset{1}{\rightarrow}$ B $\overset{2}{\rightarrow}$ 2C $\overset{3}{\rightarrow}$ D was used for the HMX (equations 2.15) and the binder was treated as inert. Illustrative results are given in figure 5.1 for initial conditions representative of a shock at 9.5 GPa input pressure. The temperature profile shows that the HMX (with radius <0.45 μm) is initially cooler than the binder (radius >0.45 μm). For ~1.5 μs, heat conduction from the binder causes the temperature of the HMX to increase. The species histories show that the endothermic reaction A → B progresses over the first 1.3 μs, until the first exothermic reaction B → 2C takes hold and causes the temperature in the centre of the HMX crystal to rise further. The third, highly-exothermic reaction 2C → D takes over at 1.85 μs when there is a sudden increase in the HMX temperature and the composition transforms almost instantaneously to pure D. This sudden transformation is a thermal explosion and the time at which it occurs depends on the size of the HMX crystals, and the thickness and reactivity of the binder layer.

For a 9.5 GPa input shock, the minimum time to explosion observed for any crystal size or binder thickness was 1.5 μs for PBX9501 and 1 μs for EDC37. These timescales are well above the run-to-detonation time of 0.35 μs in PBX9501 and 0.55 μs in EDC37, extrapolated from experimental Pop-plot data [12, 134]. This implies that, if shock heating of crystals and binder were the only hotspot mechanism in simulations of these explosives, none of the HMX crystals would explode within the experimental run-time and detonation would certainly not be produced. ReactDiff simulations were also undertaken using initial temperatures representative of input pressures between 1.3 and 6.3 GPa. No thermal explosion occurred within 10 μs, in contrast to experiments which detonate within 10 μs at these shock strengths. These observations suggest that thermal explosion caused by shock heating of the binder alone is not responsible for shock initiation in PBX9501 and EDC37.

However, ReactDiff is a static code and does not solve the hydrodynamic equations of motion. The simulations of crystals and binder, described above, had significant temperature variation through the computational domain and the only mechanism acting to smooth this was heat conduction. In reality, as the temperature of the crystals and binder

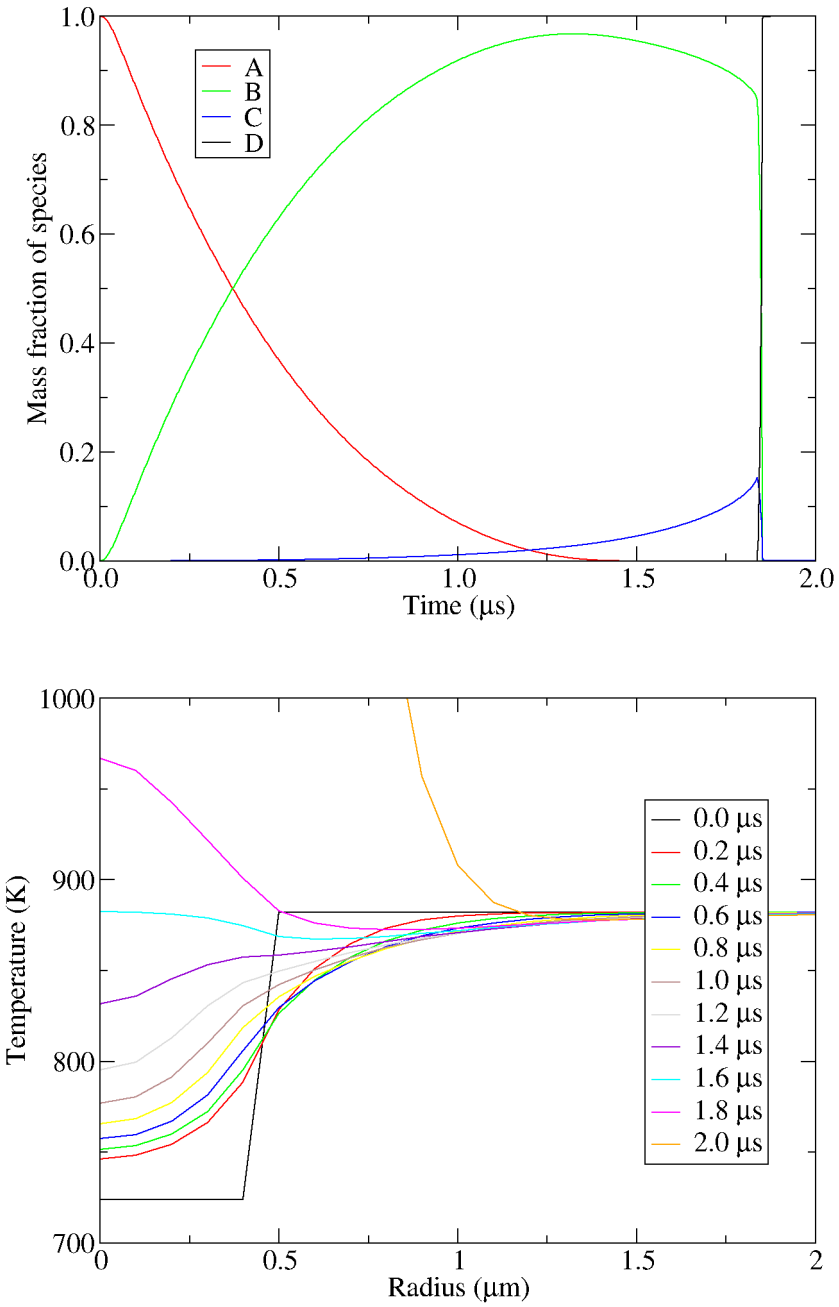

Figure 5.1: Illustrative results for a ReactDiff simulation of a spherical HMX crystal surrounded by a layer of PBX9501's binder. The graphs show HMX species histories (above) and temperature profiles (below). The time to explosion is ~1.85 μs when there is a sudden increase in the HMX temperature and the composition transforms almost instantaneously to D.

rises, the pressure also increases. In addition, high-pressure gaseous reaction products are produced when the crystals and binder react. Waves will distribute this increase in pressure throughout the computational domain on timescales several orders of magnitude faster than heat conduction. It was concluded that shock heating of crystals and binder could not be eliminated as a hotspot mechanism until hydrodynamics had been accounted for.

5.2 Results obtained using Peruse

Peruse [107] is a one-dimensional hydrocode which solves the Lagrangian reactive-flow equations 2.7 neglecting species diffusion. The incorporation of heat conduction and Arrhenius chemistry described in chapter 2 allows Peruse to be used to investigate shock heating of crystals and binder as a hotspot mechanism, accounting for the effects of hydrodynamics.

5.2.1 Planar calculations with simplified geometry

In one-dimensional planar geometry, a calculation representative of the microstructure of EDC37 would contain alternating HMX and binder layers of various thicknesses. The results of such a calculation are rather complicated, so it was decided to start by investigating simplified geometries. These are relatively easy to understand and allow confidence to be gained, before trust is placed in Peruse simulations of more realistic geometries. Since the explosives PBX9501 and EDC37 are composed mainly of HMX, with a small percentage by weight of binder, only geometries dominated by HMX are studied here. HMX and binder material properties were taken from chapter 3.

Firstly, simulations were performed in which a single HMX crystal was fired into a rigid wall. This drives a shock into the HMX crystal in a computationally efficient manner, as there is no need to represent an impactor in the simulation. The geometry is illustrated in figure 5.2. The impact velocity of 1.7 km / s was used for all the simulations in this section and corresponds to an input pressure of ~20 GPa. This is a high pressure for the shock to detonation regime, so detonation would be expected to occur promptly in the plastic-bonded explosive (although not in a single crystal as discussed in section 4.2). The Pop-plots of PBX9501 and EDC37 extrapolate to run distances of ~1 mm at this pressure.

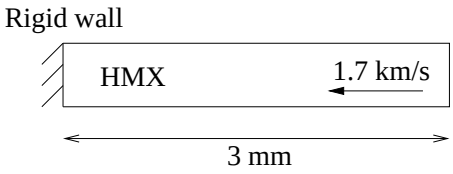

Figure 5.2: Geometry of single HMX crystal calculation in Peruse with plane geometry. The impact velocity of 1.7 km/s corresponds to ~20 GPa and was used for all the simulations described in this section.

This pressure is used as an upper limit for the shock to detonation regime: if shock heating of crystals and binder is not a feasible hotspot mechanism at this pressure, then the non-linear behaviour of the Arrhenius reaction rate equations means that it certainly will not be feasible at lower pressures.

The computational geometry is 3 mm in length to provide an adequate computational domain extent to allow reactions to build up, with some leeway over the 1 mm run distance expected from the Pop-plot. In order to prevent excessive computational run-times, 10 μm meshing was used. An investigation into the sensitivity of the results to mesh density is reported later. Virtual gauges are positioned every 0.15 mm through the geometry to record histories of temperature, pressure, species mass fractions, etc. Temperature histories from the single-crystal simulation are shown in figure 5.3. The axes are chosen to be comparable with later plots. The temperature histories show that a shock is propagated through the HMX crystal but that very little reaction occurs behind it. This is confirmed by examination of the burn fraction histories (not shown).

The first gauge, coloured black in figure 5.3, is positioned in the cell nearest the rigid wall. It is shocked to a lower temperature than the deeper cells because of wall heating errors in the simulations (see section 2.2.1). Here, wall cooling occurs because the initial velocity applied in Peruse smears the shock over too many (rather than too few) computational cells. Wall heating errors affect the first gauge in all the figures in this section, so the first temperature trace which is usually coloured black should be disregarded. This calculation shows that a single HMX crystal with these material properties (and with no defects or hotspots) will not react when shocked to 20 GPa. This is consistent with single crystal Pop-plot data [11] in which "reasonable" run-to-detonation distances (<10 mm) are only produced for shock pressures higher than ~35 GPa.

To add a level of complication, a thin layer of binder was incorporated next to the rigid wall. This geometry is illustrated in figure 5.4. The binder thickness of 0.20 mm was chosen to be comparable with the largest HMX crystal sizes in these explosives and so

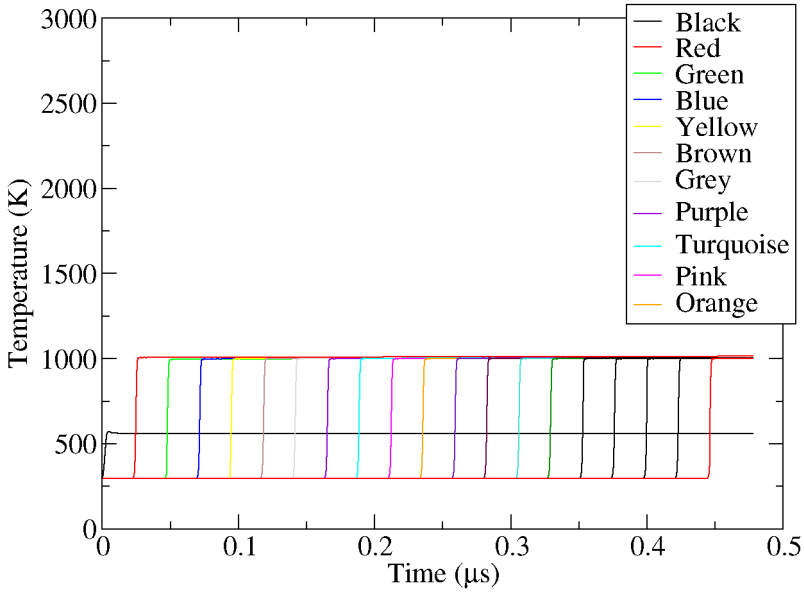

Figure 5.3: Temperature histories for a single HMX crystal calculation in Peruse. The different colours correspond to gauges located at 0.15 mm depths through the crystal and are labelled here to help with the description of later figures. The temperature at each gauge does not increase after the shock wave has passed, showing that no reaction occurs when HMX (without hotspots) is shocked to ~20 GPa.

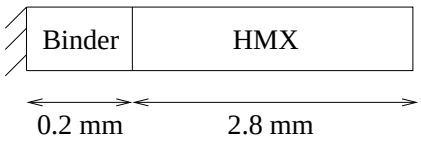

Figure 5.4: Geometry of binder/crystal calculation in Peruse.

that it could be adequately resolved with the 0.01 mm meshing used in these simulations. Temperature histories are shown in figure 5.5. Note that the black gauge is in the binder next to the rigid wall, the red gauge (at 0.15 mm) is also in the binder, but the remaining gauges are in the HMX. The temperature histories once again show that very little reaction occurs during the simulation. Ignoring the black gauge, the traces demonstrate the effect of multiple shocks on the temperature achieved. To help explain this, a time-distance plot is given in figure 5.6. The frame is moving at 1.7 km/s towards the rigid wall, so that initially the HMX and binder regions appear stationary and the rigid wall (now acting as a piston) appears to have a forward velocity. This is purely for ease of understanding. The pressure histories from the PBX9501 simulation are shown in figure 5.7. Both figures should be used together to understand the explanation below.

The green, blue and yellow gauges in the HMX are positioned close to the binder. They achieve significantly lower ultimate temperatures than the deeper gauges because they are double shocked to the final pressure of 20 GPa by a first shock at 15 GPa. This second shock is caused by a shock reverberation through the binder layer, as illustrated in figure 5.6. In contrast, the pink and orange gauges, for example, are positioned deeper into the HMX, where the second shock has amalgamated with the first shock. These gauges are single shocked straight to 20 GPa. Since multiple shocks to the same pressure result in lower temperatures than single shocks, there is a large variation in the temperature reached at different gauge positions through the HMX. For instance, HMX temperatures between 770 and 1020 K are observed in PBX9501. Figure 5.5 shows that the binder in EDC37 reaches a higher temperature than the binder in PBX9501 owing to the different equations of state of the two materials.

The next level of complication is a three-region geometry, illustrated in figure 5.8. Temperature histories from these simulations are shown in figure 5.9. Note that the black gauge is in the HMX next to the rigid wall, the red gauge (at 0.15 mm) is also in the HMX, the green gauge (at 0.30 mm) is in the binder, and the remaining gauges are in the HMX. These simulations show that reaction proceeds in the binder region, although rather slowly, but not in the HMX regions. The behaviour of the temperature traces, with

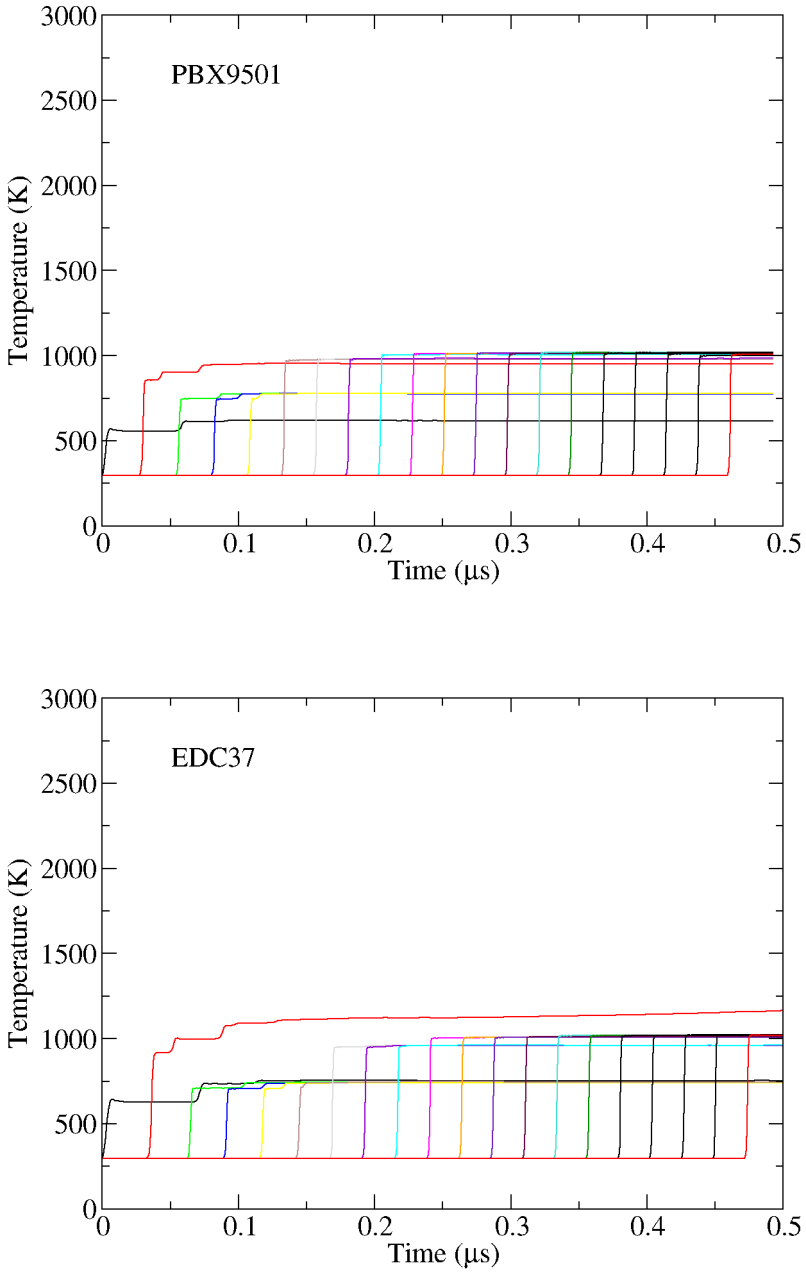

Figure 5.5: Temperature histories for binder/HMX calculations for PBX9501 (above) and EDC37 (below), showing that very little reaction occurs in HMX or binder regions.

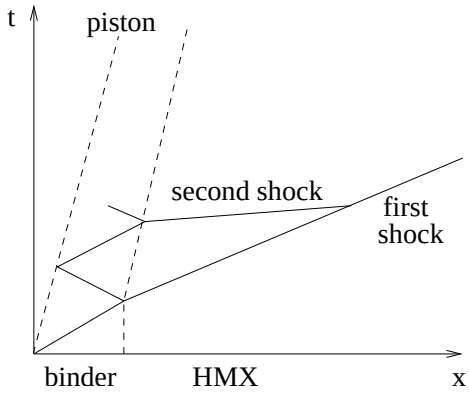

Figure 5.6: Time-distance plot for the binder/HMX simulations to aid the interpretation of figure 5.5.

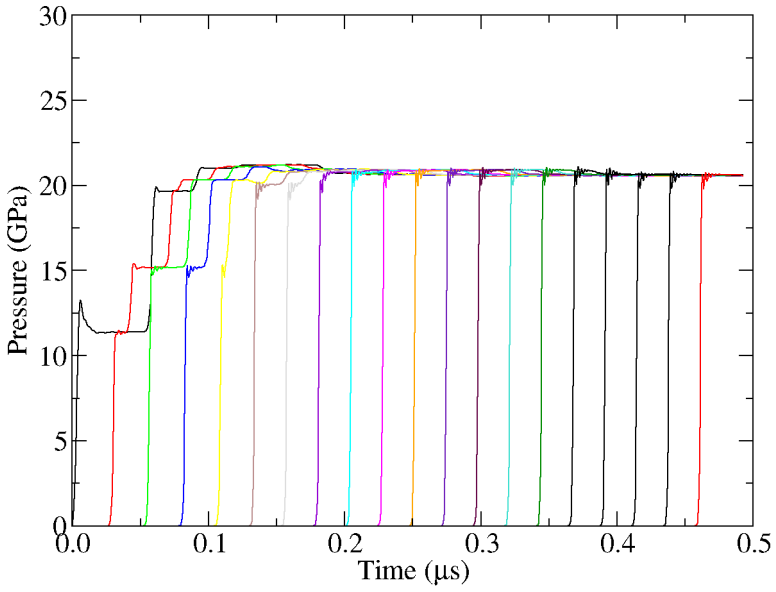

Figure 5.7: Pressure histories for binder/HMX simulations of PBX9501.

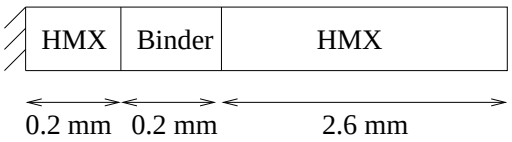

Figure 5.8: Geometry of crystal/binder/crystal calculation in Peruse.

a minimum temperature achieved at the turquoise gauge, is rather complicated and is explained below. Figure 5.10 shows a time-distance plot for the HMX/binder/HMX simulation; once again, the frame is moving at 1.7 km / s towards the rigid wall. Figure 5.11 shows pressure histories from the simulation.

The impact of the piston drives a shock into the first HMX layer, giving rise to state 1 in the HMX at a pressure of 20 GPa. This shock is transmitted into the binder and a rarefaction propagates back into the HMX, giving rise to state 2 in the first HMX layer and in the binder at 15 GPa. This rarefaction is eventually reflected back from the piston, taking the first HMX layer down to 10 GPa and propagating on through the geometry as rarefaction A. Meanwhile, once it has traversed the binder layer, the original shock propagates onwards into the second HMX layer as shock B, taking the binder and HMX to state 3 at 20 GPa. A reflected shock reverberates through the binder layer and propagates forwards into the second HMX layer as shock C.

The first gauge in the second HMX layer is coloured blue in figure 5.11. The pressure history shows that it is shocked up to state 3 at 20 GPa and then rarefaction A arrives, taking the pressure down to 15 GPa. Since it has been shocked to a high pressure, and shocks are more effective at generating heat than rarefactions are at removing it, the temperature of the blue gauge remains close to 1000 K. Rarefaction A travels faster than shock B and catches up with it, eroding its strength as it propagates further into the HMX. By the time shock B has reached the location of the turquoise gauge, it has been entirely overtaken by rarefaction A and has decayed to a strength of 15 GPa. Meanwhile, second shock C has been propagating through the second HMX layer. The turquoise gauge experiences a double shock and achieves only a fairly low temperature of ~750 K. The second shock C travels faster than the first shock B and so catches up with it around the location of the orange gauge. A single shock to a given pressure achieves a higher temperature than a double shock to the same pressure, and so the orange gauge and those deeper into the HMX are shocked to a higher temperature ~1000 K.

This fairly simple simulation demonstrates the wide range of temperatures that can be achieved in a single HMX layer simply because of the shock wave history it has been

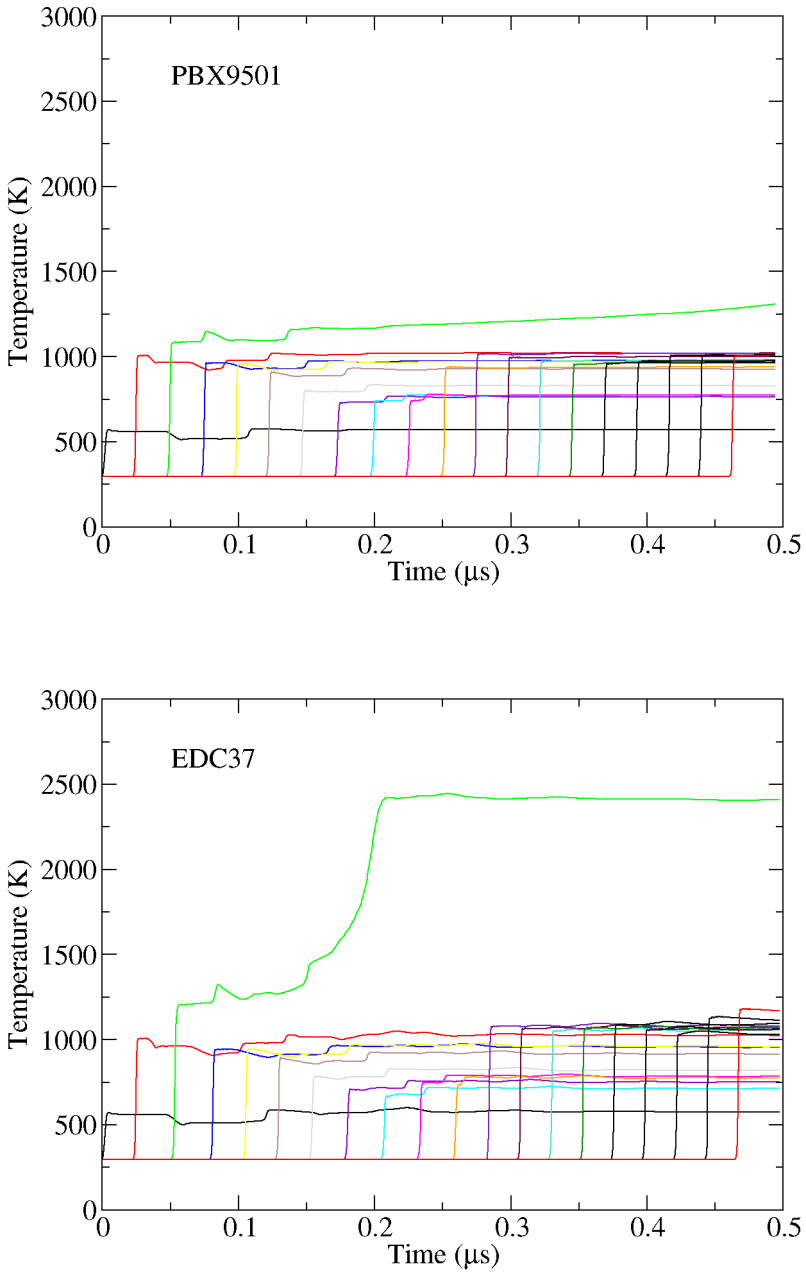

Figure 5.9: Temperature histories for HMX/binder/HMX calculations for PBX9501 (above) and EDC37 (below), showing that reaction occurs in the binder (green gauge) only.

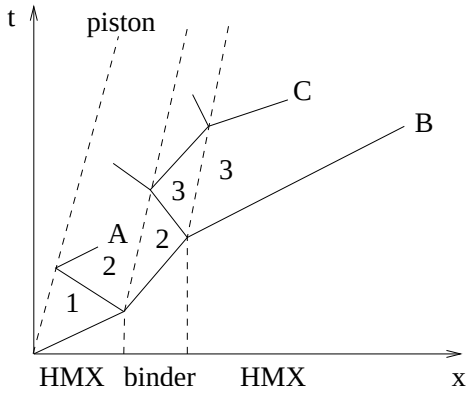

Figure 5.10: Time-distance plot for the HMX/binder/HMX simulations, to aid the interpretation of figure 5.9.

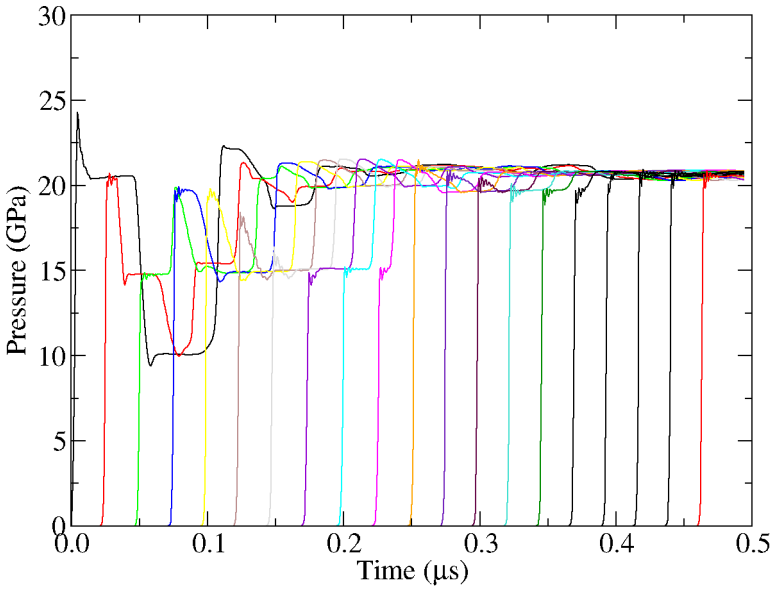

Figure 5.11: Pressure histories for HMX/binder/HMX calculations for PBX9501.

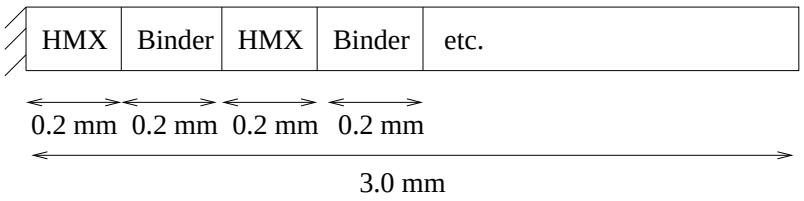

Figure 5.12: Geometry of alternating crystal/binder calculation in plane geometry.

exposed to. In a calculation with Arrhenius reaction rates, which have a strong temperature dependence, this phenomenon could lead to significant variations in reaction rate through a single crystal. With a more representative geometry, involving multiple HMX and binder layers, the computational results are difficult to understand in detail and trust must be placed in the overall conclusions of the simulation (e.g. whether detonation occurs). This demonstrates the power of the computational approach for such materials.

The final level of complication described in this section is an idealised geometry comprising alternating layers of HMX crystals and binder, as illustrated in figure 5.12. Temperature histories from these simulations are shown in figure 5.13. The PBX9501 calculation shows that no significant reaction occurs, since the temperature histories do not rise above ~1200 K. Once again, there is considerable variation in the temperatures reached by different HMX and binder layers. For EDC37, some of the binder regions do react but only slowly.

Comparing the results of these simplified geometry calculations, none of the HMX regions react to any significant extent within the duration of the simulation, and build up to detonation has certainly not occurred. In contrast, at this pressure, the experimental Pop-plot predicts a run distance of 1 mm (equivalent to the gauge which is shocked at ~0.2 μs). Since the simulations do not produce a run-to-detonation distance consistent with the experimental data, these results indicate that shock heating of crystals and binder is not a feasible hotspot mechanism.

5.2.2 Effect of meshing

The simplified calculations used 10 μm meshing. It is important to check that changes to the mesh density do not affect the conclusions drawn from the simulations. The alternating HMX and binder calculation of EDC37 in figure 5.13 led to the highest degree of reaction, making it a good test case for investigating the effect of mesh density.

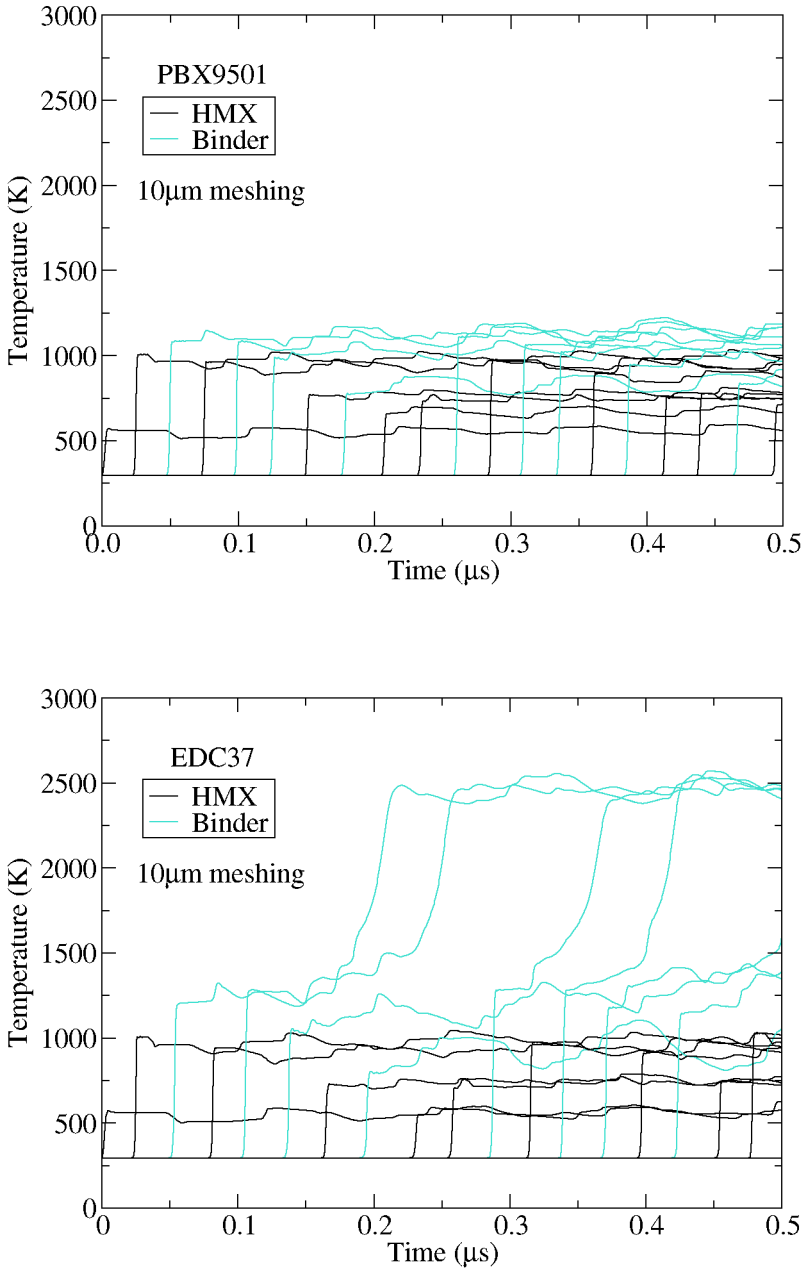

Figure 5.13: Temperature histories for alternating HMX/binder calculations for PBX9501 (above) and EDC37 (below). The temperature does not rise above ~1200 K for PBX9501 indicating that very little reaction has occurred. The temperatures of ~2500 K for EDC37 show that some of the binder regions do react but only slowly.

Figure 5.14 shows that the 10 µm-mesh calculation in figure 5.13 was not completely mesh converged, because the temperature histories change slightly as the mesh resolution is increased. However, the general behaviour is converged: only the binder shows any significant reaction at all three mesh resolutions. This confirms that the simplified Peruse calculations are sufficiently mesh-resolved.

5.2.3 Effect of geometry

The multi-region HMX and binder simulations described above are in one-dimensional plane geometry. They are not easily generalised to cylindrical or spherical geometry because the alternating regions would become concentric rings or shells of HMX and binder, which are not representative of the three-dimensional microstructure of PBX9501 and EDC37. There are two physical effects that are not correctly represented in the 1D planar calculations: shock focusing and heat conduction. A shock front that is travelling through a plastic-bonded explosive microstructure is not flat, but shows perturbations associated with the binder regions (see section 7.3). This means that 3D shock focusing can occur, leading to localised high-temperature regions. The effect of heat conduction also depends on the HMX and binder geometry because a spherical HMX crystal surrounded by hot binder will heat up more quickly than a planar sheet of HMX next to a binder sheet. It is necessary to confirm that the simplification to 1D plane geometry in this chapter, which neglects the 3D effects of shock focusing and heat conduction, is not affecting the results of the simulations.

One approach is to examine the temperature distributions produced by large microstructure simulations of EDC37 and PBX9501 (see chapter 7). These are relatively insensitive to the choice of one or two-dimensional geometry as will be demonstrated in section 7.1.4, indicating that shock focusing effects are not significant. Another approach is to run Peruse simulations of a single HMX crystal surrounded by a layer of binder in plane, cylindrical and spherical geometry, a similar configuration to critical hotspot simulations. As will be described in section 6.1.6, such calculations show small differences between plane, cylindrical and spherical geometry but the overall behaviour is unchanged. Both these approaches demonstrate that the results in this chapter are not significantly affected by the simplification to 1D plane geometry.

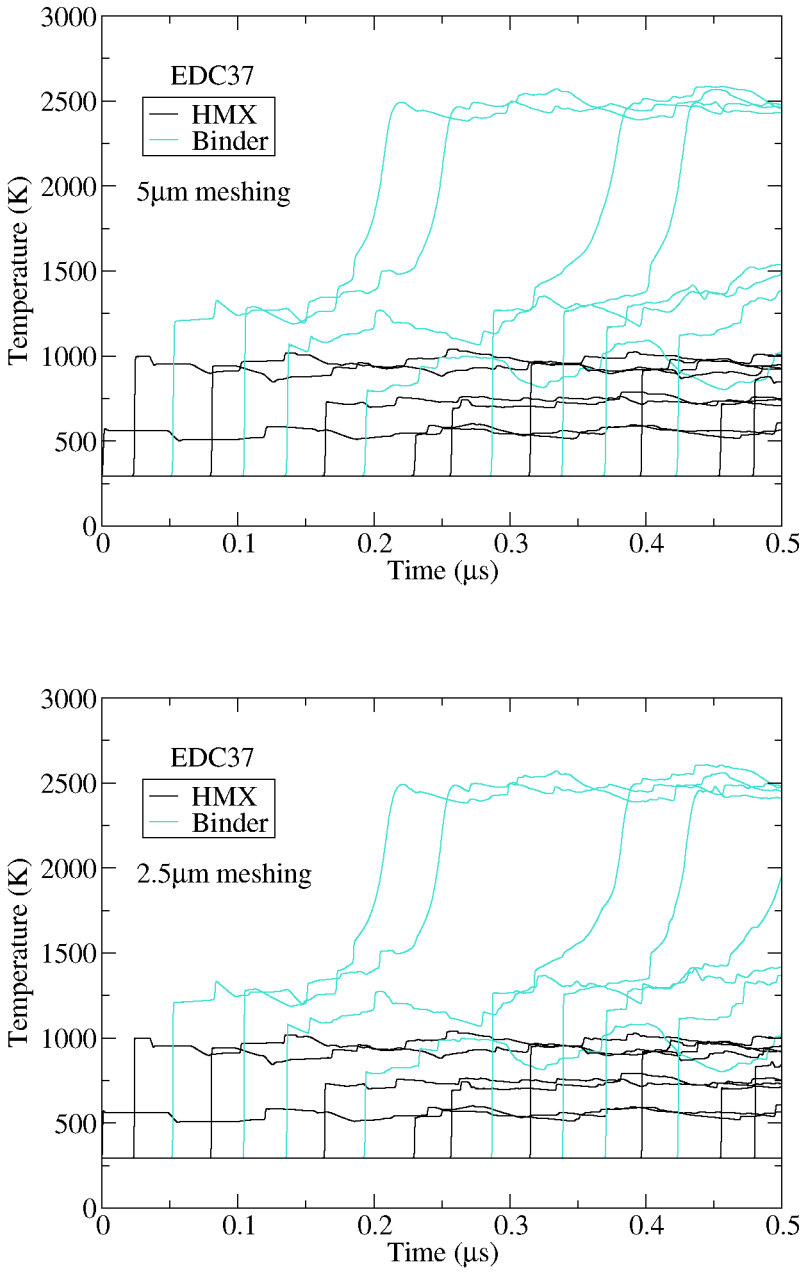

Figure 5.14: Temperature histories for alternating HMX/binder calculations for EDC37 with 5 µm meshing (above) and 2.5 µm meshing (below), for comparison with figure 5.13.

5.2.4 Representative microstructure calculations

The simplified calculations used idealised geometries where the crystal and binder layers have equal thickness. Since PBX9501 and EDC37 contain more than 90 % HMX, this is not representative of the physical microstructures of these explosives. Realistic one-dimensional computational geometries were constructed from micrographs of PBX9501 and EDC37 using the method described in section 2.4. A mesh density of 1 zone / pixel, which corresponds to ~0.3 μm and is consistent with the calculations in chapter 7, was used in "representative" Peruse simulations. Temperature histories were recorded from cells positioned at ~30 μm intervals through the calculation, so some of the cells contain HMX while others contain binder. Temperature histories from a representative simulation of EDC37 are shown in figure 5.15. The impact velocity was 1.7 km / s which is equivalent to a pressure of ~20 GPa.

The results in figure 5.15 are broadly similar to the alternating crystal/binder calculation of EDC37 in figure 5.13. Temperature histories from the representative simulation show higher-frequency oscillations due to wave reverberations in the fine structure of the

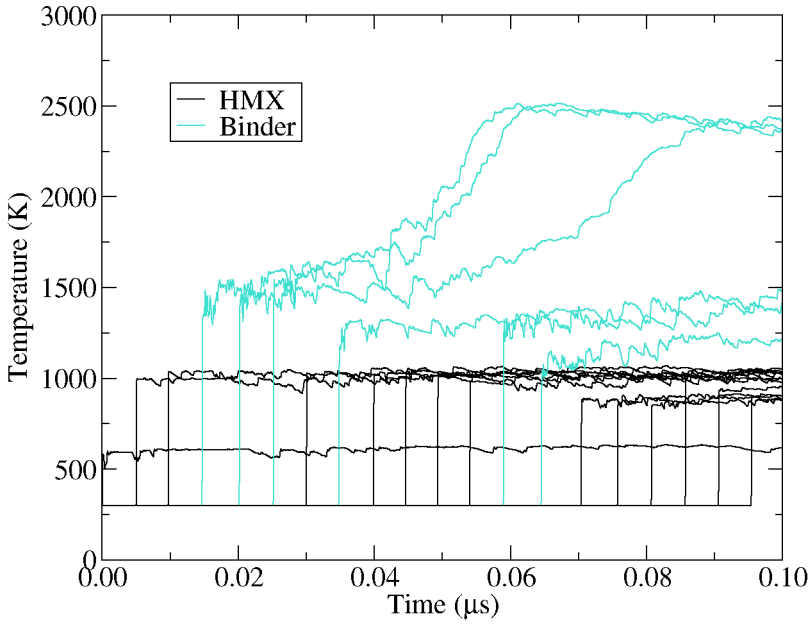

Figure 5.15: Temperature histories for representative calculation of EDC37 shocked to ~20 GPa, showing that only the binder regions react over the 0.10 μs duration of the simulation.

microstructure geometry. Some of the binder regions do react (i.e. their temperature rises significantly), but the HMX regions show very little reaction over the duration of the simulation. Similar calculations for PBX9501 show that even less reaction occurs in the binder regions than for EDC37. The results suggest that hydrodynamics is dominating the behaviour by controlling the initial temperature achieved in each computational cell. Although there is some heat conduction from binder regions into HMX, it is not sufficient to cause much chemical reaction in the HMX. This demonstrates the importance of including hydrodynamics in studies of hotspot mechanisms.

At this pressure of ~20 GPa, the experimental Pop-plots of PBX9501 and EDC37 extrapolate to a run distance of 1 mm. Although the simulated geometry is only 0.69 mm long in this case (owing to the size of the micrograph), there should certainly be significant reaction occurring if the EDC37 is to detonate shortly after the end of the computational domain. The disagreement between the simulations, where little reaction occurs in HMX regions as a result of the shock heating of crystals and binder, and the experiments, which detonate, suggests that shock heating of crystals and binder is not a feasible hotspot mechanism in PBX9501 and EDC37.

5.3 Effect of uncertainties in material properties

The results in section 5.2 indicate that, for the HMX-based explosives PBX9501 and EDC37, shock heating of crystals and binder is not a feasible hotspot mechanism, known hereafter as "the conclusion". It has already been checked that the conclusion is not sensitive to the geometry or mesh resolution. However, there is considerable uncertainty in some of the material properties data (see chapter 3), so it is important to check that reasonable changes to these data do not affect the conclusion. Although it is recognised that some parameters are thermodynamically inter-dependent (e.g., Grüneisen Γ is related to the thermal expansion coefficient, the sound speed and the heat capacity), the material model coefficients will be varied independently in this section. This has the advantages of allowing the effect of each parameter to be isolated and giving a worst-case estimate of the effect of the uncertainties. It is acknowledged that varying model coefficients that are independent of temperature or pressure does not necessarily lead to the same results as incorporating temperature or pressure dependence. However, it is a simple approach that can be used to identify which features of the material models need further development.

5.3.1 Initial temperature

An initial temperature of 295 K has been used in the Peruse simulations but, as discussed in section 3.2, this could reasonably be as low as 291 K or as high as 298 K. Lowering the initial temperature would slow down chemical reactions, leading to an even longer run-to-detonation distance, and so reinforce the conclusion that shock heating of crystals and binder is not a feasible hotspot mechanism. To test the effect of increasing the initial temperature from 295 to 298 K, the alternating HMX and binder simulations illustrated in figure 5.13 were repeated, although the results are not shown here. Some additional reaction was found to occur in the EDC37 binder regions but there was still no reaction in the HMX regions or in PBX9501's binder. This demonstrates that changing the initial temperature does not affect the conclusion.

5.3.2 Solid heat capacity

From section 3.2, solid heat capacities for HMX and the binder materials have large uncertainties. For example, a constant value of 1.1 J / g K is used for HMX but $c_{v,s}$ could be as low as 0.8 J / g K or as high as 2.1 J / g K, so the largest uncertainty corresponds to an increase in $c_{v,s}$. Increasing the heat capacities means that energy put into the system, by shock waves or chemical reactions, gives rise to smaller temperature increases. The maximum temperatures achieved would be lower and so heat conduction would be slower, reducing the degree of reaction. This would reinforce the conclusion.

The only reasonable change to the solid heat capacities that could enhance the reactivity of the system would be a decrease of $c_{v,s}$ from 1.1 to 0.8 J / g K for HMX. The alternating HMX and binder calculations of PBX9501 and EDC37 in figure 5.13 were repeated with the lower value of $c_{v,s}$ and results are shown in figure 5.16. These calculations confirm that reducing the solid heat capacity of HMX does increase the degree of reaction observed. The last gauge in the EDC37 calculation (bottom of figure 5.16) at 3 mm depth seems to indicate that detonation might have occurred, since the temperature jumps straight up to ~3000 K. However, only one of HMX regions in PBX9501 has reacted. To match the experimental Pop-plots at this shock strength, detonation would need to have occurred in both explosives by a depth of 1 mm so these calculations show that, even with a reduced $c_{v,s}$, shock heating of crystals and binder is not a feasible hotspot mechanism.

However, the calculation in figure 5.16 is of an idealised geometry with alternating

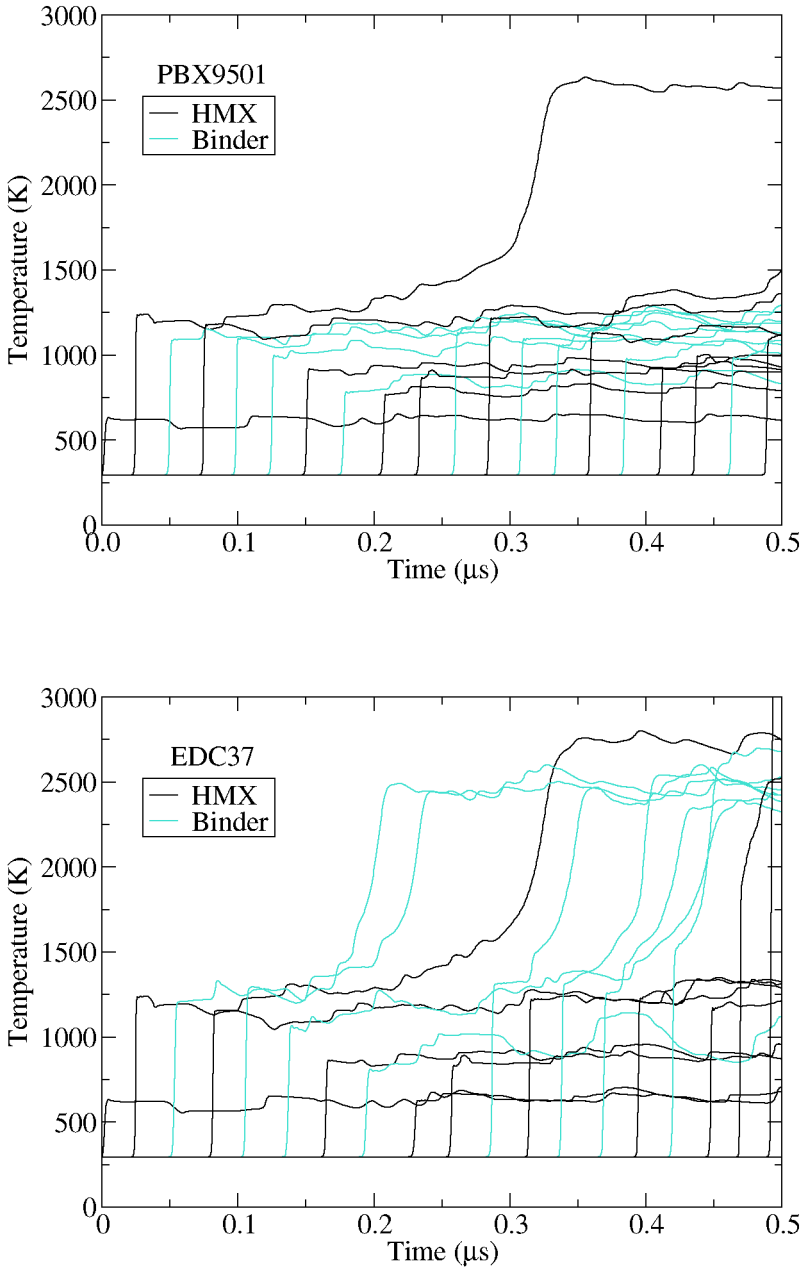

Figure 5.16: Temperature histories for alternating HMX and binder calculations of PBX9501 (above) and EDC37 (below), with $c_{v,s}$ reduced to $0.8\,\mathrm{J/g\,K}$ for HMX to investigate the effect of uncertainties in heat capacity.

HMX and binder layers of equal thickness. To check whether this was influencing the results, a representative EDC37 geometry (similar to that in section 5.2.4) was run in Peruse with $c_{v,s}$ reduced from 1.1 to 0.8 J/g K for HMX. No additional reaction was observed in this simulation than in figure 5.15 and detonation was certainly not produced. This confirms that the uncertainties in $c_{v,s}$ do not affect the conclusion.

5.3.3 Thermal conductivity

The uncertainties in the thermal conductivities of the HMX and binder layers include both increases and decreases (see section 3.2). Higher k will act to smooth out temperature gradients more quickly than lower k, giving rise to lower temperatures in the binder and higher temperatures in the HMX. The effect would be greatest with $k^{HMX} = k^{binder} = 0.5$ W/m K, and least for $k^{HMX} = 0.2$ W/m K and $k^{binder} = 0.1$ W/m K. These modifications were tried in alternating HMX and binder simulations and there was no discernable difference in the results from the three sets of calculations, showing that the effect of changes in thermal conductivity over these timescales is very slight indeed. In addition, section 7.2.5 will demonstrate that heat conduction has a small effect on the bulk temperature distributions in two-dimensional microstructure simulations. Therefore, the uncertainties on thermal conductivity do not affect the conclusion.

5.3.4 Unreacted equation of state

To investigate the effect of uncertainties on the unreacted Hugoniot parameters a and b, the following simulations were run using the parameters in section 3.2:

1. HMX maximum a and minimum b, nominal binder
2. HMX minimum a and maximum b, nominal binder
3. Binder maximum a and minimum b, nominal HMX
4. Binder minimum a and maximum b, nominal HMX

These combinations correspond to Hugoniot $U_s - u_p$ relations with extremes of gradient. The results of these simulations are shown in figure 5.17 for PBX9501 and figure 5.18 for EDC37. None of the simulations in figure 5.17 shows much reaction, except for Hugoniot parameter set 4, where only one binder region reacts within the timescale of the simulation. Therefore, reasonable changes to the PBX9501 Hugoniot parameters a and b do not affect the conclusion. Figure 5.18 can be compared to the bottom plot in fig-

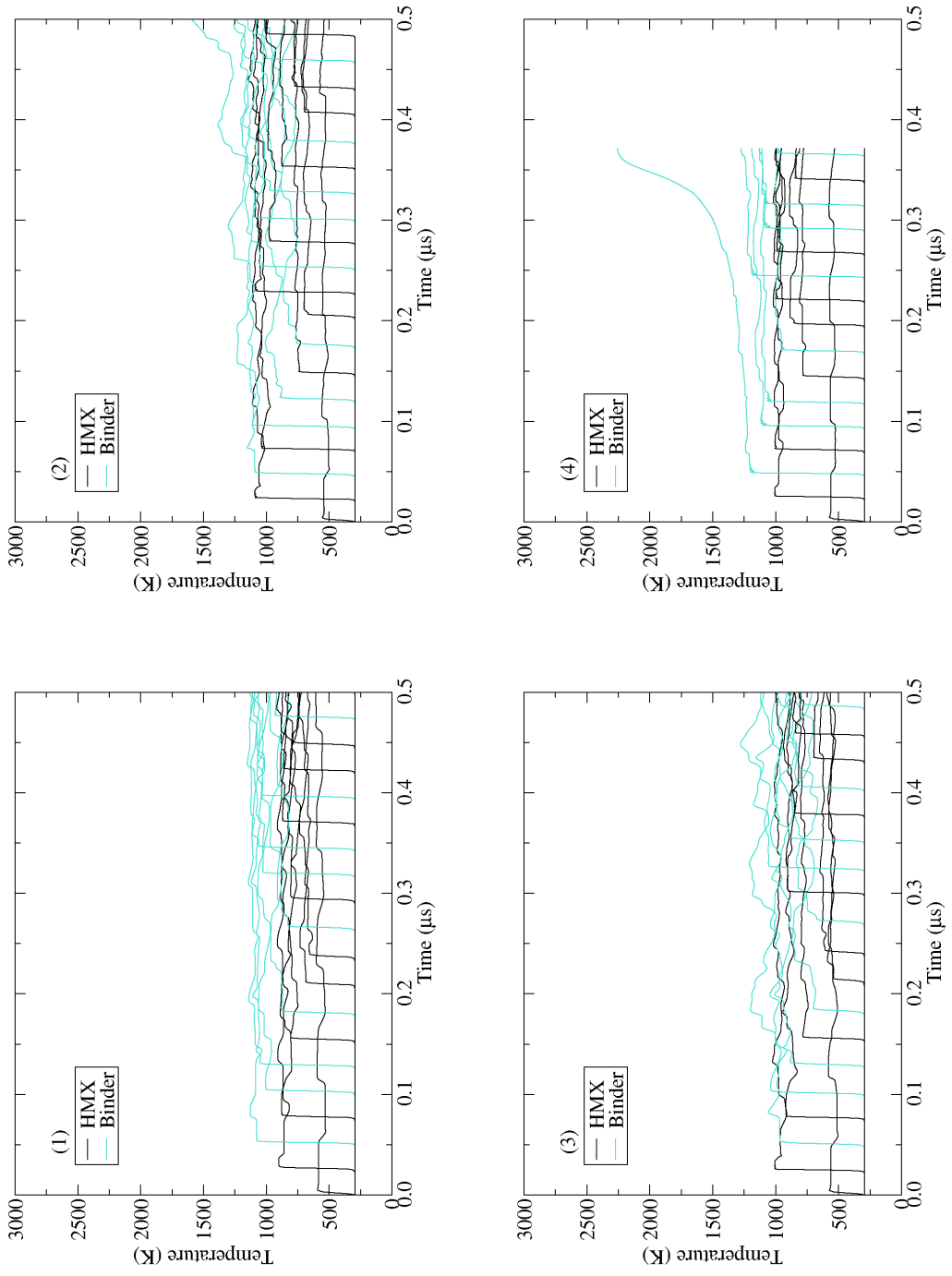

Figure 5.17: Temperature histories for alternating HMX and binder calculations of PBX9501, with a and b values adjusted according to the numbered list in the text, to investigate the effect of uncertainties in the unreacted Hugoniot parameters.

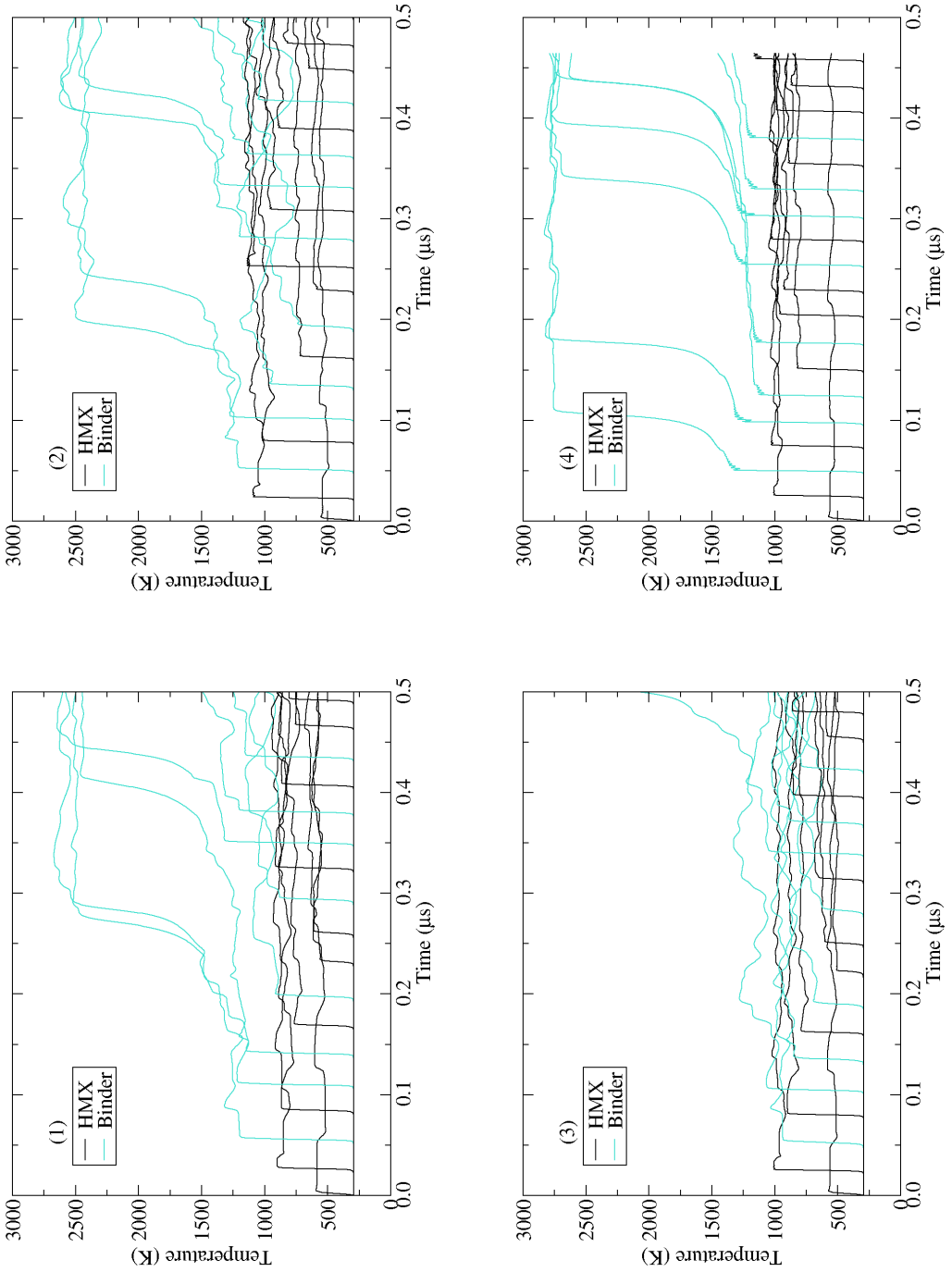

Figure 5.18: Temperature histories for alternating HMX and binder calculations of EDC37, with a and b values adjusted according to the numbered list in the text, to investigate the effect of uncertainties in the unreacted Hugoniot parameters.

ure 5.13. Hugoniot parameter set 1 produces lower temperatures in the HMX, while set 2 produces higher HMX temperatures but not high enough to increase the extent of reaction. Changing the binder parameters to set 3 lowers the binder temperature and reduces the extent of reaction. With parameter set 4, the binder reacts more quickly but none of the HMX regions shows any significant reaction. Since there is still significantly less reaction than would be necessary to be consistent with the experimental run-to-detonation distance, it seems that reasonable changes to the EDC37 Hugoniot parameters a and b do not affect the conclusion.

Another parameter controlling the unreacted equation of state is Grüneisen Γ. A value of $\Gamma = 1$ has been hardwired into the Peruse coding, but different values of Γ can be used in inert Petra calculations. Section 7.2 describes two-dimensional microstructure simulations where the value of $\Gamma = \Gamma_0 + \Gamma_1 v/v_0$ was varied, and it was found that Γ can have a significant effect on the calculated temperature distributions. This is because Γ controls the variation of temperature with specific volume via the thermodynamic relation $\left(\frac{\partial \ln T}{\partial \ln v}\right)_S = -\Gamma$. However, the maximum HMX temperatures for a 1.0 km/s impact remained well below 1000 K and so little reaction would have been produced. Therefore, reasonable changes to Γ do not affect the conclusion.

5.3.5 Reaction products equation of state

It is difficult to produce reasonable maximum and minimum values for JWL reaction products equations of state parameters, as mentioned in section 3.3. However, it is not likely that changing the JWL for HMX would affect the conclusion since so little reaction occurs in the HMX regions in figure 5.13. The binder JWL could only have an effect in regions where the binder reacts significantly. However, it is thought that there are greater uncertainties in the thermal properties of the reaction products than in the equation of state. If variations to the thermal properties in the next section do not affect the conclusion, then changes to the JWL will not do so either.

5.3.6 Reaction products thermal properties

To investigate the effects of uncertainties in the values of T_{CJ} and $c_{\mathrm{v,CJ}}$, the alternating HMX and binder simulation illustrated in figure 5.13 was repeated using the maximum

and minimum values in section 3.3. The results show that changing T_{CJ} or $c_{v,CJ}$ for the HMX in EDC37 and PBX9501 makes very little difference to the results, since hardly any reaction occurs in the HMX in these simulations. Similarly for PBX9501, changing the binder thermal properties makes very little difference to the results because so little reaction occurs in the binder. However, for EDC37 there is considerably more reaction in the binder regions in figure 5.13, which had $T_{CJ} = 2700\,\mathrm{K}$ and $c_{v,CJ} = 2.86\,\mathrm{J/g\,K}$. Simulations using the following thermal properties for the binder in EDC37 are illustrated in figure 5.19.

1. $T_{CJ} = 1900\,\mathrm{K}$ and $c_{v,CJ} = 2.86\,\mathrm{J/g\,K}$
2. $T_{CJ} = 3500\,\mathrm{K}$ and $c_{v,CJ} = 2.86\,\mathrm{J/g\,K}$
3. $T_{CJ} = 2700\,\mathrm{K}$ and $c_{v,CJ} = 1.4\,\mathrm{J/g\,K}$
4. $T_{CJ} = 2700\,\mathrm{K}$ and $c_{v,CJ} = 4.3\,\mathrm{J/g\,K}$

Decreasing T_{CJ} of the binder reduces the extent of reaction in the simulations, whereas increasing T_{CJ} not only increases the rate of reaction in the binder regions but also in the HMX regions. Decreasing $c_{v,CJ}$ also lowers the extent of reaction, whereas increasing $c_{v,CJ}$ increases the rate of reaction mainly in the binder regions. These changes arise owing to the different thermodynamic states achieved in the equation of state. Even with these increases to the values of T_{CJ} and $c_{v,CJ}$, the majority of HMX regions in the simulations have not reacted and detonation has certainly not occurred by the 1 mm or ~0.2 μs predicted by the Pop-plot. Therefore, reasonable changes to the reaction products thermal properties do not affect the conclusion.

5.3.7 Arrhenius chemistry parameters

In section 3.4, no maximum and minimum values were quoted for the heat of reaction q_1 owing to the difficulty of estimating the uncertainty on q_1, since it is necessary that the heat of reaction from the chemistry scheme be consistent with the JWL reaction products equation of state. The effect of q_1 on the simulations is likely to be two-fold. It will influence the temperature reached in the detonation products, rather like the changes to T_{CJ} and $c_{v,CJ}$ did. It will also influence the time to explosion. Using Hubbard & Johnson's approximation for the time to explosion from a single step Arrhenius rate

$$t = \frac{c_{v,s} T^2 R}{Z_1 q_1 E_1} \exp\left(\frac{E_1}{RT}\right),$$

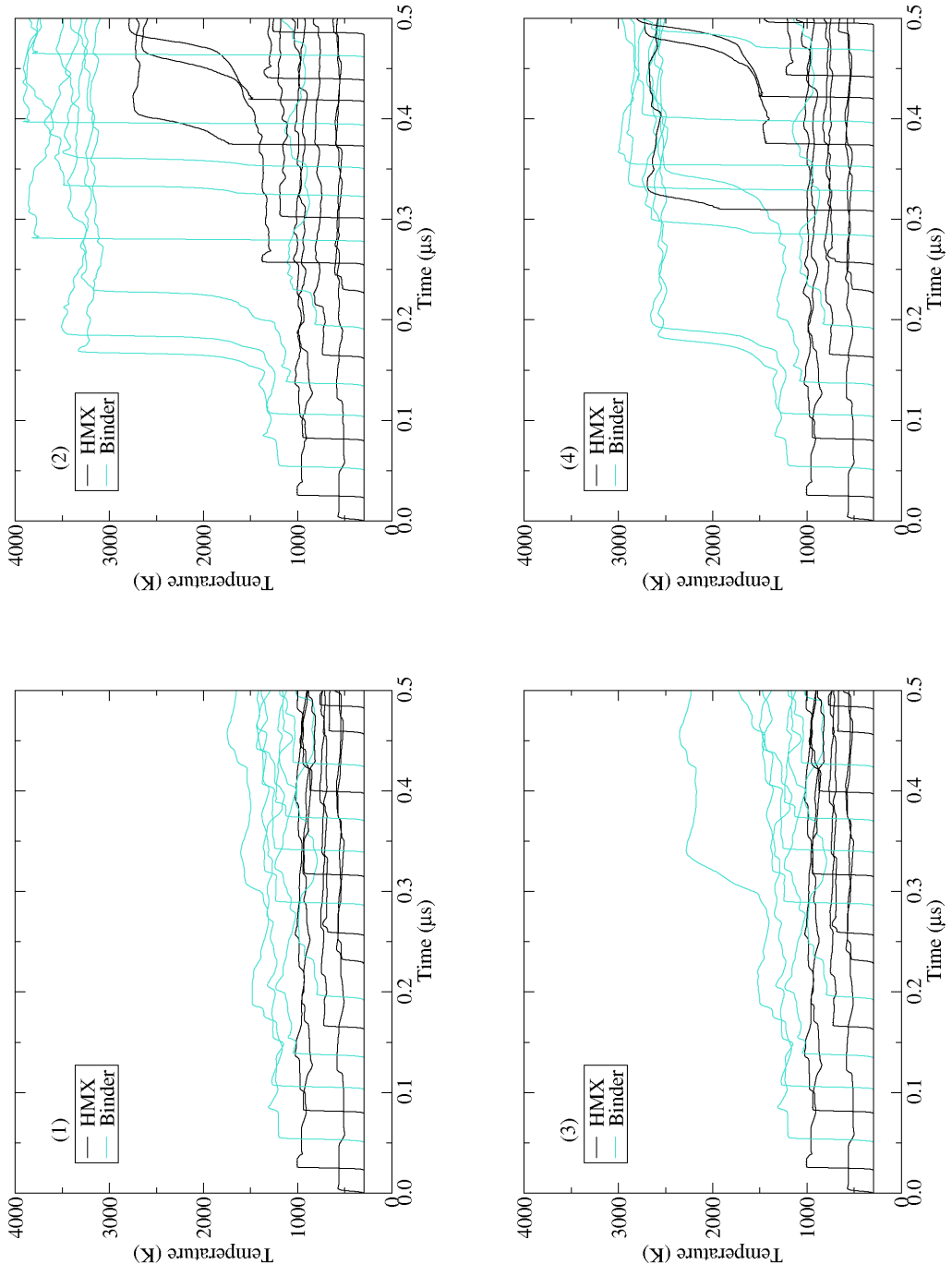

Figure 5.19: Temperature histories for alternating HMX and binder calculations of EDC37, with T_{CJ} and $c_{\mathrm{v,CJ}}$ values for the binder adjusted according to the numbered list in the text, to investigate the effect of uncertainties in the thermal properties of the reaction products.

the effect of changes to q_1 would be the same as changes to Z_1. Therefore, the effect of reasonable changes to q_1 on the conclusion can be gauged by the effects of other parameters.

The effect of changes to the Arrhenius reaction-rate parameters was investigated by repeating the alternating HMX and binder simulation, illustrated in figure 5.13, using values of $\ln Z_1$ and E_1 corresponding to the Arrhenius time to explosion curve with minimum and maximum gradient (see section 3.4). For PBX9501, these changes had very little effect on temperature histories. For EDC37, the temperature histories are illustrated in figure 5.20. Using the lower $\ln Z_1$ and E_1 values slightly lowers the reaction rate in the binder regions of EDC37, but the effect is not very great because the three sets of Arrhenius parameters produce similar explosion times in the temperature range of relevance here ($\sim$1000 K). With the higher $\ln Z_1$ and E_1 values, more reaction occurs in the simulation and even some of the HMX regions react. However, it is clear that detonation still has not been produced by the 1 mm run distance required by the experimental Pop-plot.

Similarly, a representative-geometry EDC37 simulation with these higher values of $\ln Z_1$ and E_1 showed increased reaction in the binder but not in the HMX regions; certainly detonation did not occur by the end of the simulation. In section 3.4, it was noted that the uncertainty in the Arrhenius reaction rate parameters for the binders is much greater than for HMX. If the binder reaction kinetics are set to be so fast that it reacts to completion almost immediately, using $E_1 = 160\,\mathrm{kJ/mol}$ and $\ln Z_1 = 20.0$ (for Z in $\mu\mathrm{s}^{-1}$), there is still very little reaction in the HMX regions. It is the shock temperature reached in the HMX, along with the HMX reaction rate parameters, that determines the rate of reaction in the HMX. These simulations demonstrate that uncertainties in the Arrhenius reaction parameters do not change the conclusion since no detonation was observed to occur within the 1 mm required by the extrapolation of the experimental Pop-plot.

Overall, the calculations in this section have demonstrated that the uncertainties in the material properties do not affect the conclusion of this chapter, that shock heating of crystals and binder is not a feasible hotspot mechanism in the HMX-based explosives PBX9501 and EDC37.

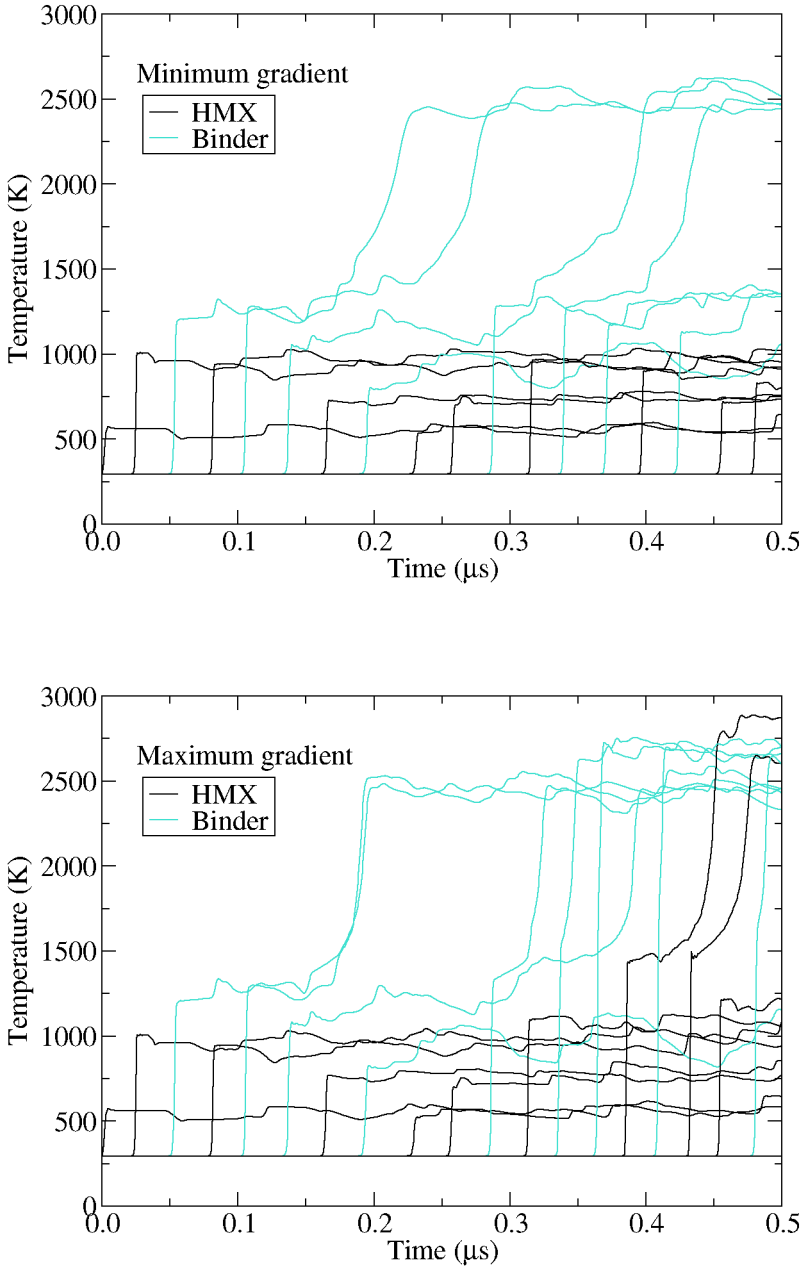

Figure 5.20: Temperature histories for alternating HMX and binder calculations of EDC37, to investigate the effect of the uncertainty in Arrhenius parameters. Values used were $E_1 = 140\,\mathrm{kJ/mol}$ and $\ln Z_1 = 11.6$ for HMX and $\ln Z_1 = 12.4$ for binder (above), and $E_1 = 160\,\mathrm{kJ/mol}$ and $\ln Z_1 = 13.8$ for HMX and $\ln Z_1 = 14.6$ for binder (below), for Z in $\mu\mathrm{s}^{-1}$.

5.4 Summary

The Peruse hydrocode, with Arrhenius chemistry and heat conduction, has been used to investigate the feasibility of shock heating of crystals and binder as a hotspot mechanism. Multi-region HMX and binder calculations have been performed at a shock pressure of 20 GPa. At this pressure, the experimental Pop-plot can be extrapolated to give an expected run-to-detonation distance of 1 mm and run time of ~0.15 μs. None of the simulations has produced detonation within this length or timescale, and there is no reaction at all in lower pressure simulations, demonstrating that shock heating of crystals and binder is not a feasible hotspot mechanism. It is believed that this is the first time this has been explicitly demonstrated. It has been checked that this conclusion is not dependent on the geometry or meshing used for the simulations, and that reasonable changes to the material properties data do not change the result significantly.

Chapter 6

Critical hotspots and flame propagation

In this chapter, the models constructed for HMX and the binders in PBX9501 and EDC37 will be used to determine critical hotspot criteria and investigate mechanisms for reaction to spread outwards from hotspots. Section 6.1 will describe critical hotspot simulations to examine the behaviour of hotspots in Peruse, to gauge the effect of changes to the initial temperature, geometry and mesh density on the results, and to investigate whether a thin layer of binder can impede or enhance the spread of reaction through HMX. Critical hotspot criteria for HMX and the binders will be compared to results in the literature in section 6.2. Flame propagation data will be used to validate the reaction propagation speed in hotspot simulations. Section 6.3 will describe diamond anvil cell experiments and initial simulations to establish the sensitivity to uncertainties in material properties data. The results from a series of flame propagation simulations in Peruse will be compared to the experimental data in section 6.4 and suggestions will be made for improving the simulations in future. The implications of the observed reactive wave speed for hotspots in PBX9501 and EDC37 will be discussed in section 6.5.

6.1 Critical hotspot calculations

Previous studies of critical hotspots in explosives [24, 25, 26] have modelled hotspots of uniform high temperature, surrounded by cooler regions of uniform lower temperature. This is a simple configuration that allows comparison between different studies and is broadly representative of a variety of hotspot mechanisms, so it will be used through-

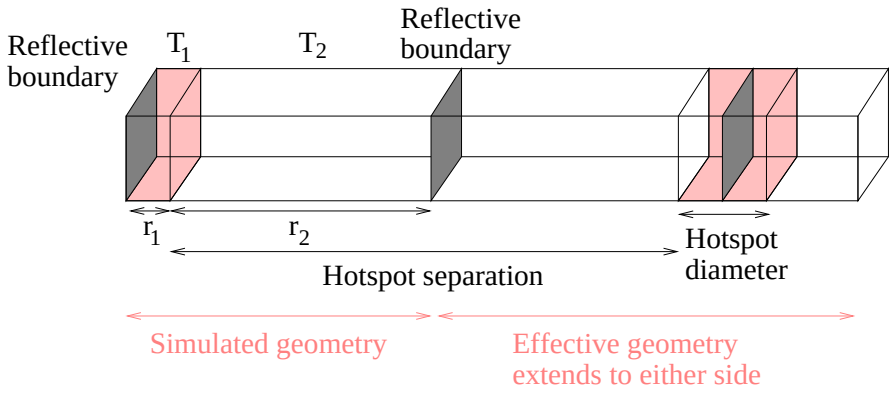

Figure 6.1: Plane geometry used to investigate critical hotspots. The reflective boundary conditions mean that the simulated geometry effectively extends to either side of the computational domain. Physically, an infinite series of planar hotspots are being modelled, with hotspot diameter $2r_1$ and separation $2r_2$.

out this chapter. The computational geometry comprises a hot region of temperature T_1 and thickness r_1, surrounded by a cooler region of temperature T_2 and thickness r_2. In spherical geometry, this corresponds to a hot sphere surrounded by a cool shell. In plane geometry, it represents a line through the microstructure of the explosive perpendicular to a planar hotspot, as sketched in figure 6.1. Reflective boundary conditions are used at each end of the computational domain. It is widely assumed that hotspots in plastic-bonded explosives occupy only a small proportion of the microstructure, so that $r_1 < r_2$. For the initial calculations in this section, geometries with $r_1 \sim r_2$ are used to minimise the computational expense. Peruse is used to solve the Lagrangian reactive-flow equations 2.7 neglecting species diffusion, with material models from chapter 3. Plane geometry is used for the majority of this chapter; the effect of switching between plane, cylindrical and spherical geometry is investigated in section 6.1.6.

The results from an initial calculation with $r_1 = r_2 = 1\,\mu\text{m}$ are shown in figure 6.2. Virtual gauges were positioned at $0.1\,\mu\text{m}$ intervals through the HMX and their temperature histories are shown by the different curves in the top graph. The mesh size was $0.05\,\mu\text{m}$; it will be demonstrated in section 6.1.7 that this is mesh-converged. Initial conditions representative of a post-shock state were imposed on the geometry by specifying the values of specific internal energy and density at the start of the hydrocode calculation. The values in the cooler region were chosen to correspond to a point on the HMX Hugoniot with $T_2 = 1022\,\text{K}$. The hotspot was given the same initial density but elevated specific internal energy, corresponding to a temperature of $T_1 = 1500\,\text{K}$. These states are consistent with constant-volume heating within the hotspot, an assumption that will be

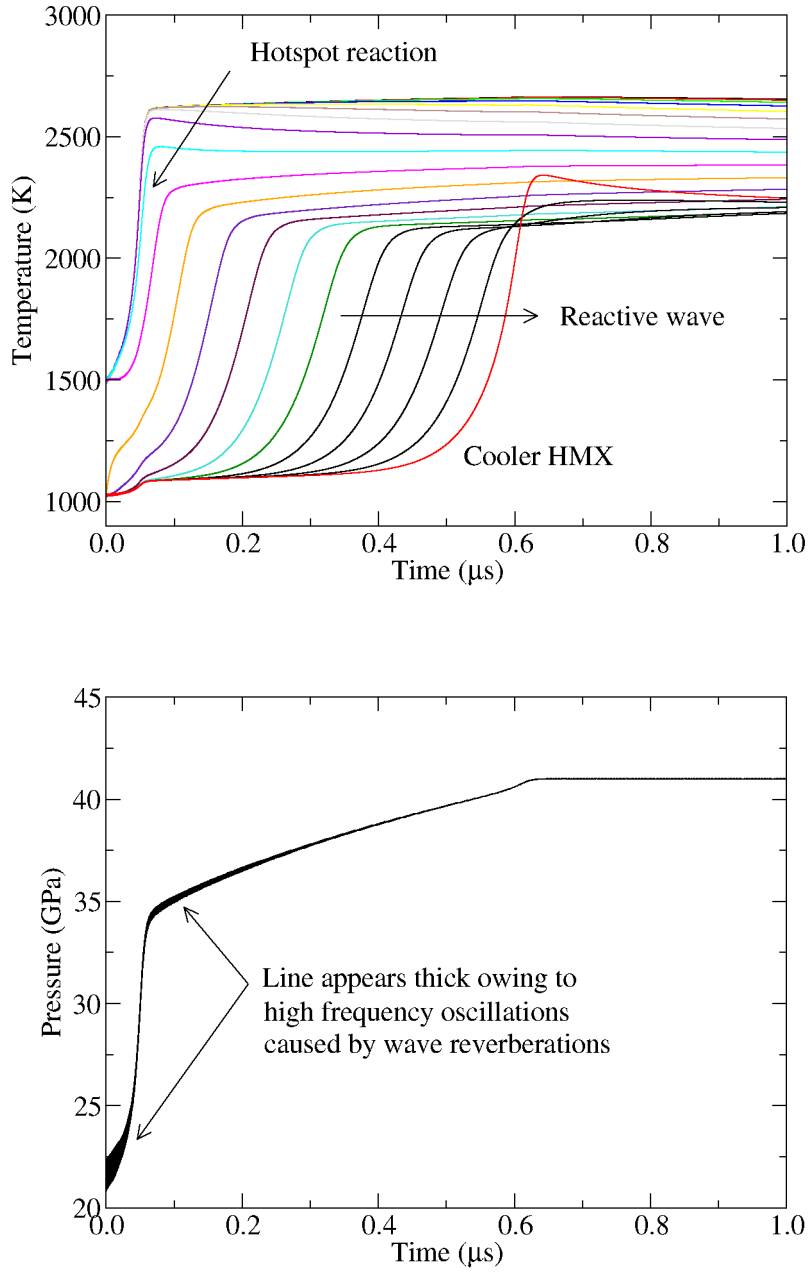

Figure 6.2: Planar HMX hotspot calculation with $r_1 = r_2 = 1\,\mu\text{m}$, $T_1 = 1500\,\text{K}$ and $T_2 = 1022\,\text{K}$, as an example of the typical behaviour of hotspot simulations in Peruse. Temperature histories from gauges positioned at 0.1 μm intervals through the geometry are shown above, with a pressure trace below.

tested in section 6.1.5.

As shown by figure 6.2, the first computational zones to react are those within the hotspot. These start at temperature $T_1 = 1500\,\mathrm{K}$ and react to completion in $\sim 0.05\,\mu\mathrm{s}$, as determined by the Arrhenius reaction delay time [179]. As these zones react, their temperature rises dramatically causing a reactive wave to propagate outwards into the cooler HMX surrounding the hotspot until, by $\sim 0.6\,\mu\mathrm{s}$, all the HMX has reacted. The wave propagation speed can be calculated by examining the time at which each gauge rises above a given temperature. The wave speed of $\sim 1\,\mathrm{m/s}$ will be discussed in more detail below. There is a small temperature rise in the cooler HMX when the hotspot reacts, caused by a general pressurisation of the system to 35 GPa when the hotspot converts from solid unreacted explosive to gaseous reaction products. The pressure plot shows that the system continues to pressurise as the reactive wave spreads from the hotspot into the cooler HMX. Only one pressure history is shown in figure 6.2 because the traces from all the different gauges overlay each other. This is because the computational domain is so small (only $2\,\mu\mathrm{m}$ in extent) that the wave reverberation time is very short ($< 1\,\mathrm{ns}$) and approximate pressure equilibrium is maintained at all times.

The reactive wave is driven by heat conduction, as will be demonstrated by comparing the calculation with normal thermal conductivity (figure 6.2) to one with reduced thermal conductivity. Figure 6.3 shows the results of a simulation where the thermal conductivity k of HMX was reduced by a factor of 10. In both calculations, the hotspot reacts promptly and there is a small temperature rise in the cooler HMX as the system pressurises. However, the propagation speed of the reactive wave into the cooler HMX is significantly lower in the calculation with reduced k, indicating that the reactive wave is driven by heat conduction. It has been suggested that a hydrodynamic mechanism might contribute to the reactive wave [53]; shocks generated by exploding hotspots would heat the cooler surrounding explosive, enhancing its reaction rate. However, this effect is not observed in figure 6.2 because the wave-reverberation time is much quicker than the hotspot reaction time as will be discussed below.

To investigate whether different behaviour would be produced if the hotspot reacted more quickly, or if the wave reverberation time were longer, two more calculations were run. Figure 6.4 shows results for the first 2 ns of the simulations. In both calculations, the hotspot temperature $T_1 = 5000\,\mathrm{K}$ is considerably higher than is likely to be achieved in a real explosive microstructure. It was chosen to yield rapid reaction; the burn fraction plot in figure 6.4 shows that 50 % reaction is achieved within $\sim 0.1\,\mathrm{ns}$ in the hotspot. The

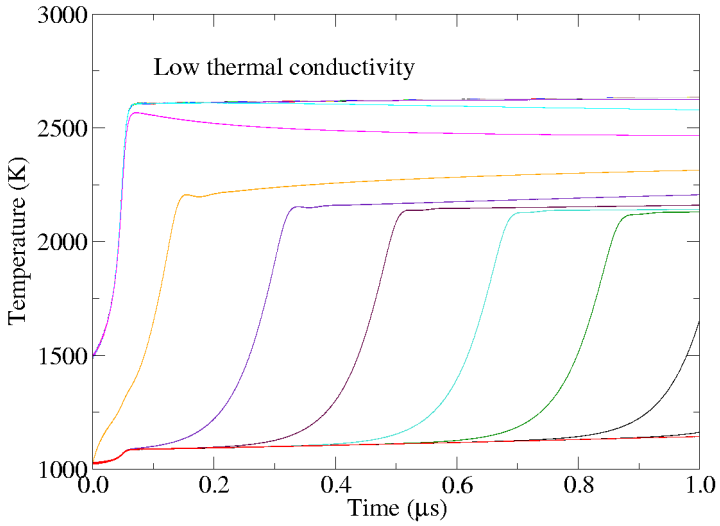

Figure 6.3: Planar HMX hotspot calculation with $r_1 = r_2 = 1\,\mu\text{m}$, $T_1 = 1500\,\text{K}$ and $T_2 = 1022\,\text{K}$ as in figure 6.2, but with the thermal conductivity k of HMX reduced by a factor of 10, to demonstrate that the reactive wave is driven by heat conduction.

pressure and temperature traces in figure 6.4 show that the rapid reaction in the hotspot drives a pressure wave through the cooler surrounding HMX. For the blue traces, the computational domain is so small that the wave is reflected from the boundary before reaction has completed. The black traces correspond to a longer computational domain, and demonstrate that reaction in the hotspot causes a ~60 K jump in the temperature of the surrounding cooler HMX. However, this temperature jump is insufficient to cause any significant reaction over μs timescales and no reaction is observed in the burn fraction plot outside the hotspot. This indicates that a hydrodynamic mechanism of reaction spreading does not occur in these simulations.

The following observations can be made from the initial simulations:

- A wave driven by heat conduction is the only mechanism by which reaction spreads from a hotspot into the surrounding cooler material.
- If the hotspot is so hot that it reacts almost instantaneously, a shock can be driven into the surroundings, but it is only responsible for a ~60 K rise in temperature (which doubles to ~120 K when the wave is reflected from the boundary). This is insufficient to cause significant chemical reaction in the cool HMX over μs timescales.

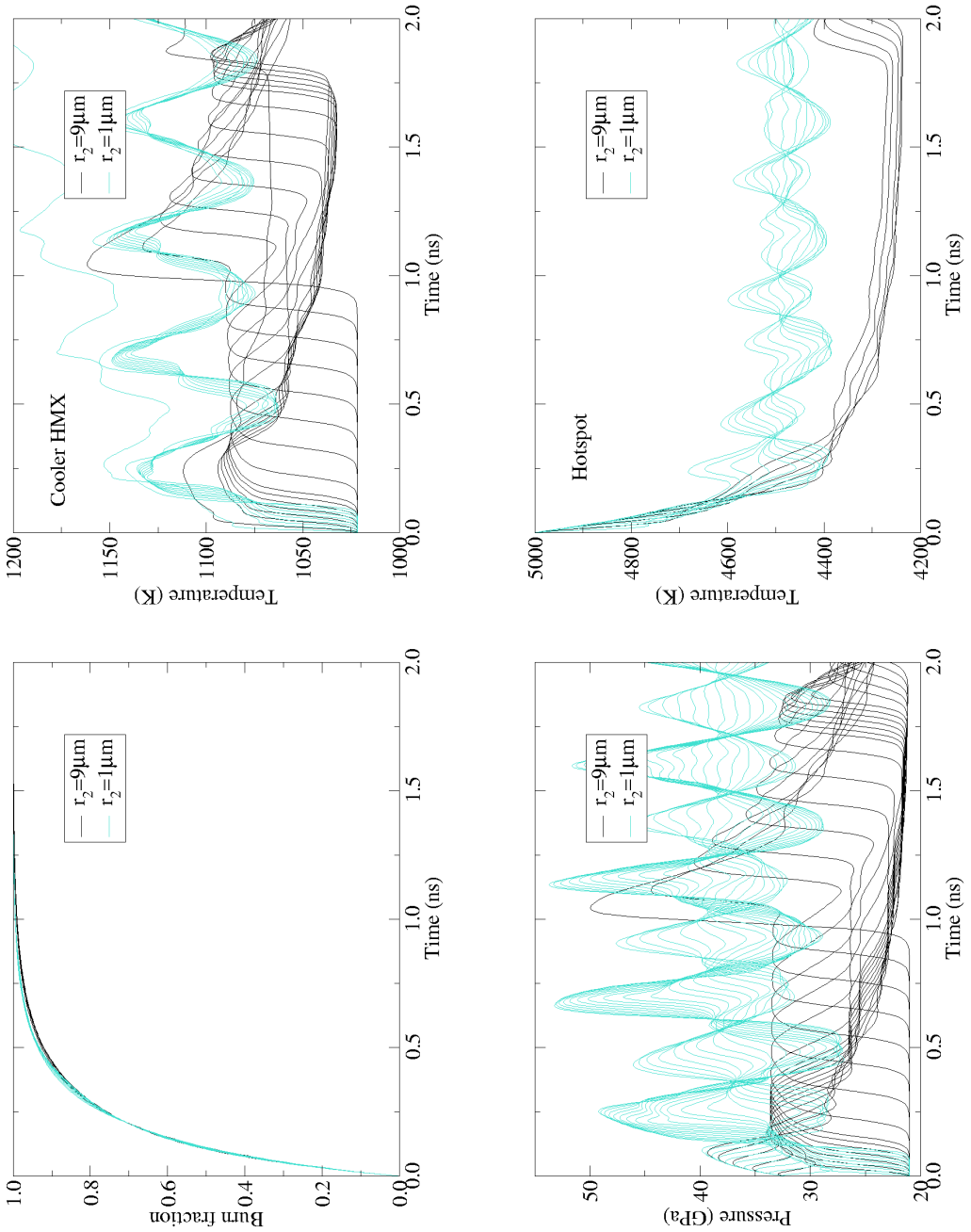

Figure 6.4: HMX hotspot calculations with $T_1 = 5000\,\mathrm{K}$, $T_2 = 1022\,\mathrm{K}$ and $r_1 = 1\,\mu\mathrm{m}$. The cooler explosive has thickness $r_2 = 1\,\mu\mathrm{m}$ for the blue traces and $r_2 = 9\,\mu\mathrm{m}$ for the black traces. This configuration was designed to investigate whether hotspot simulations would behave differently if the hotspot reacted more quickly, or if the wave reverberation time were longer, than in typical simulations.

- If the hotspot has a more realistic initial temperature, it reacts relatively slowly. Although a compression wave propagates into the cooler surroundings, this leads to only a small rise in temperature.
- In most cases, the wave reverberation time is so small that approximate pressure equilibrium is maintained throughout the computational domain.

The following sections will investigate the effects of hotspot temperature, background temperature, hotspot size, background size, initial conditions, geometry and mesh density on the results of hotspot simulations in Peruse. Material properties for HMX and the binders in PBX9501 and EDC37 are taken directly from chapter 3. Uncertainties on the data are not considered, since the aim of this section is to establish how the baseline models perform.

6.1.1 Effect of hotspot temperature

To investigate the effect of varying the hotspot temperature T_1, four Peruse simulations were run with $r_1 = r_2 = 1\,\mu\text{m}$, $T_1 = 1000$, 1200, 1400 or 1600 K and $T_2 = 1000\,\text{K}$. Figure 6.5 shows that there is very little reaction over a 1 µs timescale for HMX at 1000 K. As the hotspot temperature T_1 is increased to 1200 K, it is hot enough that significant reaction can proceed. At higher temperatures, the hotspot reacts sooner but the reactive wave speed is constant $\sim 1.6\,\text{m/s}$ for all four simulations. The "explosion time" of the first black gauge (positioned at the centre of the hotspot) can be determined from the steep temperature rise in figure 6.5. This is compared to predictions using the Hubbard & Johnson delay-time equation 3.5 in table 6.1. The simulated explosion time is roughly three times the predicted time, due to the effects of hydrodynamics and the equation of state treatment in Peruse. In contrast, a ReactDiff simulation with $T_1 = 1200\,\text{K}$ has an explosion time of $\sim 0.2\,\mu\text{s}$, much closer to the Hubbard & Johnson predictions. This is

T_1(K)	1000	1200	1400	1600
t^{exp}(µs)	>1	0.47	0.085	0.022
t^{HJ}(µs)	2.4	0.17	0.028	0.0073

Table 6.1: Time to explosion t^{exp} from Peruse simulations (with $r_1 = r_2 = 1\,\mu\text{m}$, $T_2 = 1000\,\text{K}$ and hotspot temperature T_1) compared to predicted explosion times t^{HJ} using the Hubbard & Johnson delay-time equation [179]. The difference in explosion times illustrates the importance of hydrodynamics on hotspot simulations.

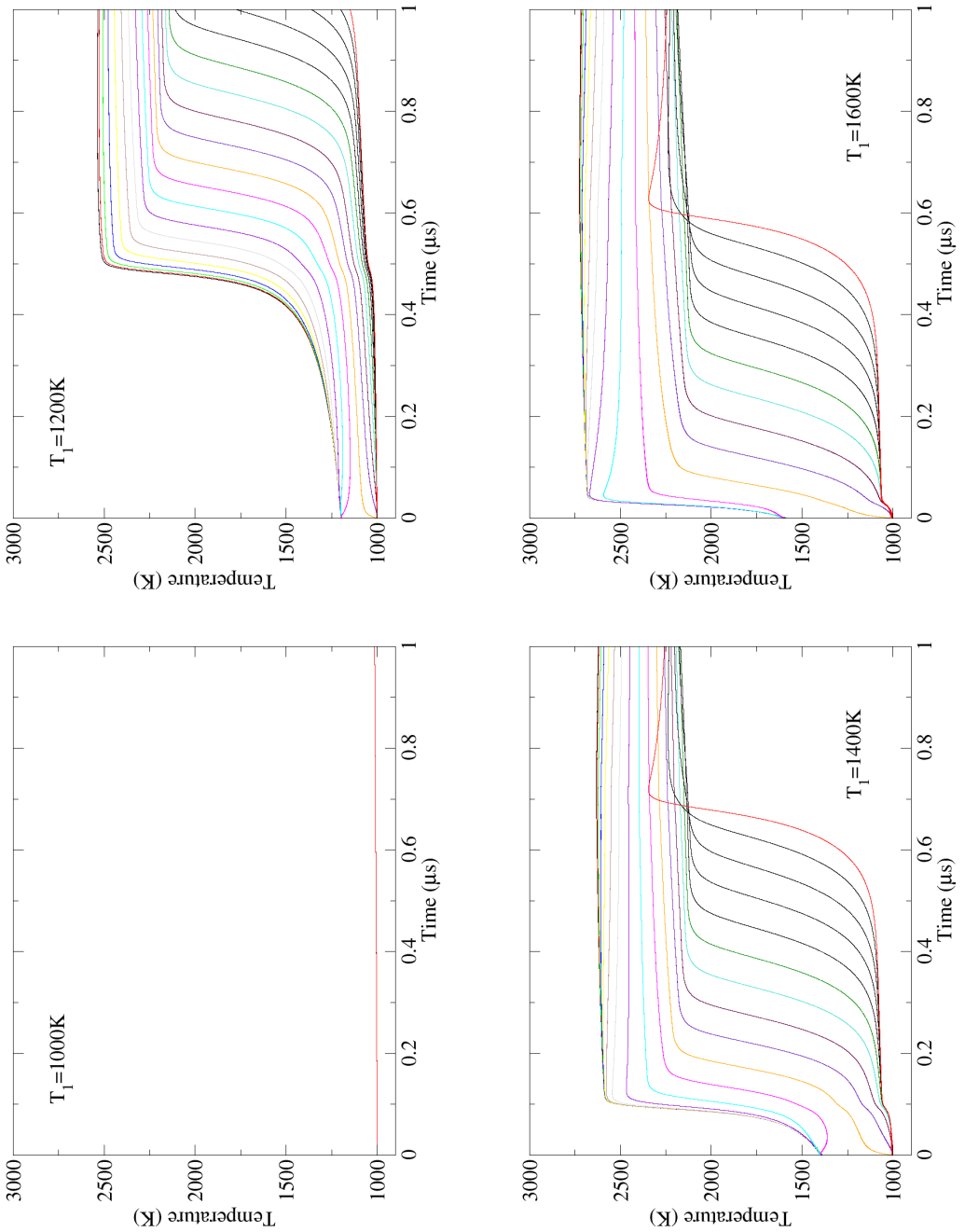

Figure 6.5: Planar HMX hotspot calculations with $r_1 = r_2 = 1\,\mu\text{m}$ and $T_2 = 1000\,\text{K}$, but with varying $T_1 = 1000$, 1200, 1400 or 1600 K to illustrate the effect of changing the hotspot temperature on the Peruse simulations.

because ReactDiff is a thermal conduction and Arrhenius chemistry code only, and does not model the equation of state response of the HMX. Table 6.1 illustrates the importance of including hydrodynamic effects in hotspot simulations, since the results will be significantly different to those from static calculations.

6.1.2 Effect of background temperature

The effect of background temperature T_2 was investigated using a series of Peruse calculations with $r_1 = r_2 = 1\,\mu\text{m}$, $T_1 = 1200\,\text{K}$ and $T_2 = 1100$, 1000, 900 or 800 K. The results are shown in figure 6.6. Reducing the background temperature T_2 has very little effect on the temperature histories near the centre of the hotspot (the first black and red gauges), where the time to explosion is 0.47 µs. This is because these zones are not greatly influenced by heat conduction into the cooler background HMX over these timescales. The most obvious effect of the reduction in T_2 is that the reactive wave propagates into the cooler HMX at a lower speed. The reactive wave speed is $\sim 3\,\text{m/s}$ for $T_2 = 1100\,\text{K}$ and $\sim 1\,\text{m/s}$ for $T_2 = 800\,\text{K}$, and it will be even slower for the lower temperatures more typical of shock initiation experiments (see chapter 7 for temperature distributions in shocked PBX9501 and EDC37).

6.1.3 Effect of hotspot size

The effect of hotspot size r_1 was investigated using a series of calculations with $r_1 = 1$, 0.5 or 0.25 µm, $r_2 = 1\,\mu\text{m}$, $T_1 = 1200\,\text{K}$ and $T_2 = 1000\,\text{K}$. The results in figure 6.7 show that the explosion time increases as r_1 is reduced, because heat conduction exerts a greater influence and reduces the temperature of the hotspot, thereby increasing its time to explosion. For the smallest hotspots, heat conduction has so great an effect that they do not react significantly within the 1 µs duration of the simulation. These are sub-critical hotspots. The minimum size r_1 that allows the hotspot to react within 1 µs and propagate a reactive wave into the cooler surrounding material is defined as the "critical hotspot size" in this work. In this case, figure 6.7 shows that the critical hotspot size is between 0.25 and 0.5 µm, and the results of additional calculations narrow the range to between 0.3 and 0.4 µm. In general, the critical hotspot size depends on the hotspot temperature T_1 and the background temperature T_2. Critical hotspot results will be presented in section 6.2.

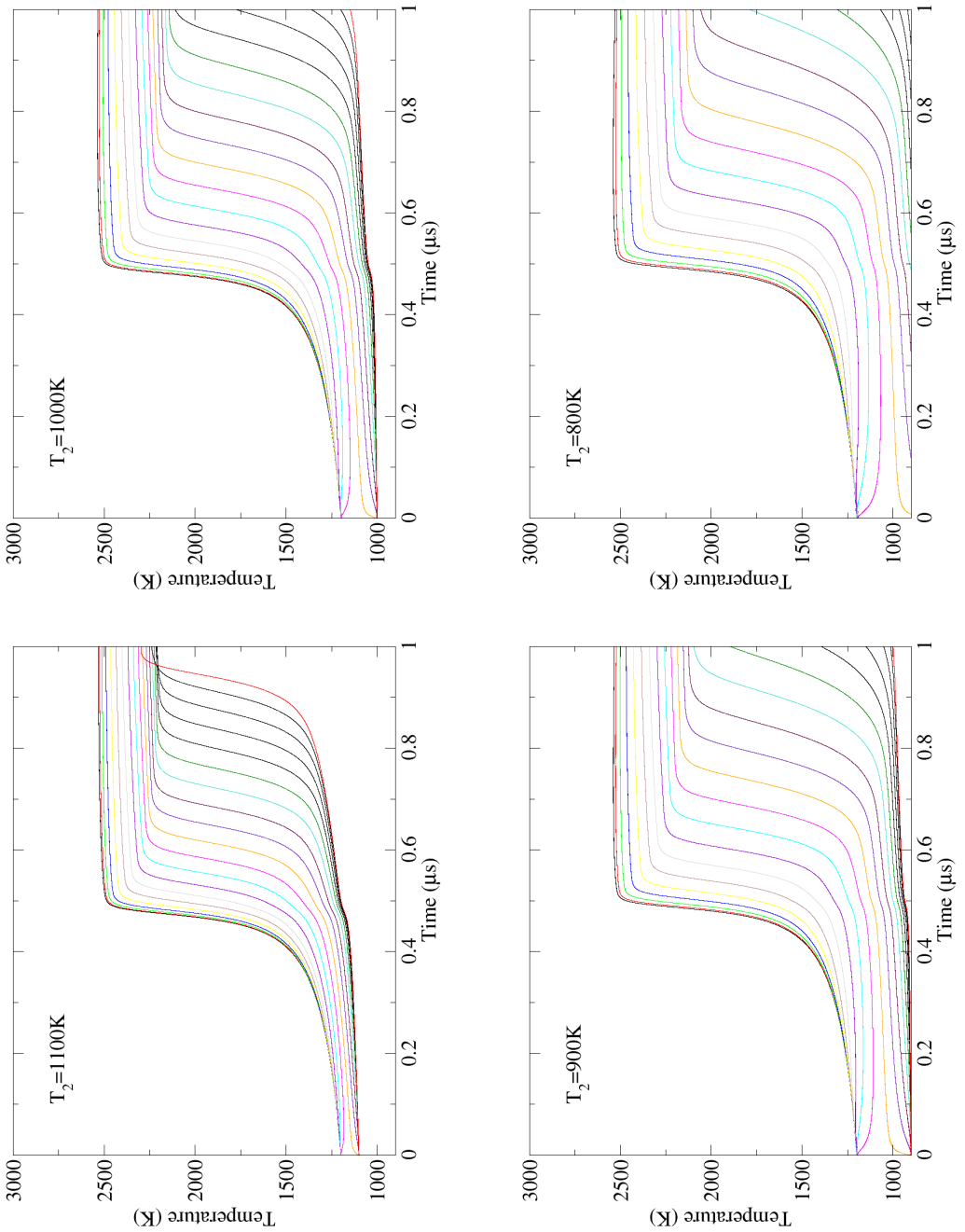

Figure 6.6: Planar HMX hotspot calculations with $r_1 = r_2 = 1\,\mu\text{m}$ and $T_1 = 1200\,\text{K}$, but with varying $T_2 = 1100$, 1000, 900 or 800 K to illustrate the effect of changing the background temperature on the Peruse simulations.

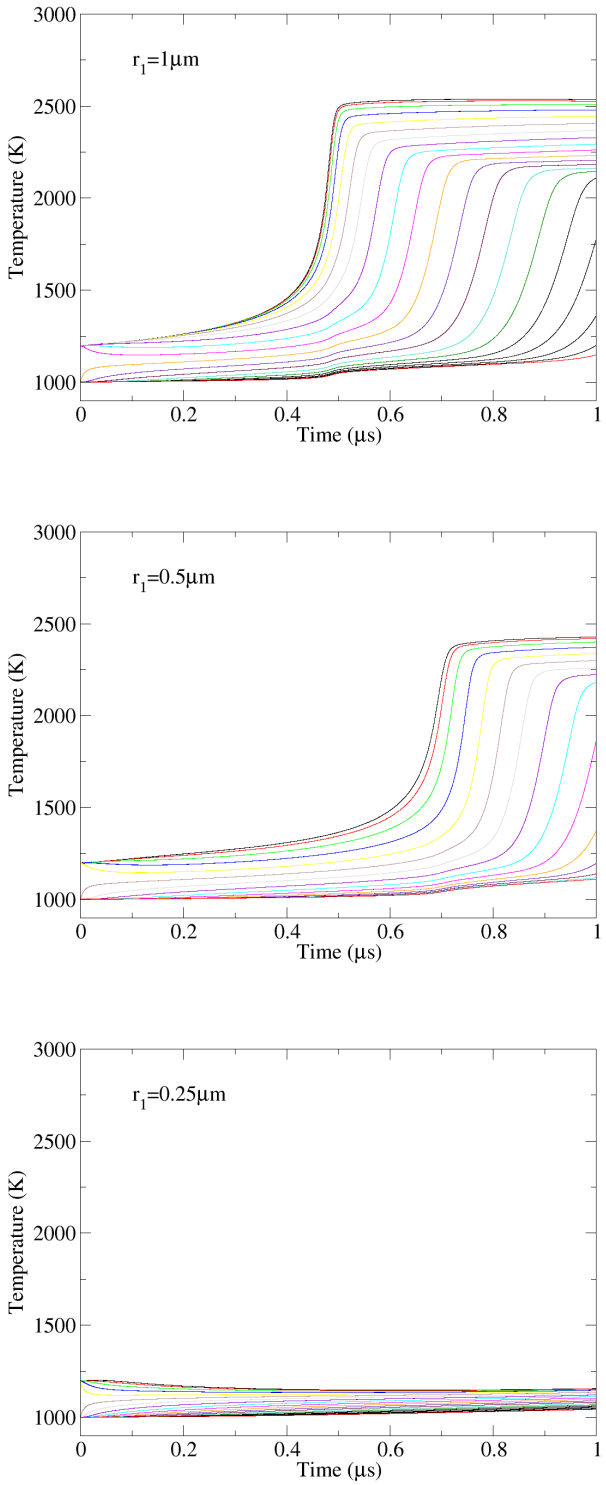

Figure 6.7: Planar HMX hotspot calculations with $r_2 = 1\,\mu m$, $T_1 = 1200\,K$ and $T_2 = 1000\,K$, but with varying $r_1 = 1$, 0.5 or $0.25\,\mu m$ to illustrate the effect of changing the hotspot size on the Peruse simulations. Since the simulation with $r_1 = 0.5\,\mu m$ reacts within $1\,\mu s$, but the $0.25\,\mu m$ calculation does not react, the critical hotspot size is between 0.5 and $0.25\,\mu m$.

6.1.4 Effect of background size

To investigate the effect of the size r_2 of the cooler background HMX, three calculations were run with $r_1 = 0.5\,\mu\text{m}$, $r_2 = 1.0$, 0.5 or $0.2\,\mu\text{m}$, $T_1 = 1200\,\text{K}$ and $T_2 = 1000\,\text{K}$. Although $r_2 > r_1$ in plastic-bonded explosives, a configuration with $r_2 < r_1$ is used here to emphasize the effect. The gauge colours are consistent between the different calculations, although there is a different total number of zones in each case. The results in figure 6.8 show that the time to explosion at the centre of the hotspot (black gauge) is not greatly affected by the reduction in r_2. However, the reactive wave spreads from the hotspot into the background explosive more quickly as r_2 is reduced. This is due to two effects: firstly, as r_2 is reduced, there is a smaller heat sink to absorb the heat from the hotspot and so the temperature at the edge of the hotspot is not so greatly reduced by heat conduction, and secondly the background heats up more quickly. In a geometry which is below the critical radius r_1, it might be expected that the hotspot would become viable again if r_2 were reduced so heat conduction into the background HMX was less significant. The two calculations in figure 6.9 show that this is not the case. In fact, the size of the background HMX has little effect on the critical hotspot size.

6.1.5 Effect of initial conditions

The initial density and specific internal energy of each region in the Peruse simulations are chosen to provide an appropriate pressure and temperature at the start of the calculation. For the majority of the simulations described in this chapter, the assumption of constant volume heating is used to select the initial conditions. For example, for a calculation with $T_1 = 1200\,\text{K}$ and $T_2 = 1000\,\text{K}$, the background state is chosen to lie on the HMX Hugoniot and the hotspot is given the same initial density $\rho_1 = \rho_2$ but with e_1 adjusted to give $T_1 = 1200\,\text{K}$. This means that different initial pressures are produced in the two regions. To investigate whether this assumption is important, an additional simulation was run with the same background state but with hotspot ρ_1 and e_1 chosen to give pressure equilibrium $p_1 = p_2$. The initial states of both calculations are listed in table 6.2. The results in figure 6.10 show that there is little difference between the two simulations. This demonstrates that the choice of initial density and specific internal energy state (at constant temperature) is not very important in determining the results of critical hotspot simulations.

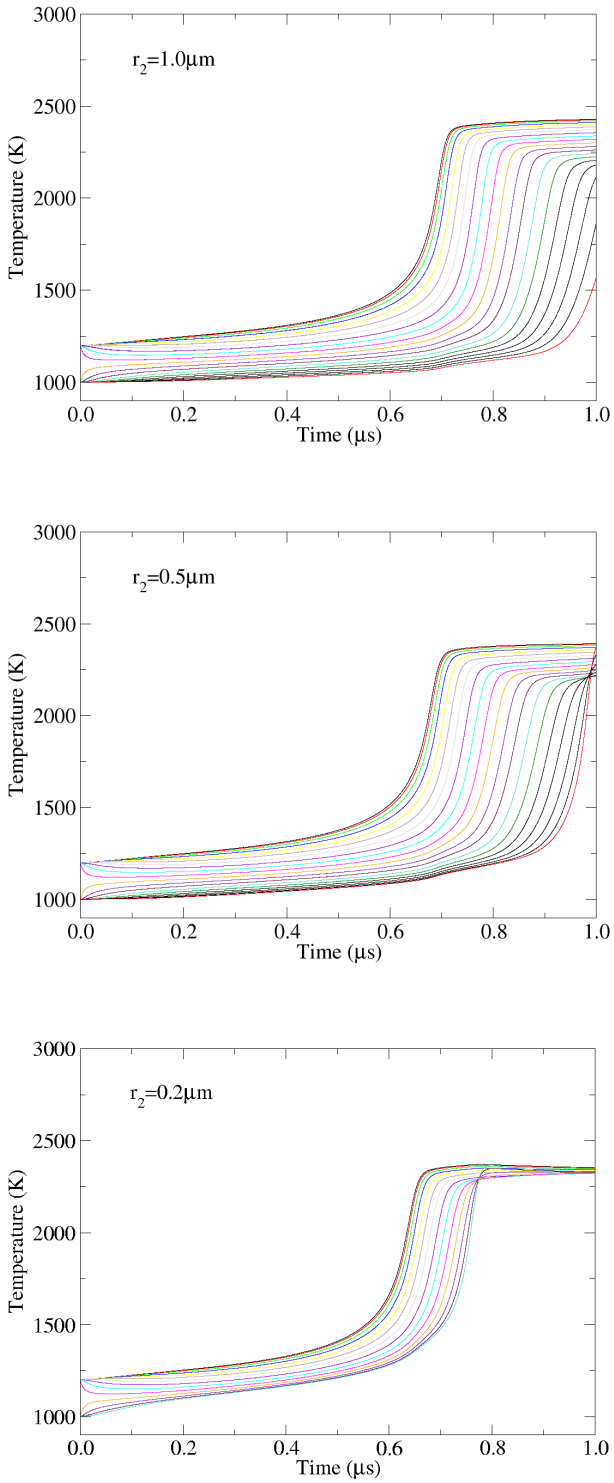

Figure 6.8: Planar HMX hotspot calculations with $r_1 = 0.5\,\mu m$, $T_1 = 1200\,K$ and $T_2 = 1000\,K$, but with varying $r_2 = 1.0$, 0.5 or $0.2\,\mu m$ to illustrate the effect of changing the background size on the Peruse simulations.

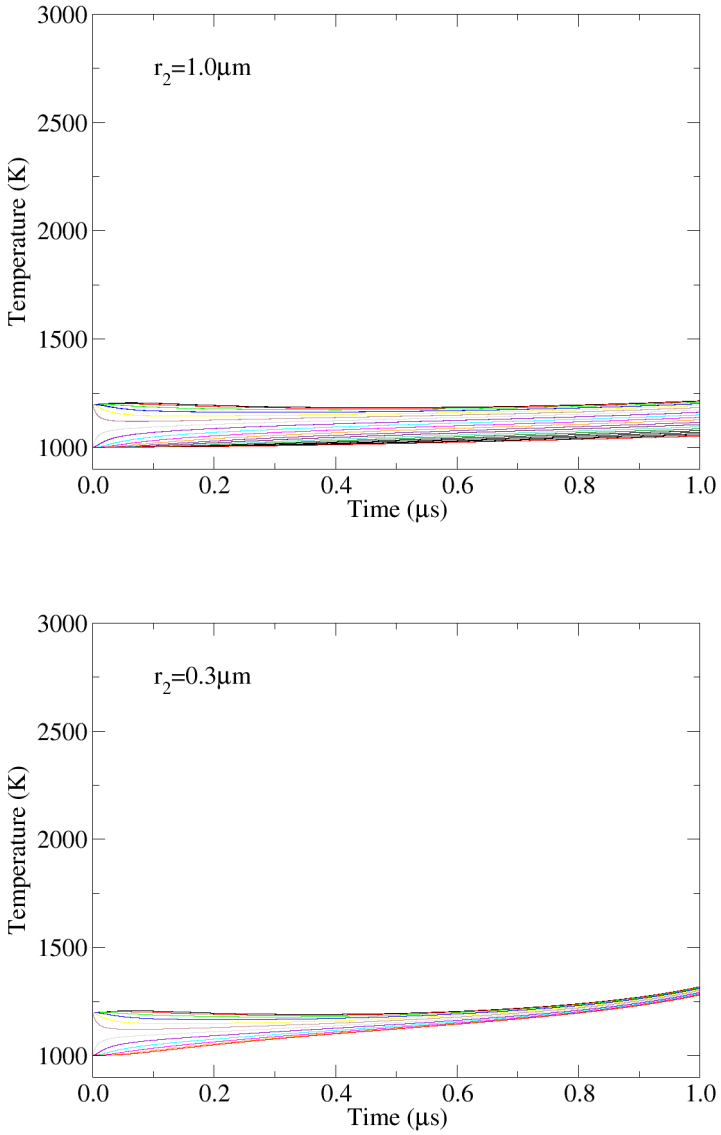

Figure 6.9: Planar HMX hotspot calculations with $r_1 = 0.3\,\mu m$, $T_1 = 1200\,K$ and $T_2 = 1000\,K$, but with varying $r_2 = 1.0$ or $0.3\,\mu m$ to demonstrate that the background size has little effect on the critical hotspot size.

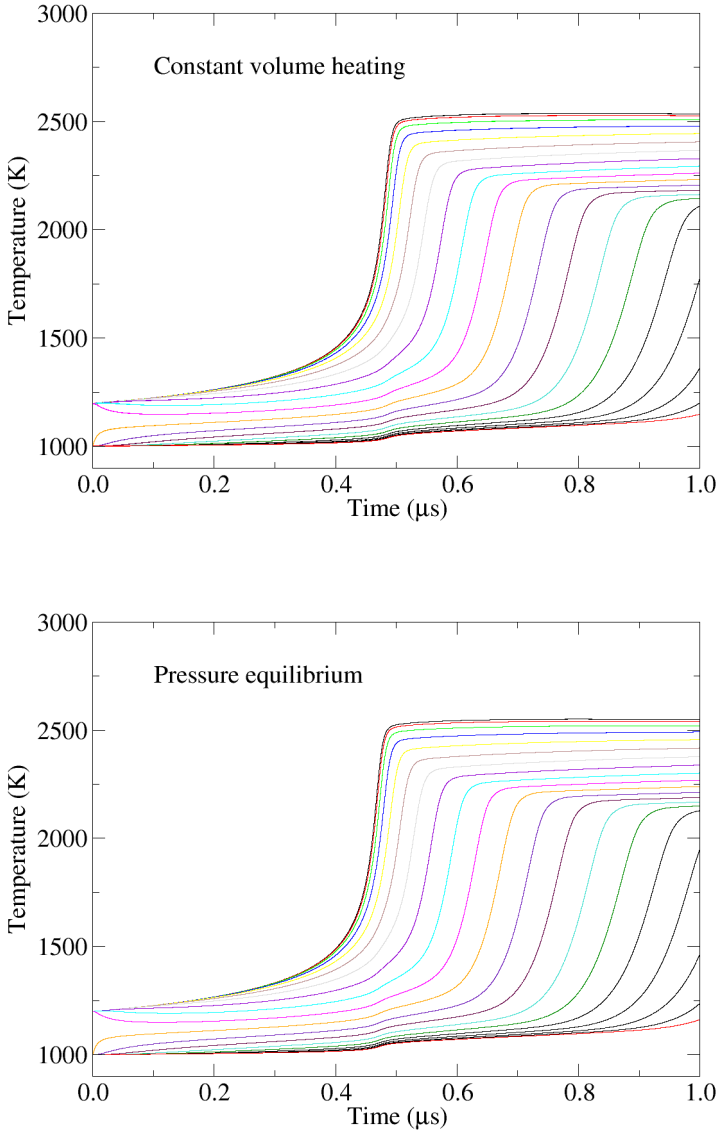

Figure 6.10: Planar HMX hotspot calculations with $r_1 = r_2 = 1\,\mu\text{m}$, $T_1 = 1200\,\text{K}$ and $T_2 = 1000\,\text{K}$, demonstrating that the assumption of constant volume heating or of pressure equilibrium for generating the initial conditions makes little difference to hotspot simulations.

Simulation	Constant volume heating		Pressure equilibrium	
Region	1	2	1	2
T (K)	1200	1000	1200	1000
p (GPa)	21.134	20.565	20.565	20.565
ρ (g/cm^3)	2.5749	2.5749	2.5661	2.5749
e (kJ/g)	1.6643	1.4443	1.6409	1.4443

Table 6.2: Initial states of the hotspot region 1 and the background region 2 in Peruse simulations to investigate the effect of changing the initial conditions. Results are shown in figure 6.10.

6.1.6 Effect of geometry

Most of the simulations described in this chapter are in plane geometry. To investigate the effect of switching to cylindrical or spherical geometry, with reflective boundary conditions, three simulations were run with $r_1 = r_2 = 1\,\mu\text{m}$, $T_1 = 1200\,\text{K}$ and $T_2 = 1000\,\text{K}$. The results in figure 6.11 show that the explosion time at the centre of the hotspot increases slightly with the increased divergence associated with moving from plane to cylindrical to spherical geometry. This is because the temperature of a spherical hotspot surrounded by a cool shell falls more rapidly than a planar hotspot in contact with a cool plane. There is little change to the speed at which the reactive wave propagates away from the hotspot. Overall, figure 6.11 shows that changing the geometry does not alter the character of hotspot simulations. However, it can influence the size of critical hotspots. For example, for a hotspot with $T_1 = 1200\,\text{K}$ and background $T_2 = 1000\,\text{K}$, the critical radius lies between 0.8 and 0.9 μm in spherical geometry, compared to 0.3–0.4 μm in plane geometry and in agreement with figure 5 in reference 24. This is consistent with the factor of 2.20 difference between spherical and planar critical hotspot radii, determined from a numerical solution of the chemistry and heat conduction equations 2.9 and 2.11 without hydrodynamics [23].

6.1.7 Effect of mesh density

The critical hotspot simulations in this section use 0.05 μm meshing. To check that the results are mesh-converged, three calculations were run with 0.1 μm, 0.05 μm or 0.025 μm meshing. The colours in figure 6.12 correspond to similar locations, even though the number of zones is different in each simulation. The temperature overshoots in the 0.1 μm simulation indicate that this is not quite mesh-converged, and these overshoots are not

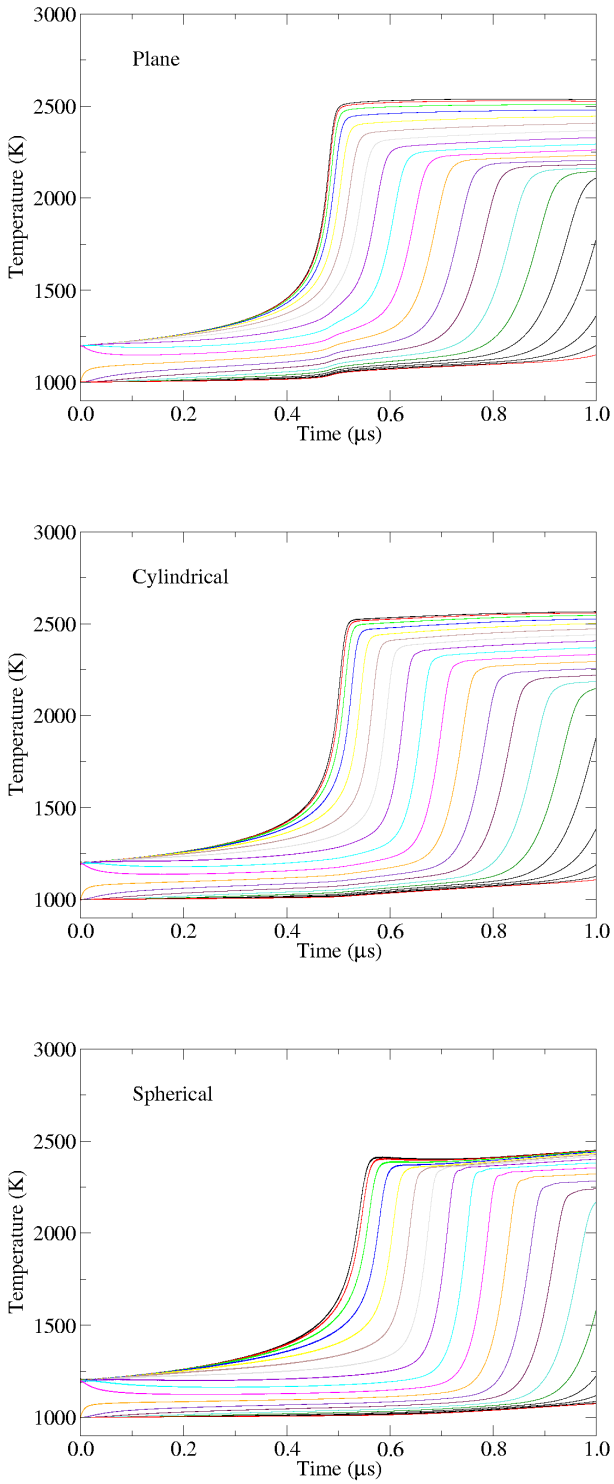

Figure 6.11: HMX hotspot calculations with $r_1 = r_2 = 1\,\mu\text{m}$, $T_1 = 1200\,\text{K}$ and $T_2 = 1000\,\text{K}$ in plane, cylindrical or spherical geometry, to demonstrate that changing the geometry does not alter the character of hotspot simulations.

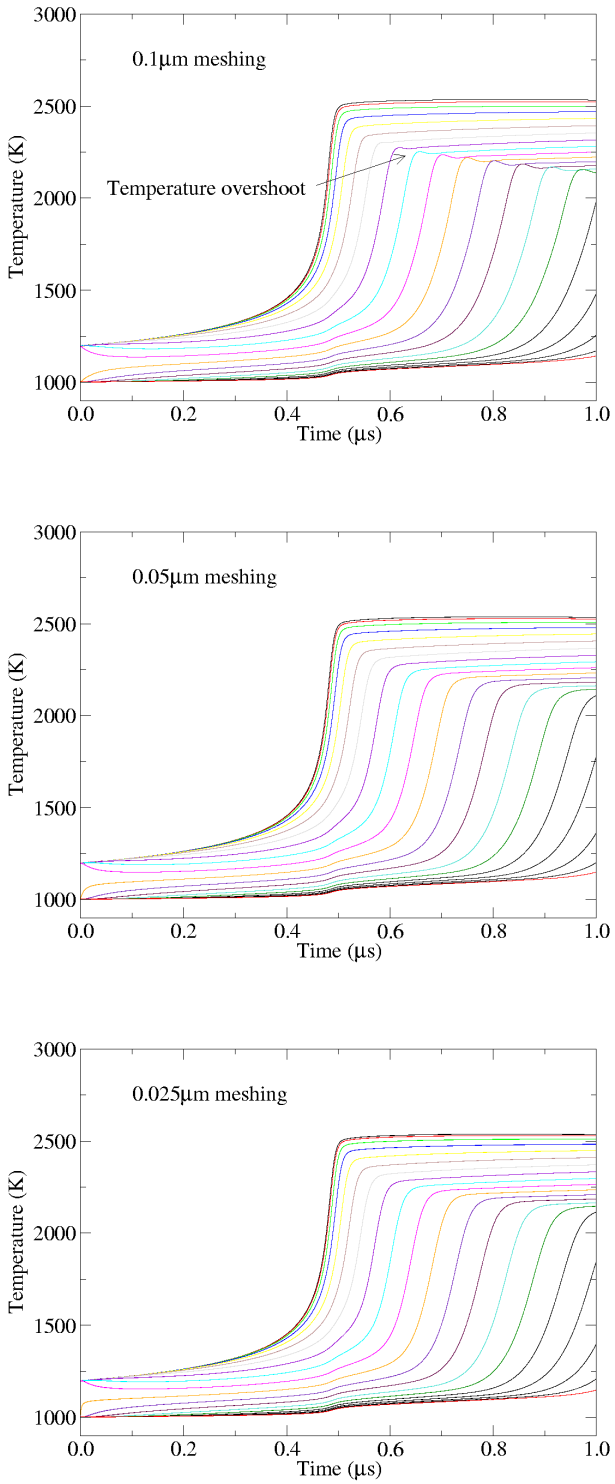

Figure 6.12: Planar HMX hotspot calculations with $r_1 = r_2 = 1\,\mu\text{m}$, $T_1 = 1200\,\text{K}$ and $T_2 = 1000\,\text{K}$, but with 0.1, 0.05 or 0.025 μm meshing. The temperature overshoots indicate that the 0.1 μm calculation is not mesh-converged. The close agreement between the 0.05 and 0.025 μm results demonstrates that the 0.05 μm meshing used for the majority of simulations in this chapter is converged.

present at 0.05 μm. Close examination shows that 0.05 μm and 0.025 μm meshing produce almost identical temperature histories; in particular the time to explosion and reactive wave propagation velocity is unchanged. This initial study demonstrates that 0.05 μm meshing is adequate for critical hotspot simulations.

6.1.8 Propagation through binder layers

The microstructures of PBX9501 and EDC37 contain crystals of HMX separated by a thin binder layer. To investigate whether a layer of binder could impede or enhance the spread of reaction through HMX, several simulations were run using the geometry in figure 6.13. The hotspot temperature $T_1 = 1600\,\mathrm{K}$ ensures quick reaction and $r_1 = 0.5\,\mu\mathrm{m}$ is well above the critical hotspot size at this temperature. The background regions each have thickness $r_2 = r_3 = r_4 = 1\,\mu\mathrm{m}$ which is approximately the distance over which the reactive wave can propagate in 1 μs. Initial temperatures in the background regions 2 to 4 were chosen to be broadly representative of microstructural calculations at 20 GPa input pressure (see chapter 7). For EDC37 $T_2 = T_4 = 1000\,\mathrm{K}$ and $T_3 = 1300\,\mathrm{K}$ and for PBX9501 $T_2 = T_4 = 1000\,\mathrm{K}$ and $T_3 = 1150\,\mathrm{K}$. Initial density and specific internal energy states were selected to give approximate pressure equilibrium ($p_2 = p_3 = p_4 \simeq 20\,\mathrm{GPa}$) between HMX and binder layers, to prevent significant changes to the temperatures at the start of the calculation when pressure waves act to bring the system to pressure equilibrium.

Results from two EDC37 calculations are shown in figure 6.14. For reactive binder, the binder reacts over approximately the same timescale as the HMX hotspot. Reactive waves propagate into the cooler HMX background regions in both directions from the HMX hotspot and from the binder, so that reaction has completed within 0.7 μs through

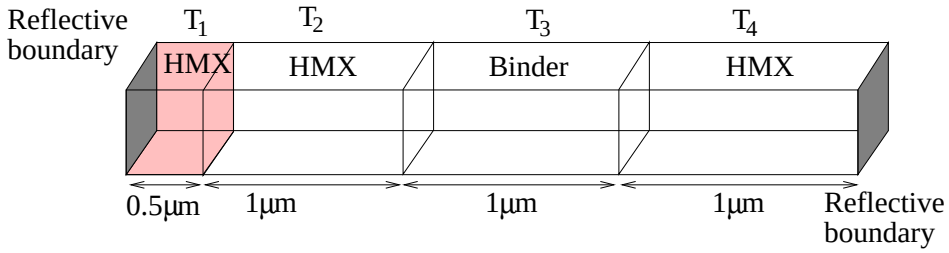

Figure 6.13: Planar geometry used to investigate the propagation of a reactive wave through a binder layer. Results are shown in figure 6.14 for EDC37 and figure 6.15 for PBX9501.

the whole geometry. This would seem to imply that binder regions can act as seeds for reaction, in addition to HMX hotspots. As discussed in section 3.4, binder reaction rates are poorly known and it is possible that the binder in EDC37 could be considerably less reactive than has been assumed. A worst case simulation with inert binder shows that reaction completes in the HMX region within ~1.7 μs, because the binder is sufficiently hot for heat conduction to initiate reaction in the cooler HMX region 4. Overall, these two simulations suggest that the presence of a binder layer does not impede the spread of reaction in EDC37, and may enhance it.

Similar results for PBX9501 are shown in figure 6.15. Again, a reactive binder has sufficient time to react independently, before the reactive wave from the HMX hotspot has reached it. Reaction spreads both forwards and backwards through the geometry from the hotspot and binder layers. For inert binder, the binder temperature is somewhat lower than for EDC37 and is insufficient to initiate reaction in the cooler HMX region 4. For PBX9501, it seems as though an inert binder layer would impede the spread of reaction from one HMX crystal to another.

Each of the four calculations in figures 6.14 and 6.15 have HMX background temperatures of $T_2 = T_4 = 1000$ K, with higher binder temperatures. While broadly representative of the temperatures generated by a 20 GPa input shock, these are considerably higher than typical shock initiation experiments. For a 9.4 GPa input shock (a high pressure for the shock initiation regime), simulations described in section 7.3 show that the mean HMX and binder temperatures are ~500 K and ~700 K respectively for EDC37, and ~550 K and ~640 K for PBX9501. At these temperatures, the binder will not react significantly before the arrival of the reactive wave from the hotspot. This implies that the presence of a binder layer will not significantly enhance the spread of reaction from hotspots in HMX. However, provided the binder layer is not inert, it should not impede the spread of reaction either. In contrast, the low HMX temperatures mean that HMX crystals will hinder the spread of reaction outwards from hotspots in binder regions.

6.2 Critical hotspot results

In section 6.1.3, it was shown that there is a critical hotspot size below which heat conduction has so great an effect that the hotspot does not react significantly within 1 μs. This timescale is based on a 10 μs upper limit for chemical reactions to contribute to shock

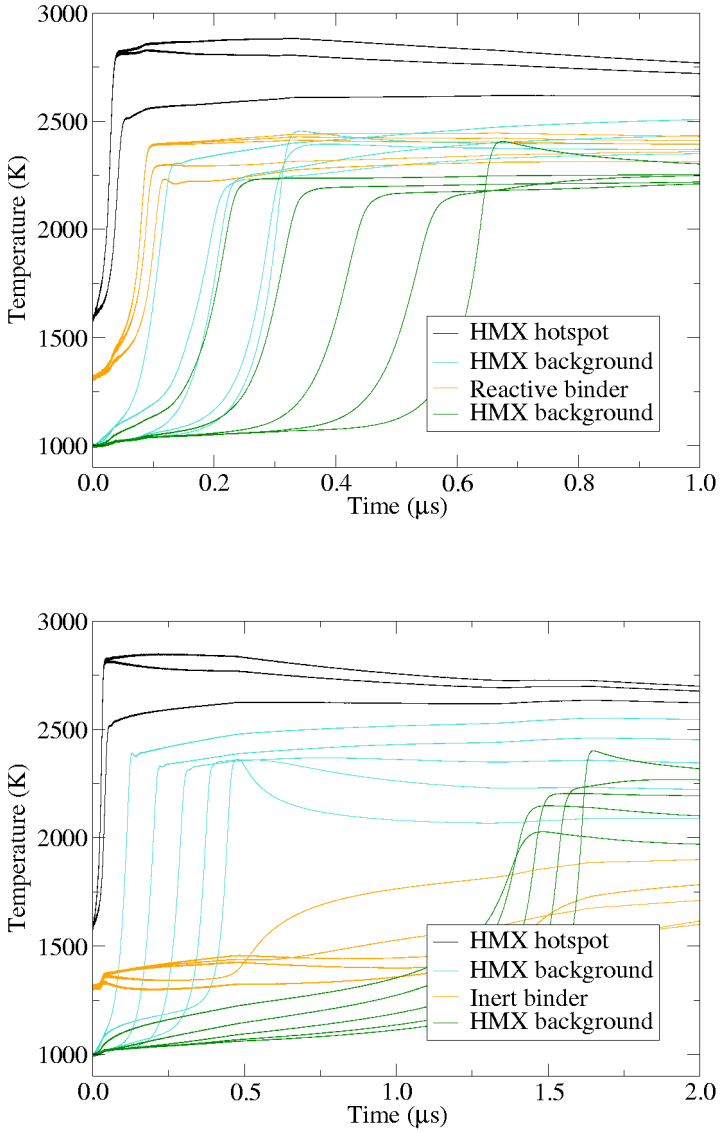

Figure 6.14: Planar calculations to investigate the propagation of a reactive wave through a binder layer in EDC37 with $r_1 = 0.5\,\mu\text{m}$, $r_2 = r_3 = r_4 = 1\,\mu\text{m}$, $T_1 = 1600\,\text{K}$, $T_2 = T_4 = 1000\,\text{K}$ and $T_3 = 1300\,\text{K}$. The first calculation (above) uses chemical reaction rates from section 3.4 but the second simulation (below) models the binder as inert, to take account of the uncertainty in binder reaction rates. Note that different time axes are used for the two plots.

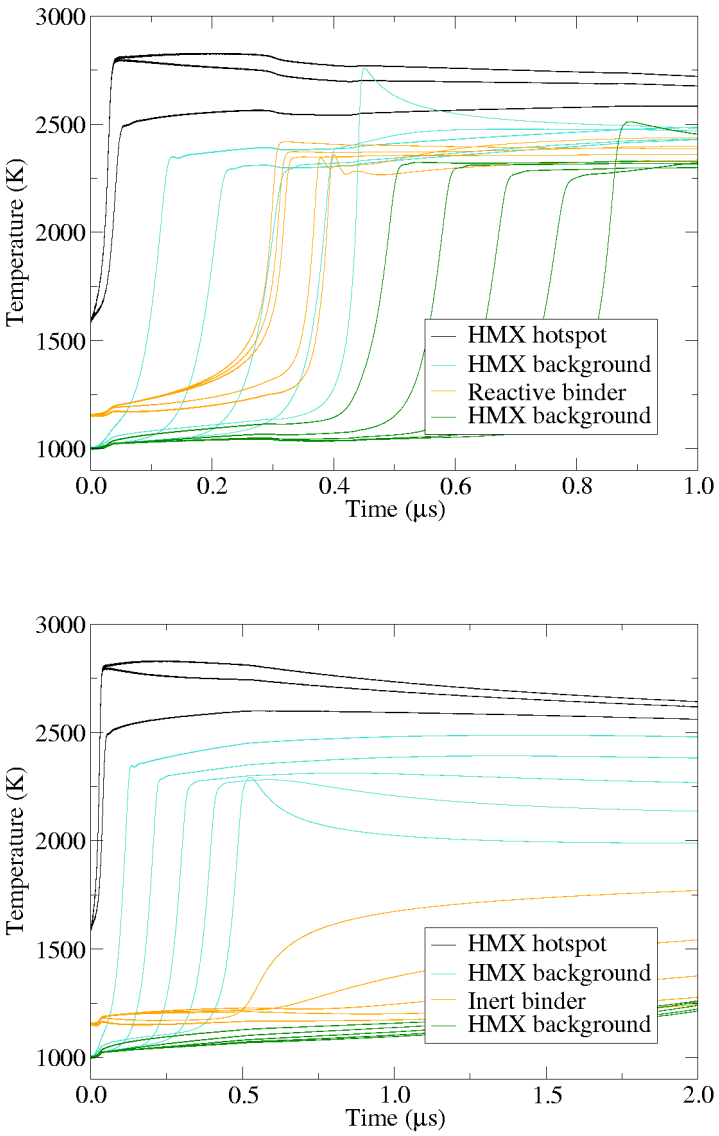

Figure 6.15: Planar calculations to investigate the propagation of a reactive wave through a binder layer in PBX9501 with $r_1 = 0.5\,\mu\text{m}$, $r_2 = r_3 = r_4 = 1\,\mu\text{m}$, $T_1 = 1600\,\text{K}$, $T_2 = T_4 = 1000\,\text{K}$ and $T_3 = 1150\,\text{K}$. Note that different time axes are used for reactive binder (above) and inert binder (below).

initiation, since PBX9501 and EDC37 charges detonate within 10 µs when subjected to flat-topped shocks above ~2 GPa [12, 134]. For hotspots to be able to contribute to the overall reaction, they must react on considerably shorter timescales so 1 µs is a reasonable limit. A series of Peruse simulations has been used to establish the critical hotspot size for a variety of hotspot and background temperatures T_1 and T_2. The results are summarised below and will be compared to the literature in section 6.2.3. The simulations are in plane geometry so the critical size r_1 corresponds to half the total hotspot thickness (see figure 6.1). In most of the Peruse simulations $r_2 = 1\,\mu m$ but this was reduced for very small hotspot sizes, where fine meshing was required to resolve the hotspot, in order to reduce the computational run-time. It has been demonstrated in section 6.1.4 that this should not affect the critical hotspot results.

6.2.1 HMX

The critical hotspot results for HMX are given in figure 6.16. The error bars reflect the difference in hotspot size between a sub-critical simulation and a super-critical simulation, and could be reduced by running further calculations, i.e. they are not associated with uncertainties in the method. For a given background temperature T_2, the critical hotspot size r_1 falls as the hotspot temperature T_1 increases. This is because a hotter hotspot will react more quickly, before it is cooled by the effects of heat conduction, so a smaller hotspot is viable. The critical hotspot curves move upwards (to larger hotspot sizes r_1) as the background temperature T_2 falls but only so far; the critical hotspot sizes for $T_2 = 600\,K$ and 400 K are identical. Since heat conduction depends on the temperature gradient, it is less effective at cooling the hotspot for high background temperatures. This allows smaller hotspots to be viable than at lower background temperatures. At low background temperatures, the difference between the hotspot and background temperatures is so large that any further reduction in background temperature T_2 has little effect on the rate of cooling of the hotspot.

6.2.2 Binders

Critical sizes for hotspots in the binder materials from Peruse simulations are shown in figure 6.17, for background temperature $T_2 = 1000\,K$. The results show that smaller hotspots are viable in the binder materials than in HMX. This is because HMX has the

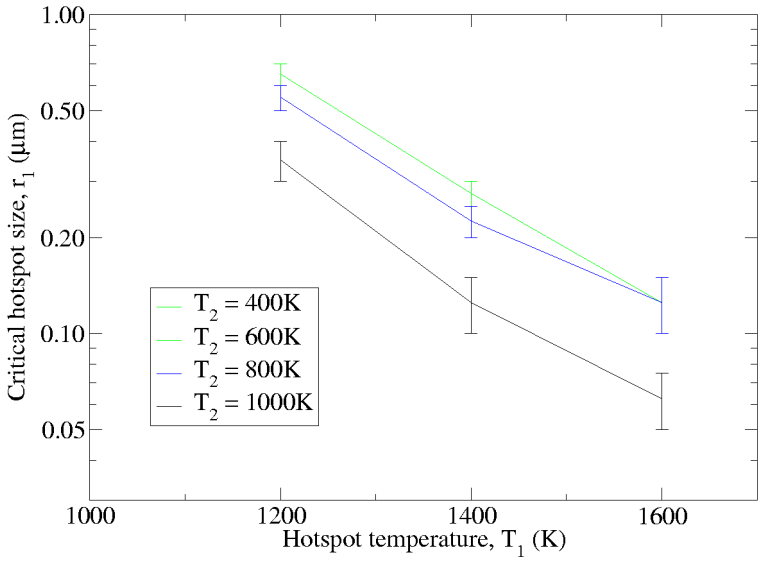

Figure 6.16: Critical hotspot results for HMX in plane geometry. The critical hotspot size is affected by the hotspot and background temperatures, but not by the size of the background region, so $r_2 = 1\,\mu$m for the majority of the Peruse simulations.

highest thermal conductivity and the lowest heat capacity of all three materials, so heat will be conducted away from the hotspot most efficiently and larger hotspot sizes are needed. Despite the fact that the two binders have the same thermal conductivities and similar heat capacities, their critical hotspot curves are different to each other. This is due to the different values of T_{CJ}, which result in higher reaction-product temperatures in EDC37's binder than PBX9501's. Smaller hotspots can be maintained in EDC37's binder because the higher temperatures take longer to dissipate by heat conduction. Since there are very few data points on which to base the Arrhenius reaction rates for the binders in EDC37 and PBX9501, as discussed in section 3.4, these results should be treated with caution. Nevertheless, this is the first time that critical hotspot sizes have been investigated for the binder in EDC37, and I am not aware of any previous studies on the binder in PBX9501.

6.2.3 Comparison with the literature for HMX

Bowden [18] showed experimentally that hotspots need to have dimensions of typically 0.1 to 10 μm, durations of 10^{-5} to 10^{-3} s, and temperatures greater than ~700 K. These criteria are based on hotspot ignition in situations where detonation is produced via

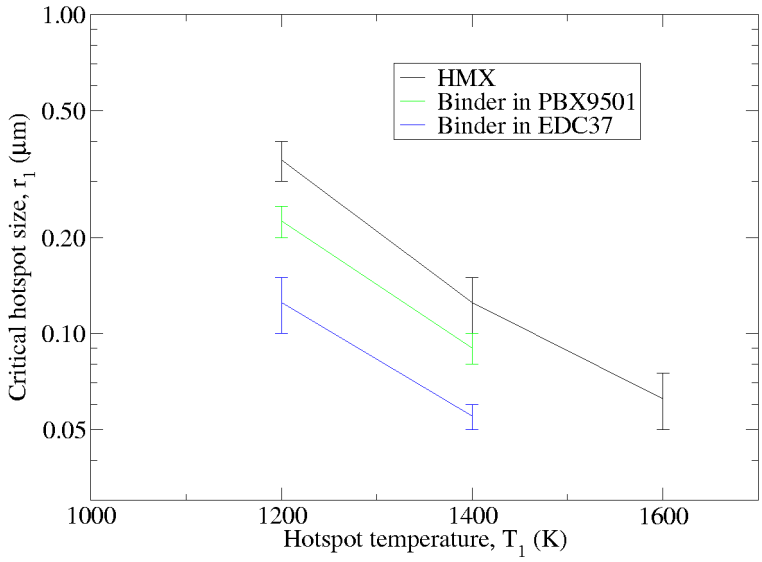

Figure 6.17: Critical hotspot results for HMX and binder in plane geometry with background temperature $T_2 = 1000\,\mathrm{K}$ demonstrating that, for the reaction rates used here, smaller hotspots are viable in the binder materials than in HMX.

the deflagration-to-detonation transition [17] which operates over longer, more easily-measured timescales than the shock-to-detonation transition. This is why the critical hotspot durations are considerably longer than the 10^{-6} s time limit applied here, and it makes direct comparisons between the Peruse results in figure 6.16 and the experimental criteria difficult. Nevertheless, the calculated critical hotspot sizes of 0.1 to 1 μm for low background temperatures are consistent with the experimental hotspot dimensions. In his discussion of the experimental data, Field [17] suggests that hotspots "with sizes <0.1 μm would cause some decomposition but quench too quickly to produce ignition". In contrast, the simulations show that smaller hotspots (with $r_1 < 0.1\,\mu\mathrm{m}$) can be supercritical but only at very high hotspot temperatures. The experimental temperature limit of 700 K is less stringent than in Peruse, where significant reaction occurs only for hotspot temperatures >1000 K, owing to the difference in timescales. Overall, the critical hotspot simulations are not inconsistent with the experimental criteria.

Merzhanov [23] derived an empirical formula for critical hotspots in planar, cylindrical and spherical geometry. Figure 6.18 shows the critical hotspot sizes obtained by substituting relevant material properties from chapter 3 in Merzhanov's formula, compared to the Peruse simulations for HMX. There is close agreement owing to the use of constant heat capacity and single step Arrhenius reaction rates in both models. The

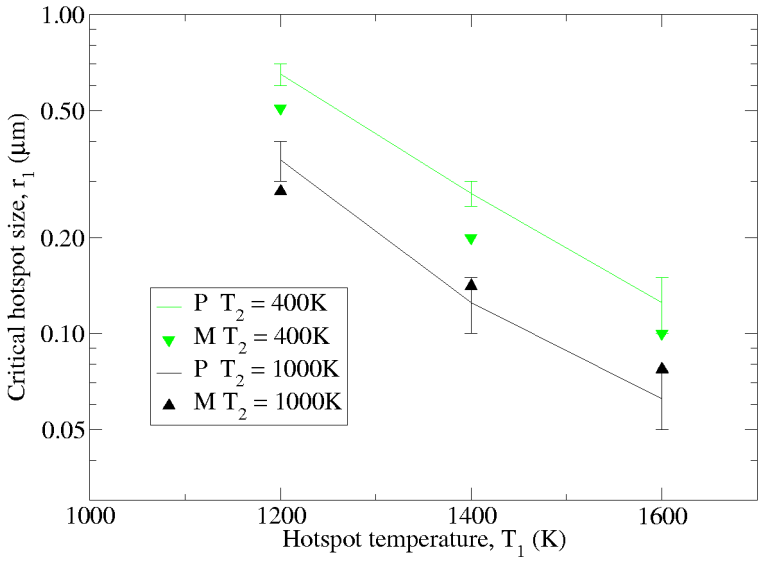

Figure 6.18: Critical hotspot results for HMX in plane geometry from Peruse simulations (P) and from Merzhanov's [23] empirical formula (M).

agreement is not perfect because Merzhanov's formula does not account for the effects of hydrodynamics. Tarver [24] also investigated critical hotspots in a static code. He found that the time to explosion was less than 1 μs for HMX hotspots with radius $\lesssim$1 μm, for which the critical hotspot temperature is greater than 1000 K. For hotspot and background temperatures of $T_1 = 1200$ K and $T_2 = 293$ K respectively, his critical hotspot radius is approximately 0.1 μm. In contrast, figure 6.18 shows that significantly larger critical hotspot sizes are given by Merzhanov's formula (0.5 μm) and Peruse simulations (0.6 – 0.7 μm) for $T_1 = 1200$ K and $T_2 = 400$ K. The difference is caused by Tarver's use of a three-step reaction scheme and temperature-dependent thermal properties.

More recently, Tarver [25] investigated critical hotspots in a hydrocode, ALE3D, and his results for outward growing hotspots in HMX are most relevant here. Figure 4 of reference 25 gives the time for a spherical hotspot of 0.1 μm radius to grow to eight times its original diameter. The reaction time is <1 μs for background temperatures between 500 and 650 K. Although the hotspot temperature is not specified, this implies that a very high temperature was used. Indeed, Tarver's calculations of inward reaction-growth have boundary temperatures between 1000 and 4000 K, and it seems likely that the maximum temperature of 4000 K was used for the outward growing hotspot calculations. This temperature is considerably higher than the maximum hotspot temperatures used in Peruse simulations, making comparison difficult. However, figure 6.16 shows

that a planar hotspot of radius 0.1 μm in HMX at $T_2 = 600$ K would explode in < 1 μs if it had temperature $T_1 > 1600$ K, which is consistent with Tarver's prediction of ~0.2 μs time to complete reaction. Reaugh also used ALE3D to investigate critical hotspots in HMX [26]. For a hotspot at ~2800 K with background temperatures less than 650 K, his critical radius varied between 0.13 and 0.04 μm. Once again, this is the same order of magnitude as the Peruse results in figure 6.16, if the $T_2 = 600$ K line is extrapolated to higher hotspot temperatures.

Overall, reasonable agreement has been obtained between the Peruse simulations and critical hotspot sizes for HMX in the literature. Since similar results have been produced using different codes, material models and reaction rates, increased confidence can be placed in Peruse simulations. The implications of these results will be discussed in section 6.5.

6.3 Flame propagation

As discussed in section 6.1, a heat-conduction-driven reactive wave with velocity ~1 m/s is the only method by which reaction can spread from hotspots into the surrounding background material in Peruse simulations. The aim of this section is to validate this reactive wave velocity by comparison to flame propagation data. Diamond anvil cell experiments have been used to determine high-pressure reaction propagation rates in a range of energetic materials [e.g., 185, 186 and 187]. Figure 6.19 shows how the cylindrical sample, contained in a gasket of diameter 150 – 400 μm, is compressed by two opposing diamonds to pressures $\lesssim 40$ GPa. A laser with a 5 μm spot size is used to ignite the sample along the axis of symmetry and a streak camera is used to record the disturbance of a laser speckle pattern with time, giving the rate at which the deflagration spreads outwards through the sample. The sample is initially at ambient temperature and the pressure is measured by the fluorescence of ruby powder on the surface of one of the diamonds.

Diamond anvil cell experiments have been conducted on nitromethane, a homogeneous explosive, providing a useful comparison to HMX. The nitromethane data [186] show that the reaction propagation rate increases from 5 m/s at 1 GPa to about 100 m/s at 30 GPa. Above 30 GPa, the propagation rate decreases with pressure to near 40 m/s at 41 GPa. This change in behaviour has been attributed to a visible change in the reaction chemistry of nitromethane at pressures above 25 GPa.

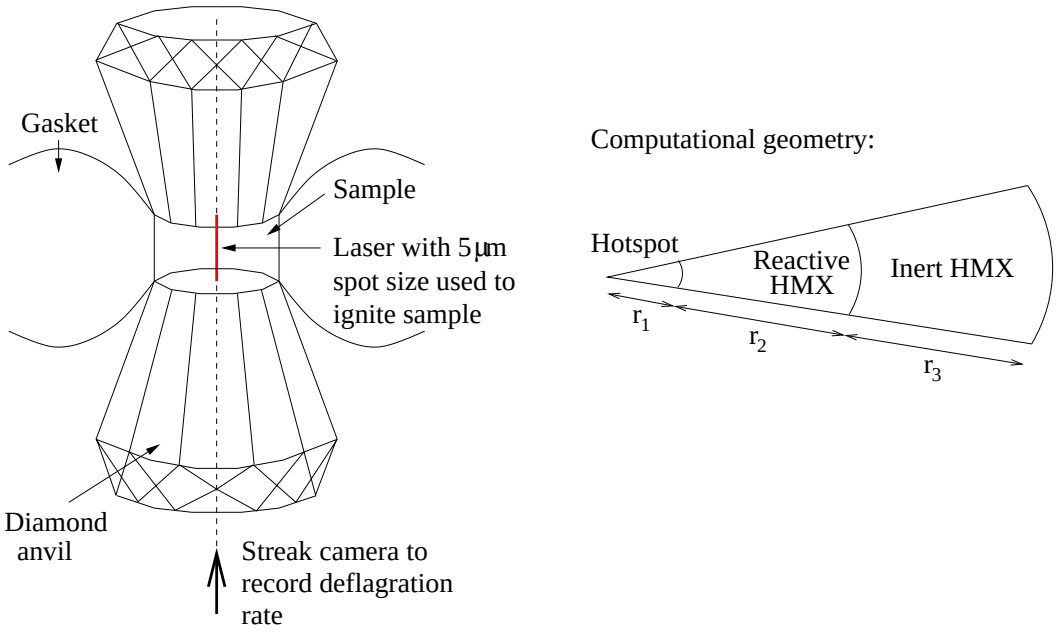

Figure 6.19: Sketch of diamond anvil cell experiments to study high-pressure reaction propagation rates (left) and the cylindrical geometry used in Peruse simulations (right). The HMX region that will not be reached by the reactive wave before the end-time of the simulation is modelled as inert to reduce the computational run-time.

Diamond anvil cell data for HMX show an order-of-magnitude variability in deflagration rate depending on the sample and technique used [187]. For example, the deflagration rate at 8 GPa varies between ~10 and 100 m/s. This may be due to incomplete compaction of the HMX powder in the gasket, leading to the diffusion of hot gaseous reaction products through the sample [185]. However, the pressures generated in diamond anvil cell experiments are above the yield strength of HMX (which is between 0.1 and 0.3 GPa [80]), so it is likely that the grains would be fused together, preventing the diffusion of hot gases through the sample [188]. Despite the variability, the HMX data indicate that the deflagration rate increases with pressure from 2 to 30 GPa.

For comparison to the experimental data, Reaugh modelled the high-pressure deflagration of HMX in a hydrocode, ALE3D. Although his initial simulations produced deflagration rates that were several orders of magnitude slower than the experimental data [87], model improvements led to rates in the range 2 to 10 m/s for pressures between 1 and 30 GPa [103]. A later study produced flame speeds rising non-linearly from ~20 m/s at 1 GPa to just under 60 m/s at 20 GPa, before falling to 40 m/s at 30 GPa [26]. This is broadly in agreement with the diamond anvil cell data for HMX, although the simulated flame speeds lie outside the experimental scatter. The simulations are difficult because the

deflagration rate depends on the thermal properties of both the unreacted explosive and the reaction products, as well as the reaction rate, so all three components of the material model need to be accurate in the deflagration regime. This is particularly challenging for shock to detonation models, like those constructed in chapter 3, where the thermodynamic states achieved in the explosive are very different. Therefore, good quantitative agreement between Peruse simulations and HMX flame propagation data is not expected.

6.3.1 Computational method

The computational geometry used to simulate the diamond anvil cell experiments in Peruse is shown in figure 6.19. Cylindrical geometry is used with rigid adiabatic boundary conditions at each end of the computational domain. This gives the best representation of the experimental configuration, but it contrasts with the use of plane geometry and constant pressure boundary conditions by Reaugh. The geometry comprises three regions: a hotspot with radius r_1 representing the HMX that is ignited by the laser, a reactive HMX region of thickness r_2 and an inert HMX region of thickness r_3 both representing the ambient HMX sample. Since the reactive wave does not propagate to the edge of the sample during the simulation, the unburnt region is modelled as inert to reduce the computational run-time. It is important to include this inert region rather than restricting the size of the computational domain, to ensure that the pressurisation of the system as the HMX reacts is representative of the experiment. All three regions were given material properties of HMX from chapter 3 and initial density and specific internal energy values consistent with the applied pressure (2 to 20 GPa), with the hotspot region 1 having an initial temperature of 1600 K and the reactive and inert HMX regions 2 and 3 having ambient temperature (295 K). The initial hotspot temperature is an approximate value that ensures prompt reaction, and it was checked that it does not affect the results.

The deflagration rate is calculated, using Lagrangian gauges positioned at regular intervals through the computational geometry, from the time at which the temperature of each gauge rises above 1500 K and the initial gauge location. This is common practice in shock wave simulations, but it is an approximation for flame propagation simulations because the gauges have time to move before the sub-sonic deflagration wave arrives. To check whether this has a significant effect, a diamond anvil cell simulation was run with $r_1 = 1\,\mu\text{m}$, $r_2 = 9\,\mu\text{m}$, $r_3 = 0\,\mu\text{m}$, 5 zones / µm meshing and 0.4 µm initial gauge spacing. The calculated deflagration rate of 1.06 m / s is sufficiently close to the true rate

of 1.22 m/s (using the current gauge location) to conclude that using the initial location is a reasonable approximation.

6.3.2 Flame propagation simulations

Temperature histories from a typical diamond anvil cell simulation are shown in figure 6.20. The results are similar in character to super-critical hotspot simulations, but the focus is on the behaviour of the reactive wave rather than the hotspot. The deflagration rate decreases as the wave propagates further into the HMX (i.e. the separation between the gauge traces increases). This is because the system pressurises as the HMX is converted into gaseous reaction products, causing the temperature of the reaction products to fall, which reduces the rate of heat conduction. The unreacted HMX takes longer to heat up before it can react, so the reactive wave speed is lower. The initial deflagration rate in this simulation is 2.9 m/s, somewhat lower than the experimental data and Reaugh's simulations. To investigate the reasons for the low deflagration rate in Peruse, the sensitivity of the simulations to material properties and geometry will be explored below. Coarse meshing (5 zones/μm) was used for many of these initial calculations to reduce the computational run-time; the effect of mesh density is investigated later.

Since the reactive wave is driven by thermal conduction (see section 6.1), any material properties that affect the temperature of the unreacted HMX and the reaction products could affect the flame speed. The temperature of the gaseous reaction products is controlled by the CJ temperature T_{CJ} and specific heat capacity $c_{\mathrm{v,CJ}}$. Nominal values of $T_{\mathrm{CJ}} = 3000\,\mathrm{K}$ and $c_{\mathrm{v,CJ}} = 2\,\mathrm{J/g\,K}$ from chapter 3 give an initial deflagration rate of 1.1 m/s in a diamond anvil cell simulation. A similar calculation with $T_{\mathrm{CJ}} = 4000\,\mathrm{K}$ had an initial deflagration rate of 1.7 m/s owing to higher temperatures in the gaseous reaction products. If $c_{\mathrm{v,CJ}}$ is increased to $3\,\mathrm{J/g\,K}$ instead, the initial deflagration rate is unchanged but the deflagration rate falls less quickly as the system pressurises, because the gas temperature is higher. The temperature of the unreacted HMX depends on specific heat capacity $c_{\mathrm{v,s}}$. Reducing $c_{\mathrm{v,s}}$ from its baseline value of $1.1\,\mathrm{J/g\,K}$ to $0.8\,\mathrm{J/g\,K}$ increases the deflagration rate from 1.1 to 1.4 m/s.

Other parameters that could affect the flame speed are the thermal conductivity k and the Arrhenius reaction rate parameters $\ln Z_1$ and E_1. Increasing k from $0.4\,\mathrm{W/m\,K}$ to $0.5\,\mathrm{W/m\,K}$ modifies the deflagration rate by 0.2 m/s. Changing the Arrhenius parameters to the maximum and minimum values in section 3.4 affects the deflagration rate

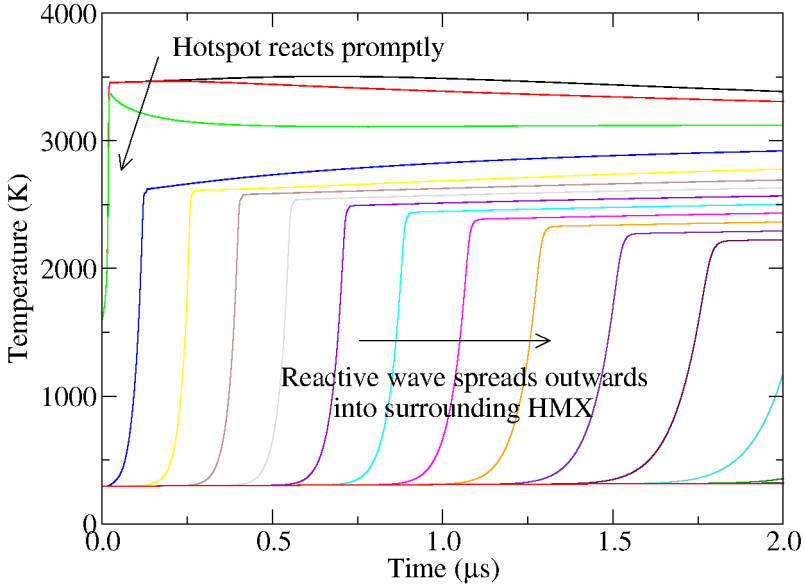

Figure 6.20: Temperature histories from a diamond anvil cell flame propagation simulation at 10 GPa with $r_1 = 1\,\mu m$, $r_2 = 9\,\mu m$, $r_3 = 0\,\mu m$ and 40 zones/μm meshing. The hotspot, with an initial temperature of 1600 K, reacts promptly and its temperature rises to ~3500 K (black, red and green gauges). A heat-conduction-driven reactive wave propagates outwards into the surrounding HMX. When it arrives at each gauge location (blue, yellow, brown, etc.), the temperature rises from 295 to ~2500 K as chemical reaction converts the unreacted HMX into gaseous reaction products.

by less than 0.1 m / s. In his flame propagation simulations, Reaugh uses a four-step reaction scheme for HMX from reference 135 but with the frequency factor Z_4 increased by a factor of 80, in order to match the results of molecular dynamics simulations of HMX decomposition [26, 87]. These rate parameters can be used with a single-step Arrhenius rate to give an over-estimate of the behaviour that would be obtained using Reaugh's reaction scheme. Peruse simulations with $\ln Z_1 = 18.67$ (for Z in μs^{-1}) and $E_1 = 117.7\,\mathrm{kJ/mol}$ give a deflagration rate of 4.0 m / s for these reaction-rate parameters, compared to 1.1 m / s for the baseline values.

These initial simulations show that the effect of changing material properties T_{CJ}, $c_{v,CJ}$, $c_{v,s}$, k, $\ln Z_1$ and E_1 is relatively small. It does not change the character of the simulations from that in figure 6.20 and, in particular, the deflagration rate always falls as the system pressurises.

Effect of meshing and geometry

Mesh resolution is important for flame propagation simulations. Figure 6.21 shows the deflagration rate as a function of mesh resolution for simulations with $r_1 = 1\,\mu m$, $r_2 = 9\,\mu m$ and $r_3 = 0\,\mu m$. The maximum deflagration rate increases from 1 m / s to almost 3 m / s as the meshing is raised from 5 to 40 zones / μm. The close agreement between the results of the 40 and 100 zones / μm calculations shows that mesh convergence has been achieved. Figure 6.21 also shows temperature histories from the simulations with 5 zones / μm and 40 zones / μm meshing. The temperature overshoots at 5 zones / μm reduce in magnitude as the mesh density is increased, and disappear altogether once mesh convergence has been achieved at 40 zones / μm. Reaugh's simulations gave similar behaviour [87]: "My general observation was that if the temperature profiles were smooth curves, then the resolution was adequate. If they were very steep, or the temperature wiggled around, then a finer mesh was called for." The resolution required to achieve mesh convergence depends on the simulation, but either 40 or 100 zones / μm was used to produce the final results in section 6.4. For comparison, the critical hotspot simulations used 20 zones / μm meshing because: "with slower flame speed, one can get away with a coarser mesh because the heat is spread out" [87].

As has already been mentioned, the size of the computational domain has a significant effect on the character of flame propagation simulations because it controls the rate at which the system pressurises. For example, a simulation similar to that in figure 6.20 was

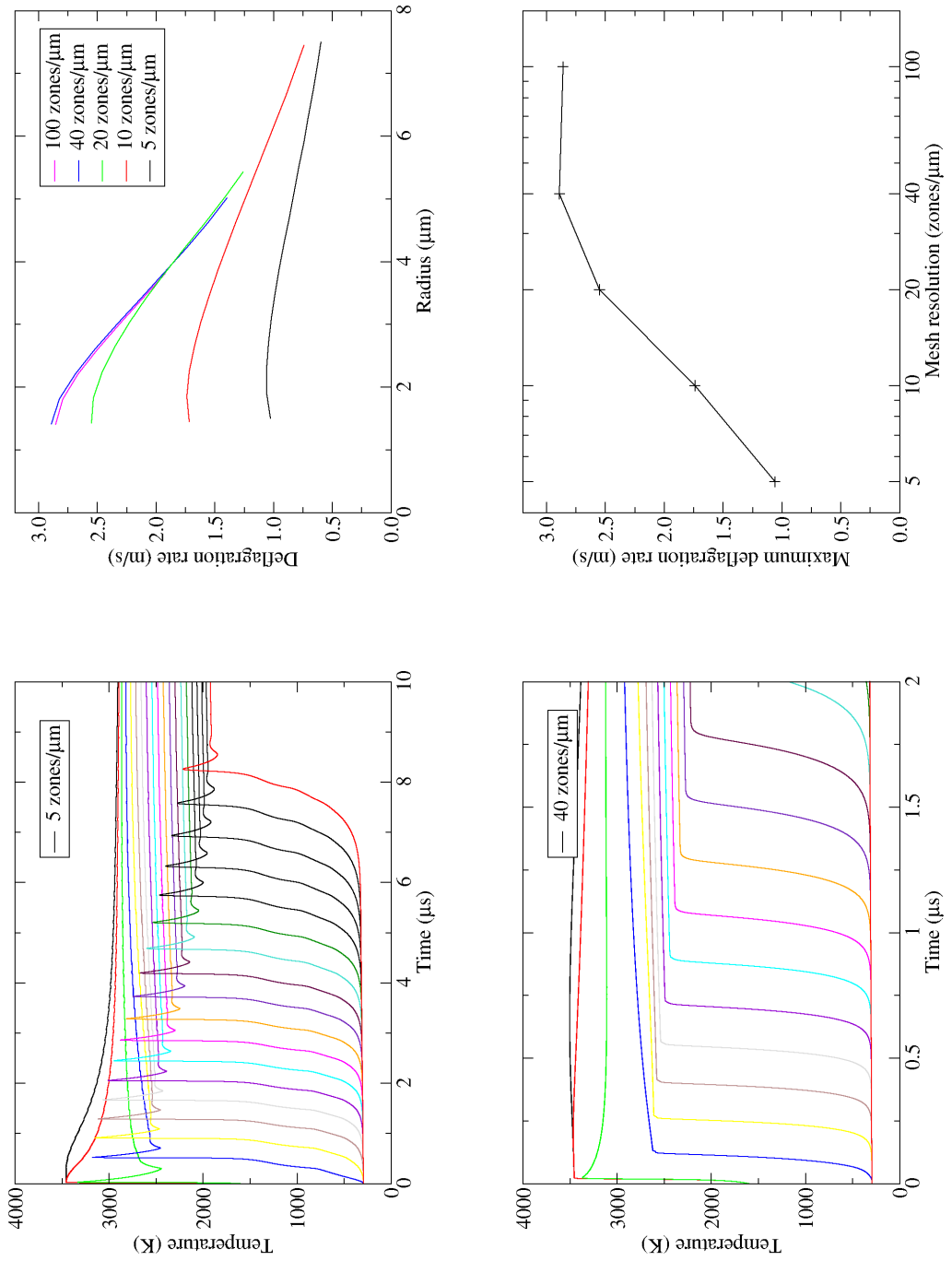

Figure 6.21: The effect of mesh resolution on flame propagation simulations in Peruse. The temperature overshoots that occur after the steep temperature rise indicate that the results are not converged at 5 zones / µm. Also, the maximum deflagration rate (which occurs at ~2 µm radius) increases significantly with mesh resolution from 5 to 40 zones / µm. Convergence is achieved at 40 zones / µm and above, where the temperature histories are smooth and there is no further increase in the maximum deflagration rate.

run with r_2 reduced from 9 to 1 μm. The reactive wave fails to propagate in this geometry because the high pressures generated when the hotspot reacts reduce the temperature of the reaction products, and therefore the rate of thermal conduction into the unreacted HMX. This strong dependence on the size of the computational domain means that a geometry as close as possible to the experimental configuration should be used. In the experiments, $r_1 = 2.5\,\mu\text{m}$ and $150\,\mu\text{m} \leq r_2 \leq 400\,\mu\text{m}$. Unfortunately, a computational geometry this big would be prohibitively expensive to run. A compromise geometry with $r_1 = 1\,\mu\text{m}$, $r_2 = 9\,\mu\text{m}$ and $r_3 = 10\,\mu\text{m}$ was used to generate results for comparison with the experimental data.

6.4 Flame propagation results

The results from a series of flame propagation simulations in Peruse are shown in figure 6.22. The deflagration rates are similar in magnitude to the experimental data. Con-

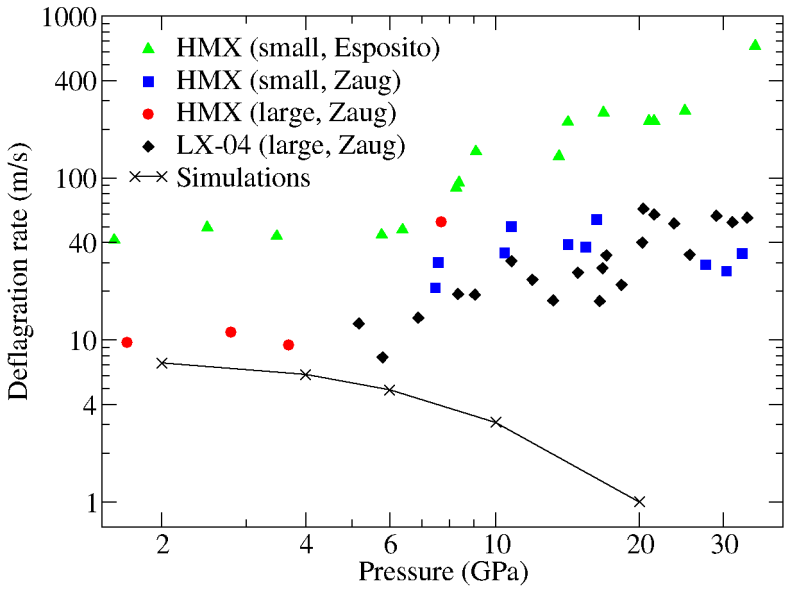

Figure 6.22: Final results from diamond anvil cell flame propagation simulations in Peruse compared to the experimental data for small and large-grain HMX from Esposito [185] and Zaug [187]. The simulated deflagration rate is similar in magnitude to the experimental data in the pressure range 2 – 6 GPa but, in contrast to the data, the deflagration rate falls as the pressure is increased.

sidering the variability in the data, the agreement could be considered to be good in the pressure range 2 to 6 GPa. Here, the small differences between the simulations and the data could be due to porosity or grain size effects in the HMX samples, which are treated as a single fully-dense material in Peruse. However, these effects are not likely to be responsible for the significant differences above 6 GPa, where the experimental deflagration rate increases with pressure but the simulated rate falls. The positive pressure dependence in the experimental data is consistent with high pressure strand burner data for HMX [187], diamond anvil cell data for nitromethane [186], Reaugh's hydrocode simulations [26, 103] and a low-pressure reaction model [189]. However, negative pressure dependence has been observed for laminar burning in gases [190, 191].

A negative pressure dependence occurs in Peruse because the temperature of the gaseous reaction products decreases with pressure. To understand why this is requires some analysis of the equations of state $p(v, e)$ and $T(v, e)$ for the reaction products. The partial derivatives of pressure p and temperature T with respect to specific volume v and specific internal energy e are given by equations 6.1 to 6.4. Substituting typical values for the gaseous reaction products of $\Gamma = 0.3$, $v = 0.6\,\mathrm{cm^3/g}$, $p = 10\,\mathrm{GPa}$, $c^2 = 0.2\,\mathrm{cm^2/\mu s^2}$, $c_{v,CJ} = 2.0\,\mathrm{J/g\,K}$ and $T = 4000\,\mathrm{K}$ into these equations gives

$$\left(\frac{\partial p}{\partial e}\right)_v = \frac{\Gamma}{v} \approx 0.5\,\mathrm{g/cm^3} \tag{6.1}$$

$$\left(\frac{\partial p}{\partial v}\right)_e = \frac{\Gamma p}{v} - \frac{c^2}{v^2} \approx -50\,\mathrm{GPa\,g/cm^3} \tag{6.2}$$

$$\left(\frac{\partial T}{\partial e}\right)_v = \frac{1}{c_{v,CJ}} \approx 0.5\,\mathrm{g\,K/J} \tag{6.3}$$

$$\left(\frac{\partial T}{\partial v}\right)_e = -\left.\frac{\partial T}{\partial e}\right|_v \left.\frac{\partial e}{\partial v}\right|_T = \frac{p}{c_{v,CJ}} - \frac{\Gamma T}{v} \approx 3 \times 10^3\,\mathrm{g\,K/cm^3}, \tag{6.4}$$

i.e. the pressure and temperature both increase with e at constant v, while the pressure decreases and the temperature increases with v at constant e. If the pressurisation that is observed in flame propagation simulations is at approximately constant v, then the internal energy must increase and likewise the temperature of the reaction products. This would cause the deflagration rate to increase with pressure. However the post-reaction specific internal energy is approximately constant in Peruse, both as pressurisation occurs within a single simulation and in several simulations with different initial pressures. For a system that pressurises at constant e, the specific volume must decrease with pressure and likewise the temperature of the reaction products falls. This causes the deflagration rate to decrease with pressure.

The thermodynamic equations 6.2 and 6.4 explain why the post-reaction temperature falls with pressure in Peruse calculations. The difficulty of temperature measurements means that it is not yet possible to confirm this behaviour experimentally, although suitable techniques are under development [192]. The post-reaction states achieved in the simulations are a function of the JWL equation of state used for the gaseous reaction products and, to some extent, the assumption of pressure and temperature equilibrium in the reacting mixture since this controls the thermodynamic heating path. Reaugh used a tabular equation of state derived from Cheetah thermochemical calculations in his flame propagation simulations. Cheetah [136] calculations (using the exp6.3 library) of HMX in the vicinity of $v = 0.6\,\mathrm{cm}^3/\mathrm{g}$ and $T = 4000\,\mathrm{K}$ confirm that the pressure and temperature both increase with e at constant v, but the temperature increases and the pressure decreases with v at constant e. Reaugh also observed that the flame speed falls with pressure above 20 GPa, but he did not identify a reason in reference 26. He has since confirmed that falling gas temperatures were indeed responsible [87]. A similar reduction in the deflagration rate of nitromethane has been observed experimentally above 30 GPa, and was attributed to a visible change in the reaction chemistry [186]. As a result of the Peruse simulations, it is suggested that the reduction in flame speed is instead caused by a fall in the temperature of the gaseous reaction products at high pressures, which may subsequently result in changes to the reaction mechanism.

There are several reasons that could explain why the deflagration rate of HMX increases with pressure in the diamond anvil cell experiments and in Reaugh's low-pressure simulations, but not in Peruse:

Equation of state. The JWL equation of state for the reaction products is widely used in the shock and detonation regimes but it was not designed for flame propagation simulations, which are in a different thermodynamic regime, and its thermal properties have been questioned [167]. Using a better reaction products equation of state in Peruse might increase the post-reaction temperatures in flame propagation simulations, improving the agreement to the experimental data.

Thermal conductivity. Experimental evidence shows that thermal conductivity k depends on pressure and temperature [140], and Reaugh used pressure-dependent transport properties [26]. To investigate the effect of variable k, an additional Peruse simulation was run at 10 GPa initial pressure with 40 zones/μm meshing. The deflagration rate increased from 3.1 m/s for baseline $k = 0.4\,\mathrm{W/m\,K}$ to 6.4 m/s for $k = 2.0\,\mathrm{W/m\,K}$, an upper limit for HMX reaction products based on transport

theory [141]. This is closer to, but still less than, the experimental data, suggesting that the use of a constant thermal conductivity in Peruse is responsible for some of the disagreement between the simulations and the data in figure 6.22, but not all.

Species diffusion. Numerical simulations of steady flame propagation show that deflagration velocities depend on the ratio of the species and thermal diffusivities [193], although the dependence weakens when the thermal diffusivity is more than twice the species diffusivity. This suggests that better results might be obtained if species diffusion could be included in Peruse simulations, although Reaugh did not find it necessary to include it in his simulations [103].

Reaction kinetics. Reaugh [185] attributed the positive pressure dependence in his simulations to "the separation of hot gas products from the cold surface that is large for the low-density, low-pressure products, and is small for the high-density, high-pressure products." Menikoff has suggested that this effect is only significant for multi-step reaction schemes [188], such as that used by Reaugh. A simplified model for deflagration in HMX with a two-step reaction scheme [189] also produces deflagration rates that increase with pressure. Using multi-step reactions in Peruse might improve the agreement to experimental data.

Turbulence. It has been reported that a turbulent mechanism of energy transfer can enhance the burning rate in explosives [149, 150] from $<1\,\mathrm{m/s}$ to $\sim 100\,\mathrm{m/s}$. Applying a similar scaling factor to the simulations in figure 6.22 would give better agreement with the experimental data above 8 GPa, implying that turbulence may be an important factor in governing reaction propagation in HMX.

Cracking. It has been suggested that fragmentation of large HMX crystals could enhance the burning rate by increasing the contact area between the hot reaction products and the unreacted explosive [25]. While this could be significant in some experiments, e.g. strand burners, the high pressures in diamond anvil experiments and in shocked explosives are likely to be sufficient to prevent cracks opening.

Pressure-dependent burning. Pressure-dependent burning is widely used in ignition and growth models of explosives and is often represented using Vieille's law [194]. This is an empirical model, whose parameters are fitted to deflagration data and do not extrapolate neatly to the detonation regime [9]. In addition, Lambourn [53] has shown that pressure-based burning is counter to observations that the global reaction rate in plastic-bonded explosives is primarily dependent on shock

strength [175]. Therefore, it is not appropriate to include pressure-dependent burning in mesoscale models; rather, the models should contain the correct physics to be able to reproduce the experimental observations on which empirical pressure-dependent models are based.

It is suggested that these effects are investigated in future work. In conclusion, figure 6.22 shows that Peruse simulations give deflagration rates in broad agreement with diamond anvil cell data. Therefore, the reactive wave velocity has been validated within the constraints of modelling assumptions made in this work. The highest pressure (20 GPa) diamond anvil cell simulation had a deflagration rate of 1 m/s. This is consistent with the critical hotspot simulations in section 6.1 which are at similar initial pressures. The implications of ~1 m/s burning rates for the spread of reaction from hotspots into the surrounding cooler explosive are explored below.

6.5 Discussion

The critical hotspot simulations in figure 6.5 on page 127 demonstrate that HMX hotspots must have temperatures >1000 K to react within 1 μs, and similar results were obtained for the binder materials. This is a consequence of using reaction rate coefficients tuned to Henson's compilation of experimental data for HMX [82], which give an explosion time of 10 μs at 1000 K (see section 3.4). It is consistent with chapter 5, where it was demonstrated that little chemical reaction occurs in hydrocode calculations without hotspots because the temperatures produced by the passage of a shock wave are too low. Therefore, hotspot mechanisms must be able to produce temperatures >1000 K in order to be responsible for shock initiation in PBX9501 and EDC37.

The ~1 m/s reactive wave velocity places a limit on the maximum separation of hotspots, because it controls how much of the explosive can be consumed by reaction spreading outwards from hotspots. During the 1 μs timescales of relevance to shock initiation, the reactive wave can propagate ~1 μm from a hotspot. Making the conservative assumption that 50 % of the microstructure must react for the explosive to complete the shock-to-detonation transition, a simple geometric analysis can be used to calculate the proportion of the microstructure that must be contained within hotspots, and how widely separated the hotspots are. The results in table 6.3 provide a set of criteria which can be used to evaluate different hotspot mechanisms.

Hotspot size	Proportion of explosive in hotspots		Hotspot separation	
r_1	Planar	Spherical	Planar	Spherical
1 μm	25 %	6 %	6 μm	4.0 μm
0.1 μm	5 %	0.04 %	4.2 μm	2.2 μm
0.01 μm	0.5 %	0.00005 %	4.02 μm	2.0 μm

Table 6.3: Results of a simple geometric analysis to determine the maximum separation of hotspots in PBX9501 and EDC37, based on a ~1 m / s reactive-wave propagation velocity and the assumption that 50 % of the explosive must react.

Bigger hotspots can have lower temperatures (see section 6.2) but they need to engulf a greater proportion of the explosive. Smaller hotspots must have high temperatures, so they can react before they are cooled by heat conduction, but they need occupy only a small fraction of the explosive. In plastic-bonded explosives, it is widely assumed that hotspots comprise only a few per cent of the composition. Indeed, the proportion must be small to avoid raising the average temperature of the explosive above the calculated bulk temperature distribution at a given shock strength. From table 6.3, this means that the hotspots must be separated by $\lesssim$4 μm. With HMX particle sizes ranging between 1 and 1000 μm diameter in PBX9501 and between 0.1 and 200 μm in EDC37, this implies that hotspots must form within the HMX crystals and not just in the binder or at the HMX/binder interface. Table 6.3 shows that, if <5 % of the explosive comprises hotspots, then planar hotspots have size $r_1 < 0.1$ μm. Figure 6.16 shows that planar hotspots of this size must be hotter than ~1600 K in HMX, for background temperatures <600 K which are typical for gas-gun shock initiation experiments (see section 7.3). Similar criteria could also be derived for cylindrical or spherical hotspots, placing a stringent requirement on hotspot mechanisms which can be used to eliminate candidate mechanisms in future studies of shock initiation.

Different conclusions have been drawn from critical hotspot simulations in the literature. Tarver and Nichols concluded that “heat conduction alone cannot account for the reaction rates in large explosive particles necessary to cause shock initiation” [25]. However, they assumed that hotspots are only produced by pore collapse so, for low-porosity explosives like PBX9501 and EDC37, the HMX particles contain only a few internal hotspots or a larger number of external hotspots. Table 6.3 demonstrates that heat conduction is sufficient to cause shock initiation if hotspots are distributed throughout the explosive crystals and binder, with $\lesssim$4 μm separation.

6.6 Summary

It has been demonstrated that it is important to include hydrodynamic effects in critical hotspot simulations and that thin binder layers do not impede the spread of reaction from one HMX crystal to another. Critical hotspot sizes have been determined for HMX and, for the first time, the binders over a range of temperatures and these compare favourably to previous results for HMX in the literature. In the Peruse simulations, a heat-conduction-driven wave is the only mechanism by which reaction spreads from the hotspot into the surrounding explosive, and its velocity has been validated by comparison to diamond anvil cell data. A new explanation has been given for the negative pressure dependence sometimes observed in flame propagation experiments, based on the temperature of the gaseous reaction products. The reactive wave speed implies that hotspots must be separated by $\lesssim 4\,\mu\text{m}$ in PBX9501 and EDC37, so they must be positioned within the HMX crystals and not just in the binder or at the HMX/binder interface.

Chapter 7

Bulk temperature distributions

The passage of a shock wave through the microstructure of a plastic-bonded explosive produces a distribution of temperatures behind the shock front. This can be divided into two components, a "hotspot" temperature distribution caused by hotspot mechanisms and a "bulk" distribution. The bulk temperature distribution includes the temperature localisation that occurs because of shock interactions of crystals and binder, but does not include hotspots. Although not by itself responsible for shock initiation (see chapter 5), this bulk temperature distribution has several important effects. These include influencing how reaction proceeds within hotspots as they are cooled by heat conduction and how reaction spreads from hotspots into the bulk explosive during the shock-to-detonation transition (see chapter 6). Therefore, the bulk temperature distribution forms an important component in a mesoscale model of explosives. Unfortunately, experimental temperature data are scarce owing to the difficulty of measuring temperatures in the bulk of a sample within the microseconds available before reaction consumes the explosive. Hydrocode modelling may provide the best way to obtain bulk temperature distributions for some time to come.

In this chapter, hydrocode simulations are used to determine bulk temperature distributions in shocked EDC37 and PBX9501. Any computational study is vulnerable to errors associated with the numerical scheme and the assumptions made in constructing material models, so considerable work was done to establish their influence. Section 7.1 describes the computational method including the extraction of temperature distributions, the effect of changing the computational settings and the choice of one, two or three-dimensional geometry. The effects of uncertainties in the material properties data

and modelling assumptions are presented in section 7.2. From this sensitivity study, it is concluded that the hydrocode calculations provide reliable temperature distributions for EDC37 and PBX9501. Results from a limited number of computationally-expensive 2D microstructure simulations are given in section 7.3. This is the first time that temperature distributions have been determined for shocked EDC37, but previous results [69] are used to validate the PBX9501 distributions. Pressure versus specific volume data and pressure/temperature profiles are also presented in section 7.3, allowing several novel conclusions to be drawn. The chapter is summarised in section 7.4.

7.1 Computational method

Two different hydrocodes are used to determine bulk temperature distributions in shocked explosive. As discussed in chapter 2, Peruse is a one-dimensional hydrocode which solves the Lagrangian reactive-flow equations 2.7 neglecting species diffusion. Petra is a two-dimensional hydrocode which solves the Eulerian reactive-flow equations 2.1 to 2.5 neglecting chemistry, heat conduction and species diffusion. Three types of hydrocode simulations will be described: full calculations of the entire 2D microstructure (type A), calculations of a limited 2D microstructure (type B), and one-dimensional calculations (type C). Their geometries are sketched in figure 7.1. In each case, a shock is driven into the explosive by firing the microstructure into a rigid wall. The crystal and binder components are initially at room temperature and pressure but with a velocity downwards, towards the wall.

Type A simulations in Petra model an entire 2D micrograph, with dimensions 0.6911×1.0289 mm for EDC37 (figure 2.10) and 0.6936×1.0322 mm for PBX9501 (figure 2.11). The computational mesh size is set equal to the micrograph pixel size, so there are 2611×3887 zones for EDC37 and 2611×3886 for PBX9501. The effect of changing the mesh size will be discussed in section 7.1.4. These calculations take approximately 24 hours to run to $\sim 0.2\,\mu$s (enough time for the shock to cross the geometry once) in parallel on 100 processors of a Cray XT3 supercomputer. Type B simulations model a small section of the 2D micrograph, with 2611×100 zones in Petra. These calculations take less than an hour to run in serial and so are useful for testing the effect of code settings, material properties, etc. Type C calculations model a 1D line through the 2D micrograph, with 2611 zones. They can be run quickly in serial in both Petra and Peruse, allowing the comparison of results generated using two different hydrocodes and investigation of the

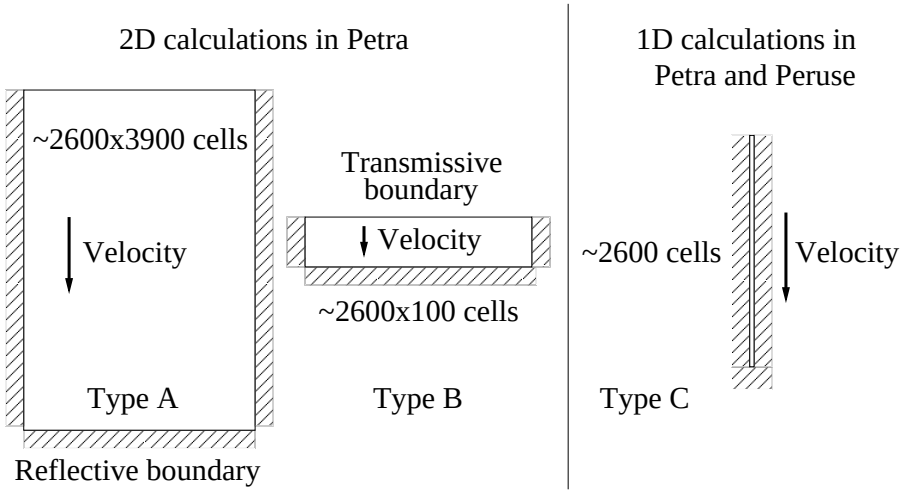

Figure 7.1: Geometries of the planar hydrocode simulations used to obtain bulk temperature distributions.

	ρ_0 (g/cm^3)	T_0 (K)	$c_{v,s}$ (J/g K)	a (cm/µs)	b	Γ_0
HMX crystals	1.891	300	1.1	0.2901	2.058	1.0
EDC37 binder	1.391	300	1.6	0.2	1.4	1.0
PBX9501 binder	1.27	300	1.6	0.24	1.70	1.0

Table 7.1: Unreacted equation of state parameters used in hydrocode simulations to determine bulk temperature distributions.

effects of heat conduction and chemistry in Peruse.

Simulations were run using four different impact velocities: 0.3, 0.5, 1.0 and 1.7 km/s. The lowest three velocities generate shocks of comparable strength to those in shock initiation experiments. The highest velocity of 1.7 km/s provides an extreme upper limit, equivalent to an input pressure of approximately 20 GPa. Experimental Pop-plots for EDC37 and PBX9501 extrapolate to a run-to-detonation time of ~0.15 µs at this pressure, comparable to the duration of the simulations. Apart from a few simulations in section 7.2.6, the HMX and binder regions are treated as inert, unreacted material using a linear Grüneisen equation of state ($U_s = a + bu_p$). The equations of state coefficients (listed in table 7.1) are taken from chapter 3 apart from T_0 which is set to the Petra default value of 300 K. The effect of changing T_0 will be discussed in section 7.1.3.

7.1.1 Temperature distributions

To obtain temperature data from the hydrocode simulations, temperature prints were requested at selected time intervals. Data from these prints were analysed using two different versions of a purpose-built Fortran script. These read the temperature prints, count the number of cells for which the temperature falls into user-defined bins and convert these statistics to probability distribution functions. The Petra version is more complicated because it must deal with both pure and mixed cell data in two dimensions, while the Peruse version need only read pure cell data in one dimension. In Peruse, the probability distribution function (PDF) is calculated using

$$\mathrm{PDF}(\mathrm{K}^{-1}) = \frac{\eta}{\aleph\omega},$$

where η is the number of cells assigned to each temperature bin, $\aleph$ is the total number of cells that have been shocked (i.e. whose temperature is greater than the initial temperature) and ω is the width of each temperature bin in K. Since all cells are pure, η is an integer. In Petra, the probability distribution function is calculated using

$$\mathrm{PDF}(\mathrm{K}^{-1}) = \frac{\sum_i \varphi_i}{\aleph\omega},$$

where φ_i is the volume fraction of the material i whose temperature lies within the temperature bin. The total number of shocked cells $\aleph$ is calculated by summing volume fractions and so need not be an integer. Currently, the script does not have the capability to analyse spatial variations in temperature distributions. Note that the probability is quoted at the temperature in the centre of each bin.

A typical temperature distribution is shown in figure 7.2. The detached feature on the far left-hand side is due to unshocked material at 300 K. The dominant spike in the centre of the distribution corresponds to shocked HMX, while the rounded hump on the right is due to shocked binder cells. The HMX peak is always at a lower temperature than the binder peak because the binder is softer than HMX, and so is shocked to higher temperatures. Details of the temperature distributions will be discussed in section 7.3. Figure 7.2 also illustrates the variation with time that occurs in type C calculations. Although the HMX and binder spikes remain centred around 500 K and 670 K respectively, and have similar widths, the magnitude of the features varies with time as the shock travels through the microstructure. Results in section 7.3 will show that the time variation is smaller in

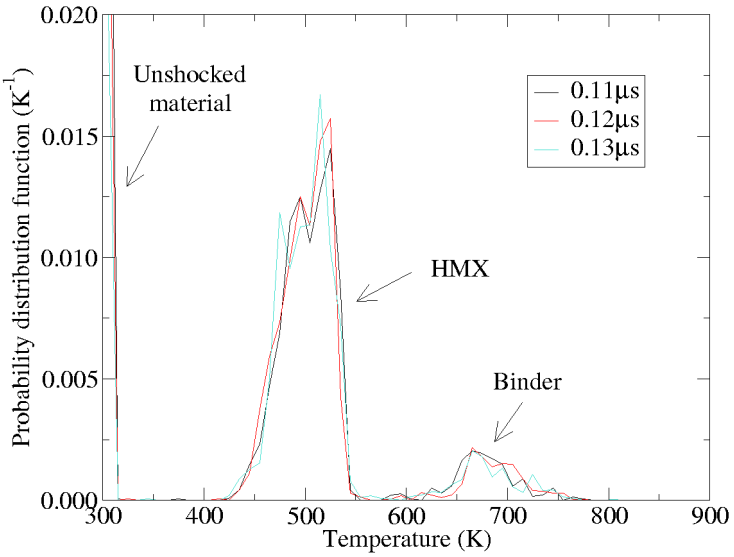

Figure 7.2: Petra calculations of a type C geometry at 0.11 μs, 0.12 μs and 0.13 μs, to illustrate the variation that occurs with time.

type A simulations. For now, the time variation in figure 7.2 provides a baseline against which other factors will be compared.

7.1.2 Hydrocode comparisons

A simple test of any computational simulation is to run it in two different codes to check whether the same results are produced. To allow comparison between Petra and Peruse, the one-dimensional type C geometry was used with a microstructure representative of EDC37. The results in figure 7.3 show that, while the temperature distributions produced by the two hydrocodes are not identical, the differences are similar to the variation that occurs with time. This provides confidence that the choice of numerical scheme is not significantly affecting the results, and allows both codes to be used to investigate the effect of changes to material properties data, for example. This is a significant advantage because the tabular equation of state treatment in Petra allows heat capacity and Grüneisen Γ to be varied (which is not possible in the current Peruse implementation), while Peruse allows the effect of heat conduction and Arrhenius chemistry to be evaluated.

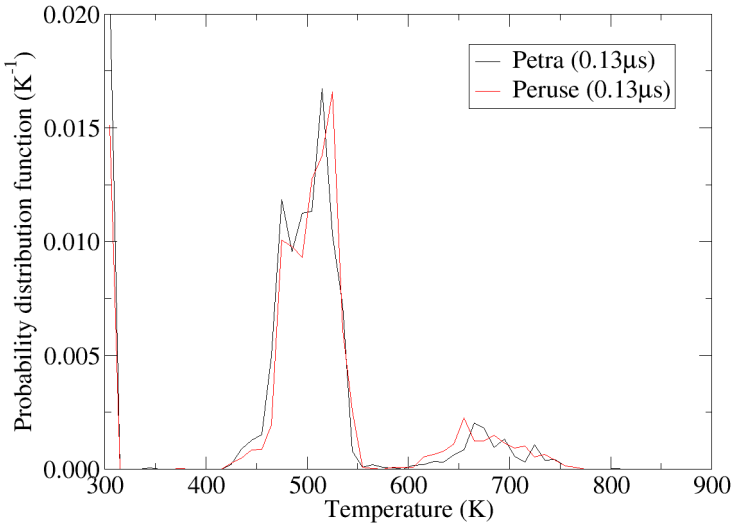

Figure 7.3: Type C calculations of EDC37 in Petra and Peruse, to compare the temperature distributions produced using two different hydrocodes.

7.1.3 Effect of computational settings

Peruse and Petra each contain a number of computational settings whose values need to be chosen to avoid influencing the temperature distributions. Settings that were found to have a negligible effect include the option to retain partial densities for mixtures, a function to remove small volume fractions of material left behind during advection, the default maximum value of four Lagrangian steps per Eulerian remap step in Petra, and cutoffs to prevent numerical rounding errors causing motion in cells that should be at rest. The settings that were found to have a significant effect on the results are discussed below.

Timestep settings

The timestep used to advance the numerical solution in Peruse and Petra is controlled by the Courant factor (see section 2.2.1). In addition, an initial timestep can be specified by the user and timestep growth factors control the rate at which the timestep can change. Within appropriate ranges, it was found that the choice of values for the timestep controls has very little effect on the temperature distributions, demonstrating that the results are timestep-converged. A Courant factor of 0.2 in Petra and 0.5 in Peruse has been used for all the simulations described in this chapter, with an initial timestep of 10^{-5} μs and

a growth factor of 2.0 in Petra. The reasons why the two codes need different Courant factors is currently under investigation [110].

Artificial viscosity

The Wilkins form [98] of artificial viscosity is commonly used in Petra while a monotonic artificial viscosity [27] is recommended in situations where there is a suspicion of artificial viscosity over-heating, and this can either use an estimate of the sound speed or the actual value calculated from the equation of state. Monotonic artificial viscosity is also available in Peruse. Changing the artificial viscosity treatment was found to have a slight effect on the temperature distributions, but it is small compared to the variation that occurs as a function of time (figure 7.2). For consistency between Peruse and Petra, the monotonic artificial viscosity option with sound speed calculated from the equation of state and coefficients $\beta_L = 0.5, \beta_Q = 0.75$ has been used in this chapter.

Pressure relaxation and energy dissipation

Pressure relaxation is available in Petra to allow the materials within a mixed cell to approach pressure equilibrium at the end of the Lagrangian step (see section 2.2.1). As shown in figure 7.4, pressure relaxation makes a bigger difference to the binder temperature distribution than to that of HMX, because the small proportion of binder in the plastic-bonded explosive means that much of it is located in mixed cells. Since pressure relaxation is designed to improve the accuracy of the numerical solution, it is switched on in the Petra calculations described in this chapter.

An energy dissipation function is available in Petra to add the kinetic energy lost from each cell during advection to its internal energy, similar to that implemented in Chec. The effect of using energy dissipation is shown in figure 7.5. When dissipation is turned off, the temperatures reached in the simulation are lower than when it is turned on because energy has been lost. Since it helps conserve total energy, energy dissipation is turned on for the simulations in this chapter.

Pressure relaxation and energy dissipation are not applicable to Peruse which is a Lagrangian code with no advection step and no mixed cells.

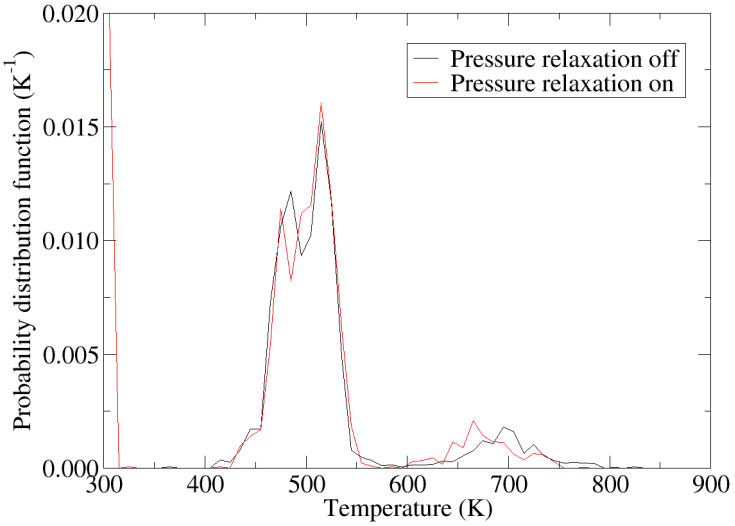

Figure 7.4: Effect of pressure relaxation in a Petra type C calculation. Pressure relaxation is switched on for the other simulations in this chapter.

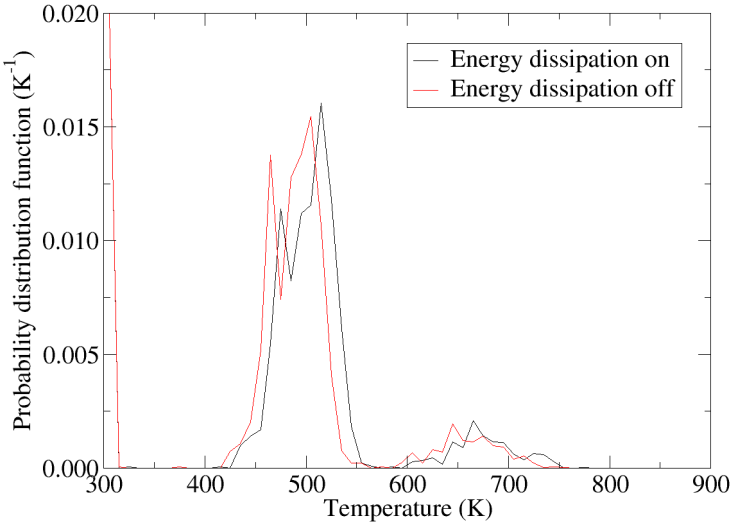

Figure 7.5: Effect of energy dissipation in a Petra type C calculation. Energy dissipation is switched on for the other simulations in this chapter.

Boundary conditions

Type A, B and C calculations in Petra use a reflective boundary as a rigid wall at the bottom of the computational geometry, as illustrated in figure 7.1, with several rows of void cells and a transmissive boundary at the top. The void cells are included to allow inflow through the transmissive boundary at the top of the computational domain. It was checked that the choice of either transmissive or reflective lateral boundary conditions at the left and right of the domain makes very little difference to the resulting temperature distributions, so reflective lateral boundaries are used. The effect of introducing an initial gap between the explosive microstructure and the rigid wall in a type C Petra calculation was found to be much smaller than the variation that occurs as a function of time (figure 7.2), so the majority of the simulations in this chapter have no gap.

In Peruse, a reflective boundary is used as a rigid wall with a free surface at the other end of the computational geometry. It was found that the temperature distributions obtained using a rigid-wall boundary or a symmetrical-impact geometry are almost identical.

7.1.4 Effect of geometry and meshing

A single micrograph has been used to derive the type A computational geometries for each of EDC37 and PBX9501. It is important to check that the choice of micrograph has not affected the results, but running several type A simulations with geometries derived from different micrographs would be computationally expensive. An efficient solution is to use type C simulations to investigate the effect of choosing different 1D slices through the 2D micrograph, since it is expected that the variation between micrographs would be no worse than the variation between 1D slices. The temperature distributions from three type C Petra simulations of EDC37 in figure 7.6 show that the choice of microstructure does have an effect, but the overall width and magnitude of the HMX and binder distributions is unchanged. The effect is of similar magnitude to the variation that occurs as a function of time (figure 7.2). The size of the computational domain is fixed by the micrographs. No additional simulations have been run to prove that this is sufficiently large to be a representative volume element [195], but it is comparable to the domain sizes used by Baer [163] and others for modelling HMX-based explosives.

Figure 7.7 shows that temperature distributions produced using a 1D type C geometry are similar to those from a 2D type B geometry and those from a 2D type A geometry.

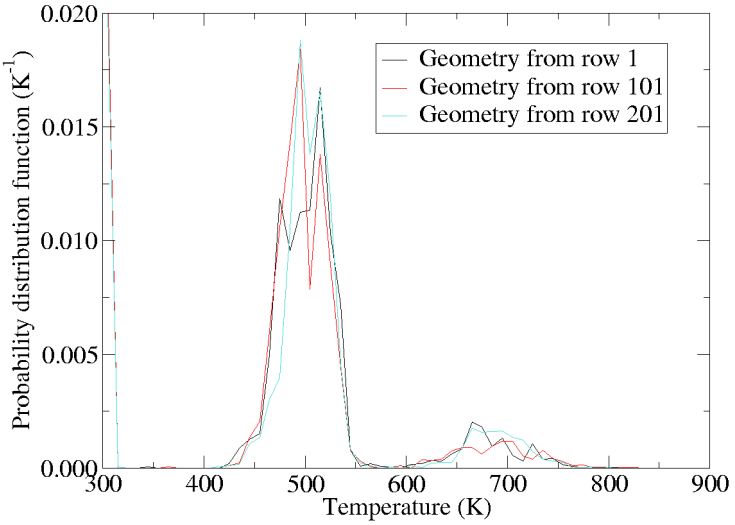

Figure 7.6: Comparison between Petra type C simulations with computational geometries derived from different 1D slices of an EDC37 micrograph.

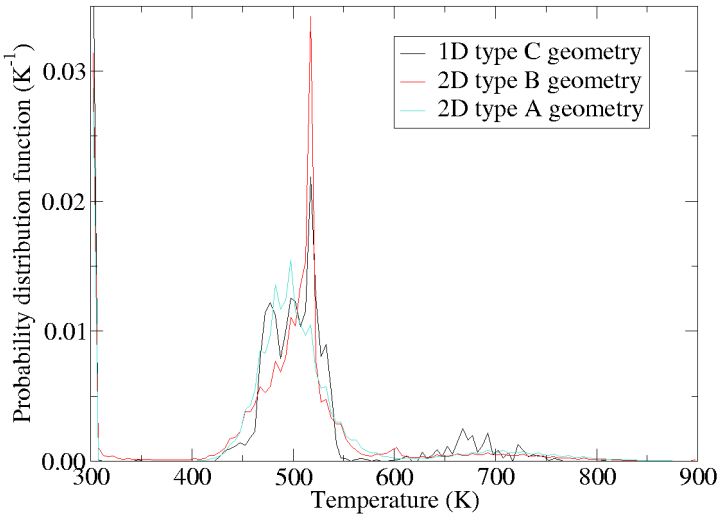

Figure 7.7: Temperature distributions from type A, type B and type C Petra calculations of EDC37 at 1.0 km / s impact velocity, to investigate the effect of geometry.

There are two obvious differences. Firstly, the HMX peak has a higher spike in the type B geometry owing to the greater proportion of HMX cells that are shocked cleanly, without being influenced by the presence of binder regions. This is a result of using a long, thin computational geometry (see figure 7.1) and is not physically realistic. Secondly, the binder peak is more noisy and finishes at ~770 K in the type C geometry, compared to ~920 K for type A and B. This is because there are considerably fewer computational cells in a type C geometry so the temperature distributions are subject to greater statistical variation. However, the distributions are centred around the same peak temperature and have approximately the same width and shape. This indicates that shock focusing effects in 2D do not cause dramatically different shock temperatures to be developed.

A similar effect might be expected if 3D microstructure calculations could be undertaken at sufficient mesh resolution. Unfortunately, 2D type A calculations take roughly 12 hours to run on 100 processors on a Cray XT3 supercomputer, and $n \sim 1000$ zones in the third dimension would make the simulations take at least n times as long to run. Even running on more processors, such calculations are unlikely to be feasible for some years to come. Figure 7.7 suggests that 3D microstructure calculations are unlikely to produce dramatically different temperature distributions to those from 1D or 2D calculations. Therefore, the uncertainties associated with the simplification to 1D or 2D geometry are considerably lower than those due to material properties data (see section 7.2).

The effect of mesh resolution was investigated using three type C calculations in Peruse with approximately 1 μm, 0.5 μm and 0.1 μm meshing. The results in figure 7.8 show that the width of the temperature distributions reduces as the mesh is refined, since a smaller proportion of the cells suffer from the wall heating effect (see section 7.2.5). In addition, two type B Petra calculations with 1 zone / pixel or 4 zones / pixel, equivalent to 0.26 μm or 0.13 μm meshing respectively, produced nearly-identical temperature distributions. These results confirm that the use of 1 zone / pixel meshing is perfectly adequate for microstructure simulations.

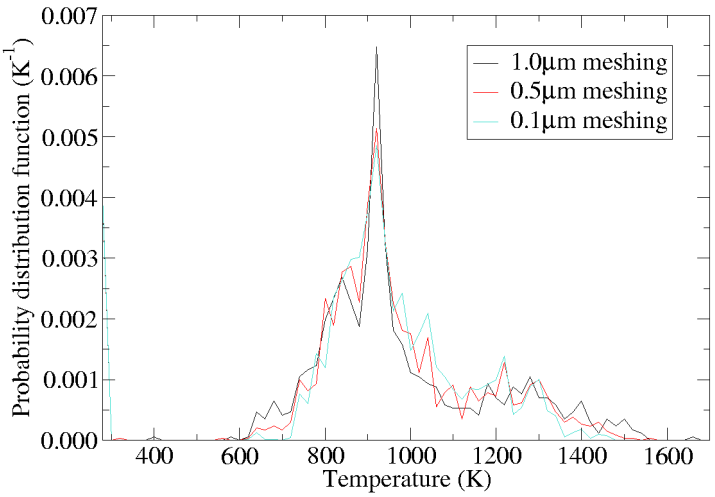

Figure 7.8: Temperature distributions from three type C Peruse calculations with 1 μm, 0.5 μm and 0.1 μm meshing, to investigate the effect of mesh resolution.

7.2 Material modelling

It was expected that the uncertainties in the material properties data could have a significant effect on the temperature distributions in type A, B and C calculations. The material modelling uncertainties, assumptions and the numerical wall heating effect will be investigated below. The model parameters will be varied independently to be consistent with section 5.3.

7.2.1 Temperature calculation

As discussed in section 3.1, Petra's equation of state package uses numerical integration to construct temperature tables for the unreacted equation of state. To avoid the microstructure simulations crashing, the temperature tables must be large enough to cover any possible state that may be generated during the hydrocode calculation, so the temperature range was specified at $300 - 10,000$ K. Although this results in relatively coarsely-resolved temperature tables, a type C Petra simulation was used to check that the effect on temperature distributions is very small. The temperature tables cover a compression range of $0.5 - 1.93$ for HMX, $0.5 - 3.0$ for the binder in EDC37 and $0.5 - 2.4$ for the binder

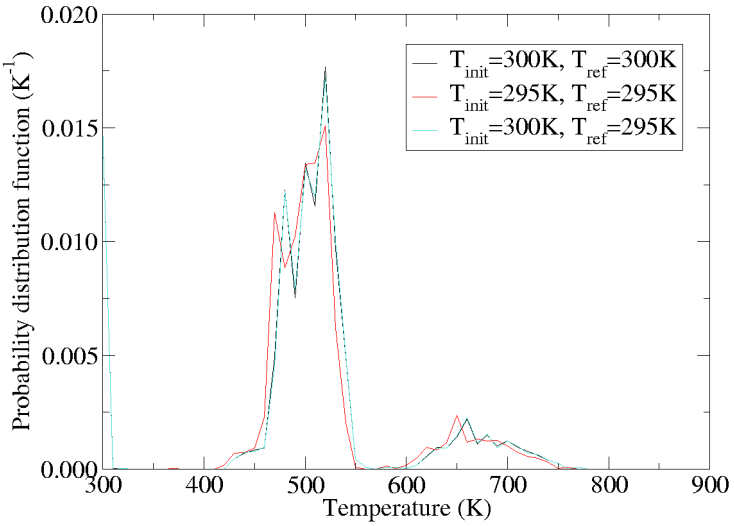

Figure 7.9: Effect of the initial temperature T_{init} and reference temperature T_{ref} in a Peruse type C calculation. Usually, these are both set equal to $T_0 = 300\,\text{K}$.

in PBX9501. As the linear Grüneisen equation of state contains a singularity at ρ^* (see section 3.2), the compression range must be chosen to avoid densities above this value, which is different for each material. Although the pressure tends to infinity as the singularity is approached, so theoretically no cells in the calculation should return densities higher than ρ^*, the finite timestep means that this can sometimes occur. It was checked that such errors only affect a handful of cells in each hydrocode calculation, and only for a few timesteps. Unfortunately, equation of state errors do cause a type A calculation of EDC37 at 1.7 km/s to fail but, since the other simulations finish containing only a few error messages, it is judged that these errors can be ignored.

The equation of state routines used in Petra are restricted to an initial temperature of 300 K, and this is also used as a reference temperature for the unreacted equation of state. Three type C Peruse simulations were used to investigate the effect of changing the initial temperature from 295 K to 300 K. Figure 7.9 shows that changing the reference temperature, but not the initial temperature, has a tiny effect on the temperature distributions. Altering the initial temperature by 5 K has more effect on the temperature distributions, but it is no bigger than the natural time-variation (figure 7.2). A baseline initial temperature of 300 K is used throughout this chapter, for consistency between Peruse and Petra.

7.2.2 Heat capacity

As discussed in section 3.2, there is considerable uncertainty in the value of heat capacity for unreacted HMX and the binder materials, because experimental measurements are difficult at shock temperatures and pressures. Figure 7.10 shows the effect of changing the constant value of $c_{v,s}$ for HMX within the uncertainty limits. The HMX temperature distribution shifts to higher temperatures and broadens as its heat capacity is reduced, while the binder distribution is unchanged. The broadening occurs because a given distribution of specific internal energies corresponds to a wider range of temperatures for low heat capacities. (Note that these Petra simulations do not include thermal conduction.) To check the validity of the assumption of constant heat capacity, the tabular heat capacity data for HMX in table 3.1 were used in a Petra type C simulation. The results in figure 7.11 show that, while there is a difference in the temperature distributions, the use of a constant $c_{v,s} = 1.1\,\mathrm{J/g}$ is a reasonable approximation.

The effect of the uncertainty in the heat capacity of EDC37's binder is shown in figure 7.12. Although there is no difference to the temperature distribution for HMX, the binder distribution changes significantly. Unfortunately, little can be done to reduce the uncertainty on the experimental data because the binders begin to decompose at shock temperatures. The 100 K differences in binder temperature in figure 7.12 would have a

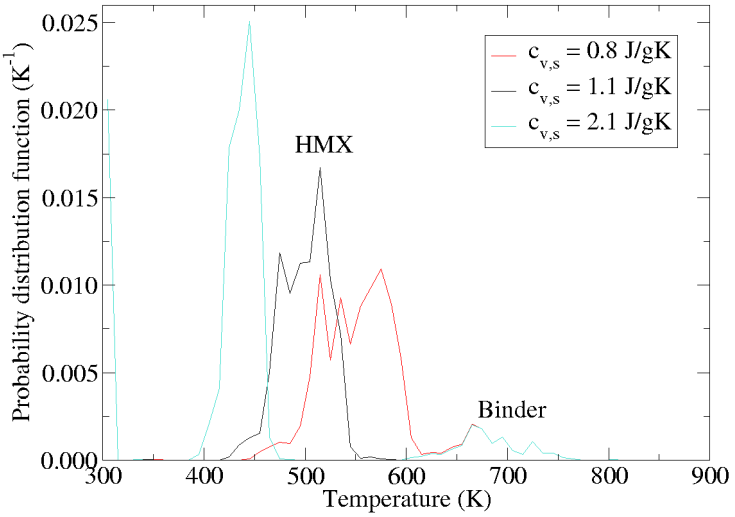

Figure 7.10: Effect of the uncertainty in HMX heat capacity in a Petra type C calculation.

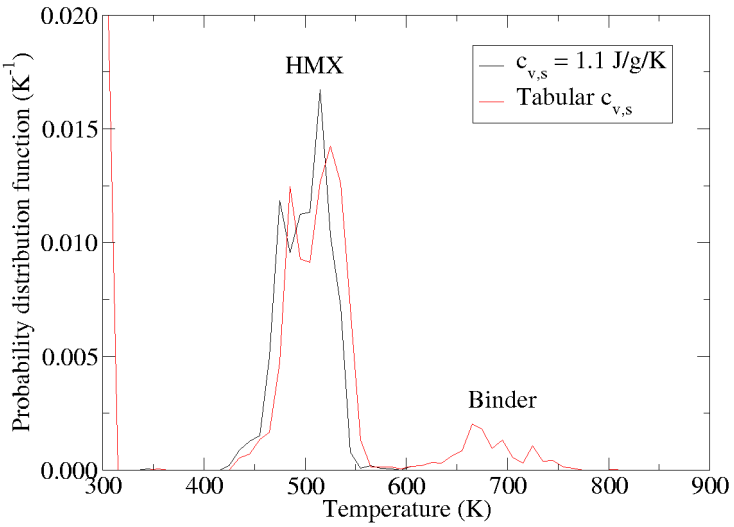

Figure 7.11: Effect of using a tabular HMX heat capacity rather than constant $c_{v,s}$ in a Petra type C calculation.

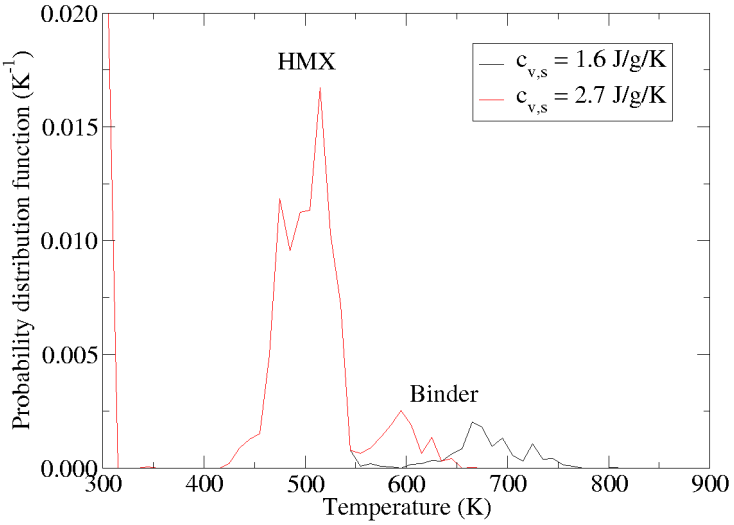

Figure 7.12: Effect of the uncertainty in binder heat capacity in a Petra type C calculation of EDC37.

significant effect on the Arrhenius rates in a fully-reactive simulation, and the binder in PBX9501 is expected to behave similarly.

7.2.3 Hugoniot parameters

The effect of the uncertainty in Hugoniot parameters (see section 3.2) was investigated by running three type C Petra simulations for each material: a baseline, one with the maximum reasonable Hugoniot gradient and one with the minimum. Figure 7.13 shows the results for HMX. The most significant effect of reducing the gradient of the Hugoniot is to shift the HMX temperature distribution to lower temperatures. However, the binder temperature distribution is also affected because the temperatures achieved are a function of the wave interactions between the two materials. Figure 7.14 shows the effect of changes to the binder Hugoniot. As before, while the most obvious effect of a shallower Hugoniot gradient is a shift of the binder temperature distribution to lower temperatures, the HMX distribution is also affected. The effect of changing the Hugoniot of PBX9501's binder is expected to be similar.

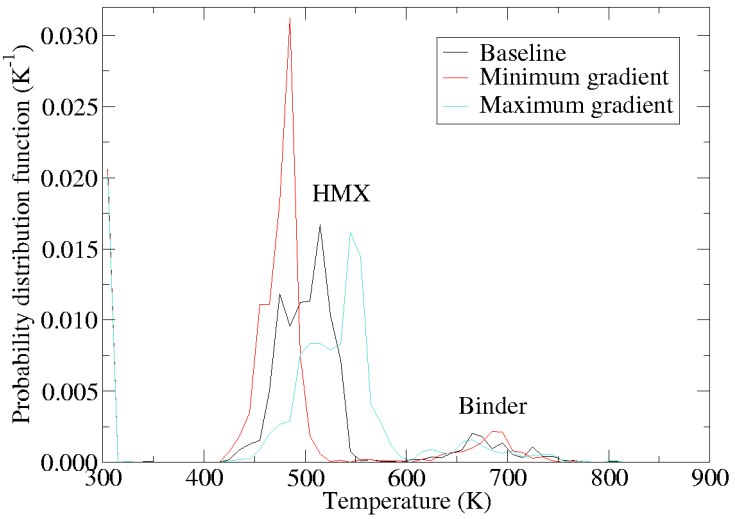

Figure 7.13: Effect of the uncertainty in HMX Hugoniot in a Petra type C calculation of EDC37.

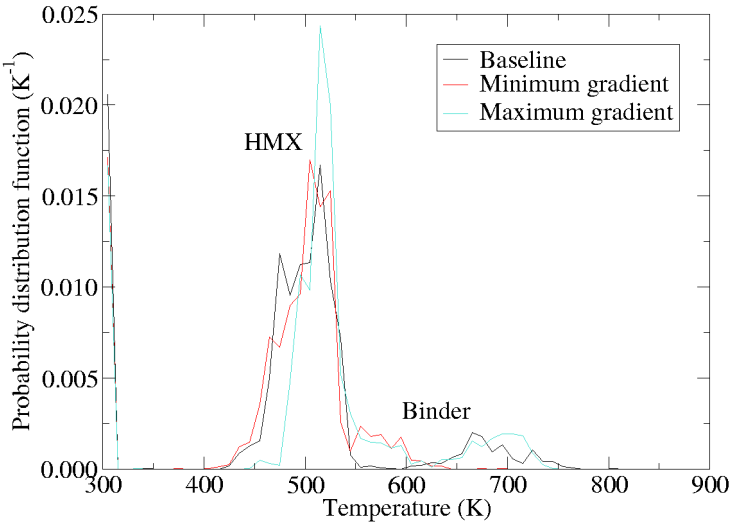

Figure 7.14: Effect of the uncertainty in binder Hugoniot in a Petra type C calculation of EDC37.

7.2.4 Grüneisen Γ

Peruse simulations are currently restricted to a value of Grüneisen $\Gamma = 1$ only (see section 3.1.4). The tabular temperature-calculation method in Petra was used to investigate the effect of changes to the value of $\Gamma = \Gamma_0 + \Gamma_1 v/v_0$. The results in figure 7.15 show that changing the value of Γ can have a significant effect on the temperature distributions.

7.2.5 Heat conduction and the wall heating effect

To investigate the effect of the uncertainty in thermal conductivity k of HMX and the binders, three type C Peruse simulations were run: a baseline, one with maximum reasonable k from section 3.2, and one with minimum k. The results in figure 7.16 show that, as k is increased, the tails of the overall temperature distribution reduce while the overlap between HMX and binder distributions increases. However, the effect is similar to the natural variation that occurs with time (figure 7.2) and is smaller than the effect of $c_{v,s}$ and the Hugoniot parameters.

To gauge the effect of almost removing heat conduction from Peruse, a further type C simulation was run with k reduced by a factor of 10^4. Figure 7.17 shows temperature

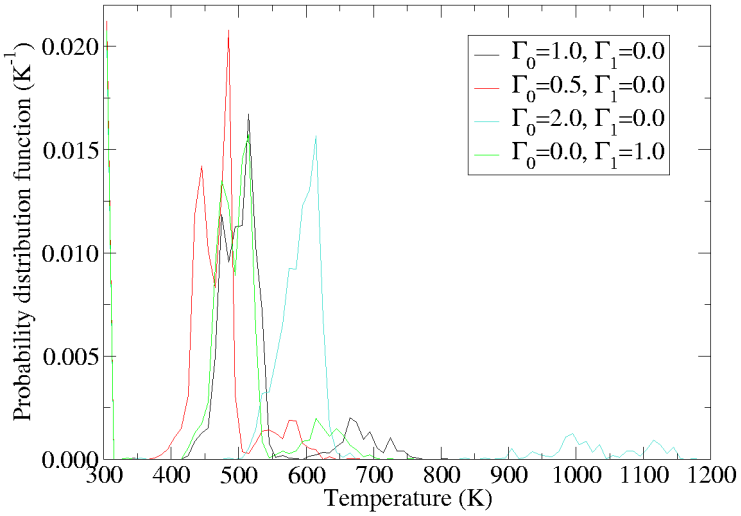

Figure 7.15: Effect of the uncertainty in Grüneisen Γ in a Petra type C calculation of EDC37.

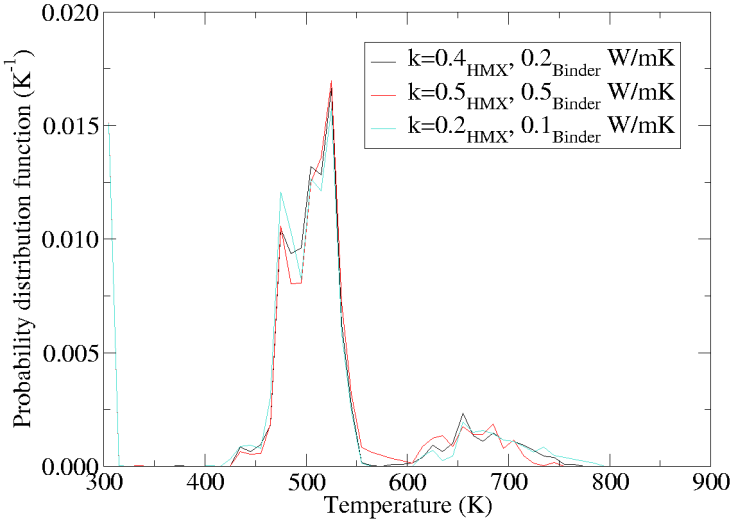

Figure 7.16: Effect of the uncertainty in thermal conductivity *k* in a Peruse type C calculation of EDC37.

profiles from two regions containing alternating layers of HMX crystals and binder. In the case of negligible heat conduction (red curves), ~50 K temperature spikes are observed at the interfaces between HMX and binder layers, caused by wall heating errors (see section 2.2.1). With baseline values for thermal conductivity, over time the temperature spikes in figure 7.17 are smoothed out by the effects of heat conduction. Close behind the shock front, the temperature spikes are present (bottom plot) but, well behind the shock front, the spikes are almost completely removed (top). In addition, heat conduction acts to smear out the physically-correct temperature differences between HMX and binder regions. The importance of this depends on the timescales of thermal conduction in HMX and the binders. From section 2.1, this timescale is $\Delta t \sim (5 \times 10^6\,\mathrm{s/m^2})\Delta x^2$ so, for the 0.3 μs duration of simulations in this chapter, the maximum distance that can be influenced by thermal conduction is ~0.2 μm. This is consistent with figure 7.17, where the temperature spikes are smoothed out by the effects of heat conduction but there is little degradation to the temperatures in the middle of the HMX and binder regions. Since the effect of baseline k on these simulations is to remove the wall heating spikes but not the temperature differences between regions, significantly reducing k allows the effect of wall heating errors to be established.

Temperature distributions from the type C simulations with baseline and reduced thermal conductivity are shown in figure 7.18. The main effects of reducing k are that the low-temperature tail of the HMX distribution is extended, and the binder distribution is broadened and shifted to higher temperatures. It is not surprising that the temperature distribution of the binder is most greatly affected, because the binder is located in small isolated pockets. Figure 7.18 indicates that the wall heating effect broadens the calculated temperature distributions but does not significantly change their peaks, and the difference is comparable in magnitude to the variation that occurs as a function of time (figure 7.2).

A temperature profile from just behind the shock front in a type C Petra calculation indicates that the wall heating effect is less significant in Eulerian codes. Figure 7.17 (bottom) for Peruse can be compared directly with figure 7.19 for Petra, as they are both at the same position through the microstructure. The Petra temperature profile does not have any spikes, even when the temperatures of the components of mixed cells are examined (red lines). Although Petra does not include heat conduction, the additional dissipation associated with the advection step removes the spikes. Figure 7.20 shows that the temperature distributions from the Peruse and Petra calculations are similar to each other, indicating that the overall effects of heat conduction in Peruse (with baseline k) are similar to the

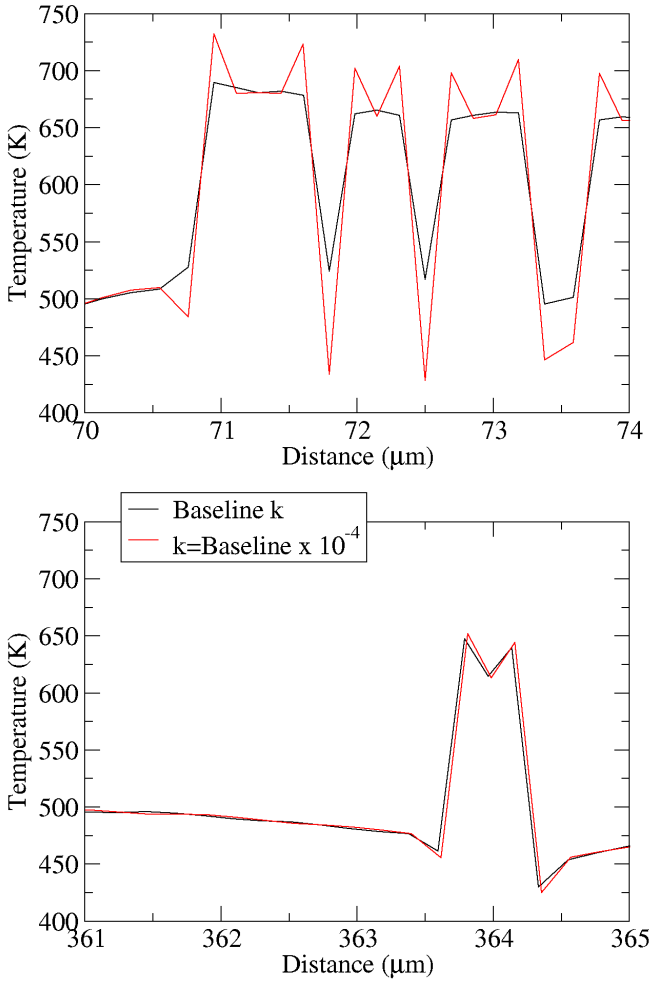

Figure 7.17: Temperature profiles from a type C Peruse simulation at 0.11 µs well behind the shock front (above) and close to the shock front (below). Baseline k values are taken from section 3.2.

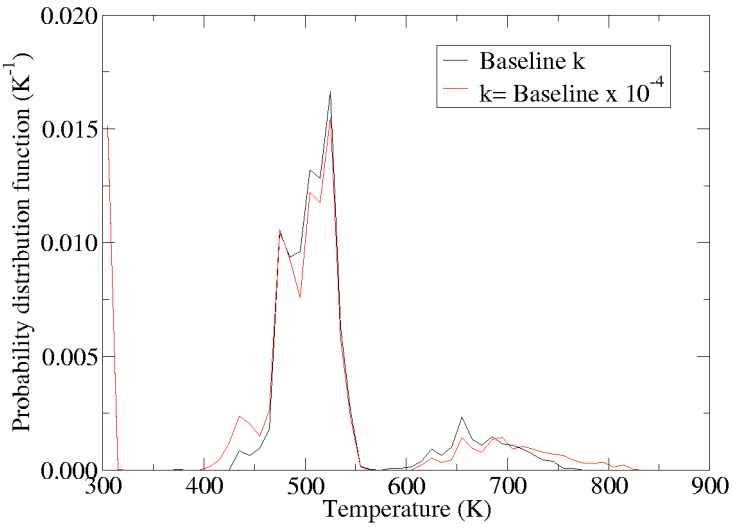

Figure 7.18: Effect of almost removing thermal conductivity k from a Peruse type C calculation. Baseline k values are taken from section 3.2.

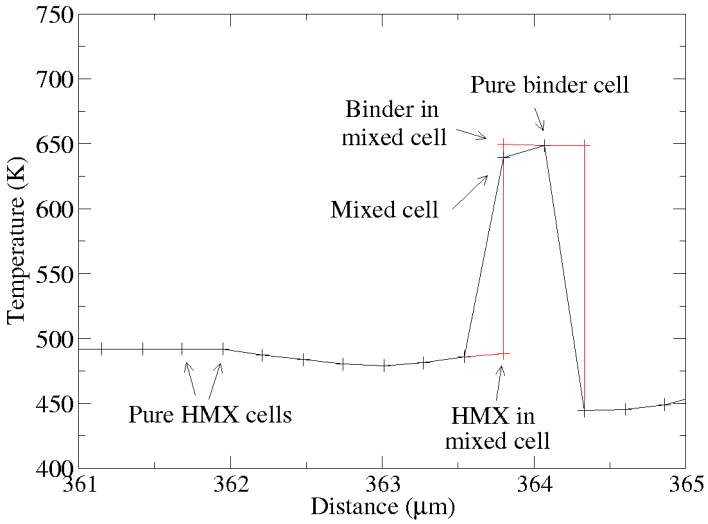

Figure 7.19: Temperature profile from a type C Petra calculation at 0.11 μs close to the shock front, at the same position as figure 7.17 (bottom).

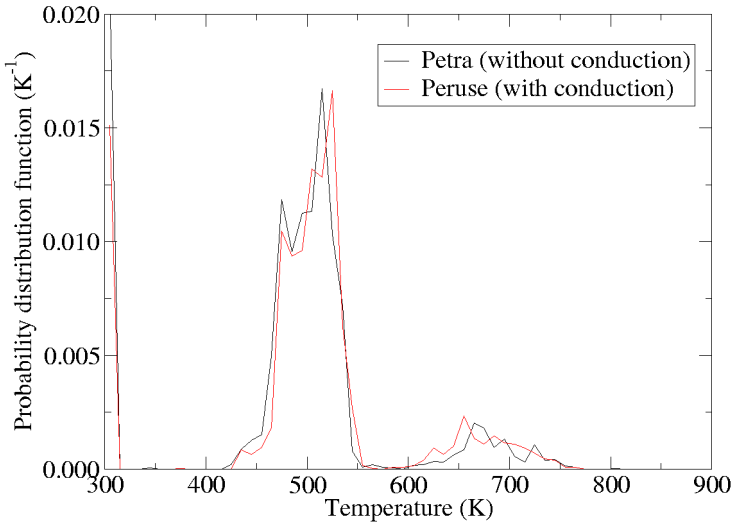

Figure 7.20: Comparison between a Peruse type C calculation with heat conduction and a Petra calculation without.

effects of the additional dissipation in Petra.

Another way to establish the influence of the wall heating effect is to increase the mesh resolution, so a smaller proportion of cells lie in the immediate vicinity of an interface and have inaccurate properties. As discussed in section 7.1.4, halving the mesh size in Petra from 0.26 μm to 0.13 μm has very little effect on temperature distributions. In Peruse, where the wall heating effect is more pronounced, figure 7.8 shows that increasing the mesh size from 0.1 μm to 1 μm broadens the temperature distributions. However, the effect is comparable to the natural time variation (figure 7.2).

Careful examination of graphical results from type A Petra calculations (see section 7.3) shows that there is a thin strip of hot cells at the bottom of the geometry, where the shock caused by the impact of the microstructure into the rigid boundary is first established. Fortunately, these correspond to only 0.1 % of the total number of shocked cells by the end of the simulation, and so they have a negligible effect on the calculated temperature distributions.

All of the factors described above show that, while it is possible to discern the influence of the wall heating effect on the calculated temperature distributions, the effect is minimal in type A Petra simulations. In addition, over the ~0.3 μs timescales of relevance for this work, it is concluded that heat conduction has a small effect on bulk temperature

distributions and can be neglected in the Petra calculations.

7.2.6 Effect of chemical reaction

The hydrocode simulations described in this chapter are all for inert explosive. Fully-reactive Peruse type C calculations were used to check the effect of this approximation. The HMX and binder components of EDC37 are more reactive than in PBX9501 owing to the higher temperatures achieved when a shock is passed through the microstructure, so it seems sensible to use EDC37 to investigate this effect. With 1.0 km / s impact velocity, a Peruse simulation of EDC37 produces almost no reaction; the maximum burn fraction achieved is less than 10^{-6} and the temperature distribution is almost identical to that from an inert simulation.

To establish the maximum realistic effect of chemical reaction, the impact velocity was increased to 1.7 km / s or approximately 20 GPa impact pressure, which is above the shock strengths generally relevant for shock initiation experiments. At this velocity, some of the binder regions in a type C calculation of EDC37 fully react within 0.10 µs. Figure 7.21 shows that the binder temperature distribution extends to ~2500 K in the reactive calculation but only ~1500 K in the inert case, and pressurisation of the system by the

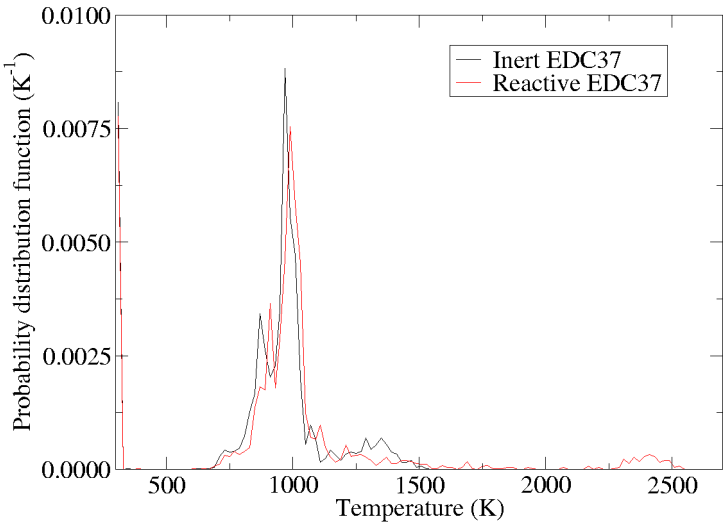

Figure 7.21: Effect of chemical reactions on a Peruse type C calculation with 1.7 km / s impact velocity.

conversion of some binder regions into gaseous products causes a slight increase in HMX temperatures. Overall, the effect of including chemical reactions is not great, even at this high shock strength.

These results suggest that temperature distributions derived from the inert calculations in this chapter can be used with confidence, as chemical reactions have very little effect on bulk temperature distributions at shock strengths of relevance to shock initiation.

7.2.7 Effect of strength

Although strength has been neglected in this work (see section 3.1), a variety of strength models are available in Petra. An isotropic, rate-independent model with constant shear modulus G and von Mises yield strength Y is used for HMX with $G = 12.0\,\text{GPa}$ and $Y = 0.26\,\text{GPa}$ from references 80 and 158. The results of a type B simulation in figure 7.22 show that slightly higher temperatures are produced in the HMX with strength than without. The difference between the two temperature distributions is sufficiently small that it is reasonable to neglect strength in the shock initiation and detonation regimes.

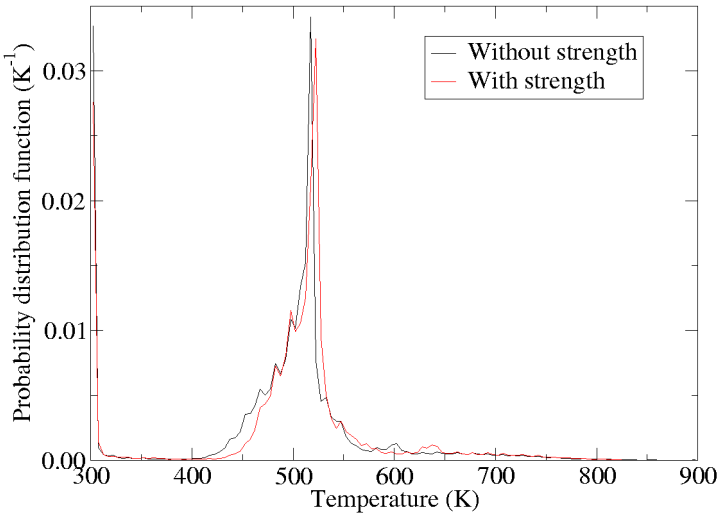

Figure 7.22: Effect of strength on a Petra type B calculation of EDC37 with 1.0 km/s impact velocity.

7.3 Results

The type B and type C calculations described in sections 7.1 and 7.2 have been used to investigate the effect of computational settings and material models on hydrocode simulations of PBX9501 and EDC37 microstructures. Most of the factors have a small effect on the calculated temperature distributions, comparable to the variation that occurs with time. However, the Hugoniot parameters, Grüneisen Γ and heat capacity of the HMX and binder materials all have a significant effect and it is recommended that future work should aim to reduce the uncertainties in these quantities (see section 8.2). Despite this, it is concluded that both Peruse and Petra can be used to generate reliable temperature distributions for PBX9501 and EDC37. Type B and type C simulations are limited in their applicability to real explosives by the extent of their computational geometry. Two-dimensional type A calculations are more representative but they are also computationally expensive, and so results from only seven such calculations will be described below.

7.3.1 Visual results

Graphical results from an EDC37 type A simulation are shown in figures 7.23, 7.24 and 7.25. These figures show average values and not the density, temperature or pressure of the individual components within a mixed cell.

The density map in figure 7.23 shows the location of crystal and binder regions within the explosive. The unshocked HMX crystals appear yellow, with blue/green binder between. A void region is present at the top of the geometry (dark blue) as mentioned in section 7.1. Initially, the entire microstructure was given a uniform downwards velocity of 0.3 km / s, which drives a shock upwards through the HMX crystals and binder. The shock has passed through the majority of the microstructure by this time and is visible as the boundary between the mainly-yellow and mainly-orange regions. The shock is not planar, as would be expected for a homogeneous geometry, but shows perturbations caused by the different shock velocity in the crystal and the binder regions. The shock has run ahead on the right-hand side where the proportion of HMX in the geometry is higher. This is an artefact caused by the EDC37 micrograph (figure 1.5 on page 10) fading away towards the right-hand side, as discussed in section 2.4. Binder cells are shocked to a lower density than the HMX, so they appear yellow/green in figure 7.23. There are density perturbations within the HMX crystals although these are difficult to see.

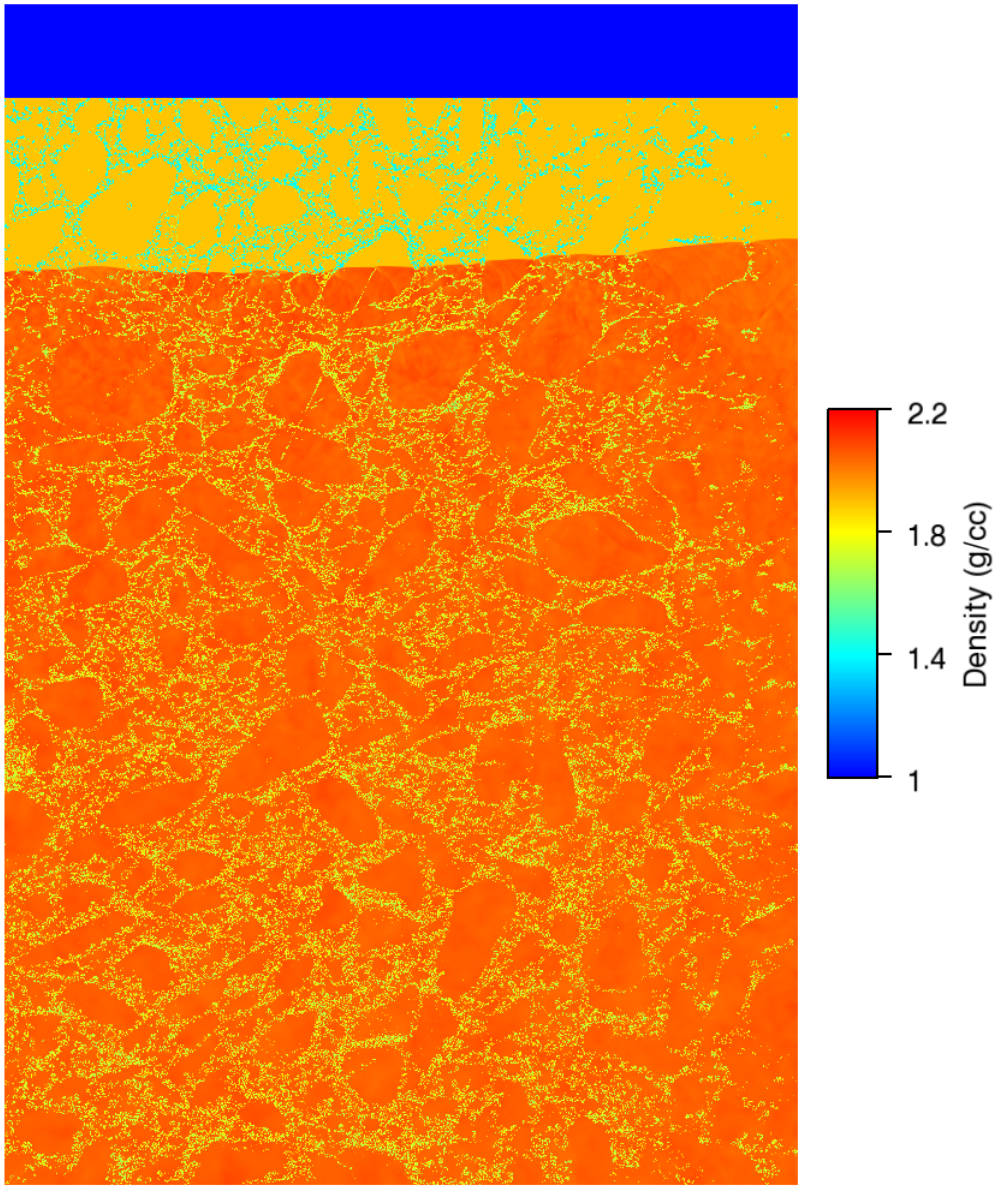

Figure 7.23: Density map from a type A calculation of EDC37 in Petra with 0.3 km / s impact velocity at 0.27 µs. Three distinct regions are visible; from top to bottom, these are the void (dark blue), unshocked explosive (mainly yellow) and shocked explosive (mainly orange).

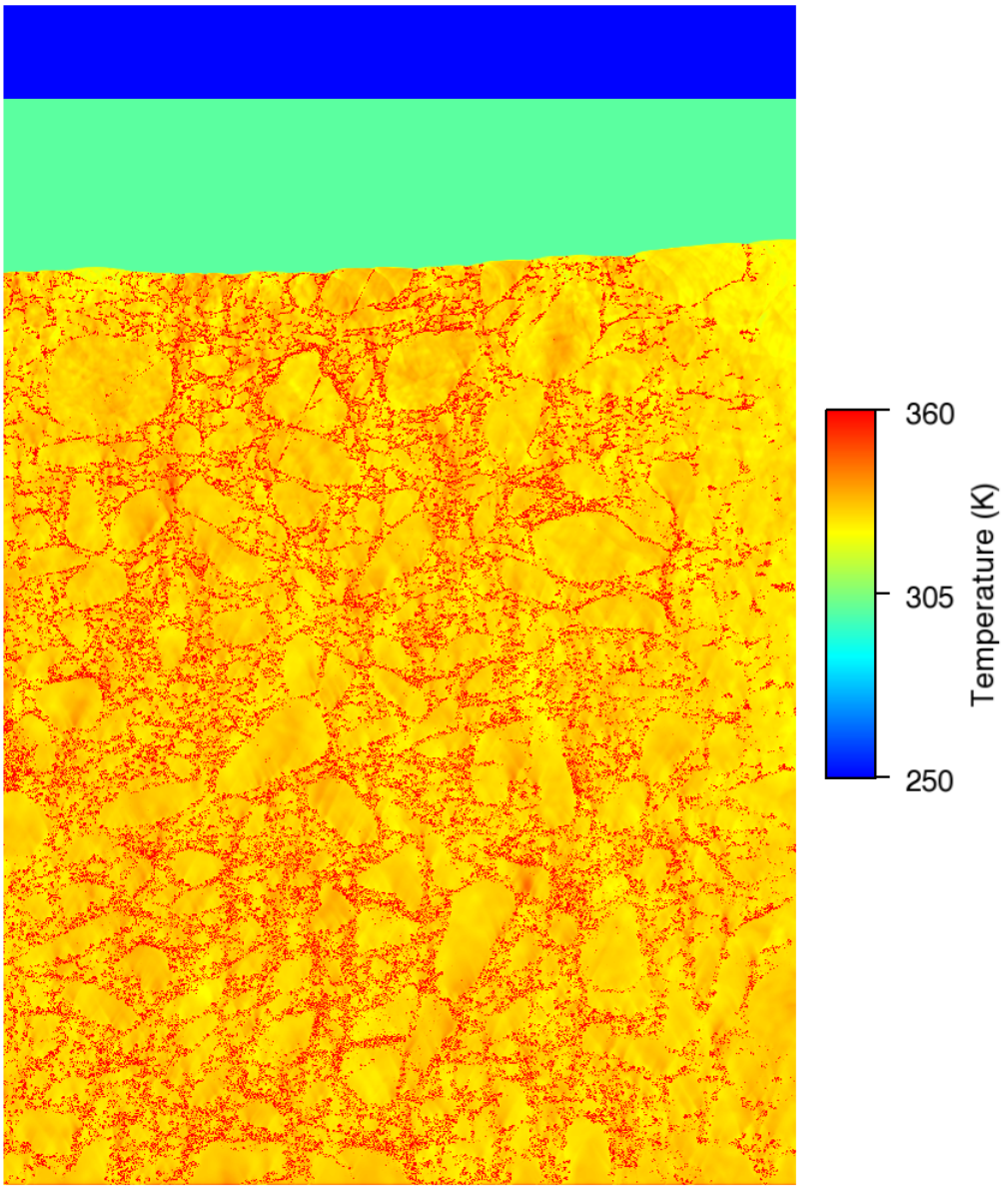

Figure 7.24: Temperature map from a type A calculation of EDC37 in Petra with 0.3 km / s impact velocity at 0.27 µs. From top to bottom, the three regions are the void (dark blue), unshocked explosive (green) and shocked explosive (yellow, orange and red).

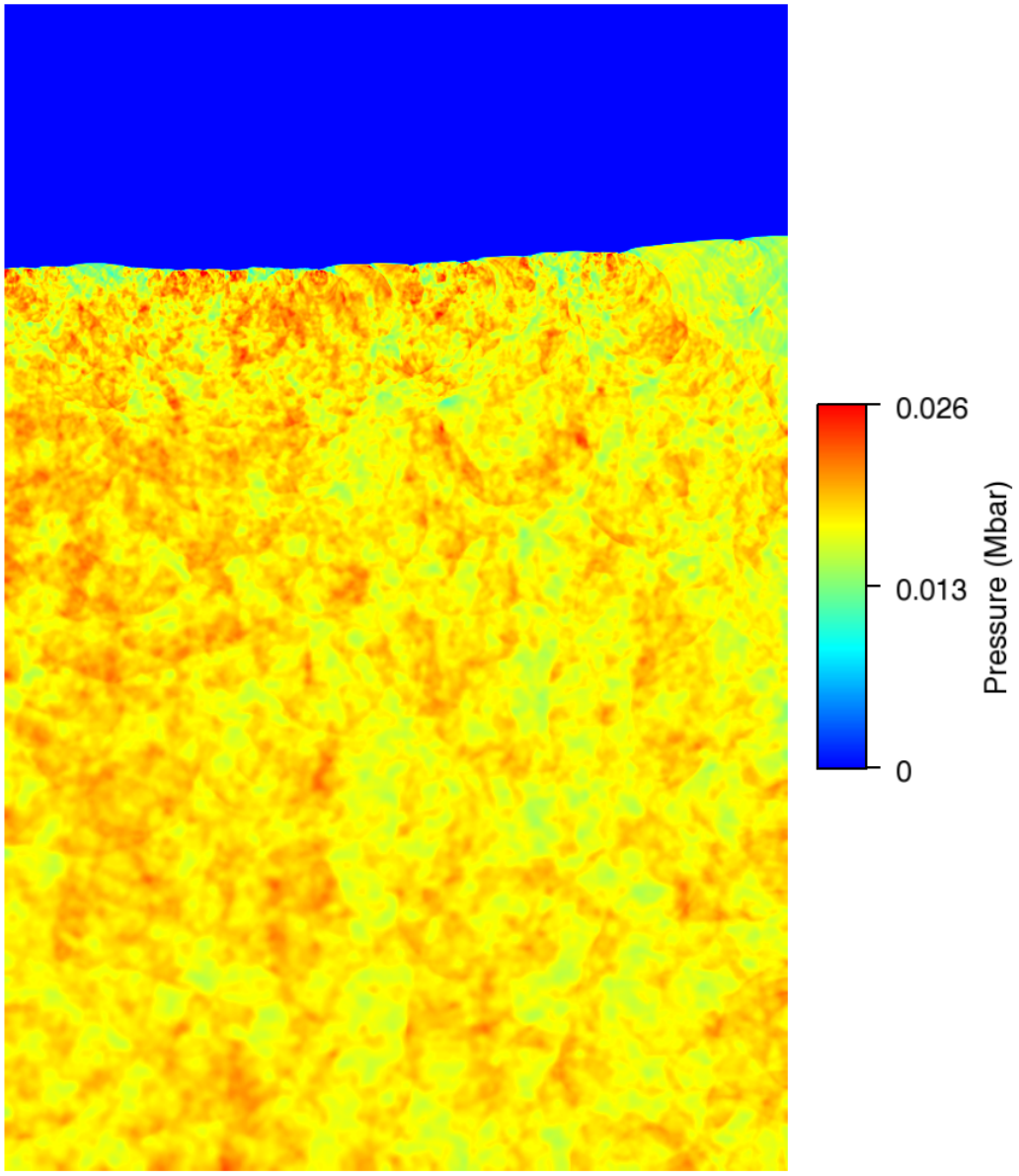

Figure 7.25: Pressure map from a type A calculation of EDC37 in Petra with 0.3 km/s impact velocity at 0.27 µs. Two distinct regions are visible; from top to bottom, these are the void and unshocked explosive (dark blue) and the shocked explosive (green, yellow and red).

The temperature map in figure 7.24 shows the binder cells as isolated hot regions (red) within the cooler shocked HMX (yellow), while the unshocked explosive has a uniform initial temperature of 300 K (green) and the void is dark blue. HMX temperatures are perturbed in diagonal shadow regions above the binder cells owing to two-dimensional shock-wave interactions. It is just possible to see a thin strip of hot cells at the bottom of the microstructure, caused by wall heating errors. Temperature distributions were extracted from each of the simulations of PBX9501 and EDC37 and will be discussed in more detail below.

The pressure map in figure 7.25 shows the pressure distribution in the shocked microstructure. The void and unshocked material both have zero pressure (dark blue). The colours are most vivid just behind the shock front, where red, yellow and green regions demonstrate that the pressure varies between 1.3 and 2.6 GPa. Well behind the shock front, the colours are more diffuse as the pressure waves, coupled with numerical diffusion, act to bring the microstructure closer towards pressure equilibrium. The colours are not associated with HMX crystal or binder regions, since pressure differences cannot be maintained across material interfaces.

Graphical results from a PBX9501 type A simulation with 0.3 km/s impact velocity are shown in figures 7.26, 7.27 and 7.28. The density map in figure 7.26 shows the void (dark blue), unshocked explosive (mainly yellow) and shocked explosive (mainly orange). Binder cells are clearly visible between the HMX crystals. The temperature map in figure 7.27 is similar to that for EDC37. The pressure map in figure 7.28 illustrates the pressure fluctuations that occur in the shocked microstructure; circular waves can be seen propagating away from binder-rich regions and interacting with each other. These are more obvious than they were in EDC37 owing to the large HMX crystal size in PBX9501. As before, the pressure fluctuations are greatest just behind the shock front (red to green) but die away behind the shock front as the system begins to approach pressure equilibrium. Pressure and temperature fluctuations will be discussed further in section 7.3.6.

7.3.2 Temperature distributions

Type A simulations of EDC37 and PBX9501 have been run at three different impact velocities: 0.3, 0.5 and 1.0 km/s, with an additional calculation at 1.7 km/s for PBX9501. As mentioned in section 7.1, these impact velocities generate shock pressures typical of

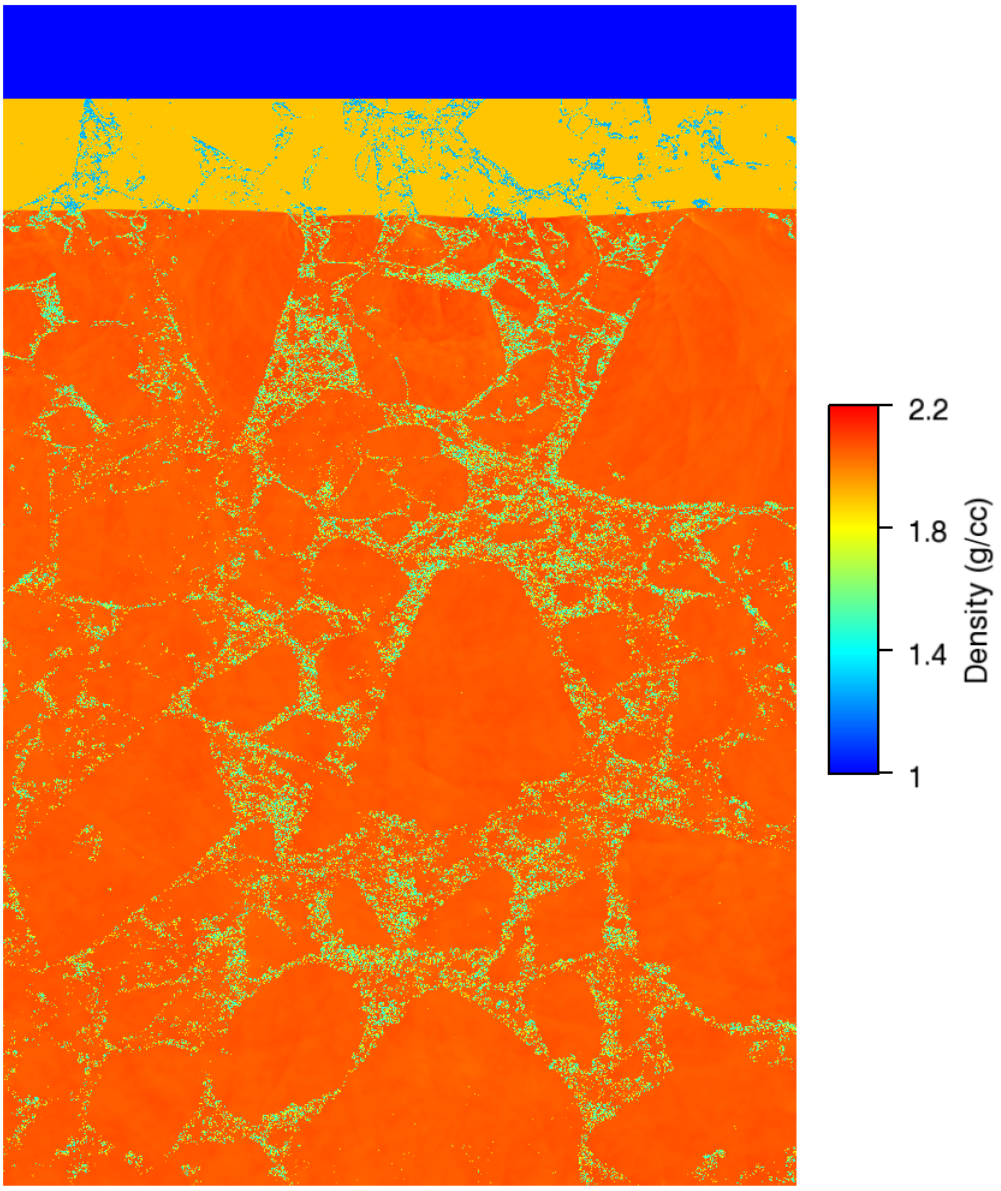

Figure 7.26: Density map from a type A calculation of PBX9501 in Petra with 0.3 km / s impact velocity at 0.27 µs. Three distinct regions are visible; from top to bottom, these are the void (dark blue), unshocked explosive (mainly yellow) and shocked explosive (mainly orange).

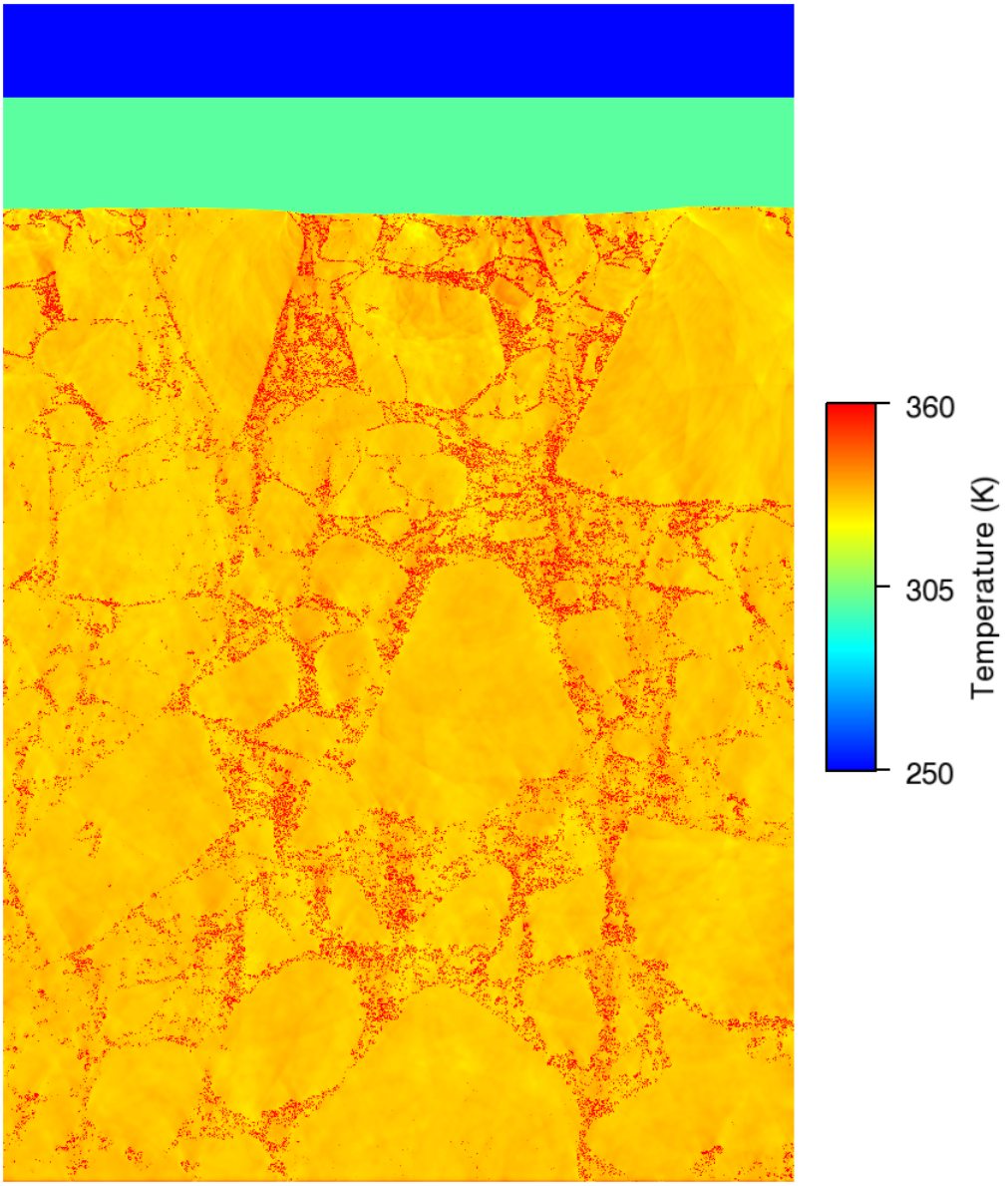

Figure 7.27: Temperature map from a type A calculation of PBX9501 in Petra with 0.3 km / s impact velocity at 0.27 µs. From top to bottom, the three regions are the void (dark blue), unshocked explosive (green) and shocked explosive (yellow, orange and red).

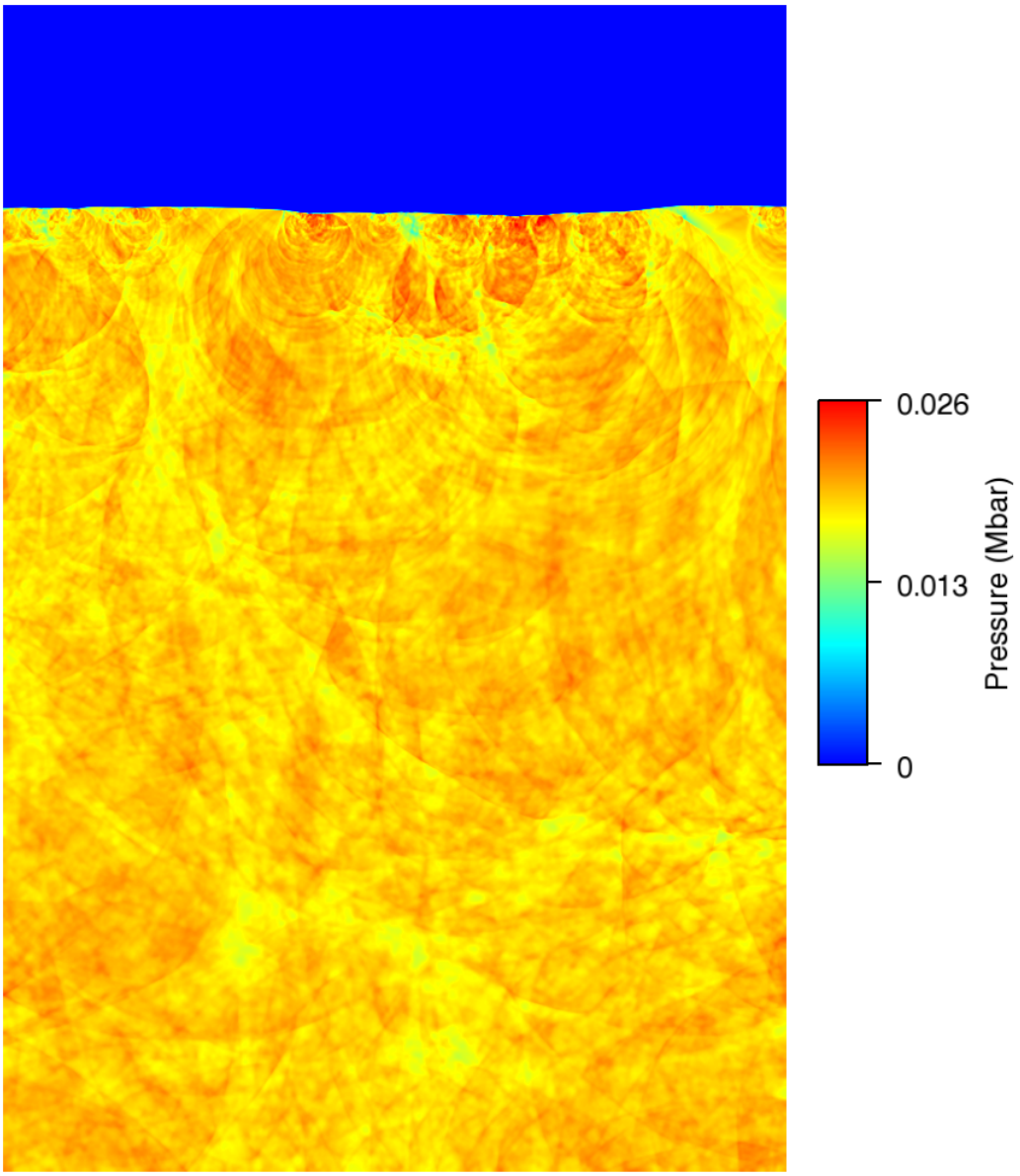

Figure 7.28: Pressure map from a type A calculation of PBX9501 in Petra with 0.3 km / s impact velocity at 0.27 µs. Two distinct regions are visible; from top to bottom, these are the void and unshocked explosive (dark blue) and the shocked explosive (green, yellow and red).

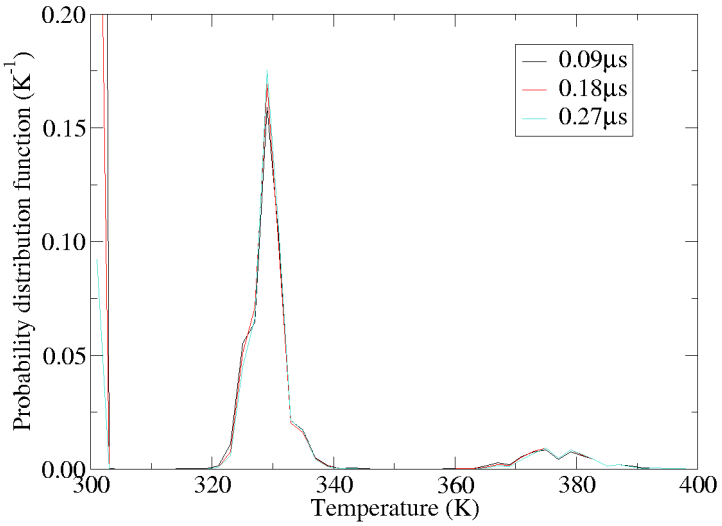

Figure 7.29: Temperature distributions from a type A simulation of EDC37 with 0.3 km / s impact velocity, to illustrate the variation that occurs with time.

initiation experiments. Temperature distributions have been produced from each simulation using the method described in section 7.1.1. An indication of the time variability is given by figure 7.29. Less variability is observed than in the smaller type C calculations (figure 7.2), because the type A geometry is sufficiently large that occasional temperature discrepancies associated with the passage of the shock through the microstructure do not significantly affect the bulk distribution. This stability allows comparisons between EDC37 and PBX9501 temperature distributions to be made at a single time.

The temperature distributions are shown in figure 7.30. In each case, the HMX peak is taller for PBX9501 than for EDC37 because PBX9501 contains a greater proportion (95 %) of HMX crystals in its microstructure than EDC37 (91 %). Although the scale on the axes makes it difficult to see, the binder peak is smaller in amplitude for PBX9501 than EDC37 owing to the lower proportion of binder in the composition. The HMX temperature distribution is at slightly higher temperatures for PBX9501 than EDC37, and the binder temperatures are lower. This is because the binder in EDC37 is softer than the binder in PBX9501, so it is shocked up to higher temperatures. Since the softer binder transmits a weaker shock into neighbouring crystals, the HMX is shocked to lower temperatures in EDC37 than in PBX9501. The fine structure in the temperature distribution curves (e.g. for EDC37 at 1.0 km / s) is believed to be caused by multiple shock processes, as the HMX and binder components ring up to their final state. It is more pronounced for

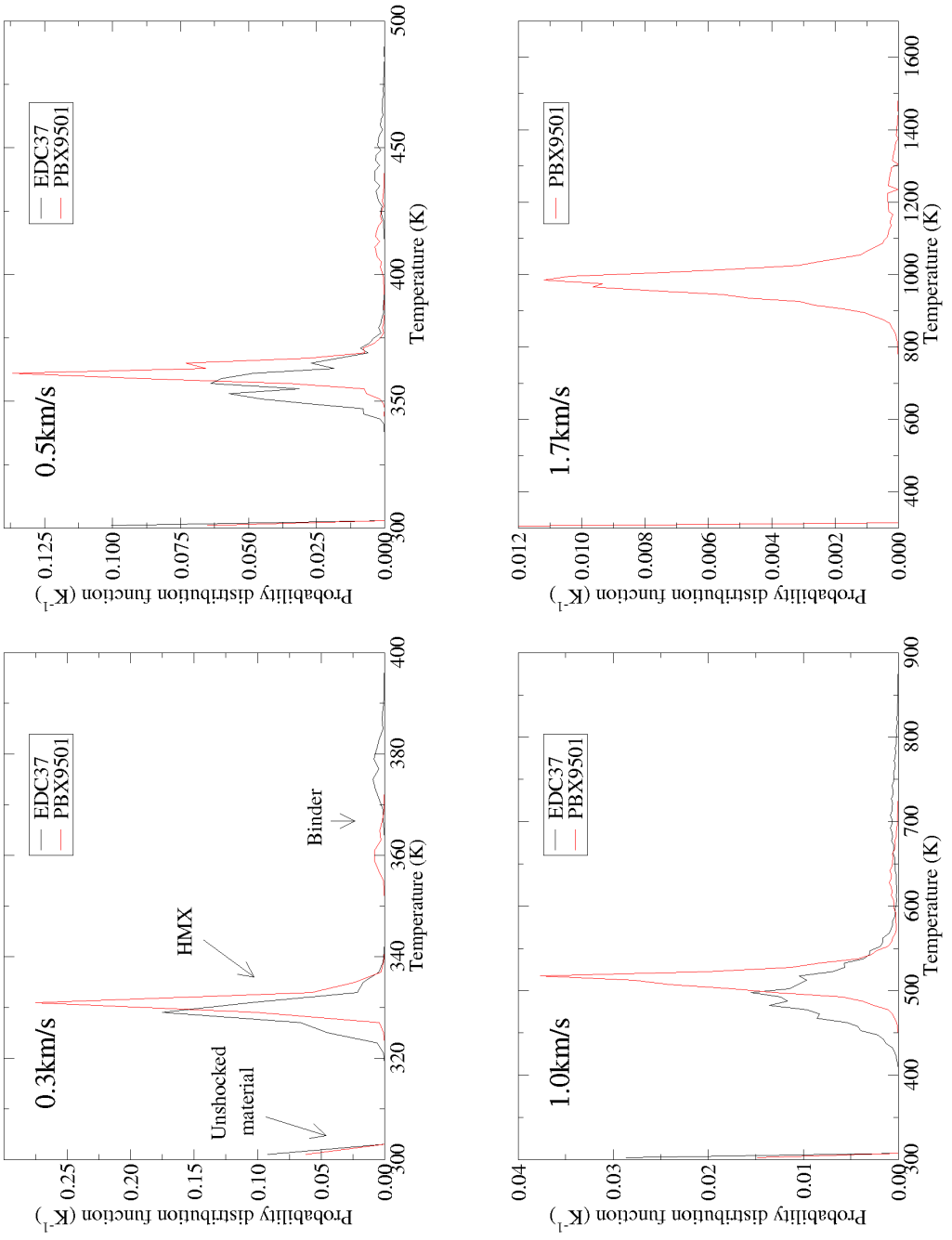

Figure 7.30: Temperature distributions from type A simulations of EDC37 and PBX9501 with impact velocities of 0.3, 0.5, 1.0 and 1.7 km / s. Note the different axis scales.

EDC37 than for PBX9501 owing to the greater difference in Hugoniot properties between the HMX and binder components in EDC37. At low shock strengths, the HMX and binder temperature distributions are narrow and well separated. As the shock strength increases, the HMX and binder distributions shift to higher temperatures and extend over a wider temperature range.

This is the first time that temperature distributions have been determined for EDC37 under shock conditions. The PBX9501 distributions compare favourably to previous results from the literature. For a 0.5 km/s impact, Conley [69] predicted a peak HMX temperature of ~370 K, with a distribution extending from ~320 to 420 K. At 1.0 km/s, his distribution covered the temperature range ~420 to 620 K, with a peak at ~500 K. The peak HMX temperatures in figure 7.30 are close to Conley's values but the distributions are narrower. This discrepancy is likely to be due to the different material properties used in the two sets of simulations.

The results in this section provide temperature distributions for inert EDC37 and PBX9501 over a range of impact velocities applicable to shock initiation. The impact velocities of 0.3, 0.5 and 1.0 km/s used in the simulations correspond approximately to input pressures of 2.0, 3.7 and 9.4 GPa. Experiments on PBX9501 and EDC37 at these shock strengths detonate within 10 μs. The highest temperature achieved in figure 7.30 at 1.0 km/s is approximately 700 K for HMX and 900 K for binder, but Arrhenius reaction rates for these materials produce very little reaction on μs timescales for temperatures below 1000 K (see section 6.5). Therefore, even if the HMX and binder regions were reactive, the mesoscale simulations would not detonate. This confirms the results in chapter 5 that shock heating of crystals and binder is not by itself responsible for shock initiation in these explosives.

7.3.3 Bulk properties

It is important to check that the computational microstructures produce bulk behaviour that is representative of the macroscopic properties of PBX9501 and EDC37. For two reasons, it is not yet possible to compare the type A simulations to physical shock initiation or detonation behaviour. Firstly, Petra does not have heat conduction or Arrhenius chemistry capabilities. Secondly, even if type C Peruse simulations were used instead, the chemical reaction rates generated by shock interactions between crystals and binder are not sufficient to explain shock initiation and hotspots have not been included in these sim-

ulations. Instead, the microstructure simulations are compared to density and unreacted Hugoniot data.

From the precise weight percentage and density of HMX and binder in the computational microstructures, the bulk density can be determined using the following equation:

$$\frac{1}{\rho} = \frac{\text{wt.}\%^{\text{HMX}}}{\rho^{\text{HMX}}} + \frac{\text{wt.}\%^{\text{binder}}}{\rho^{\text{binder}}}.$$

The bulk density of the computational microstructures is $1.846\,\mathrm{g/cm^3}$ for PBX9501 and $1.831\,\mathrm{g/cm^3}$ for EDC37. These are close to the usual working densities for these compositions, of $1.83\,\mathrm{g/cm^3}$ for PBX9501 and $1.84\,\mathrm{g/cm^3}$ for EDC37, but are lower than their theoretical maximum densities (TMD) owing to the use of an HMX equation of state at $1.891\,\mathrm{g/cm^3}$. As discussed in section 3.1.7, mesoscale simulations should ideally have bulk densities equal to the TMD of the composition. Achieving this will require the HMX equation of state to be corrected to TMD in future work (see section 8.2).

The unreacted Hugoniot was determined from the pressure maps for each type A simulation as follows. Shock velocities were obtained from the position of the shock front at four well-separated vertical lines through the microstructure at discrete time intervals. These were averaged with respect to both time and location to give the bulk shock velocity, and the average particle velocity was taken as the initial rigid-wall impact velocity for each simulation. Figures 7.31 and 7.32 show that the simulations lie within the scatter on the data from gas-gun particle-velocity-gauge experiments, and also between two historical best fit lines. This demonstrates that the simulations are reproducing the bulk properties of PBX9501 and EDC37. However, figures 7.31 and 7.32 both show that the mesoscale Hugoniot has a slightly steeper gradient than the recent best fits through the experimental data. Suggested changes to the material models to improve the fit to Hugoniot data will be discussed in section 8.2. Here, it is sufficient that the type A mesoscale simulations are producing such a good fit to the Hugoniot data for PBX9501 and EDC37 in figures 7.31 and 7.32.

7.3.4 Shear velocities

Particle velocity maps from a type A calculation of EDC37 are shown in figure 7.33. At approximately 9.4 GPa input pressure, the particle velocity varies by $\pm 0.2\,\mathrm{km/s}$ behind the shock front so an estimate of the maximum shear velocity that could occur is

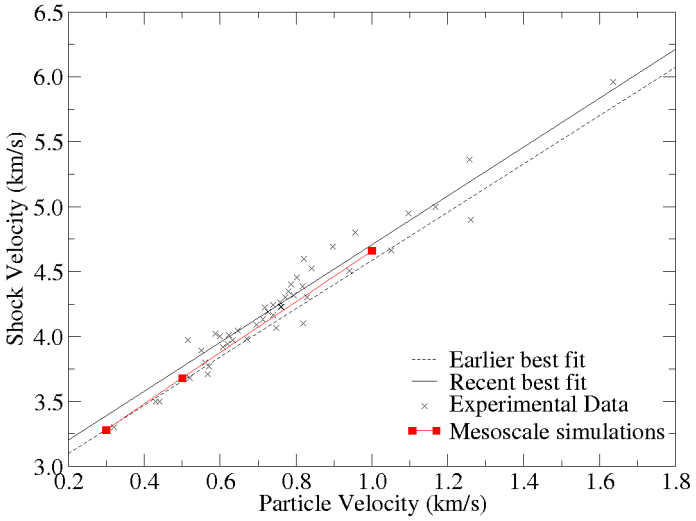

Figure 7.31: Hugoniot points from type A simulations of EDC37, compared to experimental data points [12] and best fit lines [196].

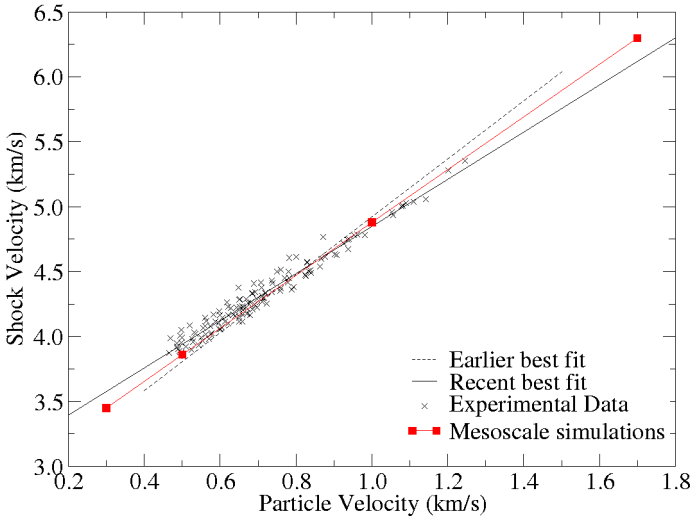

Figure 7.32: Hugoniot points from type A simulations of PBX9501, compared to experimental data points [134] and best fit lines [196] which have been corrected to theoretical maximum density.

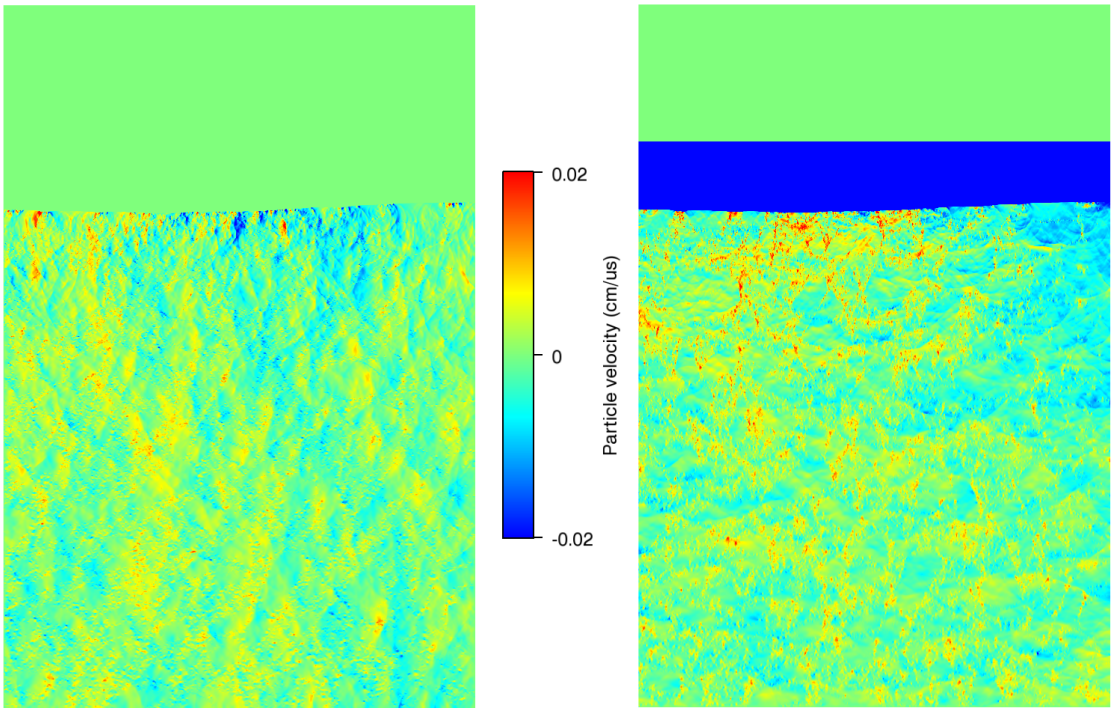

Figure 7.33: Particle velocity maps (in cm/μs) from a type A calculation of EDC37 in Petra with 1.0 km / s impact velocity at 0.20 μs. The green region at the top of both maps corresponds to the void which is stationary. The y component of particle velocity (right) contains a dark blue region corresponding to the unshocked material. Behind the shock, the x (left) and y components show particle velocity variations of ±0.2 km / s.

0.4 km / s. Similar velocities were used by Frey in his work on shear initiation [15]. His quasi-steady-state model showed that temperatures >1000 °C can be produced for shear velocities ~0.1 km / s and input pressures ≥1.4 GPa. This suggests that shear banding could be an important hotspot mechanism in EDC37 if the shear velocities are sufficiently long-lived. Frey found that the time needed for a shear band to form is ~2 μs for a 2 mm region at 1.03 GPa, but the time decreases if the shear is applied over a shorter distance. The large discrepancy between the mesh size in the simulations of ~0.26 μm, which represents the smallest distance over which shear velocities can arise, and the millimetre thicknesses considered by Frey means that it is not possible to determine whether the shear velocities in figure 7.33 have long enough durations to cause significant temperature localisation without further detailed analysis. Therefore, it is recommended that the feasibility of shear banding as a hotspot mechanism in PBX9501 and EDC37 be investigated in future work.

7.3.5 Pressure versus specific volume data

Pressure and specific volume results were also obtained; it is believed that this is the first time that the results of microstructure simulations of plastic-bonded explosives have been analysed in this way. Figure 7.34 shows pressure versus specific volume points from each computational cell in a type C Peruse simulation of EDC37 at eleven print times (0.00, 0.01, 0.02, ..., 0.10 μs). The scale on the axes is such that pre-shock values (with 0 GPa pressure), and pressure-volume states from cells that are in the process of being shocked, are not shown. The points form two distinct distributions, with the HMX distribution having a steeper gradient than the binder distribution. Each set of points lies above the principal isentrope for that material, but runs approximately parallel to it. The principal Hugoniots pass through each distribution, but many of the points lie some way away from their Hugoniot. This is because each of the cells in the calculation may have been shocked, partially released and re-pressurised many times. Figure 7.34 corresponds to an input shock of approximately 20 GPa. At lower shock pressures, the two distributions do not cross because the principal Hugoniot and isentropes for HMX and binder are more widely separated. Pressure versus specific volume information has also been determined for PBX9501. Owing to the stiffer binder, the HMX and binder distributions do not overlap but form two distinct curves above and approximately parallel to their principal isentropes.

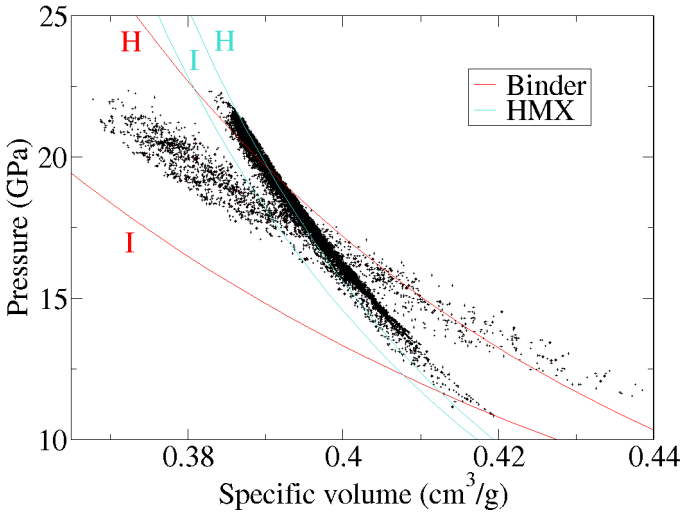

Figure 7.34: Pressure versus specific volume points for EDC37 with impact velocity 1.7 km/s, from a type C calculation in Peruse. The curves labelled H are the principal Hugoniots for HMX and the binder, and the curves labelled I are the principal isentropes.

Since the pressure versus specific volume points lie parallel to the principal isentrope for that material, it is interesting to compare the points to other isentropes. The binder distribution lies between two isentropes with $\phi(S) = 0.48$ and $0.88\,\mathrm{kJ/g}$, where $\phi(S)$ is a function of entropy that is equal to the value of the internal energy at $v = v_0$ and is constant along the isentrope (see appendix C and reference 138). The HMX distribution lies between two isentropes with $\phi(S) = 0.165$ and $0.605\,\mathrm{kJ/g}$. This illustrates the range of entropies that may be produced within an inert explosive microstructure. This range would be wider if hotspots were included in the simulations. If the pressure versus specific volume history for a particular computational cell in the calculation is examined, the entropy variation is much smaller. For the same HMX cell as will feature in figures 7.37 and 7.38 below, the post-shock pressure versus specific volume points remain within $\phi(S) = 0.132$ and $0.1375\,\mathrm{kJ/g}$. This demonstrates that, in an inert simulation, the strength of the incident shock determines the entropy of each zone in the microstructure; the pressure waves propagating through the microstructure behind the shock cause the temperature of each cell to fluctuate but the entropy remains approximately constant.

7.3.6 Pressure and temperature traces

The profiles in figures 7.35 and 7.36 provide a snapshot of the pressure or temperature in each cell of a type C Peruse calculation at three times: 0.09, 0.11 and 0.13 μs. The pressure profiles in figure 7.35 show that waves reverberate through the microstructure long after the shock wave has passed, in agreement with other research [66, 69]. These oscillations have large amplitude and short wavelength close behind the shock, but dissipate over time to smaller amplitude, longer wavelength perturbations well behind the shock front. This behaviour can also be seen in type A Petra calculations (figure 7.25). The temperature profiles in figure 7.36 appear to show dramatic fluctuations, but these are due to the presence of HMX and binder regions. Within a region, for example at the positions indicated by the arrows, the temperature profiles are roughly constant with time. These "time-independent" features arise because the temperature in a zone is most strongly determined by the first shock it experiences.

Further light can be shed on this behaviour by examining pressure and temperature histories from a single HMX cell. Figure 7.37 shows that the pressure histories are similar in character to the pressure profiles in figure 7.35; the large amplitude, short wavelength oscillations close behind the shock dissipate over time to smaller amplitude, longer wave-

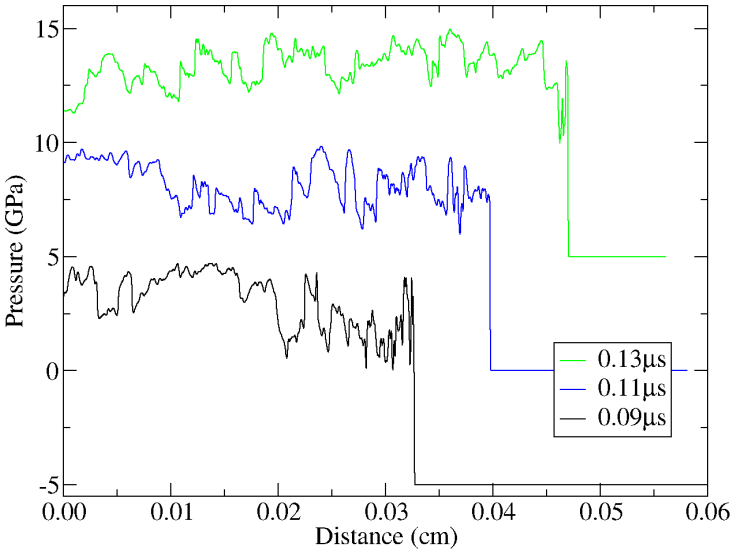

Figure 7.35: Pressure profiles for EDC37 with impact velocity 1.0 km/s, from an inert type C calculation in Peruse. Curves at 0.09 μs and 0.13 μs have been shifted by ±5 GPa.

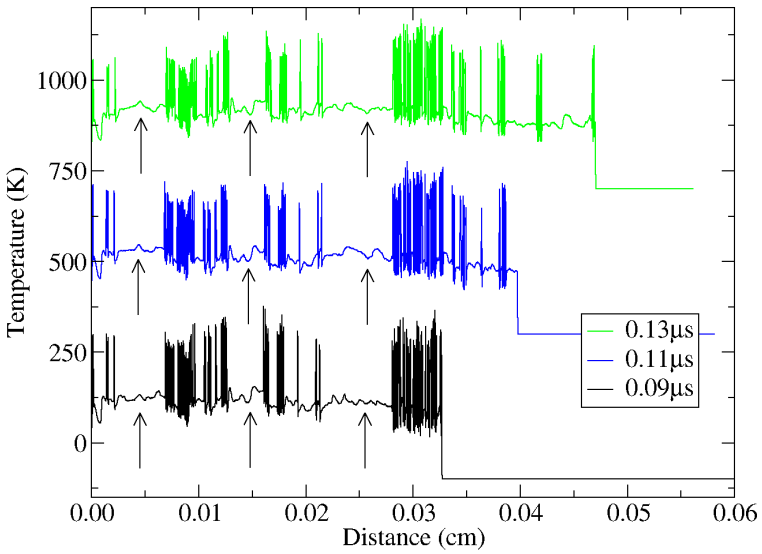

Figure 7.36: Temperature profiles for EDC37 with impact velocity 1.0 km/s, from an inert type C calculation in Peruse. Curves at 0.09 μs and 0.13 μs have been shifted by ±400 K. Arrows indicate time-independent features.

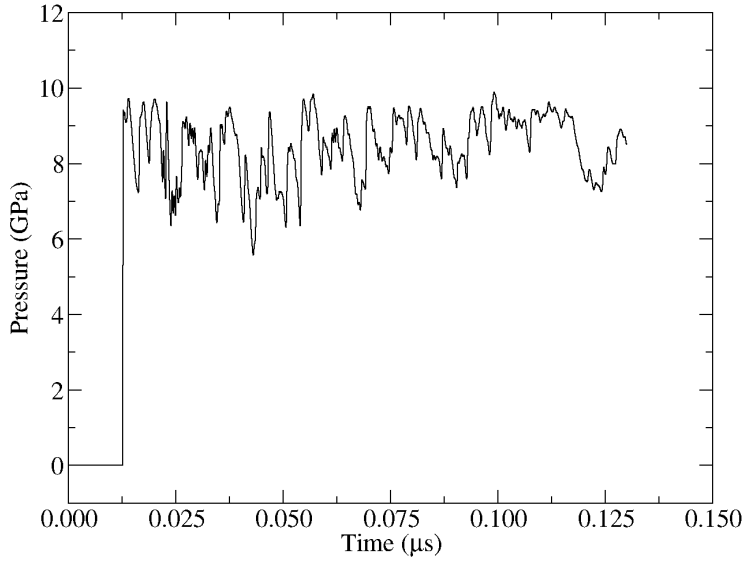

Figure 7.37: Pressure histories for an HMX zone in an inert type C calculation of EDC37, with impact velocity 1.0 km / s in Peruse.

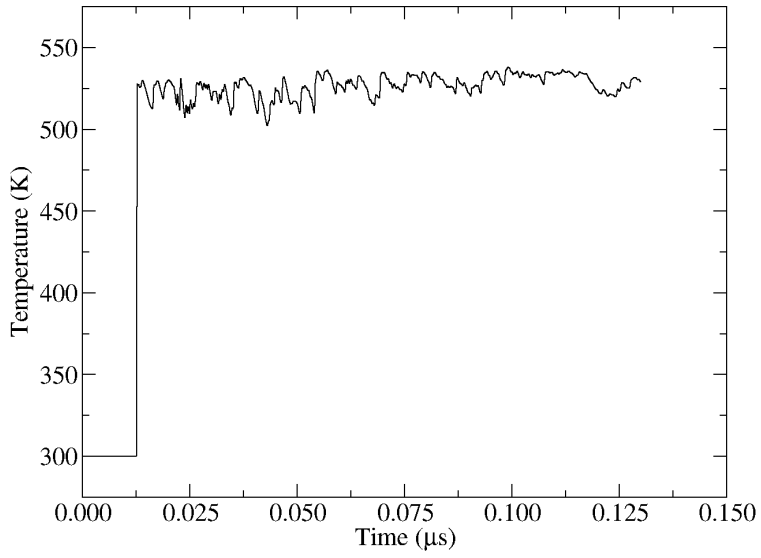

Figure 7.38: Temperature histories for an HMX zone in an inert type C calculation of EDC37, with impact velocity 1.0 km / s in Peruse.

length perturbations. The temperature histories in figure 7.38 show that, within an HMX cell, the temperature fluctuates in a similar fashion to the pressure as waves reverberate through the microstructure. However, the temperature oscillations are smaller than the pressure oscillations, when compared to the change in temperature or pressure across the shock front. To investigate this further, a simple statistical analysis method was used. Ignoring pre-shock values, it was found that the standard deviation of pressure with time is 12 % of the average value, while the standard deviation of temperature is only 6 % of the average, measured with respect to the pre-shock value of 300 K. The oscillations in pressure with time caused by waves reverberating through the system are proportionally larger than the oscillations in temperature with time. This can be explained using thermodynamic arguments. At constant entropy S,

$$\left(\frac{\partial \ln T}{\partial \ln p}\right)_S = \frac{\Gamma p}{K_S},$$

where T is temperature, Grüneisen $\Gamma = 1$, pressure $p \sim 8\,\text{GPa}$ and the isentropic bulk modulus $K_S = \rho c^2 \sim 16\,\text{GPa}$ for HMX. Rearranging, the equation becomes

$$\frac{\Delta T}{T} = \frac{1}{2}\frac{\Delta p}{p},$$

i.e. for a given computational cell, which has already been shown to be at approximately constant entropy, the fractional change in temperature is expected to be half the fractional change in pressure. The relatively small change in temperature with time in a single computational cell means that temperature differences between cells, caused by shock interactions (see, e.g., section 5.2), persist for the duration of the simulation. This is why time-independent features are visible on the temperature profiles in figure 7.36, but not on the pressure profiles in figure 7.35. Similar behaviour has been observed previously [69], but it was attributed to "viscous work instead of compressive heating". Here, the HMX and binder materials are strength-less so the thermodynamic argument presented above is the only possible explanation.

To investigate the effect of including strength in the HMX crystals, two Petra type C simulations were run with and without the strength model from section 7.2.7. The binder was treated as strength-less. Figure 7.39 shows that strength reduces the amplitude of the pressure fluctuations but does not significantly alter their character, demonstrating that the decision to neglect strength in this work has not adversely affected the results.

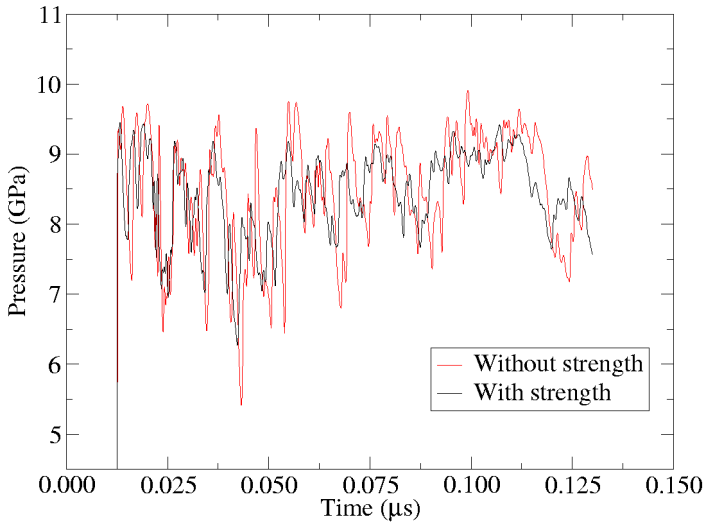

Figure 7.39: Pressure histories for an HMX zone in two Petra type C calculations of EDC37 with impact velocity 1.0 km / s, to investigate the effect of strength.

7.4 Summary

One and two-dimensional hydrocode calculations have been used to determine bulk temperature distributions in inert PBX9501 and, for the first time, EDC37. The sensitivity to material properties data was investigated; the calculated temperature distributions are highly sensitive to the Hugoniot, Grüneisen Γ and heat capacity of the HMX crystals and binder materials. Nevertheless, the "background" effect of the shock heating of crystals and binder in PBX9501 and EDC37 has been established, and these temperature distributions provide an important basis for the continuing development of mesoscale models. Pressure versus specific volume data were obtained; this is believed to be a novel approach for analysing microstructure simulations of explosives. A new explanation is given for time-independent features in temperature profiles.

Chapter 8

Conclusions

This thesis describes the considerable progress that has been made towards a mesoscale model for shock initiation and detonation propagation in two plastic-bonded explosives, PBX9501 and EDC37. Computational and material models have been constructed for the HMX crystal and binder components of these two explosives, which account for the effects of hydrodynamics, heat conduction and chemistry. The models have been validated by comparison to applicable experimental data, before being used to investigate the response of the bulk explosive. The key points of interest are summarised below:

Gaps in the literature. A review in chapter 1 identified several gaps in the mesoscale modelling literature that are addressed in this work. Many studies have investigated the mesoscale response of PBX9501 but few have compared it to other HMX-based explosives. In particular, the microstructure of EDC37 has not previously been modelled despite its being a well-characterised explosive. The shock heating of crystals and binder has been overlooked as a possible hotspot mechanism despite its being responsible for significant temperature localisation in plastic-bonded explosives.

Code capabilities. Heat conduction and Arrhenius chemistry are important for mesoscale modelling but were not previously included in available hydrocodes. As discussed in chapter 2, their implementation in a one-dimensional Lagrangian hydrocode led to the identification of two correction factors χ and $\mathrm{d}e/\mathrm{d}\lambda$. These factors improve total energy conservation by reducing errors associated with converting between specific internal energy and temperature. An extensive suite of

test problems was used to validate the new conduction and chemistry coding. A simple method to analyse optical micrographs and convert them into computational geometries for use in hydrocode calculations has also been developed.

New material models. Material models have been constructed for HMX and the binders in chapter 3, using well-established equations of state and reaction rate schemes. Appropriate material properties data have been gathered from the literature or estimated from data on similar materials. The models have been validated by comparison to Hugoniot data, Pop-plot data and detonation wave profiles in chapter 4. This is the first time that a material model that is suitable for use in mesoscale shock-to-detonation simulations has been developed for the binder in EDC37.

Shock heating of crystals and binder. The simulations in chapter 5 have demonstrated that, although the shock heating of crystals and binder does cause temperature localisation, it is not a feasible hotspot mechanism in PBX9501 and EDC37. A thorough parametric study confirmed that this conclusion is not dependent on the geometry or meshing used for the simulations, and that reasonable changes to the material properties data do not change the results significantly. It is believed that this is the first time this has been explicitly demonstrated.

Critical hotspots. This is the first time that critical hotspot criteria have been determined for the binders in PBX9501 and EDC37, but the results for HMX in chapter 6 compare favourably with earlier studies. The calculated $\sim$1 m / s speed of reaction propagation from hotspots into the bulk explosive, which has been validated by comparison to diamond anvil cell data, implies that hotspots must be separated by $<4\,\mu$m in PBX9501 and EDC37. Therefore, hotspots must be positioned within the HMX crystals and not just in the binder or at the HMX/binder interface. Falling temperatures in the gaseous reaction products have been identified as being responsible for the negative pressure dependence sometimes observed in flame propagation experiments.

Inert microstructure simulations. Chapter 7 describes one and two-dimensional hydrocode calculations that were used to determine bulk temperature distributions in inert PBX9501 and, for the first time, EDC37. The sensitivity to material properties data has been investigated; the calculated temperature distributions are highly sensitive to the Hugoniot parameters, Grüneisen Γ and heat capacity of the HMX crystals and binder materials. Pressure versus specific volume points extracted from the simulations lie above the principal isentrope for each material but approximately

parallel to it. This is thought to be a novel approach for analysing microstructure simulations of explosives. In addition, a new explanation based on thermodynamic arguments has been given for time-independent features in temperature profiles. They arise because the temperature in an element is most strongly determined by the first shock it experiences, and temperature oscillations due to wave reverberations are proportionally smaller than pressure oscillations.

Three phases for the development of a mesoscale model for PBX9501 and EDC37 were laid out in section 1.5. This work completes phase 1 to establish the bulk response of the explosive to shock and detonation waves. Specifically, the "background" effect of the shock heating of crystals and binder has been established, providing an important basis for the continuing development of mesoscale models. Some elements of phase 2 have also been addressed through the identification of critical hotspot criteria, the elimination of shock heating of crystals and binder as a possible hotspot mechanism and the discussion of reaction propagation mechanisms. However, there is much still to do.

8.1 Future research

As mentioned in section 1.5, phase 2a of the development of a mesoscale model for PBX9501 and EDC37 focuses on the individual hotspot mechanisms that may be responsible for shock initiation. At least ten different hotspot mechanisms have been proposed [16], each of which needs to be evaluated using theoretical and/or simple computational models to determine which mechanisms are dominant. As previous reviews [13, 68, 114] have demonstrated, a vast literature on hotspot mechanisms already exists so it should be possible to adapt earlier results to PBX9501 and EDC37. There are then two possible strategies for incorporating hotspots in hydrocode simulations: either they can be modelled explicitly if sufficient mesh resolution is available, or an approximate model can be introduced that is based on the results of detailed hotspot calculations.

Phase 2b, which can run in parallel to phase 2a, is to understand how reaction spreads from hotspots into the bulk explosive. Although reaction propagation has been modelled using only hydrodynamics, heat conduction and chemistry in this work, the predicted propagation rates are slower than observed in diamond anvil cell experiments and other mechanisms have been suggested as being important, e.g. turbulence [149]. Many models neglect the underlying physical basis of reaction propagation and instead use an empir-

ical pressure-dependent burn rate tuned to experimental data. However, this seems to contradict observations that reaction depends on shock strength and not on the evolving pressure field behind the shock [53]. Reaction propagation is currently an unresolved topic and will form an important part of future mesoscale modelling research. Once the physical mechanisms for the spread of reaction have been identified, there are two possibilities for incorporating them in hydrocode simulations: either they can be modelled explicitly or an approximate model can be used.

An interesting topic for study during phase 2b is how the reactive waves propagating from multiple hotspots interact. In particular, it should be possible to demonstrate the transition between homogeneous shock initiation in a system without hotspots to heterogeneous shock initiation with multiple hotspots. Several studies are already underway on nitromethane, a liquid explosive with a uniform composition. Dattelbaum has reported shock initiation experiments on neat nitromethane, nitromethane sensitised with glass beads and nitromethane sensitised with microballoons [197], which demonstrate both homogeneous and heterogeneous behaviour. Researchers at Los Alamos National Laboratory [188] and the University of Cambridge [198] are attempting to match these experimental data using reactive-burn models. Their conclusions will be incorporated in the development of mesoscale models for plastic-bonded explosives.

Phase 3 is the final step in the development of a mesoscale model for PBX9501 and EDC37, and it relies on the successful completion of the earlier phases. Models for hotspots and reaction propagation will be incorporated in a hydrocode, allowing microstructure simulations to be run containing both the bulk response from phase 1 and the hotspot response from phase 2. Statistical techniques will be used to average the reaction rate from a finite volume, for comparison to continuum reactive-burn models. If sufficient computing power is available to allow centimetre-long microstructures to be simulated, the mesoscale model will be validated against shock initiation experimental data, for example the particle-velocity-gauge experiments on PBX9501 [134] and EDC37 [75] that have been so valuable in calibrating continuum models like CREST [38, 175]. Such experiments are often treated as one-dimensional because the gauges are embedded in a region where the flow is undisturbed by side release waves. Therefore, it is possible that a 1D or 2D mesoscale model will be sufficient, providing a significant advantage in terms of computational efficiency. However, mesoscale studies on inert materials have demonstrated the importance of 3D modelling [72, 73] and so it is likely that a 3D model will eventually be needed for PBX9501 and EDC37. A 3D model for HNS and PETN

explosives is already under development at Sandia National Laboratory [67].

A key element of phase 3 will be the acquisition of suitable experimental data to establish the location of hotspot sites in plastic-bonded explosive microstructures. Some defects are relatively easy to locate owing to their physical characteristics; for example, gas-filled pores have a different refractive index to HMX crystals and can be seen using index-matched microscopy [199]. Other defects may be more difficult to find. To create mesoscale models that can predict the effect of microstructure variations, it will be necessary to determine how the defect distribution changes with the introduction of a new manufacturing technique or as the explosive ages in storage. Therefore, phase 3 presents a challenge to experimentalists as well as modellers. Following its conclusion, the validated mesoscale model for shock initiation and detonation propagation can be used to improve assessments of both the performance and safety of PBX9501 and EDC37. The steps needed to achieve this challenging goal provide an exciting long-term research project.

8.2 Model improvements

In the preceding chapters of this thesis, several topics have been identified for future work. Mainly, these are ways in which the models for the HMX and binders in PBX9501 and EDC37 can be improved. As described in chapter 3, the material models comprise an unreacted equation of state, a reaction products equation of state and a reaction rate. Relatively simple equations of state have been used in work and gains could be made by switching to more advanced equations of state like those developed for continuum reactive-burn modelling [e.g., 138 and 200], although there is no clear consensus in the literature on the best equations to use. Therefore, only the improvements that could be made within the current equations of state are considered below.

Figure 4.1 on page 81 shows that the Hugoniot parameters for HMX have a higher gradient than the experimental shock velocity versus particle velocity data for single-crystal HMX. In addition, the simulated Hugoniots of PBX9501 and EDC37 in section 7.3 are highly dependent on the properties of HMX because the microstructures comprise over 90 % HMX. Figures 7.31 and 7.32 on page 196 confirm that the HMX Hugoniot is too steep, i.e. either the Hugoniot parameter b needs to be reduced or a curved $U_s(u_p)$ relation should be used in future work. The parameters were based on solvent-pressed data from reference 159 and more data are available in the literature [e.g., 201 and 202]. A

thorough approach to improving the unreacted equation of state would require all available data for HMX to be examined and corrected back to theoretical maximum density following the method in reference 138. Since the mesoscale simulations in section 7.2 show that the uncertainties in Hugoniot data have a smaller effect than the uncertainties in thermal properties, re-calibrating the Hugoniot parameters for HMX is recommended only if the specific heat and thermal conductivity models can be improved. For the binder in PBX9501, figure 4.2 shows that the linear Hugoniot parameters give a good match to the available experimental data. The equation of state could be improved by using a curved $U_s(u_p)$ relation but this is worthwhile only if the significant uncertainties on the reaction rate and thermal properties can be reduced. For the binder in EDC37, the new experimental data in figure 4.3 will allow an improved model with lower uncertainties to be constructed in future work. The data indicate that a linear $U_s(u_p)$ Hugoniot with coefficients $a = 1.46\,\mathrm{km/s}$ and $b = 2.5$ is suitable. Ideally, further experiments should be carried out to extend the Hugoniot data to a wider range of particle velocities.

The value of Grüneisen $\Gamma_0 = 1$ used in this work was validated for HMX under ambient conditions in section 4.1, but it is difficult to determine $\Gamma(v)$ experimentally. One method is to use Hugoniot data at different porosities but such data are not available for HMX or the binder materials. Some off-Hugoniot data are available from gas-gun experiments on EDC37's binder [181] and isentropic compression experiments on PBX9501's binder [163], so it may be possible to analyse these data to improve the value of Γ for the binders. There are two strategies to enable a variable $\Gamma(v)$ to be used in Peruse. Either the unreacted equations of state could be formulated using an isentrope instead of the Hugoniot as their reference curve or a tabular temperature-calculation method could be implemented, similar to that already available in Corvus and Petra. However, this will not become necessary until experimental data prove that $\Gamma = 1$ is an unsuitable assumption for HMX and the binder materials.

Constant specific heat capacities have been used despite temperature-dependent relations being favoured in the literature, because they simplify the equations of state (see section 3.1.4). The simulations in section 4.2 indicate that temperature-dependent heat capacities are needed to model shock initiation, specifically Pop-plot data for single-crystal HMX. Therefore, it is recommended that temperature-dependent heat capacities be implemented in Peruse using either analytic or tabular $c_{v,s}(T)$ relations. Constant thermal conductivities have also been used despite experimental data indicating that k varies with temperature and pressure. As discussed in section 6.4, the use of constant k may be re-

sponsible for some of the disagreement between diamond anvil cell flame-propagation simulations and the experimental data. It is suggested that $k(T, p)$ is incorporated in Peruse in future work. If constant $c_{v,s}$ and k continue to be used, the effect of neglecting their temperature and pressure dependence can be estimated by running simulations at their maximum and minimum error bounds. Additional thermal properties data for HMX and the binder materials would enable the uncertainties on $c_{v,s}$ and k to be reduced.

JWL equations of state have been used in this work despite suggestions that the JWL form is inappropriate for use with temperature-dependent reaction rates [167]. Owing to a lack of experimental data, the JWL parameters for the binders were estimated using Cheetah [136], which fits a JWL equation to the results of thermochemical equilibrium calculations. It was noted in section 6.4 that a better reaction products equation of state, e.g. a tabular equation of state from Cheetah, might improve the match to HMX flame propagation data. All the reaction products thermal properties were estimated from thermochemical calculations because the difficulty of measuring T_{CJ} and $c_{v,CJ}$ experimentally makes this the only feasible approach. Unfortunately, the paucity of data makes the reaction products equation of state and thermal properties a significant uncertainty in mesoscale models of PBX9501 and EDC37.

Single-step Arrhenius reaction rates have been used for the HMX and binder materials. The reaction rate parameters for HMX were based on a compilation of experimental data over a wide range of temperatures [82]. Despite this solid experimental basis, it was noted in section 4.3 that the reaction was slightly too slow for modelling PBX9501 detonation wave profiles. In addition, the sensitivity of the Pop-plot simulations in section 4.2 to $c_{v,s}$ demonstrates that the calculated reaction rate depends on the unreacted equation of state. Although this is true for any reactive-burn model, the link is especially strong for Arrhenius kinetics with their exponential temperature dependence. To improve the HMX model in the future, it may be necessary to adjust the reaction rate coefficients to match experimental data in the shock to detonation regime. The single-step rates for the binders were estimated from the HMX data, owing to the paucity of relevant experimental data. Until additional experimental data become available, it is difficult to see how the reaction rates for the binders could be improved. It was suggested in section 6.4 that multi-step rates might be needed to model the positive pressure dependence observed in HMX flame propagation experiments. Since Peruse already includes a variety of Arrhenius reaction schemes, it is recommended that these be tried in future work.

Several physical effects that may be important at the mesoscale have been neglected

in this work. Strength has little effect on the bulk response of explosives in the shock and detonation regime, but it is known to be important for modelling hotspots [114]. Recent experiments [93, 203] suggest that shear may be important in shock initiation of single HMX crystals, causing reaction to begin above 10 GPa input pressure where "thermal estimates are insufficient to produce the observed reaction". Therefore, it is suggested that strength effects be included in future. The anisotropy of HMX crystals is neglected in the majority of mesoscale models, although a recent study examined its effect on pore collapse [153]. A simple method for gauging the influence of anisotropy is to adjust the isotropic material properties of the individual crystals to represent the variability that would be expected assuming random crystal orientations. Finally, the technique developed to generate computational microstructures from micrographs in section 2.4 is very simple. It is recommended that the effects of anisotropy and more advanced image analysis methods be evaluated.

8.3 Summary

The progress made towards a mesoscale model for PBX9501 and EDC37 has been described. The novel work reported in this thesis includes: the identification of several gaps in the mesoscale modelling literature; new material models for HMX and the binders; demonstrating that shock heating of crystals and binder is not a feasible hotspot mechanism; comparison of critical hotspot criteria and flame propagation simulations with results in the literature; inert microstructure simulations on PBX9501 and, for the first time, EDC37. Recommendations have been made for future research. The work described in this thesis completes phase 1 and some elements of phase 2 of the development of a mesoscale model for these HMX-based explosives.

Appendix A

Reaction rate equations

This appendix provides the detailed working that allows McGuire & Tarver's [86] three-step reaction scheme for HMX to be expressed in terms of static mass fractions N_j in equations 2.15 and dynamic mass fractions f_j in equations 2.18 in section 2.3.2.

For the three-step reaction scheme A $\overset{1}{\rightarrow}$ B $\overset{2}{\rightarrow}$ 2C $\overset{3}{\rightarrow}$ D, the Lagrangian species-conservation equations 2.10 are

$$\begin{aligned}
\frac{1}{\delta V}\frac{\mathrm{D}(n_\mathrm{A}\delta V)}{\mathrm{D}t} &= -n_\mathrm{A} z_1 e^{-E_1/RT} \\
\frac{1}{\delta V}\frac{\mathrm{D}(n_\mathrm{B}\delta V)}{\mathrm{D}t} &= n_\mathrm{A} z_1 e^{-E_1/RT} - n_\mathrm{B} z_2 e^{-E_2/RT} \\
\frac{1}{\delta V}\frac{\mathrm{D}(n_\mathrm{C}\delta V)}{\mathrm{D}t} &= n_\mathrm{B} z_2 e^{-E_2/RT} - {n_\mathrm{C}}^2 z_3 e^{-E_3/RT} \\
\frac{1}{\delta V}\frac{\mathrm{D}(n_\mathrm{D}\delta V)}{\mathrm{D}t} &= {n_\mathrm{C}}^2 z_3 e^{-E_3/RT},
\end{aligned}$$

where n_j is the molar density of species j. These equations can equally well be written in the Eulerian reference frame:

$$\begin{aligned}
\frac{\partial n_\mathrm{A}}{\partial t} + \nabla\cdot(n_\mathrm{A}\boldsymbol{u}) &= -n_\mathrm{A} z_1 e^{-E_1/RT} \\
\frac{\partial n_\mathrm{B}}{\partial t} + \nabla\cdot(n_\mathrm{B}\boldsymbol{u}) &= n_\mathrm{A} z_1 e^{-E_1/RT} - n_\mathrm{B} z_2 e^{-E_2/RT} \\
\frac{\partial n_\mathrm{C}}{\partial t} + \nabla\cdot(n_\mathrm{C}\boldsymbol{u}) &= n_\mathrm{B} z_2 e^{-E_2/RT} - {n_\mathrm{C}}^2 z_3 e^{-E_3/RT} \\
\frac{\partial n_\mathrm{D}}{\partial t} + \nabla\cdot(n_\mathrm{D}\boldsymbol{u}) &= {n_\mathrm{C}}^2 z_3 e^{-E_3/RT}.
\end{aligned} \tag{A.1}$$

In a static code like ReactDiff, the molar densities n_j can be related to the static mass fractions N_j using equation 2.16:

$$N_j = n_j M_j / \rho_0,$$

where M_j is the molar mass of species j and ρ_0 is the density (a constant). Starting from the Eulerian equations A.1, substituting for n_j and setting $\boldsymbol{u} = \mathbf{0}$ gives the static species-conservation equations 2.15 as used in ReactDiff:

$$\begin{aligned}
\frac{\partial N_\mathrm{A}}{\partial t} &= -N_\mathrm{A} Z_1 e^{-E_1/RT} \\
\frac{\partial N_\mathrm{B}}{\partial t} &= N_\mathrm{A} Z_1 e^{-E_1/RT} - N_\mathrm{B} Z_2 e^{-E_2/RT} \\
\frac{\partial N_\mathrm{C}}{\partial t} &= N_\mathrm{B} Z_2 e^{-E_2/RT} - {N_\mathrm{C}}^2 Z_3 e^{-E_3/RT} \\
\frac{\partial N_\mathrm{D}}{\partial t} &= {N_\mathrm{C}}^2 Z_3 e^{-E_3/RT},
\end{aligned}$$

where $Z_1 = z_1$, $Z_2 = z_2$ and $Z_3 = z_3 \rho_0 / M_\mathrm{C}$.

In a dynamic code like Peruse, the derivation is more involved. To account for the variation of density with time, begin by using the identity

$$\frac{\mathrm{D}(\delta V)}{\mathrm{D}t} = (\nabla \cdot \boldsymbol{u}) \delta V$$

to re-write the left-hand side of the Lagrangian species-conservation equations 2.10 as

$$\frac{1}{\delta V} \frac{\mathrm{D}(n_j \delta V)}{\mathrm{D}t} = \frac{\mathrm{D}n_j}{\mathrm{D}t} + n_j \nabla \cdot \boldsymbol{u}.$$

Substituting, the equations become

$$\frac{\mathrm{D}n_\mathrm{A}}{\mathrm{D}t} = -n_\mathrm{A} \nabla \cdot \boldsymbol{u} - n_\mathrm{A} z_1 e^{-E_1/RT} \tag{A.2}$$

$$\frac{\mathrm{D}n_\mathrm{B}}{\mathrm{D}t} = -n_\mathrm{B} \nabla \cdot \boldsymbol{u} + n_\mathrm{A} z_1 e^{-E_1/RT} - n_\mathrm{B} z_2 e^{-E_2/RT} \tag{A.3}$$

$$\frac{\mathrm{D}n_\mathrm{C}}{\mathrm{D}t} = -n_\mathrm{C} \nabla \cdot \boldsymbol{u} + n_\mathrm{B} z_2 e^{-E_2/RT} - {n_\mathrm{C}}^2 z_3 e^{-E_3/RT} \tag{A.4}$$

$$\frac{\mathrm{D}n_\mathrm{D}}{\mathrm{D}t} = -n_\mathrm{D} \nabla \cdot \boldsymbol{u} + {n_\mathrm{C}}^2 z_3 e^{-E_3/RT}. \tag{A.5}$$

Now, integrate the first equation A.2 over the cell volume $\mathrm{d}V$:

$$\int \frac{\mathrm{D}n_\mathrm{A}}{\mathrm{D}t}\mathrm{d}V = -\int n_\mathrm{A}(\nabla\cdot\boldsymbol{u})\mathrm{d}V - \int n_\mathrm{A} z_1 e^{-E_1/RT}\mathrm{d}V. \tag{A.6}$$

Using the identity

$$\int \frac{\mathrm{D}\phi}{\mathrm{D}t}\mathrm{d}V = \frac{\mathrm{D}}{\mathrm{D}t}\left[\int \phi\,\mathrm{d}V\right] - \int \phi(\nabla\cdot\boldsymbol{u})\mathrm{d}V,$$

where ϕ is any physical quantity, equation A.6 can be rewritten as

$$\int \frac{\mathrm{D}n_\mathrm{A}}{\mathrm{D}t}\mathrm{d}V = \frac{\mathrm{D}}{\mathrm{D}t}\left[\int n_\mathrm{A}\mathrm{d}V\right] - \int n_\mathrm{A}(\nabla\cdot\boldsymbol{u})\mathrm{d}V. \tag{A.7}$$

Combining equations A.6 and A.7, the terms containing $\nabla\cdot\boldsymbol{u}$ cancel out leaving

$$\frac{\mathrm{D}}{\mathrm{D}t}\left[\int n_\mathrm{A}\mathrm{d}V\right] = -\int n_\mathrm{A} z_1 e^{-E_1/RT}\mathrm{d}V.$$

To first order, this can be discretised as follows. The superscripts n and $n+1$ refer to values at the current and next timestep respectively, but the cell position subscripts have been omitted for clarity.

$$\frac{{n_\mathrm{A}}^{n+1}\mathrm{d}V^{n+1} - {n_\mathrm{A}}^{n}\mathrm{d}V^{n}}{\Delta t} = -{n_\mathrm{A}}^{n} z_1 e^{-E_1/RT^n}\mathrm{d}V^{n}. \tag{A.8}$$

In equation A.8, the molar density n_A can be converted to the dynamic mass fraction f_A using equation 2.17:

$$f_\mathrm{A} = \frac{n_\mathrm{A} M_\mathrm{A}}{\rho},$$

where M_A is the molar mass of species A and ρ is the density (a variable). Also, the Lagrangian mass conservation equation specifies that $\rho^{n+1}\mathrm{d}V^{n+1} = \rho^{n}\mathrm{d}V^{n}$. Therefore, equation A.8 becomes

$$\frac{{f_\mathrm{A}}^{n+1} - {f_\mathrm{A}}^{n}}{\Delta t} = -{f_\mathrm{A}}^{n}\mathcal{Z}_1 e^{-E_1/RT^n},$$

where $\mathcal{Z}_1 = z_1$. Following a similar analysis, the other chemical reaction equations for

HMX can be re-written in terms of mass fraction as follows:

$$\begin{aligned}
\frac{{f_\mathrm{B}}^{n+1} - {f_\mathrm{B}}^{n}}{\Delta t} &= {f_\mathrm{A}}^{n}\mathcal{Z}_1 e^{-E_1/RT^n} - {f_\mathrm{B}}^{n}\mathcal{Z}_2 e^{-E_2/RT^n} \\
\frac{{f_\mathrm{C}}^{n+1} - {f_\mathrm{C}}^{n}}{\Delta t} &= {f_\mathrm{B}}^{n}\mathcal{Z}_2 e^{-E_2/RT^n} - ({f_\mathrm{C}}^{n})^2\mathcal{Z}_3 e^{-E_3/RT^n} \\
\frac{{f_\mathrm{D}}^{n+1} - {f_\mathrm{D}}^{n}}{\Delta t} &= ({f_\mathrm{C}}^{n})^2\mathcal{Z}_3 e^{-E_3/RT^n},
\end{aligned}$$

where $\mathcal{Z}_2 = z_2$ and $\mathcal{Z}_3 = z_3\rho/M_\mathrm{C}$. Comparing these equations with the static species-conservation equations 2.15, we find that $\mathcal{Z}_1 = Z_1$, $\mathcal{Z}_2 = Z_2$ and $\mathcal{Z}_3 = Z_3\rho/\rho_0$. In the limit that $\Delta t \to 0$, the species-conservation equations for HMX become the dynamic equations 2.18 used in Peruse:

$$\begin{aligned}
\dot{f}_\mathrm{A} &= -f_\mathrm{A} Z_1 e^{-E_1/RT} \\
\dot{f}_\mathrm{B} &= f_\mathrm{A} Z_1 e^{-E_1/RT} - f_\mathrm{B} Z_2 e^{-E_2/RT} \\
\dot{f}_\mathrm{C} &= f_\mathrm{B} Z_2 e^{-E_2/RT} - \frac{\rho}{\rho_0} {f_\mathrm{C}}^2 Z_3 e^{-E_3/RT} \\
\dot{f}_\mathrm{D} &= \frac{\rho}{\rho_0} {f_\mathrm{C}}^2 Z_3 e^{-E_3/RT}.
\end{aligned}$$

In general, density factors ρ/ρ_0 arise in second- and higher-order terms in the dynamic chemical reaction equations. These are needed to convert the frequency factors Z_i from the static mass-fraction-based scheme used by McGuire & Tarver [86] to the dynamic mass-fraction-based scheme in Peruse.

Appendix B

Energy conservation

This appendix provides the detailed working that allows equation 2.21 to be written as equation 2.22 in section 2.3.2. Starting from equation 2.21:

$$\frac{\mathrm{D}e}{\mathrm{D}t} = \underbrace{\left(\frac{\partial e}{\partial T}\right)_{v,v_\mathrm{s},\lambda} \frac{\mathrm{D}T}{\mathrm{D}t}}_{1} + \underbrace{\left(\frac{\partial e}{\partial v}\right)_{T,v_\mathrm{s},\lambda} \frac{\mathrm{D}v}{\mathrm{D}t}}_{2} + \underbrace{\left(\frac{\partial e}{\partial v_\mathrm{s}}\right)_{T,v,\lambda} \frac{\mathrm{D}v_\mathrm{s}}{\mathrm{D}t}}_{3} + \underbrace{\left(\frac{\partial e}{\partial \lambda}\right)_{T,v,v_\mathrm{s}} \frac{\mathrm{D}\lambda}{\mathrm{D}t}}_{4},$$

consider each of the terms in turn. For term 1,

$$\begin{aligned}
\left(\frac{\partial e}{\partial T}\right)_{v,v_\mathrm{s},\lambda} &= (1-\lambda)\left(\frac{\partial e_\mathrm{s}}{\partial T}\right)_{v_\mathrm{s}} + \lambda\left(\frac{\partial e_\mathrm{g}}{\partial T}\right)_{v_\mathrm{g}} \\
&= (1-\lambda)c_{\mathrm{v,s}} + \lambda c_{\mathrm{v,CJ}} \\
&= c_\mathrm{v} \quad \text{by definition.}
\end{aligned}$$

For term 2, the operator splitting means that $\mathrm{D}v = 0$ during the chemistry and heat conduction steps, so this term can be neglected. For term 4,

$$\left(\frac{\partial e}{\partial \lambda}\right)_{T,v,v_\mathrm{s}} = (1-\lambda)\left(\frac{\partial e_\mathrm{s}}{\partial \lambda}\right)_{T,v,v_\mathrm{s}} + \lambda\left(\frac{\partial e_\mathrm{g}}{\partial \lambda}\right)_{T,v,v_\mathrm{s}} + (e_\mathrm{g} - e_\mathrm{s}).$$

The first term on the right hand side is zero because $e_\mathrm{s}(T, v_\mathrm{s})$ so if T and v_s are held constant, then e_s is constant. For the second term, differentiate $v = (1-\lambda)v_\mathrm{s} + \lambda v_\mathrm{g}$ to give

$$\mathrm{D}v = (1-\lambda)\mathrm{D}v_\mathrm{s} + \lambda\mathrm{D}v_\mathrm{g} + (v_\mathrm{g} - v_\mathrm{s})\mathrm{D}\lambda.$$

Since v and v_s are held constant, this can be rearranged to give

$$\frac{Dv_g}{D\lambda} = \frac{v_s - v_g}{\lambda}.$$

Therefore,

$$\lambda\left(\frac{\partial e_g}{\partial \lambda}\right)_{T,v,v_s} = \lambda\left(\frac{\partial e_g}{\partial v_g}\frac{Dv_g}{D\lambda}\right)_{T,v,v_s} = (v_s - v_g)\left(\frac{\partial e_g}{\partial v_g}\right)_T.$$

Substituting,

$$\left(\frac{\partial e}{\partial \lambda}\right)_{T,v,v_s} = e_g - e_s + (v_s - v_g)\left(\frac{\partial e_g}{\partial v_g}\right)_T.$$

For term 3,

$$\left(\frac{\partial e}{\partial v_s}\right)_{T,v,\lambda} = (1-\lambda)\left(\frac{\partial e_s}{\partial v_s}\right)_T + \lambda\left(\frac{\partial e_g}{\partial v_g}\frac{Dv_g}{Dv_s}\right)_{T,v,\lambda}.$$

Using the differential Dv above for $Dv = 0$ and $D\lambda = 0$ then

$$\frac{Dv_g}{Dv_s} = \frac{\lambda - 1}{\lambda}.$$

Substituting,

$$\left(\frac{\partial e}{\partial v_s}\right)_{T,v,\lambda} = (1-\lambda)\left[\left(\frac{\partial e_s}{\partial v_s}\right)_T - \left(\frac{\partial e_g}{\partial v_g}\right)_T\right].$$

Now, Dv_s/Dt can be expressed in terms of DT/Dt and $D\lambda/Dt$ by using $p = p_s(v_s, e_s) = p_g(v_g, e_g)$ and $T = T_s(v_s, e_s) = T_g(v_g, e_g)$. These can be differentiated to give

$$\left(\frac{\partial p_s}{\partial v_s}\right)_{e_s} Dv_s + \left(\frac{\partial p_s}{\partial e_s}\right)_{v_s} De_s = \left(\frac{\partial p_g}{\partial v_g}\right)_{e_g} Dv_g + \left(\frac{\partial p_g}{\partial e_g}\right)_{v_g} De_g$$

$$\left(\frac{\partial T_s}{\partial v_s}\right)_{e_s} Dv_s + \left(\frac{\partial T_s}{\partial e_s}\right)_{v_s} De_s = DT$$

$$\left(\frac{\partial T_g}{\partial v_g}\right)_{e_g} Dv_g + \left(\frac{\partial T_g}{\partial e_g}\right)_{v_g} De_g = DT.$$

These can be rearranged to eliminate $\mathrm{D}e_\mathrm{s}$ and $\mathrm{D}e_\mathrm{g}$. Using the differential $\mathrm{D}v$ once again, for $\mathrm{D}v = 0$, gives

$$\mathrm{D}v_\mathrm{g} = \frac{\lambda - 1}{\lambda}\mathrm{D}v_\mathrm{s} + \frac{v_\mathrm{s} - v_\mathrm{g}}{\lambda}\mathrm{D}\lambda.$$

Substituting gives

$$\mathrm{D}v_\mathrm{s} = \frac{\Theta}{\Psi}\mathrm{D}T + \frac{\Xi}{\Psi}\mathrm{D}\lambda,$$

where

$$\Theta = \frac{\left(\frac{\partial p_\mathrm{g}}{\partial e_\mathrm{g}}\right)_{v_\mathrm{g}}}{\left(\frac{\partial T_\mathrm{g}}{\partial e_\mathrm{g}}\right)_{v_\mathrm{g}}} - \frac{\left(\frac{\partial p_\mathrm{s}}{\partial e_\mathrm{s}}\right)_{v_\mathrm{s}}}{\left(\frac{\partial T_\mathrm{s}}{\partial e_\mathrm{s}}\right)_{v_\mathrm{s}}}$$

$$\Xi = \left(\frac{\partial p_\mathrm{g}}{\partial v_\mathrm{g}}\right)_{e_\mathrm{g}} \frac{(v_\mathrm{s} - v_\mathrm{g})}{\lambda} - \left(\frac{\partial p_\mathrm{g}}{\partial e_\mathrm{g}}\right)_{v_\mathrm{g}} \frac{\left(\frac{\partial T_\mathrm{g}}{\partial v_\mathrm{g}}\right)_{e_\mathrm{g}}}{\left(\frac{\partial T_\mathrm{g}}{\partial e_\mathrm{g}}\right)_{v_\mathrm{g}}} \frac{(v_\mathrm{s} - v_\mathrm{g})}{\lambda}$$

$$\Psi = \left(\frac{\partial p_\mathrm{s}}{\partial v_\mathrm{s}}\right)_{e_\mathrm{s}} - \left(\frac{\partial p_\mathrm{s}}{\partial e_\mathrm{s}}\right)_{v_\mathrm{s}} \frac{\left(\frac{\partial T_\mathrm{s}}{\partial v_\mathrm{s}}\right)_{e_\mathrm{s}}}{\left(\frac{\partial T_\mathrm{s}}{\partial e_\mathrm{s}}\right)_{v_\mathrm{s}}} - \left(\frac{\partial p_\mathrm{g}}{\partial v_\mathrm{g}}\right)_{e_\mathrm{g}} \frac{(\lambda - 1)}{\lambda} + \left(\frac{\partial p_\mathrm{g}}{\partial e_\mathrm{g}}\right)_{v_\mathrm{g}} \frac{\left(\frac{\partial T_\mathrm{g}}{\partial v_\mathrm{g}}\right)_{e_\mathrm{g}}}{\left(\frac{\partial T_\mathrm{g}}{\partial e_\mathrm{g}}\right)_{v_\mathrm{g}}} \frac{(\lambda - 1)}{\lambda}.$$

Substituting terms 1 to 4 into equation 2.21 gives equation 2.22:

$$\frac{\mathrm{D}e}{\mathrm{D}t} = \left(c_\mathrm{v} + \underbrace{\left(\frac{\partial e}{\partial v_\mathrm{s}}\right)_{T,v,\lambda}}_{\chi} \frac{\Theta}{\Psi} \right) \frac{\mathrm{D}T}{\mathrm{D}t} + \frac{\mathrm{D}\lambda}{\mathrm{D}t} \left(\underbrace{e_\mathrm{g} - e_\mathrm{s} + (v_\mathrm{s} - v_\mathrm{g}) \left(\frac{\partial e_\mathrm{g}}{\partial v_\mathrm{g}}\right)_T + \left(\frac{\partial e}{\partial v_\mathrm{s}}\right)_{T,v,\lambda} \frac{\Xi}{\Psi}}_{\frac{\mathrm{d}e}{\mathrm{d}\lambda}} \right).$$

Appendix C

Temperature calculation

The contents of this appendix are excerpts reproduced directly from reference 139. They show how temperature should be calculated from Grüneisen equations of state, with the linear shock velocity versus particle velocity unreacted equation of state and the JWL reaction products equation of state as specific examples.

Introduction

For normal use in a hydrocode, the equation of state (EOS) need only express the relationship between pressure p, specific volume v and specific internal energy e, with an ability to calculate sound speed c for stability time step control. Frequently the EOS will be of Grüneisen form, which in this appendix is defined as any p-v-e relationship in which p varies linearly with e at constant v.

Grüneisen Γ

Grüneisen Γ is thermodynamically defined as

$$\Gamma = v\left(\frac{\partial p}{\partial e}\right)_v . \tag{C.1}$$

The pressure-volume-internal energy relation

The basic assumption in the Grüneisen EOS is that Grüneisen Γ is purely a function of volume, i.e.

$$\Gamma = \Gamma(v). \tag{C.2}$$

Integrating equation C.1 using equation C.2 gives the general form of Grüneisen EOS

$$p - p_{\mathrm{r}}(v) = \frac{\Gamma(v)}{v}\,(e - e_{\mathrm{r}}(v)) \tag{C.3}$$

or

$$p = p_{\mathrm{r}}(v) + g(v)\,(e - e_{\mathrm{r}}(v))\,,$$

where

$$g(v) = \frac{\Gamma(v)}{v} \tag{C.4}$$

and $p_{\mathrm{r}}(v)$, $e_{\mathrm{r}}(v)$ are functions describing the variation of pressure and internal energy with volume along a chosen "reference" curve.

For initially solid materials, it is convenient, though not essential, to choose the reference curve to pass through $p = 0$, $v = v_0$, at a temperature T_0. It is also convenient to choose the origin of internal energy to be at the same state so that

$$p_{\mathrm{r}}(v_0) = 0 \quad \text{and} \quad e_{\mathrm{r}}(v_0) = 0. \tag{C.5}$$

For gases, e.g., the JWL EOS for detonation products, the origin of the internal energy is usually taken at $v = \infty$ (i.e. zero density). Care must be taken in choosing internal energy origins, but there is no effect on the form of the relations between thermodynamic parameters.

The internal energy-volume-entropy relationship

Substituting for p using

$$p = -\left(\frac{\partial e}{\partial v}\right)_S \tag{C.6}$$

in the Grüneisen EOS (equation C.3) gives a differential equation for the isentrope:

$$\left(\frac{\partial e}{\partial v}\right)_S + g(v)e = -p_{\mathrm{r}}(v) + g(v)e_{\mathrm{r}}(v). \tag{C.7}$$

Using an integrating factor

$$\tau(v) = \exp\left\{-\int g(v)\mathrm{d}v\right\}, \tag{C.8}$$

equation C.7 becomes

$$\left(\frac{\partial}{\partial v}\left[\frac{e}{\tau}\right]\right)_S = \frac{-p_{\mathrm{r}}(v) + g(v)e_{\mathrm{r}}(v)}{\tau(v)} = f'(v)$$

so that the e-v-S relation is of the form

$$e = \tau(v)\int f'(v)\mathrm{d}v + \tau(v)\phi(S), \tag{C.9}$$

where ϕ is a function of entropy. If we define $\phi(S_0)$ to be zero at the standard point $p = 0$, $v = v_0$, then the lower limit of the integral in equation C.9 is v_0 and the first term on the right-hand side of equation C.8 is a defined function of v. Formally integrating $f'(v)$ gives for the isentropic relation

$$e = \tau(v)\left[f(v) - f(v_0)\right] + \tau(v)\phi(S). \tag{C.10}$$

Equation C.10 represents an isentrope through any chosen point e, v. If we now consider an isentrope through a point at the same volume but on the reference curve, we find that

$$e_{\mathrm{r}}(v) = \tau(v)\left[f(v) - f(v_0)\right] + \tau(v)\phi_{\mathrm{r}}(v), \tag{C.11}$$

where ϕ_{r} is the value of ϕ on the reference curve. Equations C.10 and C.11 lead to the

second linear relation for the Grüneisen EOS:

$$e - e_{\mathrm{r}}(v) = \tau(v)\left[\phi(S) - \phi_{\mathrm{r}}(v)\right]. \tag{C.12}$$

The function $\tau(v)$ is defined from equation C.8 by the differential equation

$$\frac{\mathrm{d}\tau}{\mathrm{d}v} = -g\tau = -\frac{\Gamma}{v}\tau \tag{C.13}$$

and, in order to non-dimensionalise τ, it is convenient to choose the arbitrary constant so that

$$\tau(v_0) = 1. \tag{C.14}$$

Hence

$$\tau(v) = \exp\left\{-\int_{v_0}^{v} g(v)\mathrm{d}v\right\}. \tag{C.15}$$

A simple meaning for ϕ can be derived from equation C.12. If we consider the variation of ϕ with e at $v = v_0$ and define

$$\phi_{\mathrm{r}}(v_0) = 0, \tag{C.16}$$

then from equations C.5 and C.14 it follows that

$$\phi(S) = e(v_0, S), \tag{C.17}$$

so that the value of ϕ at any state (v, S) of the material is the value of the internal energy at $v = v_0$ on the isentrope through the point v, S. Using temperature as an implicit parameter, it follows that $\phi(S)$ is given by

$$\phi = \int_{T_0}^{T} c_{\mathrm{v}}\mathrm{d}T \tag{C.18}$$

at $v = v_0$, where

$$S = \int_{T_0}^{T} \frac{c_{\mathrm{v}}}{T}\mathrm{d}T.$$

Special case: an isentrope as the reference curve

When the reference curve is an isentrope (subscript S)

$$p_{\mathrm{S}}(v) = \frac{-\mathrm{d}e_{\mathrm{S}}(v)}{\mathrm{d}v}, \tag{C.19}$$

equation C.7 becomes

$$\left(\frac{\partial e}{\partial v}\right)_S + g(v)e = \frac{\mathrm{d}e_{\mathrm{S}}}{\mathrm{d}v} + g(v)e_{\mathrm{S}}(v), \tag{C.20}$$

which directly integrates using the integrating factor $\tau(v)$ to

$$e = e_{\mathrm{S}}(v) + \tau(v)\phi(S). \tag{C.21}$$

It follows that if the reference curve isentrope is analytic, all other isentropes are analytic.

The pressure-volume-entropy relation

The p-v-S relation is found by substituting equation C.12 into equation C.3, giving

$$p - p_{\mathrm{r}}(v) = g(v)\tau(v)\left[\phi(S) - \phi_{\mathrm{r}}(v)\right], \tag{C.22}$$

and when the reference curve is an isentrope

$$p = p_{\mathrm{S}}(v) + g(v)\tau(v)\phi(S). \tag{C.23}$$

The temperature-volume-entropy relation

Temperature is found by differentiating equation C.12, using the thermodynamic relation

$$T = \left(\frac{\partial e}{\partial S}\right)_v \tag{C.24}$$

so that

$$T = \tau(v)\dot{\phi}(S), \tag{C.25}$$

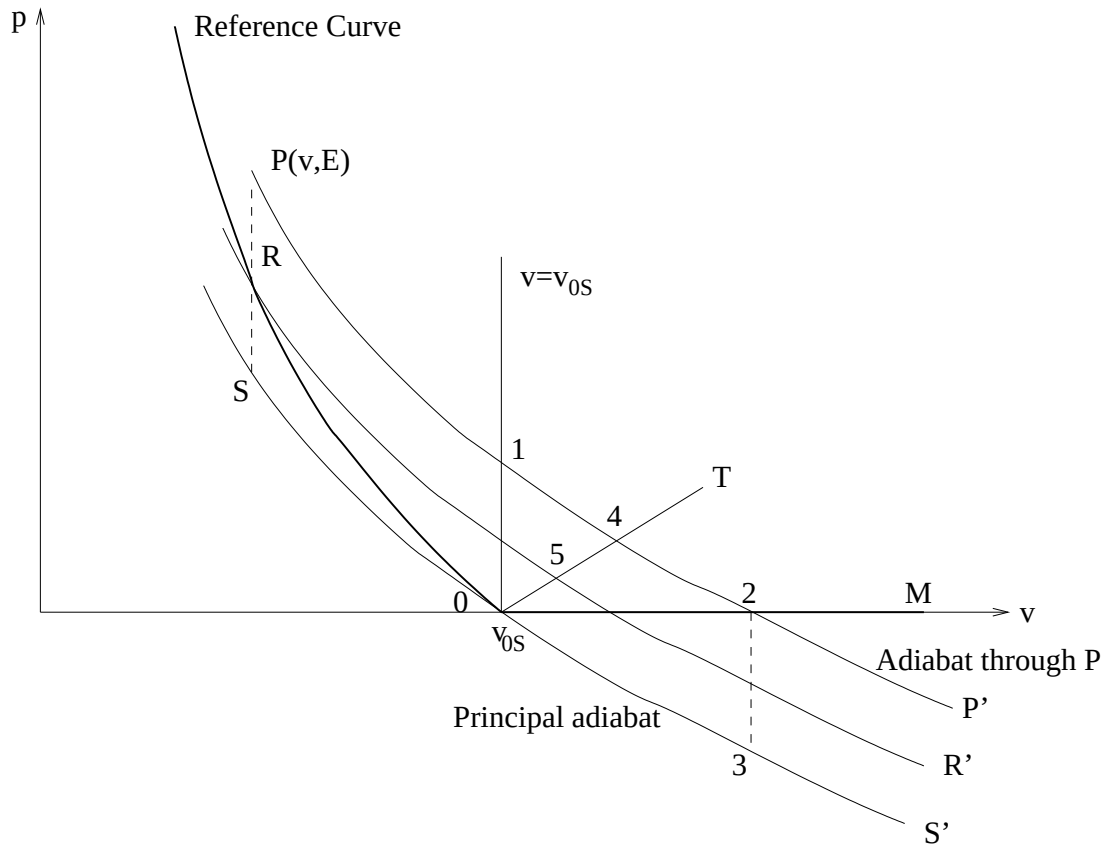

Figure C.1: Calculation of temperature

where the dot indicates differentiation with respect to S.

The importance of equation C.25 is that on any isentrope, temperature is proportional to $\tau(v)$ so that, if the temperature is T_1 at volume v, then the temperature at any other volume v on the same isentrope is given by

$$T = \frac{\tau(v)}{\tau(v_1)} T_1. \tag{C.26}$$

General *e-v-T* and *p-v-T* relations for a Grüneisen EOS

Assuming that $\tau(v)$ and either $\phi_r(v)$, $f(v)$ or $e_S(v)$ have been determined separately, then either equation C.10, C.12 or C.21 can be used to determine ϕ for any given point P (figure C.1) with state e, v. For simplicity of writing only, the known function is taken to

be $e_S(v)$. Then

$$\phi = \frac{e - e_S(v)}{\tau(v)}. \tag{C.27}$$

But from the choice of origins for ϕ, e_S and τ, equation C.17 shows that ϕ is equal to the internal energy at the point 1 in figure C.1 where the isentrope through P crosses the line $v = v_0$, i.e.

$$\phi = e_1.$$

Hence ϕ is related to the temperature at state 1 by equation C.18

$$\phi = \int_{T_0}^{T_1} c_v \mathrm{d}T$$

at $v = v_0$ and the required temperature T is given by

$$T = \tau(v) T_1 \tag{C.28}$$

from equation C.26 since

$$\tau(v_1) = \tau(v_0) = 1.$$

Hence by evaluating ϕ from equation C.27, T_1 from C.18, temperature can be determined from C.28. Formally T_1 and ϕ can be eliminated to write the general form of e-v-T equation for a Grüneisen EOS

$$e = e_S(v) + \tau(v) \int_{T_0}^{T/\tau(v)} c_v \mathrm{d}T. \tag{C.29}$$

Determination of auxiliary functions

Initially any Grüneisen EOS will have defined $e_r(v)$, $p_r(v)$ and $\Gamma(v)$, from which pressure can be calculated for any v and e. The auxiliary functions can be determined as follows:

- $\tau(v)$.

$$\tau(v) = \exp\left\{-\int_{v_0}^{v} g(v)\mathrm{d}v\right\}$$

which in many cases can be evaluated analytically, but will otherwise need to be in tabular form.

- $f(v)$, $e_S(v)$.

  From equation C.9,

  $$f(v) - f(v_0) = \int_{v_0}^{v} \left\{ \frac{-p_r(v) + g(v)e_r(v)}{\tau(v)} \right\} dv \tag{C.30}$$

  and hence the variation of internal energy on the principal isentrope is

  $$e_S(V) = \tau(v) \left[f(v) - f(v_0) \right]. \tag{C.31}$$

  The integral C.30 is only analytic for certain forms of Grüneisen EOS.

- $\phi_r(v)$.

  The function $\phi_r(v)$ is most easily determined from the variation of internal energy on any isentrope with known value of ϕ, e.g., from the principal isentrope – curve SOS' in figure C.1 on which $e = e_S(v)$ and $\phi = 0$.

  Then if point 3 is on the principal isentrope at $v = v_2$, and $e_S(v_2)$ is the internal energy at point 3, the value of $\phi_r(v_2)$ is obtained from equation C.21:

  $$\phi_r(v_2) = \frac{e_r(v_2) - e_S(v_2)}{\tau(v_2)}. \tag{C.32}$$

The Linear $U_s(u_p)$ EOS

The linear shock velocity-particle velocity EOS with constant Grüneisen Γ is

$$p = \frac{a^2(v_0 - v)\left\{1 - \frac{\Gamma_0}{2}\left(\frac{v_0 - v}{v}\right)\right\}}{[v_0 - b(v_0 - v)]^2} + \frac{\Gamma_0 e}{v}, \tag{C.33}$$

with

$$\tau(v) = \left(\frac{v_0}{v}\right)^{\Gamma_0}.$$

Hence from equation C.31 the internal energy on the principal isentrope is given by

$$e_S(v) = -\left(\frac{v_0}{v}\right)^{\Gamma_0} \int_{v_0}^{v} \frac{a^2(v_0 - v)\left[1 - \frac{\Gamma_0}{2}\left(\frac{v_0 - v}{v}\right)\right]\left(\frac{v}{v_0}\right)^{\Gamma_0}}{[v_0 - b(v_0 - v)]^2} \mathrm{d}v. \tag{C.34}$$

It so happens that many metals have Γ_0 close to the values 1, 1.5 or 2 and the integral is analytic, if algebraically tedious to carry out, in each of these cases. To save space the expressions

$$x = v_0 - v \quad \text{and} \quad X = v_0 - b(v_0 - v) = v_0 - bx$$

will be used, and only the results will be quoted. For $\Gamma = 1$,

$$e_S(v) = \frac{-a^2}{b^3}\left(\frac{v_0}{v}\right)\left\{\frac{3}{2}\frac{bx}{v_0} + (3 - b)\ln\frac{X}{v_0} - \left(b - \frac{3}{2}\right)\frac{bx}{X}\right\}. \tag{C.35}$$

It will be noted that in each case $e_S(v)$ has a singularity when $X = 0$, i.e. when

$$v = \frac{b - 1}{b} v_0,$$

and it is not recommended that the linear $U_s(u_p)$ EOS be used if v is likely to get close to this limit.

Temperature for a gaseous EOS

For a material for which it is convenient not to arrange the zero of internal energy to be at $p = 0$, $v = v_0$, the simple definition of ϕ given by equation C.18 does not hold and the calculation of temperature is slightly more complicated.

To illustrate the problem we examine the JWL EOS for which the origin of internal energy is conventionally taken as $p = 0$, $v = \infty$. The problem is further exacerbated by almost no knowledge of temperature or specific heat data. However, to make some headway it is supposed that the temperature and specific heat data are determined at the CJ point by chemical equilibrium calculations.

The JWL EOS for detonation products is

$$p = \left(1 - \frac{w}{R_1}\frac{v_0}{v}\right) A \exp\left(-R_1\frac{v}{v_0}\right) + \left(1 - \frac{w}{R_2}\frac{v_0}{v}\right) B \exp\left(-R_2\frac{v}{v_0}\right) + \frac{we}{v}, \tag{C.36}$$

which has constant Grüneisen $\Gamma = w$ and a reference curve which is apparently $e = 0$, but is in fact the CJ isentrope $p_S(v)$, $e_S(v)$, where

$$p_S(v) = A\exp\left(-R_1\frac{v}{v_0}\right) + B\exp\left(-R_2\frac{v}{v_0}\right) + w\left(\frac{v_0}{v}\right)^{1+w}\frac{\phi_{CJ}}{v_0} \tag{C.37}$$

$$e_S(v) = \frac{v_0 A}{R_1}\exp\left(-R_1\frac{v}{v_0}\right) + \frac{v_0 B}{R_2}\exp\left(-R_2\frac{v}{v_0}\right) + \left(\frac{v_0}{v}\right)^{w}\phi_{CJ}. \tag{C.38}$$

The third term in equation C.37 has been written in a form to make it consistent with the terminology used in this appendix and the special significance of ϕ. It is more normally written

$$C = \frac{w\phi_{CJ}}{v_0}. \tag{C.39}$$

At p_{CJ}, v_{CJ} the temperature is taken to be T_{CJ} and suppose that specific heat at constant volume is given by

$$c_v(T) = c_{v*} + \gamma_*(T - T_{CJ}). \tag{C.40}$$

From equation C.20, the general e-v-S relationship can be written

$$e = e_S(v) + \tau(v)(\phi - \phi_{CJ}). \tag{C.41}$$

Hence for any v, e state off the CJ isentrope, ϕ can be evaluated by inverting

$$\phi = \phi_{CJ} + \frac{e - e_S(v)}{\tau(v)}. \tag{C.42}$$

Knowing ϕ, equation C.41 can be used to find the internal energy e_1 at v_{CJ} on the isentrope through the unknown point

$$e_1 = e_S(v_{CJ}) + \tau_{CJ}(\phi - \phi_{CJ}). \tag{C.43}$$

Then by integrating, the temperature T_1 corresponding to (e_1, v_{CJ}) is given by

$$e_1 = e_{CJ} = \int_{T_{CJ}}^{T_1} c_v \mathrm{d}T = c_{v*}(T_1 - T_{CJ}) + \frac{1}{2}\gamma_*(T_1 - T_{CJ})^2, \tag{C.44}$$

and the temperature at the unknown point is given by

$$T = T_1 \frac{\tau(v)}{\tau(v_{CJ})}. \tag{C.45}$$

Combining equations C.42 to C.45, the e-v-T relationship is

$$e = e_S(v) + \tau(v)\left[c_{v*}\left(\frac{T}{\tau(v)} - \frac{T_{CJ}}{\tau_{CJ}}\right) + \frac{1}{2}\gamma_*\tau_{CJ}\left(\frac{T}{\tau(v)} - \frac{T_{CJ}}{\tau_{CJ}}\right)^2\right], \tag{C.46}$$

or, for a general $c_v(T)$ at $v = v_{CJ}$,

$$e = e_S(v) + \frac{\tau(v)}{\tau_{CJ}} \int_{T_{CJ}}^{\frac{\tau_{CJ}T}{\tau(v)}} c_v \mathrm{d}T. \tag{C.47}$$

Bibliography

[1] P W Cooper. *Explosives engineering*. Wiley, 1999.

[2] J A Zukas and W P Walters, editors. *Explosives development and fundamentals of explosives technology*, chapter 2. Springer, 1998.

[3] B A Khasainov, A V Attetkov, and A A Borisov. Shock-wave initiation of porous energetic materials and visco-plastic model of hot spots. *Chemical Physics Reports*, 15(7):987–1062, 1996.

[4] M A Cook. *The science of high explosives*. American Chemical Society Monograph Series. Reinhold Publishing Corporation, 1958.

[5] R Courant and K O Friedrichs. *Supersonic flow and shock waves*. Interscience, 1948.

[6] W Fickett and W C Davis. *Detonation theory and experiment*. Dover Publications, 2000.

[7] A W Campbell, W C Davis, and J R Travis. Shock initiation of detonation in liquid explosives. In *Third Symposium on Detonation*, volume ACR 52, pages 469–498. Office of Naval Research, 1960.

[8] A W Campbell, W C Davis, J B Ramsay, and J R Travis. Shock initiation of solid explosives. In *Third Symposium on Detonation*, volume ACR 52, pages 499–519. Office of Naval Research, 1960.

[9] R Menikoff. On beyond the standard model for high explosives: challenges and obstacles to surmount. In *Shock Compression of Condensed Matter 2009*, AIP Conference Proceedings 1195, pages 18–25. New York, 2009.

[10] J B Ramsay and A Popolato. Analysis of shock wave and initiation data for solid explosives. In *Fourth (International) Symposium on Detonation 1965*, volume ACR-126, pages 233–238. Office of Naval Research, 1965.

[11] T R Gibbs and A Popolato. *LASL explosive property data*. University of California Press, 1980.

[12] R L Gustavsen, S A Sheffield, R R Alcon, L G Hill, R E Winter, D A Salisbury, and

P Taylor. Initiation of EDC37 measured with embedded electromagnetic particle velocity gauges. In *Shock Compression of Condensed Matter 1999*, AIP Conference Proceedings 505, pages 879–882. New York, 1999.

[13] N K Bourne and A M Milne. The temperature of a shock-collapsed cavity. In *Proceedings of the Royal Society of London*, volume A 459, pages 1851–1861, 2003.

[14] L E Fried, F Najjar, W M Howard, M R Manaa, E J Reed, N Goldman, S Bastea, and A L Nichols III. Multiscale simulation of hot spot ignition. In *Fourteenth International Detonation Symposium*. Office of Naval Research, 2010.

[15] R B Frey. The initiation of explosive charges by rapid shear. In *Seventh Symposium (International) on Detonation 1981*, volume NSWC MP 82-334, pages 36–42. Naval Surface Weapons Center, 1981.

[16] J E Field, N K Bourne, S J P Palmer, and S M Walley. Hot spot ignition mechanisms for explosives and propellants. *Phil. Trans. R. Soc. Lond.*, A339:269–283, 1992.

[17] J E Field. Hot spot ignition mechanisms for explosives. *Accounts of Chemical Research*, 25(11):489–496, 1992.

[18] F P Bowden and A D Yoffe. *Initiation and growth of explosion in liquids and solids*. Cambridge University Press, 1952.

[19] D Bradley. Hotspots and gasoline engine knock. *Journal of the Chemical Society - Faraday Transactions*, 92(16):2959–2964, 1996.

[20] M Braithwaite, P M Lynch, I B Parker, A F Jones, and S D R Wilson. Compressional heating of isolated gas bubbles in reactive media. *Mathematical Engineering in Industry*, 7(3):361–387, 1999.

[21] S S Rybanin and Y M Mikhailov. The number defining the realization of the hot spot mechanism on detonation of heterogeneous explosives. *Doklady Physical Chemistry*, 409(1):214–217, 2006.

[22] I V Kuz'mitsky. On the mechanism of detonation initiation from hot spots. Presented at the New Models and Hydrocodes for Shock Wave Processes in Condensed Matter conference, Dijon, France, April 2006.

[23] A G Merzhanov. On critical conditions for thermal explosion of a hot spot. *Combustion and Flame*, 10:341–348, 1966.

[24] C M Tarver, S K Chidester, and A L Nichols III. Critical conditions for impact- and shock-induced hot spots in solid explosives. *J. Phys. Chem.*, 100(14):5794–5799, 1996.

[25] C M Tarver and A L Nichols III. Hot spot growth in a thermal-chemical-mechanical reactive flow model for shock initiation of solid explosives. In *Eleventh International Detonation Symposium*, volume ONR 33300-5, pages 599–605. Office of Naval Research, 1998.

[26] J E Reaugh. Multi-scale computer simulations to study the reaction zone of solid explosives. In *Thirteenth International Detonation Symposium*, volume ONR 351-07-01, pages 1276–1285. Office of Naval Research, 2006.

[27] R L Bowers and J R Wilson. *Numerical modeling in applied physics and astrophysics*. Jones and Bartlett Publishers, 1991.

[28] D J Benson. Computational methods in Lagrangian and Eulerian hydrocodes. *Computer Methods in Applied Mechanics and Engineering*, 99:235–394, 1992.

[29] D L Chapman. On the rate of explosion in gases. *Philosophical Magazine*, 47:90, 1899.

[30] E Jouguet. *Micanique des explosifs*. Paris, O. Doin et fils, 1917.

[31] Y B Zeldovich. On the theory of the propagation of detonation waves in gaseous systems. *Journal of Experimental and Theoretical Physics (USSR)*, 10:542–568, 1940.

[32] J von Neumann. *Theory of detonation waves*, volume 6. OSRD 549, 1942.

[33] W Doering. On detonation processes in gases. *Ann. Physik*, 43:421–436, 1943.

[34] J B Bdzil, W Fickett, and D S Stewart. Detonation shock dynamics: a new approach to modeling multi-dimensional detonation waves. In *Ninth Symposium (International) on Detonation 1989*, volume OCNR 113291-7, pages 730–742. Office of the Chief of Naval Research, 1989.

[35] B D Lambourn and D C Swift. Application of Whitham's shock dynamics theory to the propagation of divergent detonation waves. In *Ninth Symposium (International) on Detonation 1989*, volume OCNR 113291-7, pages 784–797. Office of the Chief of Naval Research, 1989.

[36] E L Lee and C M Tarver. Phenomenological model of shock initiation in heterogeneous explosives. *Physics of Fluids*, 23(12):2362–2372, 1980.

[37] B L Wescott, D Scott Stewart, and W C Davis. Equation of state and reaction rate for condensed-phase explosives. *Journal of Applied Physics*, 98(053514), 2005.

[38] C A Handley. The CREST reactive burn model. In *Thirteenth International Detonation Symposium*, volume ONR 351-07-01, pages 864–870. Office of Naval Research, 2006.

[39] S Palmer. Private communication. Cavendish Laboratory, Cambridge University.

[40] C B Skidmore, D S Phillips, and N B Crane. Microscopical examination of plastic-bonded explosives. LA-UR-97-2807, Los Alamos National Laboratory Report, 1997.

[41] A C Hazelwood. Private communication. AWE.

[42] P D Peterson, M A Fletcher, and E L Roemer. Influence of pressing intensity on the microstructure of PBX9501. *Journal of Energetic Materials*, 21(4):247–260, 2003.

[43] C B Skidmore, D S Phillips, P M Howe, J T Mang, and J A Romero. The evolution of microstructural changes in pressed HMX explosives. In *Eleventh International Detonation Symposium*, volume ONR 33300-5, pages 556–564. Office of Naval Research, 1998.

[44] J M McAfee, C B Skidmore, G S Cunningham, and R A Nelson. Explosive morphology from fractal analysis of micrographs. In *Eleventh International Detonation Symposium*, volume ONR 33300-5, pages 391–398. Office of Naval Research, 1998.

[45] H Moulard. Particular aspect of the explosive particle size effect on shock sensitivity of cast PBX formulations. In *Ninth Symposium (International) on Detonation 1989*, volume OCNR 113291-7, pages 18–24. Office of the Chief of Naval Research, 1989.

[46] D Bedrov, G D Smith, and T D Sewell. Thermal conductivity of liquid octahydro-1,3,5,7-tetranitro-1,3,5,7-tetrazocine (HMX) from molecular dynamics simulations. *Chemical Physics Letters*, 324:64–68, 2000.

[47] M R Manaa, L E Fried, C F Melius, M Elstner, and T Frauenheim. Decomposition of HMX at extreme conditions: a molecular dynamics simulation. *Journal of Physical Chemistry A*, 106:9024–9029, 2002.

[48] T D Sewell. Atomistic studies of fundamental properties and processes in energetic materials: relevance to mesoscale initiation phenomena. *Central European Journal of Energetic Materials*, 3(1-2):19–38, 2006.

[49] A L Nichols III and C M Tarver. A statistical hot-spot reactive flow model for shock initiation and detonation of solid high explosives. In *Twelfth International Detonation Symposium*, volume ONR 333-05-2, pages 489–496. Office of Naval Research, 2002.

[50] Y Hamate and Y Horie. A statistical approach on modelling of high explosive ignition. In *Shock Compression of Condensed Matter 2003*, AIP Conference Proceedings 706, pages 335–338. New York, 2003.

[51] A M Milne, A W Longbottom, and J D Dunnett. Hazard reactive flow model development. CR045/02i2, Fluid Gravity Engineering Ltd, 2002.

[52] D C Swift, R N Mulford, R E Winter, P Taylor, D A Salisbury, and E J Harris. Mesoscale modelling of reaction in HMX-based explosives. In *Twelfth International Detonation Symposium*, volume ONR 333-05-2, pages 967–974. Office of Naval Research, 2002.

[53] B D Lambourn, C A Handley, H R James, and N J Whitworth. Some mesoscale implications of the CREST reactive burn model. In *Fourteenth International Detonation Symposium*. Office of Naval Research, 2010.

[54] E M Mas, B E Clements, and D C George. Direct numerical simulations of PBX9501. In *Shock Compression of Condensed Matter 2003*, AIP Conference Proceedings 706, pages 389–392. New York, 2003.

[55] B E Clements and E M Mas. Modeling high explosives with the method of cells and Mori-Tanaka effective medium theories. In *Shock Compression of Condensed Matter 2001*, AIP Conference Proceedings 620, pages 427–430. New York, 2001.

[56] R Menikoff and E Kober. Compaction waves in granular HMX. In *Shock Compression of Condensed Matter 1999*, AIP Conference Proceedings 505, pages 397–400. New York, 1999.

[57] R Menikoff. Compaction wave profiles in granular HMX. In *Shock Compression of Condensed Matter 2001*, AIP Conference Proceedings 620, pages 979–982. New York, 2001.

[58] R Panchadhar and K A Gonthier. Meso-scale heating predictions for weak impact of granular energetic solids. In *Shock Compression of Condensed Matter 2009*, AIP Conference Proceedings 1195, pages 1377–1380. New York, 2009.

[59] S G Bardenhagen, J U Brackbill, and D L Sulsky. Shear deformation in granular material. In *Eleventh International Detonation Symposium*, volume ONR 33300-5, pages 547–555. Office of Naval Research, 1998.

[60] S G Bardenhagen, K M Roessig, O Byutner, J E Guilkey, D Bedrov, and G D Smith. Direct numerical simulation of weak shocks in granular material. In *Twelfth International Detonation Symposium*, volume ONR 333-05-2, pages 497–503. Office of Naval Research, 2002.

[61] S G Bardenhagen, D R Greening, and K M Roessig. The material point method and simulation of wave propagation in heterogeneous media. In *Shock Compression of Condensed Matter 2003*, AIP Conference Proceedings 706, pages 187–192. New York, 2003.

[62] K Kline, Y Horie, J J Dick, and W Wang. Impact response of PBX9501 below 2 GPa. In *Shock Compression of Condensed Matter 2001*, AIP Conference Proceedings 620, pages 411–414. New York, 2001.

[63] Z P Tang and W W Wang. Discrete element modeling for shock processes of heterogeneous materials. In *Shock Compression of Condensed Matter 2001*, AIP Conference Proceedings 620, pages 679–684. New York, 2001.

[64] M R Baer. Computational modeling of heterogeneous reactive materials at the mesoscale. In *Shock Compression of Condensed Matter 1999*, AIP Conference Proceedings 505, pages 27–33. New York, 1999.

[65] M R Baer and W M Trott. Theoretical and experimental mesoscale studies of impact-loaded granular explosive and simulant materials. In *Twelfth International Detonation Symposium*, volume ONR 333-05-2, pages 939–950. Office of Naval Research, 2002.

[66] M R Baer, M E Kipp, and F van Swol. Micromechanical modeling of heterogeneous energetic materials. In *Eleventh International Detonation Symposium*, volume ONR 33300-5, pages 788–797. Office of Naval Research, 1998.

[67] A L Brundage, R R Wixom, A S Tappan, and G T Long. Mesoscale simulations of shock initiation in energetic materials characterized by three-dimensional nanotomography. In *Shock Compression of Condensed Matter 2009*, AIP Conference Proceedings 1195, pages 315–318. New York, 2009.

[68] P A Conley. *Eulerian hydrocode analysis of reactive micromechanics in the shock initiation of heterogeneous energetic material*. PhD thesis, University of California, San Diego, Department of Mechanical Engineering, 1999.

[69] P A Conley, D J Benson, and P M Howe. Microstructural effects in shock initiation. In *Eleventh International Detonation Symposium*, volume ONR 33300-5, pages 768–780. Office of Naval Research, 1998.

[70] P M Howe and D C Benson. An engineering model of shock initiation. In *Twelfth International Detonation Symposium*, volume ONR 333-05-2, pages 951–957. Office of Naval Research, 2002.

[71] P M Howe and D J Benson. Progress in the development of a shock initiation model. In *Shock Compression of Condensed Matter 2003*, AIP Conference Proceedings 706, pages 343–346. New York, 2003.

[72] D J Benson and W J Nellis. Dynamic compaction of copper powder: computation and experiment. *Applied Physics Letters*, 65(4):418–420, 1994.

[73] J E Flinn, R L Williamson, R A Berry, and R N Wright. Dynamic consolidation

of type 304 stainless-steel powders in gas gun experiments. *Journal of Applied Physics*, 64(3):1446–1456, 1988.

[74] R Menikoff and T D Sewell. Constituent properties of HMX needed for mesoscale simulations. *Los Alamos Technical Report LA-13546-MS*, 1999.

[75] R E Winter, S S Sorber, D A Salisbury, P Taylor, R Gustavsen, S Sheffield, and R Alcon. Experimental study of the shock response of an HMX-based explosive. *Shock Waves*, DOI:10.1007(s00193-006-0006-5), 2006. Published online at www.springer.com.

[76] P W Merchant, S J White, and A M Collyer. A WBL-consistent JWL equation of state for the HMX-based explosive EDC37 from cylinder tests. In *Twelfth International Detonation Symposium*, volume ONR 333-05-2, pages 632–640. Office of Naval Research, 2002.

[77] C Leppard. Private communication. AWE.

[78] N K Bourne. Impact on alumina I: response at the mesoscale. In *Proceedings of the Royal Society of London*, volume A 462, pages 3061–3080, 2006.

[79] S A McDonald, J C F Millett, N K Bourne, K Bennett, A M Milne, and P J Withers. The shock response, simulation and microstructural determination of a model composite material. *Journal of Materials Science*, 42:9671–9678, 2007.

[80] R Menikoff and T D Sewell. Constituent properties of HMX needed for mesoscale simulations. *Combustion theory and modelling*, 6(4):103–125, 2002.

[81] R N Mulford and D C Swift. Mesoscale modelling of shock initiation in HMX-based explosives. In *Shock Compression of Condensed Matter 2001*, AIP Conference Proceedings 620, pages 415–418. New York, 2001.

[82] B F Henson, L Smilowitz, B W Asay, P M Dickson, and P M Howe. Evidence for thermal equilibrium in the detonation of HMX. In *Twelfth International Detonation Symposium*, volume ONR 333-05-2, pages 987–992. Office of Naval Research, 2002.

[83] R Menikoff. Detonation waves in PBX9501. *Combustion Theory and Modelling*, 10:1003–1021, 2006.

[84] R V Browning and R J Scammon. Microstructural model of ignition for time varying loading conditions. In *Shock Compression of Condensed Matter 2001*, AIP Conference Proceedings 620, pages 987–990. New York, 2001.

[85] B F Henson, L Smilowitz, J J Romero, and B W Asay. Modeling thermal ignition and the initial conditions for internal burning in PBX9501. In *Shock Compression of Condensed Matter 2009*, AIP Conference Proceedings 1195, pages 257–262.

New York, 2009.

[86] R R McGuire and C M Tarver. Chemical decomposition model for the thermal explosion of confined HMX, RDX and TNT explosives. In *Seventh Symposium (International) on Detonation 1981*, volume NSWC MP 82-334, pages 56–64. Naval Surface Weapons Center, 1981.

[87] J E Reaugh. Private communication. LLNL.

[88] E S Oran and J P Boris. *Numerical simulation of reactive flow*. Cambridge University Press, 2nd ed. edition, 2001.

[89] J R Wendt, editor. *Computational fluid dynamics*. A von Karmen Institute Book. Springer, second edition, 1996.

[90] M R Baer and J W Nunziato. A two-phase mixture theory for the deflagration-to-detonation transition (DDT) in reactive granular materials. *Int. J. Multiphase Flow*, 12:861–889, 1986.

[91] J M McAfee, B W Asay, and A W Campbell. Deflagration to detonation in granular HMX. In *Ninth Symposium (International) on Detonation 1989*, volume OCNR 113291-7, pages 265–279. Office of the Chief of Naval Research, 1989.

[92] P E Luebcke, P M Dickson, and J E Field. Experimental investigation into the deflagration to detonation transition in secondary explosives. In *Tenth International Detonation Symposium*, volume ONR 33395-12, pages 242–264. Office of Naval Research, 1993.

[93] I Plaksin, C S Coffey, R Mendes, J Ribeiro, J Campos, and J Direito. Formation of CRZ 3D structure at SDT and at shear initiation of PBX: effects of front irradiation and reaction localisation in HMX crystals. In *Thirteenth International Detonation Symposium*, volume ONR 351-07-01, pages 319–330. Office of Naval Research, 2006.

[94] S Gasiorowicz. *Quantum Physics*. Wiley, second edition, 1996.

[95] D Tasker and V Whitley. Electromagnetic effects on explosive reaction and plasma. In *Fourteenth International Detonation Symposium*, 2010.

[96] M L Wilkins. *Calculation of elastic-plastic flow*, volume 3, pages 211–263. Academic Press, 1964.

[97] J von Neumann and R D Richtmyer. A method for the numerical calculation of hydrodynamic shocks. *Journal of Applied Physics*, 21:232–257, 1950.

[98] M L Wilkins. Use of artificial viscosity in multidimensional fluid dynamics calculations. *Journal of Computational Physics*, 36:381–403, 1980.

[99] E F Toro. *Riemann solvers and numerical methods for fluid dynamics*. Springer-

Verlag, 1997.

[100] G A Sod. A survey of several different methods for systems of nonlinear hyperbolic conservation laws. *Journal of Computational Physics*, 27:1–31, 1978.

[101] R P Feynman, R B Leighton, and M Sands. *The Feynman Lectures on Physics*. Addison-Wesley, sixth edition, 1977.

[102] S R Turns. *An Introduction to Combustion: Concepts and Applications*. McGraw-Hill, 1996.

[103] J E Reaugh. Computer simulations to study the high-pressure deflagration of HMX. In *Shock Compression of Condensed Matter 2003*, AIP Conference Proceedings 706, pages 401–404. New York, 2003.

[104] D Bedrov, G D Smith, and T D Sewell. Temperature-dependent shear viscosity coefficient of octahydro-1,3,5,7-tetranitro-1,3,5,7-tetrazocine (HMX): a molecular dynamics simulation study. *Journal of Chemical Physics*, 112(16):7203–7208, 2000.

[105] A Barlow. *An adaptive multi-material arbitrary Lagrangian Eulerian algorithm for computational shock hydrodynamics*. PhD thesis, University of Wales, Swansea, Department of Civil Engineering, 2002.

[106] B van Leer. Towards the ultimate conservative difference scheme. IV. A new approach to numerical convection. *Journal of Computational Physics*, 23:276–299, 1977.

[107] N J Whitworth. Simple one-dimensional model of "hot-spot" formation in heterogeneous solid explosives. Numerical Methods & Software Systems: MSc Dissertation, Royal Military College of Science, Cranfield University, 1999.

[108] N J Whitworth. Private communication. AWE.

[109] D L Youngs. Time-dependent multi-material flow with large fluid distortion. In K W Morton and M J Baines, editors, *Numerical Methods for Fluid Dynamics*, pages 273–285. Academic Press, 1982.

[110] P E Langridge. Private communication. AWE.

[111] W F Noh. Errors for calculations of strong shocks using an artificial viscosity and an artificial heat flux. *Journal of Computational Physics*, 72:78–120, 1987.

[112] R Landshoff. A numerical method for treating fluid flow in the presence of shocks. Technical Report LA-1930, Los Alamos Scientific Laboratory, 1955.

[113] W F Noh and P Woodward. SLIC (simple line interface calculation). *Lecture Notes in Physics*, 59:330–340, 1976.

[114] N J Whitworth. *Mathematical and numerical modelling of shock initiation in het-*

erogeneous solid explosives. PhD Thesis, Defence College of Science & Technology, Cranfield University, 2008.

[115] A Longbottom. *REACTDIFF user manual*. Fluid Gravity Engineering Ltd, 2004.

[116] A C Hindmarsh. Serial Fortran solvers for ODE initial value problems. *http://www.llnl.gov/CASC/odepack*, 2002.

[117] P N Brown, G D Byrne, and A C Hindmarsh. VODE, a variable-coefficient ODE solver. *SIAM Journal on Scientific and Statistical Computing*, 10(5):1038–1051, 1989.

[118] W H Press, S A Teukolsky, W T Vetterling, and B P Flannery. *Numerical recipes in Fortran 77*. Cambridge University Press, second edition, 1992.

[119] A L Nichols III and K W Westerberg. Modification of a thermal transport code to include chemistry with thermally controlled kinetics. *Numerical Heat Transfer, Part B*, 24:489–509, 1993.

[120] A L Nichols III, R Couch, R C McCallen, I Otero, and R Sharp. Modeling thermally driven energetic response of high explosives. In *Eleventh International Detonation Symposium*, volume ONR 33300-5, pages 862–871. Office of Naval Research, 1998.

[121] A L Nichols III, A Anderson, R Neely, and B Wallin. A model for high explosive cookoff. In *Twelfth International Detonation Symposium*, volume ONR 333-05-2, pages 94–102. Office of Naval Research, 2002.

[122] H S Carslaw and J C Jaeger. *Conduction of heat in solids*. Oxford University Press, 2nd edition, 1959.

[123] E Catalano, R McGuire, E Lee, E Wrenn, D Ornellas, and J Walton. The thermal decomposition and reaction of confined explosives. In *Sixth Symposium (International) on Detonation*, volume ACR-221, pages 214–222. Office of Naval Research, 1976.

[124] R L Gustavsen, S A Sheffield, and R R Alcon. Progress in measuring detonation wave profiles in PBX9501. In *Eleventh International Detonation Symposium*, volume ONR 33300-5, pages 821–827. Office of Naval Research, 1998.

[125] J E Reaugh. Grain-scale dynamics in explosives. UCRL-ID-150388, Lawrence Livermore National Laboratory, 2002.

[126] B R Schlei, L Prasad, and A N Skourikhine. Geometric morphology of granular materials. LA-UR-00-2839, Los Alamos National Laboratory Report, 2000. Submitted for the SPIE 45th Meeting, San Diego.

[127] S Maheswaran. Private communication. AWE.

[128] P D Peterson and K Y Lee. Particle characterization using light scattering and PLM image analysis. LA-UR-03-9125, Los Alamos National Laboratory Report, 2003.

[129] G I Taylor. The use of flat-ended projectiles for determining dynamic yield stress. *Proceedings of the Royal Society*, A(194):289–299, 1948.

[130] D M Williamson, S J P Palmer, W G Proud, and R Govier. Brazilian disc testing of a UK PBX above and below the glass transition temperature. In *Shock Compression of Condensed Matter 2007*, AIP Conference Proceedings 955, pages 803–806. New York, 2007.

[131] D J Steinberg. Equation of state and strength properties of selected materials. URCL-MA-106439, University of California, 1996.

[132] J J Dick, D E Hooks, R Menikoff, and A R Martinez. Elastic-plastic wave profiles in cyclotetramethylene tetranitramine crystals. *Journal of Applied Physics*, 96(1):374–379, 2004.

[133] R Menikoff, J J Dick, and D E Hooks. Analysis of wave profiles for single crystal HMX. *Journal of Applied Physics*, 97:023529, 2005.

[134] R L Gustavsen, S A Sheffield, R R Alcon, and L G Hill. Shock initiation of new and aged PBX9501 measured with embedded electromagnetic particle velocity gauges. LA-13634-MS, Los Alamos National Laboratory Report, 1999.

[135] C M Tarver and T D Tran. Thermal decomposition models for HMX-based plastic bonded explosives. *Combusion & Flame*, 137:50–62, 2004.

[136] K R Glaesemann and L E Fried. Recent advances in modeling Hugoniots with Cheetah. In *Shock Compression of Condensed Matter 2005*, AIP Conference Proceedings 845, pages 515–518. New York, 2005.

[137] M Cowperthwaite. A constitutive model for calculating chemical energy release rates from the flow fields in shocked explosives. In *Seventh Symposium (International) on Detonation 1981*, volume NSWC MP 82-334, pages 498–505. Naval Surface Weapons Center, 1981.

[138] B D Lambourn. An improved EOS for non-reacted explosives. In *Shock Compression of Condensed Matter 2005*, AIP Conference Proceedings 845, pages 165–168. New York, 2005.

[139] B D Lambourn and P G Parish. On the general linearity of the Gruneisen form of equation of state and the determination of temperature. Internal AWE Report, 1978.

[140] R G Ross, P Andersson, B Sundqvist, and G Backstrom. Thermal conductivity of

solids and liquids under pressure. *Reports on Progress in Physics*, 47:1347–1402, 1984.

[141] S Bastea. Transport properties of fluid mixtures at high pressures and temperatures. Application to the detonation products of HMX. In *Twelfth International Detonation Symposium*, volume ONR 333-05-2, pages 576–583. Office of Naval Research, 2002.

[142] C V Madhusudana. *Thermal contact conductance*. Springer, 1996.

[143] L Smilowitz, B F Henson, B W Asay, and P M Dickson. A model of the $\beta-\delta$ phase transition in PBX9501. In *Twelfth International Detonation Symposium*, volume ONR 333-05-2, pages 103–111. Office of Naval Research, 2002.

[144] C K Saw. Kinetics of HMX and phase transitions: effects of grain size at elevated temperature. In *Twelfth International Detonation Symposium*, volume ONR 333-05-2, pages 70–76. Office of Naval Research, 2002.

[145] M Herrmann, W Engel, and N Eisenreich. Thermal expansion, transitions, sensitivities and burning rates of HMX. *Propellants, Explosives, Pyrotechnics*, 17:190–195, 1992.

[146] B D Lambourn. Private communication. AWE.

[147] J S Gudmundsson and H K Celius. Gas-liquid metering using pressure-pulse technology. In *SPE Annual Technical Conference and Exhibition*, volume SPE 56584, Houston, Texas, 1999.

[148] A A Pekalski, J F Zevenbergen, M Braithwaite, S M Lemkowitz, and H J Pasman. Explosive decomposition of ethylene oxide at elevated condition: effect of ignition energy, nitrogen dilution, and turbulence. *Journal of Hazardous Materials*, A118:19–34, 2005.

[149] I I Karpenko, V G Morozov, O N Chernysheva, and Y V Yanilkin. Calculations of the rate of growth of hotspots during detonation taking into account the turbulent mechanism of energy transfer. *Russian Journal of Physical Chemistry B*, 2(2):157–161, 2008.

[150] I I Karpenko, V G Morozov, V B Titova, Y V Yanilkin, O N Chernysheva, B M Zhogov, and N A Volodina. Physical mechanism and numerical simulations of the hot spot growth rate in detonation initiation. Presented at the conference: New Models and Hydrocodes for Shock Wave Processes in Condensed Matter, 2010.

[151] R J Williams. Private communication. AWE.

[152] D E Hooks, J J Dick, and A R Martinez. Shock experiments on explosive single crystals. In *Shock Compression of Condensed Matter 2003*, AIP Conference

Proceedings 706, pages 985–988. New York, 2003.

[153] N R Barton, N W Winter, and J E Reaugh. Defect evolution and pore collapse in crystalline energetic materials. *Modelling and Simulation in Materials Science and Engineering*, 17:035003, 2009.

[154] T D Sewell and R Menikoff. Complete equation of state for β-HMX and implications for initiation. In *Shock Compression of Condensed Matter 2003*, AIP Conference Proceedings 706, pages 157–160. New York, 2003.

[155] B D Lambourn, N J Whitworth, C A Handley, and H R James. A finite strain, non-reacted EOS for PBX9502. In *Shock Compression of Condensed Matter 2007*, AIP Conference Proceedings 955, pages 137–140. New York, 2007.

[156] P C Souers, S Anderson, J Mercer, E McGuire, and P Vitello. JWL++: a simple reactive flow code package for detonation. *Propellants, Explosives, Pyrotechnics*, 25:54–59, 2000.

[157] M D Cook, P J Haskins, and C Stennett. Development and implementation of an ignition and growth model for homogeneous and heterogeneous explosives. In *Eleventh International Detonation Symposium*, volume ONR 33300-5, pages 589–598. Office of Naval Research, 1998.

[158] R Menikoff. Compaction wave profiles: simulations of gas gun experiments. *Journal of Applied Physics*, 90(4):1754–1760, 2001.

[159] S P Marsh. *LASL shock Hugoniot data*. University of California Press, 1980.

[160] B M Dobratz and P C Crawford. LLNL explosives handbook: properties of chemical explosives and explosive simulants. URCL-52997, University of California, 1985.

[161] D M Hanson-Parr and T P Parr. Thermal properties measurements of solid rocket propellant oxidizers and binder materials as a function of temperature. *Journal of Energetic Materials*, 17(1):1–48, 1999.

[162] R L Shoemaker, J A Stark, and R E Taylor. Thermophysical properties of propellants. *High Temperatures – High Pressures*, 17:429–435, 1985.

[163] M R Baer, C A Hall, R L Gustavsen, D E Hooks, S A Sheffield, and G T Sutherland. Isentropic compression studies of the mesoscale response of energetic composites and constituents. In *Thirteenth International Detonation Symposium*, volume ONR 351-07-01, pages 1070–1080. Office of Naval Research, 2006.

[164] J J Dick, A R Martinez, and R S Hixson. Plane impact response of PBX9501 and its components below 2 GPa. LA-13426-MS, Los Alamos National Laboratory Report, 1998.

[165] S J P Palmer, D M Williamson, W G Proud, and C Bauer. Thermal properties of a UK PBX and binder system. In *Shock Compression of Condensed Matter 2007*, AIP Conference Proceedings 955, pages 849–852. New York, 2007.

[166] J W Kury, H C Horring, E L Lee, J L McDonel, D L Ornellas, M Finger, F M Strange, and M L Wilkins. Metal acceleration by chemical explosives. In *Fourth (International) Symposium on Detonation 1965*, volume ACR-126, pages 3–13. Office of Naval Research, 1965.

[167] G I Kerley. XRB: a new reactive burn model for heterogeneous and homogeneous explosives. NSWCDD/TR-00/105, Naval Surface Warfare Center, 2000.

[168] W Byers Brown and M Braithwaite. Development of the Williamsburg equation of state to model non-ideal detonation. In *Tenth International Detonation Symposium*, volume ONR 33395-12, pages 377–385. Office of Naval Research, 1993.

[169] J D Dunnett, D C Swift, and M Braithwaite. Comparison of Williamsburg and JWL equations of state for nitromethane. In *Eleventh International Detonation Symposium*, volume ONR 33300-5, pages 1065–1072. Office of Naval Research, 1998.

[170] C L Mader. *Numerical modeling of explosives and propellants*. CRC Press, 1998.

[171] R Menikoff. Detonation wave profile in PBX9501. In *Shock Compression of Condensed Matter 2005*, AIP Conference Proceedings 845, pages 986–989. New York, 2005.

[172] G B Manelis, G M Nazin, Yu I Rubtsov, and V A Strunin. *Thermal decomposition and combustion of explosives and propellants*. Taylor & Francis, 2003.

[173] C A Handley. Lagrangian analysis of velocity gauge data to determine reaction rate histories in EDC37. In *Shock Compression of Condensed Matter 2005*, AIP Conference Proceedings 845, pages 1073–1076. New York, 2005.

[174] O Sharia and M M Kuklja. Effect of defects on initiation of chemistry in HMX. In *Shock Compression of Condensed Matter 2009*, AIP Conference Proceedings 1195, pages 353–356. New York, 2009.

[175] H R James and B D Lambourn. On the systematics of particle velocity histories in the shock-to-detonation transition regime. *Journal of Applied Physics*, 100(084906), 2006.

[176] R N Mulford and D C Swift. Reactive flow models for the desensitization of high explosive. In *Shock Compression of Condensed Matter 1999*, AIP Conference Proceedings 505, pages 895–898. New York, 1999.

[177] R N Mulford, D C Swift, and M Braithwaite. Temperature-based reactive flow

model for ANFO. In *Twelfth International Detonation Symposium*, volume ONR 333-05-2, pages 927–936. Office of Naval Research, 2002.

[178] B F Henson, B W Asay, L B Smilowitz, and P M Dickson. Ignition chemistry in HMX from thermal explosion to detonation. In *Shock Compression of Condensed Matter 2001*, AIP Conference Proceedings 620, pages 1069–1072. New York, 2001.

[179] H W Hubbard and M H Johnson. Initiation of detonations. *Journal of Applied Physics*, 30(5), 1959.

[180] C M Tarver. Effects of exothermic binders on times to explosion of HMX-based plastic bonded explosives. In *Fourteenth International Detonation Symposium*. Office of Naval Research, 2010.

[181] D J Chapman. Shock-compression of a binder system. University of Cambridge Report SP1213A, 2010.

[182] A W Campbell and J R Travis. The shock desensitisation of PBX9404 and composition B3. In *Eighth Symposium (International) on Detonation 1985*, volume NSWC MP 86-194, pages 1057–1068. Naval Surface Weapons Center, 1985.

[183] S A Sheffield, R L Gustavsen, and R R Alcon. In-situ magnetic gauging technique used at LANL - method and shock information obtained. In *Shock Compression of Condensed Matter 1999*, AIP Conference Proceedings 505, pages 1043–1048. New York, 1999.

[184] R L Gustavsen, B D Bartram, and N J Sanchez. Detonation wave profiles measured in plastic bonded explosives using 1550 nm photon doppler velocimetry. In *Shock Compression of Condensed Matter 2009*, AIP Conference Proceedings 1195, pages 253–256. New York, 2009.

[185] A P Esposito, D L Farber, J E Reaugh, and J M Zaug. Reaction propagation rates in HMX at high pressure. *Propellants, Explosives, Pyrotechnics*, 28(2):83–88, 2003.

[186] S F Rice and M F Foltz. Very high pressure combustion: reaction propagation rates of nitromethane within a diamond anvil cell. *Combustion and Flame*, 87:109–122, 1991.

[187] J M Zaug, C E Young, G T Long, J L Maienschein, E A Glascoe, D W Hansen, J F Wardell, C K Black, and G B Sykora. Deflagration rates of secondary explosives under static MPa–GPa pressure. In *Shock Compression of Condensed Matter 2009*, AIP Conference Proceedings 1195, pages 420–423. New York, 2009.

[188] R Menikoff. Private communication. LANL.

[189] M J Ward, S F Son, and M Q Brewster. Steady deflagration of HMX with simple

kinetics: a gas phase chain reaction model. *Combustion and Flame*, 114:556–568, 1998.

[190] G E Andrews and D Bradley. The burning velocity of methane – air mixtures. *Combustion and Flame*, 19:275–288, 1972.

[191] M Metghalchi and J C Keck. Burning velocities of mixtures of air with methanol, isooctane, and indolene at high pressure and temperature. *Combustion and Flame*, 48:191–210, 1982.

[192] B Leal, G Baudin, J C Goutelle, and H N Presles. An optical pyrometer for time resolved temperature measurements in detonation wave. In *Eleventh International Detonation Symposium*, volume ONR 33300-5, pages 353–361. Office of Naval Research, 1998.

[193] Y B Zeldovich and G I Barenblatt. Theory of flame propagation. *Combustion and Flame*, 3(1):61–74, 1959.

[194] P Vieille. Etude sur le mode de combustion des substances explosives, 1893.

[195] T Kanit, S Forest, I Galliet, V Mounoury, and D Jeulin. Determination of the size of the representative volume element for random composites: statistical and numerical approach. *International Journal of Solids and Structures*, 40:3647–3679, 2003.

[196] K L Finn. Derivation and validation of additional non-reacted Hugoniot data for EDC37 and PBX9501. Internal AWE Report, 2007.

[197] D M Dattelbaum, S A Sheffield, D B Stahl, A M Dattelbaum, W Trott, and R Engelke. Influence of Hot Spot Features on the Initiation Characteristics of Heterogeneous Nitromethane. In *Fourteenth International Detonation Symposium*. Office of Naval Research, 2010.

[198] D E A van Odyck. Private communication. Cambridge University.

[199] L Borne. Explosive crystal microstructure and shock-sensitivity of cast formulations. In *Eleventh International Detonation Symposium*, volume ONR 33300-5, pages 657–663. Office of Naval Research, 1998.

[200] B D Lambourn, N J Whitworth, C A Handley, and H R James. On the relationship between the non-reacted and detonation products equations of state for an explosive. In *Shock Compression of Condensed Matter 2009*, AIP Conference Proceedings 1195, pages 53–56. New York, 2009.

[201] C S Yoo and H Cynn. Equation of state, phase transition, decomposition of β-HMX at high pressures. *Journal of Chemical Physics*, 111(22):10229, 1999.

[202] J C Gump and S M Peiris. Isothermal equations of state of beta octahydro-1,3,5,7-

tetranitro-1,3,5,7-tetrazocine at high temperatures. *Journal of Applied Physics*, 97:53513, 2005.

[203] D E Hooks and K J Ramos. Initiation mechanisms in single crystal explosives: dislocations, elastic limits and initiation thresholds. In *Thirteenth International Detonation Symposium*, volume ONR 351-07-01, pages 455–464. Office of Naval Research, 2006.